Exciton Dynamics in Synthetic Multi-Chromophoric Model Systems

A thesis submitted to the School of Chemistry at the University of East Anglia in partial fulfilment of the requirements for the degree of Doctor of Philosophy

Giovanni Bressan

October 2019

in loving memory of my grandfather Giovanni

Acknowledgements

In this thesis I have condensed the results of three years of learning and research, during which a large number of people have been helpful in different ways. Acknowledging everyone here would result in too large of a Section, so I will mostly restrict it to the people who had a direct impact on my research project.

First and foremost I thank my first primary supervisor Ismael A. Heisler for helping me in every step of the Ph.D., from inviting me to apply at UEA despite my lack of experience on time-resolved spectroscopy, to help on the writing of the research proposal, teaching me the basics of femtosecond spectroscopies, developing the LabVIEW code used to control the experiments and analyse the data and discussing results, even after he left UEA to take a Professorship at UFPR.

Another lucky break was having Professor Steve Meech as primary supervisor. His advice has been priceless, I have learned a lot discussing experimental results with him and I have deep admiration for his scientific skills and for the way he guides the group. I am very grateful for his accurate proof reading on this thesis and for suggesting improvements.

I also thank Garth Jones for supervising me, and for the helpful discussions we had about the theory of multidimensional spectroscopy. His help in performing DFT calculations on perylene bisimides and porphyrin - subphthalocyanine dimers has been priceless. I also want to thank him for proof reading the Theory section of this thesis.

Other people in the group and at UEA who were not directly involved in this project also had considerable impact along the way have been Dale Green, Chris Hall, Jamie Conyard and Katrin Adamczyk. Moreover, I wanna thank the technicians and the administrative and IT staff from the School of Chemistry at UEA.

The samples here studied have been synthesised by the groups of Professor Phil Page and Professor Andy Cammidge at UEA and by the group of Professor Harry Anderson at University of Oxford and without their work I could have not performed the experiments which are described in this thesis.

Unrelated to the research work, I want to thank Caterina, Francesco, Livia, Marco, Nicholas and Valeria for their friendship and support during the last year of my Ph.D.. I also want to thank Gareth, Gerald, Greg, Peter, Ross, Salman, Tom, Zara and the whole of the UEA Fell and Mountaineering Club. I also wanna thank my

friends who don't live in Norwich or in the UK for their long distance support. In the same way I want to thank my mum and dad for sparking curiosity and interest for science in me and the whole of my family.
My Ph.D. would not have been possible without the funding provided by UEA, for which I am extremely grateful and I also thank the EPSRC for having funded our lab.

Abstract

Investigating the excitonic properties of synthetic multichromophoric model systems can give insights into the behaviour of larger and more intricate structures, such as the photosynthetic complexes found in autotrophs or materials with applications in the area of organic photovoltaics (OPV).

The unique properites of excitons depend critically on the electronic excited states of these systems, which present non-local character, and have short lifetimes. Hence, in order to characterise their dynamics it is helpful to employ laser spectroscopic techniques with ultrafast time resolution. Among these, the most widespread is broadband femtosecond transient absorption (fsTA), a two-pulse technique which has the drawback of being intrinsically ambiguous on the excitation frequency. A way to overcome this disadvantage is presented by two-dimensional electronic spectroscopy (2D-ES). In 2D-ES, the introduction of a third pulse allows the recovery of spectra in which excitation and detection frequencies are correlated on a two-dimensional surface. 2D-ES and fsTA have been used in a complementary fashion throughout this thesis in order to investigate photophysical processes in a range of different synthetic multichromophoric model systems.

Experiments have been performed on a series of covalently-bound perylene bisimide (PBI) J-dimers. Here 2D-ES allowed us to identify a one- to two-exciton state transition in the strongly coupled dimer, which vanishes in the monomer or when the coupling is weakened. Such a transition is purely electronic in character, as confirmed by the calculated spectra, and its energy allowed us to estimate the excitonic coupling strength.

We further report fsTA and 2D-ES studies of a subphthalocyanine-Zn porphyrin (SubPc-O-ZnTPP) heterodimer. fsTA allowed us to characterise the excitation energy transfer (EET) between the SubPc and ZnTPP moieties, which is well reproduced by the Förster model, while 2D-ES was used to observe sub-ps spectral diffusion, which is shown to be too fast to influence the incoherent EET.

These studies were extended to larger systems. fsTA has been performed on a range of fully-conjugated porphyrin nanorings. fsTA and transient anisotropy on six-membered rings, with or without an inner template, revealed structural dynamics in the ground and in the excited states of the untemplated structure, which do not disrupt the exciton delocalisation.

Finally, fsTA at increasing pump fluences allowed us to study exciton-exciton annihilation (EEA) dynamics in nanorings made up of 10, 20, 30 and 40 porphyrin units. Experiments confirmed that the exciton size is approximately 20 repeating units, and comparison with a one-dimensional diffusion model allowed estimation of the exciton diffusion coefficients, which decrease as the ring size increases, a result assigned to the increased static disorder experienced in larger structures.

List of acronyms in alphabetical order

- 2D(ES): two dimensional (electronic spectroscopy)
- 3PPE: 3 pulse photon echo
- CCD: Charge coupled device
- CLS: Centre line slope
- CPA: Chirped pulse amplifier
- DADS: Decay associated differential spectrum
- DHO: Displaced harmonic oscillator
- EADS: Evolution associated differential spectrum
- EEA: Exciton-exciton annihilation
- EET: Electronic energy transfer
- ESA: Excited state absorption
- (F)FT: Fast Fourier transform
- FRET: Förster resonant energy transfer
- FROG: Frequency resolved optical gating
- fsTA: Femtosecond transient absorption
- fsTAn: Femtosecond transient anisotropy
- FWHM: Full width at half maximum
- GSB: Ground state bleach
- GVD: Group velocity dispersion
- IC: Internal conversion

- IRF: Instrument response function
- ISC: intersystem crossing
- IVR: Intramolecular vibrational energy redistribution
- LO: Local oscillator
- NIR: Near infrared
- NMR: Nuclear magnetic resonance
- (N)OPA: (Noncollinear) optical parametric amplifier
- OD: Optical density
- OPV: Organic photovoltaic
- PES: Potential energy surface
- SE: Stimulated emission
- SNR: Signal to noise ratio
- SVD: Singular value decomposition
- SWL(G): Supercontinuum white light (generation)
- (TD-)DFT: (Time dependent) density functional theory
- TDM: Transition dipole moment
- TG: Transient grating
- UV: ultraviolet
- VC: Vibrational cooling
- YAG: Yttrium aluminium garnet

Contents

Publications

Some of the results contained in this thesis have been published in peer-reviewed journals, in detail:

- the data and results presented in Chapter 5 have been published as "One- to Two-Exciton Transitions in Perylene Bisimide Dimer Revealed by Two-Dimensional Electronic Spectroscopy" in The Journal of Physical Chemistry A. DOI: 10.1021/acs.jpca.8b11473

- the data and results presented in Chapter 6 have been published as "Electronic Energy Transfer in a Subphthalocyanine - Zn Porphyrin Dimer Studied by Linear and Nonlinear Ultrafast Spectroscopy" in The Journal of Physical Chemistry A. DOI: 10.1021/acs.jpca.9b04398

- the data and results presented in Chapter 7 have been published as "Time-Resolved Structural Dynamics of Extended π-Electron Porphyrin Nanoring" in The Journal of Physical Chemistry C. DOI: 10.1021/acs.jpcc.9b07494

Chapter 1

Introduction

Time resolved spectroscopic techniques yield information about the dynamics of matter in real time. Such techniques rely on the observation of non-linear optical signals which originate from the interaction of a number of electromagnetic fields with the material system studied. The technological developments which made the generation and amplification of ultrashort laser pulses possible sparked the investigation of phenomena occurring on the femtosecond timescale;[1] the current goal in the field is the generation and control of attosecond pulses[2;3] to further improve time resolution and to explore other regions of the electromagnetic spectrum (XUV, X rays). In molecular spectroscopy, a number of important photophysical and photochemical processes, such as energy transfer,[4;5] charge separation,[6;7] solvation dynamics,[8] photoisomerisations,[9] coherent wavepacket motion,[10] and structural dynamics[11] have been studied by ultrafast time-resolved spectroscopic techniques.
Broadly speaking, non-linear spectroscopies can be divided into two categories: resonant and non-resonant. Resonant techniques are emission and absorption based methods, which includes the experiments employed in this thesis. To track in real time the dynamical evolution of a material system with absorption spectroscopies, the time delay between, at least, a pair of laser pulses, has to be scanned. The lowest order signals measured in nonlinear spectroscopic techniques will be, at least, of second order ($\chi(2)$) in the field of the pulses. Although, for symmetry-related reasons, in isotropic media, the second order nonlinear optical susceptibility $\chi(2) = 0$, making third order ($\chi(3)$) techniques the most widely used, with the most common being broadband femtosecond transient absorption (fsTA)[1], colloquially referred to as pump-probe spectroscopy.
In a fsTA experiment, the sample interacts first with a "pump" pulse, and after a given delay time it is illuminated again with another pulse, called the "probe", which is then measured (in the frequency domain) after its interaction with the sample, as shown in Figure 1.1(a). An optical chopper is placed in the pump pulse beam, with the aim of alternately detecting probe pulses for which the sample has been previously perturbed by the pump pulse, and probe pulses recorded in the absence

of a pump pulse. Through this modulation it is possible to compute differential probe spectra between the pump-on and pump-off conditions; such differential spectra will report the effect of the pump-induced perturbation on the probe absorption spectrum at a given value of the time interval between the first (pump) and the second (probe) pulses. The systematic variation of the time interval reveals dynamical information on the system. Because fsTA is an absorption technique, it permits the

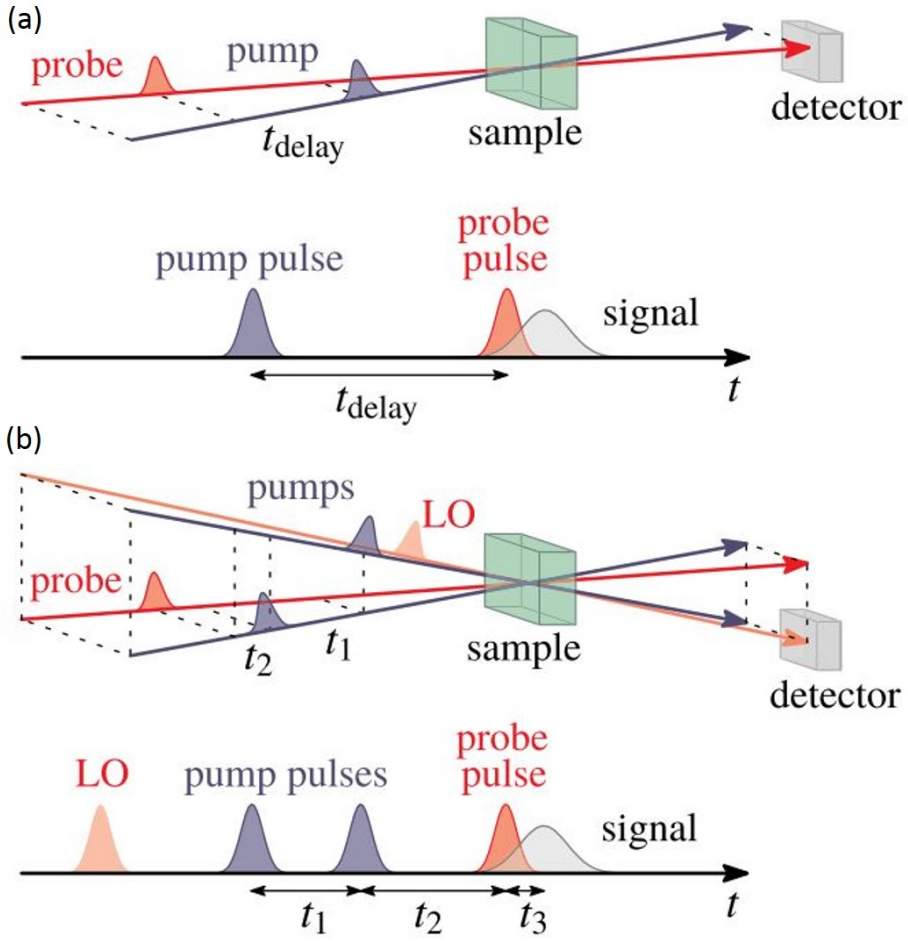

Figure 1.1: Schemes of time-resolved spectroscopic techniques that can provide time- and excitation/detection frequency-resolved information. (a) fsTA spectroscopy. (b) 2D-ES (BOXCARS scheme). Top (a, b), spatial arrangement of the pulses, sample and detector; bottom (a, b), temporal arrangement of the pulses and signal emission. The Local Oscillator (LO) is a fourth pulse which allows to perform heterodyne detection, hence to recover amplitude and phase of the measured signal. Adapted from Gelzinis *et al.*[12]

recovery of dynamics concerning both the ground and electronically excited states, while emission techniques, such as fluorescence, only retrieve information about the evolution of excited electronic. states[13] Because of the large amount of information contained in a fsTA spectrum, where there are often a number of overlapping signals, the interpretation can be challenging.

Another intrinsic problem of fsTA arises from its temporal resolution. Ultrashort laser pulses are intrinsically broad in the frequency domain, due to the time-bandwidth

uncertainity, hence a pump-probe experiment can have sub-10 fs time resolution, but the pump-induced changes in the probe absorption spectrum at a frequency ω_3 could be due to an absorption which had occurred at a different ω_1 frequency, if both ω_1, ω_3 are contained within the spectral bandwidth of the pump pulse. Conversely, if higher spectral resolution on the excitation frequency is needed, narrow-band pump pulses have to be used, but again, due to the time-bandwidth uncertainty, this pulse will be intrinsically longer, thus losing time resolution. In brief, every fsTA experiment has to deal with the trade-off between the capability of measuring ultrafast dynamics and the capacity of assigning the pump frequency responsible for them.
A way of overcoming this problem is represented by two-dimensional electronic spectroscopy[14;15] (2D-ES). 2D-ES, when experimentally implemented in a fully-noncollinear geometry, as it is in our case, combines the advantages of two three-pulse variants of pump-probe spectroscopy, transient grating (TG) and three-pulse photon echo (3PPE) spectroscopies.
In TG techniques, the pump pulse is split into two replicas which interact, at the same time, with the sample, from two different spatial directions. After the subsequent interaction with the probe pulse, the sample will emit a signal in a phase-matched direction, which will not be collinear with either the pump or the probe, allowing background-free detection and, hence, increased signal-to-noise ratio. This can be thought as the pair of pump pulses inducing periodic modulations of the refractive index in the sample, creating a (transient) grating, which diffracts the probe pulse according to the Bragg equation.
In 3PPE, high time and frequency resolution are simultaneously obtained through the use of a Fourier transform. In this case, the pump is also replaced by a pair of pump pulses, propagating along the same direction, but which interact with the sample at a relative, adjustable, time delay. Thus, the resolution over the pump frequency is obtained by scanning the relative delay between the two replicas of the pump pulse. In this way, it is possible to use pump pulses as short as needed without losing frequency resolution.
Combination of the distinctive features of TG and 3PPE spectroscopies leads to 2D-ES. In 2D-ES experiments, the pulse sequence and geometry of which are shown in Figure 1.1(b); the pair of pump pulses have different directions of propagation, and times at which they interact with the sample (t_1 in Figure 1.1(b)). Moreover, a fully-noncollinear geometry supports the use of an additional laser pulse, usually referred to as local oscillator (LO), permitting heterodyne detection, an interferometric method through which it is possible to retrieve the amplitude and phase of the third order signal.[14] Since a scan over t_1 values is performed for a number of delay points between the second pump and the probe pulses (t_2), the resulting data will be a collection of maps correlating excitation and emission frequency for every t_2 time: $S(\omega_1, t_2, \omega_3)$. We will show (in Section 2.5) how this signal is the convolu-

tion of the three laser pulses with the third order response function of the material system. We further show that this signal yields the highest amount of information which can be inferred from a third-order technique. An example of a 2D spectrum is shown in Figure 1.2, where both diagonal and off diagonal features, originating from the coupling between electronic states of neighbouring molecules, are evident.

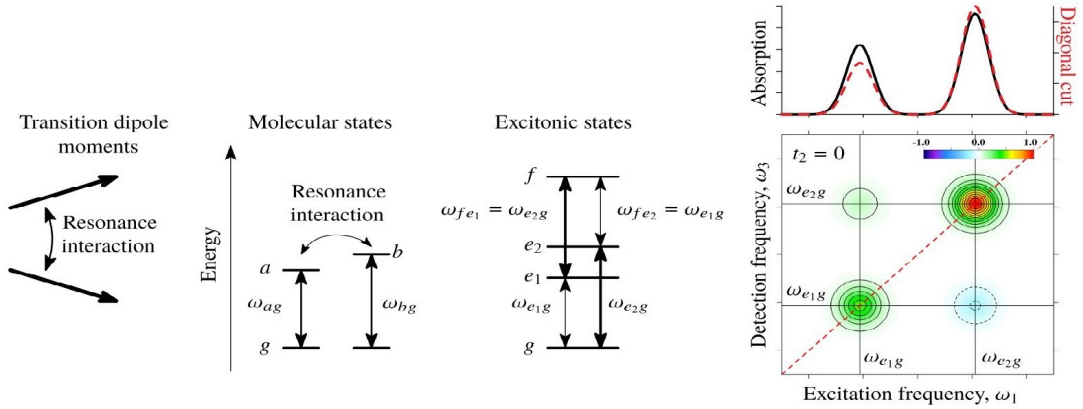

Figure 1.2: Example of a 2D spectrum of a dimer with two coupled two-level systems. Left, depiction of the orientation of the transition dipole moments; centre, energy level diagrams depicting both the molecular and the excitonic states; right, 2D spectrum of the dimer system at $t_2 = 0$; top, steady-state absorption spectrum of the dimer (solid black line) and the diagonal cut of the 2D spectrum (red dashed line). The 2D spectrum is normalised to the maximum of its positive amplitude and positive signals of increasing amplitude are depicted in green, yellow, orange and red; negative signals of increasing amplitudes are represented in light blue, blue and violet. Adapted from Gelzinis *et al.*[12]

Fourier Transform multi-pulse experiments are of course routine in nuclear magnetic resonance spectroscopy (NMR), following their first demonstration, more than forty years ago.[16] The contrast between the two frequency ranges (MHz versus multi THz) employed in the two techniques illustrates the additional challenges associated with the optical frequency domain. The main difference is that wavelengths in the visible, a region comprised between 400 and 750 nm, have their optical cycles of $\sim$ 2 fs (for light at 530 nm), compared to 2 ns for radiation at 500 MHz. Hence, in order to properly measure the excitation frequencies, the accuracy needed when scanning the time delay between the pair of pump pulses (t_1) must be a fraction of femtosecond. The main difficulty to overcome is related to the fact that vibrations of the laboratory environment and its air flow can induce sub micrometre mechanical displacement of the optical components held on the table. Such small mechanical fluctuations affect the beam path and thus substantially prejudice the quality of the measured data. This issue is known as phase-stability and it will be extensively discussed in Section 4.5.

Because of these experimental constraints, two dimensional spectroscopy was demonstrated for the first time only in the 1990s, both with visible[17] and infrared[18] laser

pulses. The phase stability condition is relatively easier to satisfy in the infrared due to longer wavelengths, so the technique was most rapidly developed in that spectral region. In addition, when working in the IR, the acquisition of data at a few t_2 delays is often sufficient to retrieve meaningful information about the structure of proteins,[18] or DNA.[19] Conversely, in the visible it is usually necessary to record a large number of 2D spectra at different t_2 values, as in a fsTA experiment; this difference translates to longer data acquisition times over which it is required to keep the phase between the pair of pump pulses stable.
A number of technical developments realised by different research groups over the years made 2D-ES a much more feasible technique, although it still presents many more challenges than standard fsTA. For this reason, in this thesis we have been using both fsTA and 2D-ES in a complementary fashion, depending on the kind of photophysical process we wanted to investigate.
In the following pages a number of photophysical and photochemical phenomena which and have been investigated with 2D-ES or fsTA are reviewed.

Intramolecular Couplings and Coherences

One of the main features that brought 2D-ES to prominence was its intrinsic capability of detecting electronic couplings. Electronic couplings are intrinsically important in some of the processes which are responsible for life on planet Earth, most notably in photosynthesis, where coupling is essential to light harvesting and charge separation. Such coupled transition give rise to off-diagonal signals, detectable from the earliest measurable population times, in 2D spectra (illustrated in Figure 1.2). Excited state electronic couplings have been observed, with 2D-ES, in studies of molecular aggregates,[20] semiconducting structures,[21–23] photosynthetic complexes,[24;25] and artificial polymers.[26] These signatures come from couplings, for example between electronic and vibrational states,[27] and they are used to discriminate between the different types of coupling.[27] In addition to the presence of off-diagonal peaks at early (zero) population times, a superposition between two coupled states can be prepared by a laser pulse which is broad enough to cover both transitions.[12;28;29] Such a coherence will oscillate during the population time with a frequency proportional to the energy splitting between the states. Hence, amplitude oscillations as a function of the population time will be found at different locations in the 2D spectra.[30] For example, Buktus *et al.*[31] used two-dimensional electronic spectroscopy to disembroil the energy level structure of a six-membered fully π-conjugated porphyrin nanoring. This was done by plotting and analysing the amplitude of the Fourier transform of the rephasing 2D data taken oven t_2 at selected (positive and negative) frequencies, which yields the splittings between the different states.

Another notable example of interchromophore coupling in an excitonic dimer revealed through 2D-ES was given by Halpin *et al.*[32] In this case 2D-ES was used to study exciton dynamics in a vibronic homodimer made up of two, covalently linked, cyanine units held together by two butyl spacers. The steady-state absorption spectrum of this system shows a strong vibronic progression, due to coupling of a C=C stretching mode in the $S_0 \rightarrow S_1$ transition, which is delocalised over the whole dimer and with a spacing of 1220 cm^{-1}. In this system, the bulk of the oscillator strength is carried by two transitions, called A and B, lying at 19730 and 18300 cm^{-1}, respectively, making the electronic and vibrational spacings quasi degenerate. 2D-ES measurements, with a laser spectrum centred at 18500 cm^{-1}, showed presence of diagonal peaks, assigned to GSB and SE, and matching the steady-state data, along with cross peaks present from $t_2 = 0$. The dynamical evolution of the 2D spectra shows enhancement of the coherence between A and B states, revealed as an intense amplitude modulation,occurring during t_2, of an excited state absorption (ESA).

Energy Transfer Mechanisms

Among the processes that can be probed by 2D-ES and fsTA, energy transfer between different excited states is well studied. Energy transfer can be observed through the time evolution of the signals of the donor and acceptor moieties in the 2D-ES or fsTA spectra. 2D-ES is well suited to study such dynamics because information about energy transfer can easily be obtained looking at the presence, and at the time evolution, of cross peaks, such as the ones centred at $(\omega_1 = \omega_{e2g}, \omega_3 = \omega_{e1g})$ and $(\omega_1 = \omega_{e1g}, \omega_3 = \omega_{e2g})$ in Figure 1.2. Energy transfer and its mechanisms have been extensively studied in both natural[25;33–38] and synthetic[32;39;40] photosynthetic systems. As an example we summarise a study by Kudisch *et al.*,[41] in which energy (and electron) transfer in a flexible perylene-phthalocyanine flexible dimers have been investigated, in a variety of solvents, via fsTA spectroscopy. The transient data, showed that, after excitation of the perylene (donor) moiety at 540 nm, the rate of the excitation energy transfer to the zinc phthalocyanine (acceptor) moiety displays a solvent dependence, which the authors explain in terms of changes in the relative equilibrium orientation of donor and acceptor moieties. These observations were rationalised with reference to the nature of the flexible linker joining the two moieties, together with the doubly degenerate nature of the Q-band transitions in Zn phthalocyanine. 2D-ES has also often been used to study EET dynamics,[42;43] as an example we mention the paper by Thyrhaug *et al.*,[37] which analysed the behaviour of cross-peaks in 2D-ES of the Fenna-Matthews-Olson (FMO) photosynthetic complex to infer information about the population dynamics between exciton states on the fs-ns timescale.

Exciton Exciton Annihilation in Multichromophoric Systems

The decay of excitons which are not strongly bound can be dominated by exciton-exciton annihilation (EEA) processes. Such an effect has been observed, with the help of fsTA, in a variety of systems such as semiconductor monolayers,[44] metal halide nanotubes,[45] graphene nanoribbons,[46] chromophoric thin films[47] and aggregates[48–51] and natural photosynthetic systems.[52;53] These deactivation process depend on the density, which is proportional to the intensity of the excitation pulse, and on the mobility of the excitons themselves.[54–56] In a work by Marciniak *et al.*[57] EEA dynamics in self assembled tetraphenoxy subsituted perylene bisimide aggregates were investigated through fsTA as a function of increasing pump fluence, in order to determine the exciton mobility. fsTA data at low excitation energy show population dynamics occurring in the ps-ns timescale without significant spectral evolution within this time window. However, with increasing pump fluence, a faster decay of the exciton signal is observed. This effect was assigned by the authors to EEA, which occurs when two excitons come close to each other, bringing one to a higher excited state and the other one back to the ground state, conserving the overall energy of the system. The rate determining step of the EEA process can be diffusion (that can take place in one or three dimensions,l depending on the aggregate structure) of the exciton, or long-range, Förster type, exciton interactions. Therefore, comparing the experimental evolution of the exciton signals at increasing pump fluence with the predictions of different models, it is possible to draw conclusions about the nature of exciton mobility and transport. In Chapter 8 we have extended such analysis to multichromophoric ring structures.

In this Chapter we have given a brief introduction to 2D-ES and fsTA. The underlying theory is reviewed in detail in Chapter 2 and their experimental implementation is described in Chapters 4 and 3, respectively. We have also introduced and provided a literature review of processes which stimulated the research presented in Chapters 5, 6, 7 and 8, on Perylene Bisimide dimers, a flexible subphthalocyanine - Zn porphyrin heterodimer, on six-membered and larger (10 to 40) fully conjugated, butadiyne linked, porphyrin nanorings, respectively.

Chapter 2

Theoretical Framework

The core of this thesis will be the study of exciton dynamics in synthetic multi-chromophoric model systems. These processes were experimentally studied in real time using 2D-ES and broadband fsTA. The *corpus* of theoretical knowledge needed in order to describe and interpret the results of these experiments properly is quite large, and it ranges from basic quantum mechanics,[58;59] classic electromagnetism,[60] to statistical mechanics.[61] Concepts from density matrices,[62] nonlinear optics,[63] lineshape theories,[64] and the physics of ultrashort laser pulses[65] are relevant to the description of the these techniques.

Giving a complete and satisfactory review of all this material is not the purpose of this Chapter. Instead, we will be focused on presenting the background needed to interpret the experimental results through the use of the double-sided Feynman diagrams (also referred as Liouville-space pathways) in the semi-classical perturbation theory framework established by Mukamel.[66]

The Chapter will be structured in the following manner: In Section 2.1 a description of the density matrix will be given. The density matrix can be shown to be the equivalent to the usual wavefunction formalism, but it allows the description of a statistical ensemble of molecules interacting with an electromagnetic field, intense enough to be described with the usual Maxwell's equations. In Section 2.2 the results from the previous section are used to tackle the general problem of obtaining dynamical information for a system evolving under a time-dependent Hamiltonian in the density matrix framework. This will be done by splitting the Hamiltonian into a stationary part plus a time-dependent perturbation, which has small energy compared to H_0. In Section 2.3 we make explicit that the time-dependent perturbation is an electromagnetic field, and we introduce the point-dipole approximation, which allows treatment the field-matter interaction in a semi-classical way. Consequently, a general expression which relates the n^{th} order polarisation of a material system with a number of interactions between transition dipole moments and the density matrix of the system is presented.

In Section 2.4, the linear (first order) response function for a two-level system is

obtained evaluating the general expression introduced in Section 2.3 for the simplest case in which $n = 1$. During the discussion, the main ideas underlying the double-sided Feynman diagram formalism are introduced, including the Rotating Wave Approximation.
The same approach is used to derive the third-order polarisation and response functions in Section 2.5. In Section 2.5 the goal is to highlight how, for higher order perturbations, the diagrammatic approach allows derivation of all the possible Liouville-space pathways in a quicker way than solving the equation derived in Section 2.3 for $n = 3$. In Section 2.6 the double-sided Feynman diagrams are connected to the observables and the experimentally controllable parameters of 2D-ES and fsTA spectroscopies, highlighting the lack of frequency resolution of fsTA in comparison to 2D-ES. This is done from the perspective of the lack of time ordering between the first two field-matter interactions in the Feynman diagrams. In Section 2.6.1 the phase matching conditions relative to a 2D signal with relation to the geometry of the experimental setup are introduced while in 2.6.2 the differences between rephasing and non rephasing Liouville-space pathways are discussed.
Section 2.7 describes how the increased number of possible transitions between the different states of a displaced harmonic oscillator (DHO) model generate 32 possible Feynman diagrams. Some of these will have a vibrational (or vibronic) coherence during T, which will lead to amplitude oscillations, occurring at positive or negative frequencies. Following that, the predicted positions of these signals on a 2D map will be discussed. The study of coherent oscillations through 2D-ES and their origin (vibronic or electronic) is a topic of intense interest in the ultrafast spectroscopy community, for this reason in Section 2.8 the same approach as in Section 2.7 is used to retrieve all the possible Feynman diagrams for an electronic system with 2 closely spaced excited electronic states and to mark their predicted position on the 2D spectra. Subsequently, comparisons between vibrational and electronic coupling cases are made.

2.1 Density Matrix

The density operator for a system consisting of a statistical average of a number N of different states $|\psi^j\rangle$, each of these corresponding to a probability p^j, is defined as:[58;66]

$$\hat{\rho} \equiv \sum_{j=1}^{N} p^j \, |\psi^j\rangle \, \langle\psi^j| \tag{2.1}$$

The density matrix formalism of quantum mechanics is completely equivalent to the wavefunction approach,[58] we need equations to compute:

- the expectation value for a given operator,
- the dynamics of the system (its time evolution).

It can be shown that the expectation value for an operator $\hat{A}$ is just the trace of the product matrix between $\hat{A}$ and $\hat{\rho}$.

$$\langle \hat{A} \rangle = \sum_n (\rho A)_{nn} = \mathrm{Tr}(\rho A) \tag{2.2}$$

The time evolution of a system in the density matrix formalism, can be described with the quantum Liouville-von Neumann equation, which is, in its most common form:

$$\frac{\partial \hat{\rho}_{nm}}{\partial t} = -\frac{i}{\hbar}\big[\hat{H}, \hat{\rho}\big] \tag{2.3}$$

If we derive Equation 2.3 starting from a mixed state, the resulting Equation will also carry a first term accounting for dynamical effects, such as **population relaxation** and **dephasing**.[67] The most general case for the quantum Liouville-von Neumann equation is:

$$\frac{\partial \hat{\rho}_{nm}}{\partial t} = \sum_{j=1}^{N} \frac{\mathrm{d}\, p^j}{\mathrm{d}\, t} c_m^{j*} c_n^j - \frac{i}{\hbar}\big[\hat{H}, \hat{\rho}\big] \tag{2.4}$$

In which $^{\mathrm{d}\, p^j}/_{\mathrm{d}\, t}$ accounts for the change of the probability of finding the system in the state j over time, in other words all the statistical dynamical information of the ensemble are contained in this derivative.

2.2 Semi-Classical Perturbative Theory

Using the Equations in Section 2.1 it is possible to model the molecular systems studied with ultrafast spectroscopy. The most effective way to include the interaction between an optical field and a material system in the Hamiltonian is perturbation theory. The physical meaning of perturbative theory is that the perturbations (the laser pulses) are too weak to change the eigenstates of the system, but they can induce changes in the coefficients (populations) of the eigenstates. We begin by splitting the total Hamiltonian into a time-independent and a time-dependent part, in the following manner:

$$\hat{H}(t) = \hat{H}_0 + \hat{W}(t). \tag{2.5}$$

To proceed, we must clarify that usually time-dependent quantum mechanics is described in the so-called **interaction picture**. The interaction picture is an intermediate case between the Schrödinger and Heisenberg pictures, in which we have, respectively, time dependent wavefunctions or operators.[58;59;66;67] Briefly, any operator (observable) can be described in the interaction picture as:

$$\hat{W}_I(t) = e^{\frac{i}{\hbar}\hat{H}_0 t} \hat{W}(t) e^{-\frac{i}{\hbar}\hat{H}_0 t}. \tag{2.6}$$

We can now substitute the operator $\hat{W}_I(t)$ defined in the manner shown above, into equation 2.5, which, after integrating, substituting it into itself and applying on

both sides the propagator $\hat{U}_0(t, t_0)$ to go back to the Schrödinger's representation, gives the following:[67]

$$\hat{\rho}(t) = \hat{\rho}^{(0)}(t) + \sum_{n=1}^{\infty} \left(\frac{i}{\hbar}\right)^n \int_{t_0}^{t} \mathrm{d}\,\tau_n \int_{t_0}^{\tau_n} \mathrm{d}\,\tau_{n-1} \int_{t_0}^{\tau_2} \mathrm{d}\,\tau_1 \times \hat{U}_0(t, t_0)[\hat{W}_I(\tau_n), [\hat{W}_I(\tau_{n-1}), ...[\hat{W}_I(\tau_1), \hat{\rho}_I(t_0)]...]]\hat{U}_0^{\dagger}(t, t_0) \quad (2.7)$$

In this case, $\hat{\rho}^{(0)}(t)$ is the density matrix of the unperturbed system and $\hat{U}_0^{\dagger}(t, t_0)$ is the Hermitian conjugate (the adjoint) of $\hat{U}_0(t, t_0)$. Applying the same notation to all the terms of the series expansion, we obtain:

$$\hat{\rho}(t) = \hat{\rho}^{(0)}(t) + \sum_{n=1}^{\infty} \hat{\rho}^{(n)}(t), \quad (2.8)$$

where, $\hat{\rho}^{(n)}(t)$ represents the density matrix at the n^{th}-order and contains information about a number n of interactions with the time-dependent operator $\hat{W}_I(t)$.

2.3 The Density Matrix Formalism in Non-linear Optics

The results presented so far were just related to the use of the density matrix as a convenient way to describe a dynamical quantum system with a statistical distribution of variables. Now, the aim of this section is to introduce an optical field as the time-dependent term in Equation 2.5. We make the assumption that the incident wavelength is much larger than the size of the molecular system, and the number of photons is high enough to treat them as a classical field, but not high enough to induce higher order perturbations.

If all the conditions stated above hold, the material system can be modelled as a point dipole, which will have an electric dipole moment operator* $\hat{\mu}$ and an electromagnetic wave with field $E(t)$. We have then:

$$\hat{W}(t) = -\hat{\mu}E(t) \quad (2.9)$$

*The matrix form of the dipole operator μ_{ij} can be described in an intuitive way if we think about the diagonal term $i = j$ as the components of the permanent dipole moment, whereas the off-diagonal terms $i \neq j$ (their squares) are proportional to the oscillator strength of the $j \leftarrow i$ transitions.[67]

Now, the substitution of Equation 2.9 into Equation 2.7, yields:

$$\hat{\rho}(t) = \hat{\rho}^{(0)}(t) - \sum_{n=1}^{\infty} \Big(- \frac{i}{\hbar} \Big)^n \int_{t_0}^{t} \mathrm{d}\,\tau_n \int_{t_0}^{\tau_n} \mathrm{d}\,\tau_{n-1} \int_{t_0}^{\tau_2} \mathrm{d}\,\tau_1 E(\tau_n)E(\tau_{n-1})...E(\tau_1) \\ \times \hat{U}_0(t,t_0)[\hat{\mu}_I(\tau_n),[\hat{\mu}_I(\tau_{n-1}),...[\hat{\mu}_I(\tau_1),\hat{\rho}_I(t_0)]...]]\hat{U}_0^{\dagger}(t,t_0). \quad (2.10)$$

Here, the n^{th} term of the truncated series contains n interactions with the electric field, as the polarisation induced in a material system is usually described in non-linear optics:[63]

$$\mathbf{P} = \epsilon_0(\chi^{(1)}\mathbf{E} + \chi^{(2)}\mathbf{EE} + \chi^{(3)}\mathbf{EEE} + ...) \quad (2.11)$$

The macroscopic polarisation P is the observable which corresponds to the expectation value of the dipole moment operator:

$$P(t) = \mathrm{Tr}(\hat{\mu}\hat{\rho}(t)) \quad (2.12)$$

Recalling that the polarisation in the macroscopic observable corresponding to the transition dipole moment operator, using the property of the trace to be invariant under cyclic permutation and changing the absolute times in time intervals between the various field-matter interactions (which are an easily controlled experimental parameter in time-resolved spectroscopy experiments) in the following manner:

$$\begin{aligned} \tau_1 &= 0 \\ t_1 &= \tau_2 - \tau_1 \\ t_2 &= \tau_3 - \tau_2 \\ &\vdots \\ t_n &= t - \tau_n. \end{aligned}$$

we obtain an expression for the polarisation (as 2.11), which is:

$$P^{(n)}(t) = -\Big(-\frac{i}{\hbar}\Big)^n \int_0^{\infty} \mathrm{d}\,t_n \int_0^{\infty} \mathrm{d}\,t_{n-1}... \int_0^{\infty} \mathrm{d}\,t_1 \\ \times E(t-t_n)E(t-t_n-t_{n-1})...E(t-t_n-t_{n-1}-...-t_1) \\ \times \langle \hat{\mu}_I(t_n+t_{n-1}+...+t_1)[\hat{\mu}_I(t_{n-1}+...+t_1),...[\hat{\mu}_I(0),\hat{\rho}(-\infty)]...]\rangle \quad (2.13)$$

Looking at Equation 2.13, we can see how the n^{th} order polarisation is just the convolution of n electric fields with the nested commutators inside the angle brackets. The main difference between the Equations 2.11 and 2.13 is that in the first we have the susceptibilities $\chi^{(n)}$, defined in the frequency domain, whilst in the second we have their time-domain counterparts, named **Response functions** $R^{(n)}(t_n,...,t_1)$,

which are explicitly defined as:

$$P^{(n)}(t) = -\left(-\frac{i}{\hbar}\right)^n \int_0^\infty \mathrm{d}\, t_n \int_0^\infty \mathrm{d}\, t_{n-1} ... \int_0^\infty \mathrm{d}\, t_1 E(t-t_n)E(t-t_n-t_{n-1}) \\ ...E(t-t_n-t_{n-1}-...-t_1) \times R^{(n)}(t_n,...,t_1), \quad (2.14)$$

where $R^{(n)}(t_n,...,t_1)$ is:

$$R^{(n)}(t_n,...,t_1) = -\left(-\frac{i}{\hbar}\right)^n \langle \hat{\mu}_I(t_n+t_{n-1}+...+t_1)[\hat{\mu}_I(t_{n-1}+...+t_1),...[\hat{\mu}_I(0),\hat{\rho}(-\infty)]...]\rangle. \quad (2.15)$$

Equations 2.14 and 2.15 describe how the system will generate a signal after a number n of interactions with the optical fields.
The transitions induced by the laser pulses are taken into account in the commutators, while the time delays between the different pulses are accounted for in the integrals. Since, for symmetry-related reasons, in isotropic media, only odd-orders response functions can be non-zero, the first nonlinear effects that have to be taken into account will be third order ones.

2.4 Linear Response Theory

In the previous pages a connection between the quantum-mechanical description of a system and non-linear optics was made (Equations 2.14 and 2.15), these results can now be used to write the simplest response function, the linear one.
This will give a physical picture for a simple system, which provide the basis for an intuitive understanding of the third-order response function, which is actually fully recovered by 2D-ES experiments. Linear response means 1^{st} order, so we start setting $n = 1$ in Equation 2.15 and expanding the nested commutator, yielding:

$$R^{(1)}(t_1) = \frac{i}{\hbar}(\langle \hat{\mu}_I(t_1)\hat{\mu}_I(0)\hat{\rho}(-\infty)\rangle - \langle \hat{\mu}_I(t_1)\hat{\rho}(-\infty)\hat{\mu}_I(0)\rangle). \quad (2.16)$$

The polarization at the first order is given by:

$$P^{(1)}(t) = \int_0^\infty \mathrm{d}\, t_1 E(t-t_1)R^{(1)}(t_1) \quad (2.17)$$

If we know the matrix form of the initial states and of the dipole moments, we can calculate all the relevant quantities, but this is not the aim of this discussion. The relevant result to highlight, is that the terms contained in the angle brackets in Equation 2.16 describe different Liouville-space pathways, in which $|g\rangle\langle e|$ and $\langle g|\langle e|$ are the kets and the bras for the ground and excited state, respectively: namely, $\langle \hat{\mu}_I(t_1)\hat{\mu}_I(0)\hat{\rho}(-\infty)\rangle$ refers to the time-evolution: $|g\rangle\langle g| \rightarrow |e\rangle\langle g| \rightarrow |g\rangle\langle g|$. Conversely, the term $\langle \hat{\mu}_I(t_1)\hat{\rho}(-\infty)\hat{\mu}_I(0)\rangle$ refers to the time-evolution: $|g\rangle\langle g| \rightarrow$

$|g\rangle\langle e| \rightarrow |g\rangle\langle g|$. All those terms can be evaluated looking at the corresponding equations, but this can be cumbersome and time consuming, especially when dealing with higher-order perturbations.

A more convenient diagrammatic way of representing interactions between the density matrix of a system and the time-dependent perturbations is given by the double-sided Feynman diagrams (informally called just Feynman diagrams), or Liouville-space pathways. In this representation, a vertical axis represents time, and the time evolution of the density matrices is shown from the bottom to the top of the time axis. The interactions with the external field(s) are included as arrows: namely an arrow pointing to the right represents an electric field $E(t) = E'(t)e^{i(kx-\omega t)}$ while an arrow pointing to the left represents an electric field $E(t) = E'(t)e^{i(kx+\omega t)}$ and a dashed arrow represents signal emission.

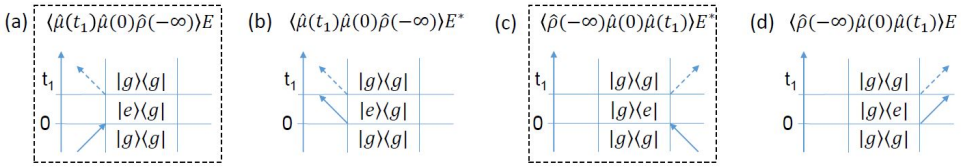

Figure 2.1: Liouville-space pathways for a 2-level system. The vertical arrow represents time, and each horizontal line marks a time in which an interaction between the field and the system takes place. The density matrix at each stage is written between two vertical lines, and the electric field of each interaction is represented by an arrow pointing towards or away from the density matrices. Arrows corresponding to $E(t) = E'(t)e^{i(kx-\omega t)}$ point to the right, while those corresponding to $E(t) = E'(t)e^{i(kx+\omega t)}$ point to the left. On the top of each pathway its corresponding term in the first order polarisation is written. The pathways that survive the rotating wave approximation are enclosed in dashed boxes.

To prove how convenient this way of representing field-matter interactions is, an interpretation of the diagram labelled (a) in Figure 2.1 will be given: the system, before any interaction is in an equilibrium ground state represented by the population $|g\rangle\langle g|$ and at time 0 interacts with an electric field which has form $E(t) = E'(t)e^{i(kx-\omega t)}$, which will excite $|g\rangle$ to $|e\rangle$ (assuming that the resonance condition is satisfied and that the system has 2 levels only) since the corresponding arrow is pointing towards the density matrix.

Now the system is left in a coherent $|e\rangle\langle g|$ state which will evolve until the next matter-field interaction happens, but, since we are describing a first-order interaction, this time will extend to infinity. In fact, the superposition prepared by the first pulse will emit a signal which is represented by the dashed arrow pointing away on the left from the density matrix, returning back to its ground state $|g\rangle\langle g|$. The first term of the linear response function accounts for a second pathway (b) in Figure 2.1, which can be shown to be negligible. In (b) at $t = 0$ the transition dipole moment operator acts from the left, but since E^* de-excites kets and excites bras, and it is not possible to remove energy from the ground state $|g\rangle$, this pathway will not

contribute to any signal.
The pathways (c) and (d) in Figure 2.1 are the adjoints of (a) and (b) respectively, but the convention is to represent double sided Feynman diagrams in which the signal emission is from the ket (left) side, without the need to make explicit the complex conjugate of the same pathways which will have an emission from the right, since they account for the same photophysical process.
Now that a connection between response functions and Feynman diagrams has been made, it can be shown that the derivation of such diagrams can be made far easier and more intuitive if we apply some constraints. For example, if we want to obtain again (a) of Figure 2.1 the following assumptions can be made:

- at any time $t < 0$ the density matrix has to be $|g\rangle \langle g|$,
- non-resonant interactions cannot generate physically meaningful pathways (rotating wave approximation),
- the emission must happen from the ket side (left) and leave the system in either an excited or ground state population,
- all interactions have to be first order (just one field at any given time t can interact with the density matrix)

Employing these rules, pathways (b) and (d) can be excluded because they do not satisfy the second condition (resonant interaction), while (c) and (d) do not satisfy the third one i.e. they are complex conjugates of another pathway.
Using a more intuitive approach we have shown that the only Feynman double-sided diagram needed to fully represent the linear response of a material system perturbed by one time-dependent electric field is (a). This type of treatment will be extremely useful when analysing higher (third) order responses, which are the ones normally involved in the description of 2D-ES and fsTA experiments.

2.5 Third Order Response Theory

It is possible to compute the third order Response Function just substituting $n = 3$ in 2.15. If we then rearrange the terms inside the angle brackets after expanding the commutators, using the invariance of the density matrix under cyclic permutations, for a simple 2 level system, comprising a ground $|g\rangle$ and an excited $|e\rangle$ states we get 8 different Response functions (4 + 4 complex conjugates). As shown for the Linear response theory before, each of these correspond to a pathway in Liouville space, which is also a physical process that can happen when matter and fields interactions occur.
The four Response functions $R_1, ..., R_4$ are shown below, following the nomenclature

used by Hamm and Schlau-Cohen:[67;68]

$$R_1 = \langle \hat{\mu}_{I3} \hat{\mu}_{I0} \hat{\rho}(-\infty) \hat{\mu}_{I1} \hat{\mu}_{I2} \rangle \tag{2.18}$$

$$R_2 = \langle \hat{\mu}_{I3} \hat{\mu}_{I1} \hat{\rho}(-\infty) \hat{\mu}_{I0} \hat{\mu}_{I2} \rangle \tag{2.19}$$

$$R_3 = \langle \hat{\mu}_{I3} \hat{\mu}_{I2} \hat{\rho}(-\infty) \hat{\mu}_{I0} \hat{\mu}_{I1} \rangle \tag{2.20}$$

$$R_4 = \langle \hat{\mu}_{I3} \hat{\mu}_{I2} \hat{\mu}_{I1} \hat{\mu}_{I0} \hat{\rho}(-\infty) \rangle \tag{2.21}$$

The interaction of these terms with three radiation fields generates an enormous number of different terms (864), but applying the experimental conditions of time-ordering together with the points stated in Section 2.4, we can reduce the number of physically meaningful interactions to 4. For example, if we consider R_2, given by Equation 2.19, $\hat{\mu}_{I0}$ perturbs the equilibrium density acting on the bra (the right side). We take the density matrix before any interaction as in a ground state population $\hat{\rho}(-\infty) = |g\rangle \langle g|$, the only resonant option is to excite the bra, corresponding to a left pointing arrow, yielding a coherent term $|g\rangle \langle e|$. Now, the $\hat{\mu}_{I1}$ operator, in this case acting from the left, can only excite the left side (ket) putting the system in an excited population state, $|e\rangle \langle e|$. Finally, the third time interval starts after the interaction of the density matrix with the operator $\hat{\mu}_{I2}$. In a two-level system, the only possible option is to de-excite the bra, yielding again a coherent state $|e\rangle \langle g|$, which will relax to a ground state population $|g\rangle \langle g|$, emitting a signal from the ket. A diagrammatic picture of this is given in Figure 2.2, together with all the other possible Liouville-space pathways, which can be obtained applying the same approach to R_1, R_3 and R_4.

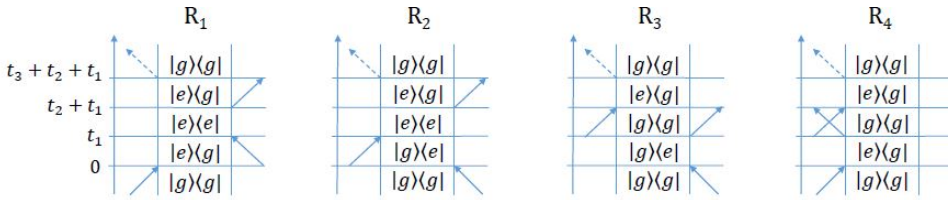

Figure 2.2: Liouville-space pathways surviving the RWA and giving significant contributions to the macroscopic polarisation.

2.6 Principles of 2D Electronic Spectroscopy and its Relation to femtosecond Transient Absorption

The aim of this Section is to give a brief presentation of the basics of 2D spectroscopy, following previously presented examples.[14;28;68] Then we will show that fsTA can be considered as a particular case of two-dimensional electronic spectroscopy. In a 2D experiment three distinct ultrashort pulses are used to generate a map correlating, for every delay time between t_1 and $t_1 + t_2$, the excitation and emission frequencies, in the same way as multidimensional NMR experiments do. Having introduced the double-sided Feynman diagrams in the previous section it is possible to describe the sequence of pulses in these terms. In Figure 2.3, as usual, time goes from the left to the right, the system is starting from a ground state population $|g\rangle\langle g|$ and this is converted to a $|g\rangle\langle e|$ or a $|e\rangle\langle g|$ coherence, which will last for the time interval t_1, named **Coherence time**, τ or t_1. then, the second pulse will convert the coherence term to a population, which can be in the excited $|e\rangle\langle e|$ or in the ground state $|g\rangle\langle g|$; both ground and excited state populations are formally stationary, so no relaxation should occur during this time interval T, or t_2, named **Population time** or **Waiting time**. Finally, the third pulse generates again a coherent superposition $|e\rangle\langle g|$ which will decay in time under the unperturbed Hamiltonian.

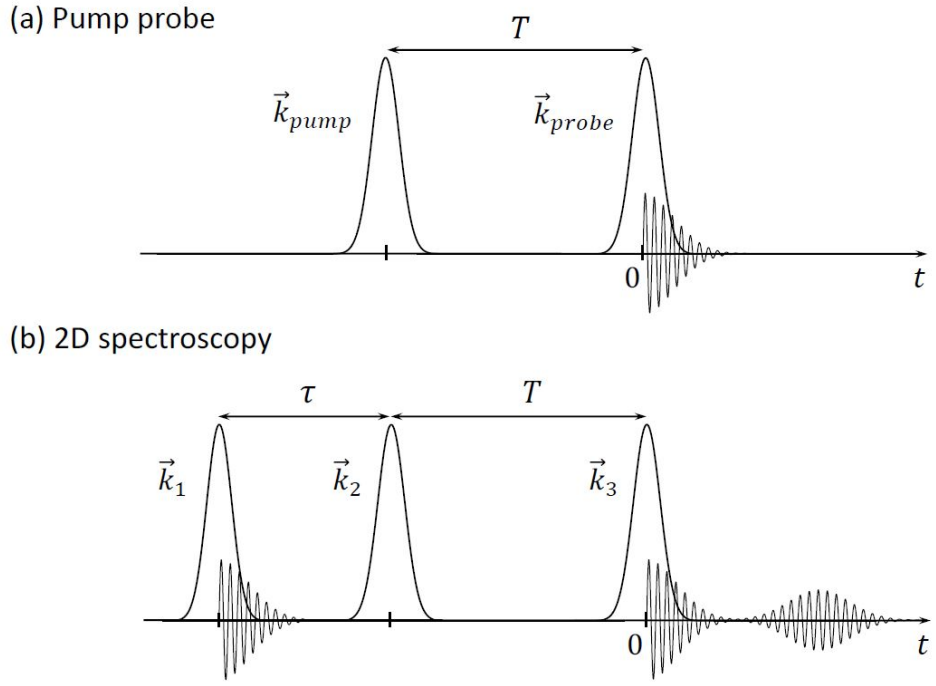

Figure 2.3: Pulse sequences and wavevectors involved in a (a) fsTA (pump probe) and in a (b) 2D-ES experiment.

The most common spectroscopic method used to obtain information about the third-order response of a material system is fsTA, which only employs one pump

and one probe pulse spaced in time by an interval T, as shown in Figure 2.3 (a). One of the main drawbacks of this third order technique is that there is an intrinsic ambiguity on the value of the excitation frequencies of any measured signal.
In terms of the double sided Feynman diagrams introduced in figure 2.2, in a fsTA experiment the single pump pulse interacts twice with the density matrix, so there is no definite time-ordering between the first and the second interactions, happening within the timescale of the pump pulse. This condition makes it impossible to recover any dynamical information relative to the system during the coherence time τ. Conversely, in 2D-ES we experimentally control the coherence τ, the population T and the signal t time delays. Although, in practice it is more convenient to disperse the signal onto a detector with a prism, in order to measure it directly in the frequency domain $\tilde{\nu}_3$. Conversely, $\tilde{\nu}_1$ is obtained taking the Fourier transform of the coherence time interval, and corresponds to the wavenumber of the first arrow in the double-sided Feynman diagrams. Achieving this for each population time T, we can obtain a correlation map between the excitation $\tilde{\nu}_1$ and the detection $\tilde{\nu}_3$ wavenumbers.

2.6.1 Phase Matching

The technical details on how to experimentally detect and compute the third order polarisation from a 2D-ES experiment will be described in detail in Chapter 4. So far, we have not taken into account a fundamental question, in which direction do we have to put the detector in order to measure the emitted signal? This degree of freedom depends on the geometry of the system, and, since the third order polarisation has products between all the electric fields, the overall phase of the polarisation at the third order will be $e^{i((\pm k_1 \pm k_2 \pm\ k_3)x \pm \phi_1 \pm \phi_2 \pm \phi_3)}$, in which x is the direction of propagation of the wave, and it can be shown that all the contributions can propagate in the $\pm k_1 \pm k_2 \pm k_3$ directions.
Again, information about the directions of the desired signal can be obtained looking at the Feynman diagrams of every response function, recalling that conjugated fields $E^*(t)$ fields will carry a $-ik$ contribution in their exponential term. Looking again at Figure 2.2 it is clear that in R_1 and R_4 the second interaction happens with a conjugated field, meaning a signal emitted in the $k_{sig} = +k_1 - k_2 + k_3$ direction, while R_2 and R_3 interact with a conjugate field (identical real part, opposite sign of the imaginary part) at the beginning of the coherence time τ and then two interactions with non-conjugated fields will take place, so the resulting propagation direction will be $k_{sig} = -k_1 + k_2 + k_3$.
In practice, many different schemes have been proposed.[69–71] A common one is the collinear, pump-probe geometry where pulses 1 and 2 are collinear and there is a small angle between them and the third pulse. In this case $k_1 = k_2$, so that the

(self-heterodyned) signal will propagate along k_3 for any pathway in Figure 2.2.
Another common geometry, which is the experimental setup chosen for this work, is the BOXCAR geometry, where the three pulses focus on the sample starting from three of the four corners of a square.
The experiment, its phase matching conditions and the procedure that allows to record R_{1-4} will be described in Chapter 4.

2.6.2 rephasing and Non-rephasing Pathways

So far, we have raised the question of the differences among the $R_{1,4}$ and $R_{2,3}$ pathways in terms of their different wavevectors. This is not the only difference between them; as an example the evolution of the density matrix over time of R_1 and R_3 is shown, step by step, in Equations 2.22 and 2.23. This has been done applying the transition dipole moments step by step, propagating the density matrix and finally taking the trace. The result that we want to highlight here is that R_1 (and R_4) have a functional dependence on $t+\tau$ while R_2 (and R_3) depend on $t-\tau$.

$$\begin{pmatrix} 1 & 0 \\ 0 & 0 \end{pmatrix} \xrightarrow{i\mu\hat{I}_0\hat{\rho}} \begin{pmatrix} 0 & 0 \\ i & 0 \end{pmatrix} \xrightarrow{\tau} \begin{pmatrix} 0 & 0 \\ ie^{-i\omega_{eg}\tau} & 0 \end{pmatrix} \xrightarrow{i\mu\hat{I}_0\hat{\rho}\mu\hat{I}_1} \begin{pmatrix} 0 & 0 \\ 0 & ie^{-i\omega_{eg}\tau} \end{pmatrix} \xrightarrow{i\mu\hat{I}_0\hat{\rho}\mu\hat{I}_1\mu\hat{I}_2}$$
$$\begin{pmatrix} 0 & 0 \\ ie^{-i\omega_{eg}\tau} & 0 \end{pmatrix} \xrightarrow{t} \begin{pmatrix} 0 & 0 \\ ie^{-i\omega_{eg}(t+\tau)} & 0 \end{pmatrix} \xrightarrow{i\langle\mu\hat{I}_3\mu\hat{I}_0\hat{\rho}\mu\hat{I}_1\mu\hat{I}_2\rangle} ie^{-ie_{eg}(t+\tau)} \quad (2.22)$$

$$\begin{pmatrix} 1 & 0 \\ 0 & 0 \end{pmatrix} \xrightarrow{i\hat{\rho}\mu\hat{I}_0} \begin{pmatrix} 0 & i \\ 0 & 0 \end{pmatrix} \xrightarrow{\tau} \begin{pmatrix} 0 & ie^{+i\omega_{eg}\tau} \\ 0 & 0 \end{pmatrix} \xrightarrow{i\mu\hat{I}_1\hat{\rho}\mu\hat{I}_0} \begin{pmatrix} 0 & 0 \\ 0 & ie^{+i\omega_{eg}\tau} \end{pmatrix} \xrightarrow{i\mu\hat{I}_1\hat{\rho}\mu\hat{I}_0\mu\hat{I}_2}$$
$$\begin{pmatrix} 0 & 0 \\ ie^{+i\omega_{eg}\tau} & 0 \end{pmatrix} \xrightarrow{t} \begin{pmatrix} 0 & 0 \\ ie^{-i\omega_{eg}(t-\tau)} & 0 \end{pmatrix} \xrightarrow{i\langle\mu\hat{I}_3\mu\hat{I}_1\hat{\rho}\mu\hat{I}_0\mu\hat{I}_2\rangle} ie^{-ie_{eg}(t-\tau)} \quad (2.23)$$

We can give a microscopic interpretation of this phenomenon thinking of the fact that the first pulse creates a microscopic alignment on many electric dipoles, forming a $|g\rangle\langle e|$ coherence during τ, which rapidly dephases because of the interactions with the environment. After the second interaction (which creates a ground or excited state population), the third pulse interacts with the system generating a $|e\rangle\langle g|$ superposition during t, but this is the adjoint of the term created during the coherence time, meaning that the two dephasing effects cancel each other, so at $t=\tau$

the dipoles will be in phase again, this is why R_2 and R_3 are called "photon echo" signals, or **rephasing** pathways. On the other hand, R_1 and R_4 generate signals which are analogous to a free-induction decay and we will refer to them as **non-rephasing** pathways. Experimentally, different strategies that allow us to record the rephasing and non-rephasing signals separately have been developed.[72–74]

2.7 Vibronically Coupled Systems

One of the early successes of two-dimensional electronic spectroscopy was to disentangle the dynamics in nanostructured coupled molecular systems of biological interest.[25;75;76] Vibrational and vibronic effects arise from the interaction of an electronic transition with the nuclear motion on a normal coordinate; as a result, the two level system introduced before cannot take into account the interactions with the sublevels.

The displaced harmonic oscillator (DHO) model, depicted in Figure 2.4, can describe a vibronic system well, as long as we restrain our treatment to the first couple of vibrational states. In the DHO model, the excited electronic excited state is displaced a distance x on the vibrational normal coordinate Q_i (the equilibrium distance for an excited state is assumed to be longer than in the ground state), and optical excitations are assumed to be vertical, so they cannot change the value of Q_i. In this Section we show how the presence of accessible sublevels within the bandwidth of the laser pulses increases the number of physically meaningful possible third-order pathways compared to the Liouville space shown for the pure electronic two-level system in Figure 2.2.

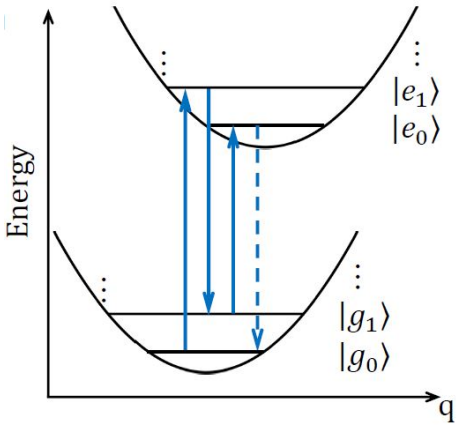

Figure 2.4: Scheme of the energy levels for an electronic transition coupled to a normal vibrational mode.

In Figure 2.4 is described in the framework of the harmonic approximation, which implies that ΔE between any pair of consecutive vibrational sublevels has to be constant, also electronic transitions between any of the levels within the ground

and excited state potential energy surfaces (PES) are allowed, while transitions between levels with different vibrational quantum number within the same PES are not taken into account. The displacement between the ground and excited state minima along the normal coordinate Q_i, will favour transitions between states with better overlap between vibrational wavefunctions, which leads to an higher value of the Franck-Condon integrals.

To define a value for the density matrix of the system before any interaction with the external field takes place, we assume the energy of the coupled vibrational mode to be greater than k_BT, this allows us to consider the system in the state $|g_0\rangle\langle g_0|$ (where the 0 labels are indicating ground vibrational levels) at $t = -\infty$. While this approximation holds in most cases for isolated molecular systems, in solid-state systems,[77] proteins[78] or, in general, for systems in which low frequency vibrational modes or optical phonons play a non-negligible role Liouville-space pathways accounting for "hot" ground states such as $|g_1\rangle\langle g_1|$ must be taken into account.

Following the conditions stated above, we can now proceed to draw the Feynman diagrams for the 4 (one ground vibrational and one excited vibrational level for both the electronic ground and excited states) level system. The initial state of the system is $|g_0\rangle\langle g_0|$ and the transition dipole operators contained in the four response functions shown in Section 2.5 will be applied. All the resonant transitions will still be between different electronic states, so that the resulting double-sided diagrams will look like the one in Figure 2.2, but the transitions will connect different pairs of vibronic sublevels.

We are expecting a much greater number of different pathways for each response function. As an example, we show what happens when the non-rephasing R_1 response function acts on a 4-level vibronic system. The first interaction, a non conjugated field, will induce transitions from $|g_0\rangle$ to either $|e_0\rangle$ or $|e_1\rangle$. Then, after the coherence time τ the conjugated field will bring the bra to $\langle e_0|$ or $\langle e_1|$. After the population time T the bra, regardless of its state, can be de-excited by the non-conjugated field either to $\langle g_0|$ or $\langle g_1|$. Finally, the signal emission must happen from the ket, yielding a population state, so only one possible transition (based on the state of the conjugate bra) is considered here. However, every field-matter interaction can induce transitions to two different (vibrational or vibronic) states, increasing the total number of possible pathways for R_1 from 2 to $2^3 = 8$, as shown in Figure 2.5. The same calculation can be applied to R_2, R_3, R_4, yielding a total number of possible double-sided Feynman diagrams $2^3 \times 4 = 32$.

Now that the diagrams accounting for all the possible interactions have been drawn in Figures 2.5, 2.6, 2.7 and 2.8 a connection between them and the features present in 2D-ES spectra can be made. First, we need to highlight that in 2D maps the excitation wavenumber $\tilde{\nu}_1$, shown on the horizontal axis, corresponds to the en-

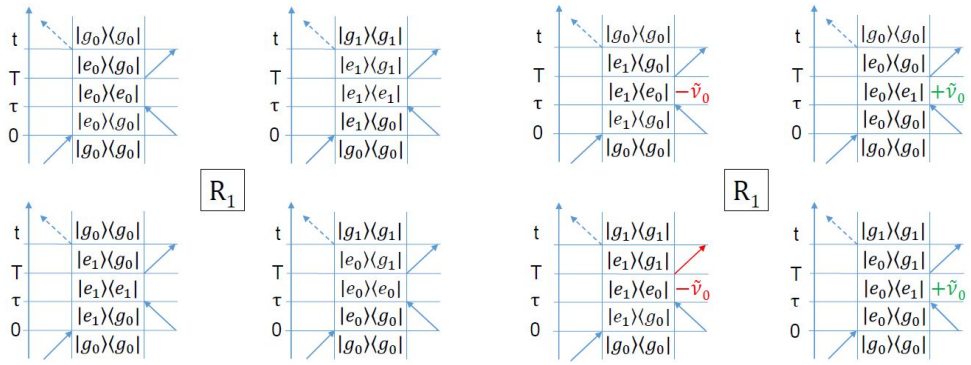

Figure 2.5: non rephasing pathways for R_1 in the DHO approximation. The four pathways on the left have excited state populations during T, while the four on the right have vibronic superpositions during T, oscillating at positive or negative frequencies in the excited state PES.

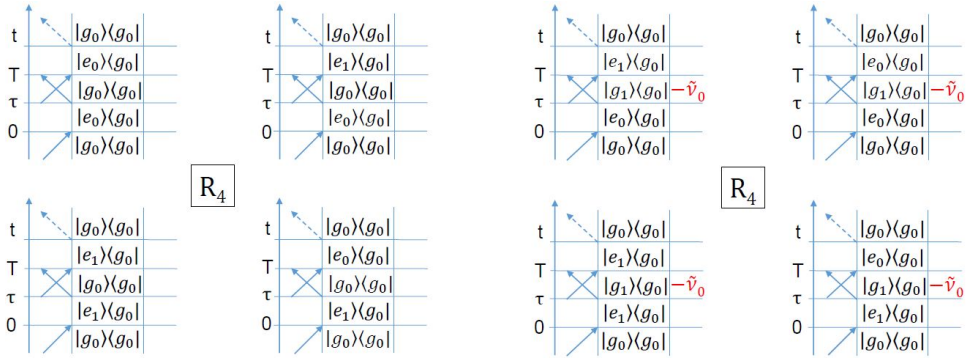

Figure 2.6: non rephasing pathways for R_4 in the DHO approximation. The four pathways on the left have ground state populations during T, while the four on the right have vibrational superpositions during T, oscillating at negative frequencies in the ground state PES.

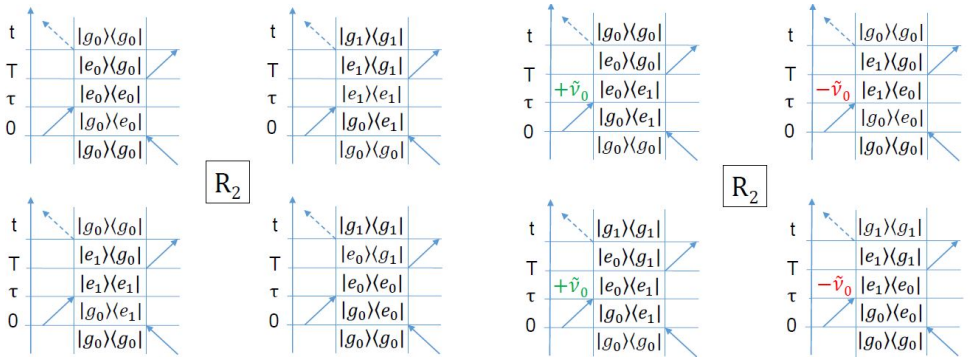

Figure 2.7: rephasing pathways for R_2 in the DHO approximation. The four pathways on the left have excited state populations during T, while the four on the right have vibronic superpositions during T, oscillating at positive and negative frequencies in the excited state PES.

ergy of the first arrow depicted in the double-sided Feynman diagrams, while the detection wavenumber $\tilde{\nu}_3$, shown on the vertical axis, corresponds to the energy of the signal, depicted as a dashed arrow pointing away from the double-sided Feynman diagram on the ket side. The wavenumber (energy) associated with the second

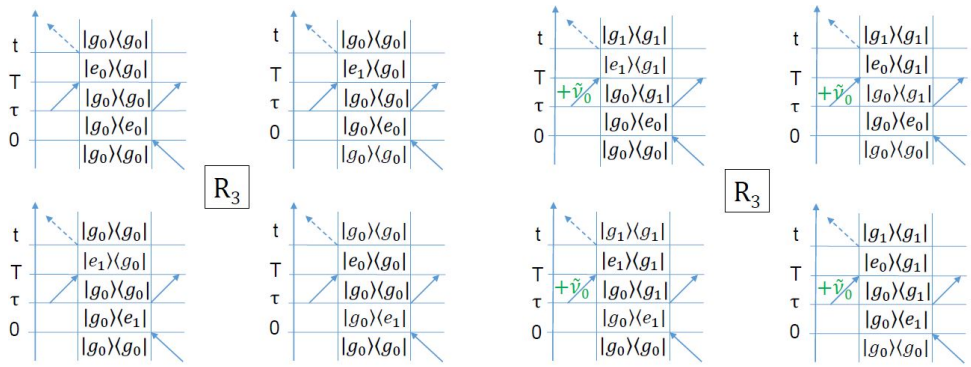

Figure 2.8: rephasing pathways for R_3 in the DHO approximation. The four pathways on the left have ground state populations during T, while the four on the right have vibrational superpositions during T, oscillating at positive frequencies in the ground state PES.

and the third interactions is not a directly recoverable parameter of the 2D-ES experiment, while the population time T is scanned in discrete steps, and for each T a two-dimensional spectum will be obtained.

In the context of a DHO model, with a given vibrational mode with wavenumber $\tilde{\nu}_0$, the four possible transitions between ground and excited state vibronic levels will have three different energies, which will translate to different positions at which the signal is expected to appear on the $(\tilde{\nu}_1, \tilde{\nu}_3)$ plane; namely $|g_0\rangle \longleftrightarrow |e_0\rangle$ and $|g_1\rangle \longleftrightarrow |e_1\rangle$ will be degenerate, at energy $\tilde{\nu}_{eg}$, $|g_0\rangle \longleftrightarrow |e_1\rangle$ will have energy $\tilde{\nu}_{eg} + \tilde{\nu}_0$ and $|g_1\rangle \longleftrightarrow |e_0\rangle$ transitions will lie at $\tilde{\nu}_{eg} - \tilde{\nu}_0$.

In Section 2.5 we pointed out how the density matrix has to be in a population state during the population time T, and the dynamics recovered during this time delay will only account for population relaxation. Although, when vibrational levels are coupled to an electronic transition (as it is in the DHO model), the first pair of field-matter interactions can happen at a different wavenumber, preparing a coherent superposition of vibronic states, either in the ground or in the excited state PES. While T is scanned, the vibrational (vibronic) coherence will evolve under the unperturbed Hamiltonian $\hat{H}_0$, modulating the amplitude of the signal located at the $(\tilde{\nu}_1, \tilde{\nu}_3)$ coordinates, which are defined by the first and the last arrows of the double-sided Feynman diagram at the $\tilde{\nu}_0$ frequency. Since the coherent superposition can either be in the ground or in the excited state, the four possibilities here are: $|g_0\rangle\langle g_1|$, $|e_0\rangle\langle e_1|$, $|g_1\rangle\langle g_0|$ and $|e_1\rangle\langle e_0|$. Now, since the density matrix is Hermitian, $|g_0\rangle\langle g_1| = |g_1\rangle\langle g_0|^*$ and $|e_0\rangle\langle e_1| = |e_1\rangle\langle e_0|^*$, if the coherent term $|g_0\rangle\langle g_1|$ beats during the population time as a function of $e^{+i\nu_0 T}$ its adjoint will modulate the signal as $e^{-i\nu_0 T}$. In fact, within a 2D-ES experiment we are capable of measuring modulations with positive and negative frequencies happening during T.

The difference between oscillations with positive and negative frequencies are the phase shift and the change in amplitude between their real and imaginary part of the signal, this effect can be shown using Euler's formulas to write the exponential

term as a sum of cosine and sine functions:

$$e^{+i\nu_0 T} = \cos(\nu_0 T) + i\sin(\nu_0 T) \tag{2.24}$$

$$e^{-i\nu_0 T} = \cos(\nu_0 T) - i\sin(\nu_0 T) \tag{2.25}$$

It is thus possible to experimentally measure and discriminate between real and imaginary part of a 2D signal (See Chapter 4). The concepts described above can be used to draw schemes that can predict where a third order signal will generate amplitude on a 2D map in the $(\tilde{\nu}_1, \tilde{\nu}_3)$ plane. In order to do this, some conventions need to be listed:[79]

- a geometrical symbol is assigned to each Liouville-space pathway: squares represent excited state population during T while triangles represent ground state populations,
- black solid symbols account for population (non oscillating) pathways, while open symbols account for coherence (oscillating) pathways,
- green colour is used to mark oscillations occurring at positive frequencies while red marks oscillations occurring at negative frequencies.

The symbols are sorted on the excitation-detection $(\tilde{\nu}_1, \tilde{\nu}_3)$ plane, according to the pair of wavenumbers at which they are supposed to appear, since multiple pathways can lead to a signal centered at the same pair of coordinates a black circle centred at the exact pair of $(\tilde{\nu}_1, \tilde{\nu}_3)$ coordinates was used to contain all the possible symbols that can give contribution to the 2D map at that point. The procedure just described leads to a the scheme shown in Figure 2.9, which highlights two important details:

- When a molecular vibration is coupled to an electronic transition, it is possible to have pathways which will leave the system in an "hot" ground state population. These pathways will appear at a detection frequency $\tilde{\nu}_3 = \tilde{\nu}_{eg} - \tilde{\nu}_0$. One might be tempted to assign this signal to a different electronic state, rather than a vibrationally excited level within the ground state PES. Therefore, a careful analysis of 2D-ES spectra must be done before claiming the presence of new electronic states.
- The analysis of oscillations occurring on pathways detected at $\tilde{\nu}_3 = \tilde{\nu}_{eg} - \tilde{\nu}_0$ can be misleading as well. From Figure 2.9 it can be seen that two out of the three coherent pathways in this region (green triangles) are caused by oscillating terms in the ground state. One might be induced to think that, since in this spectral region stimulated emission signals are detected, the coherent oscillations propagate on the excited electronic state, but we have just shown that this assignment will lead to wrong conclusions.

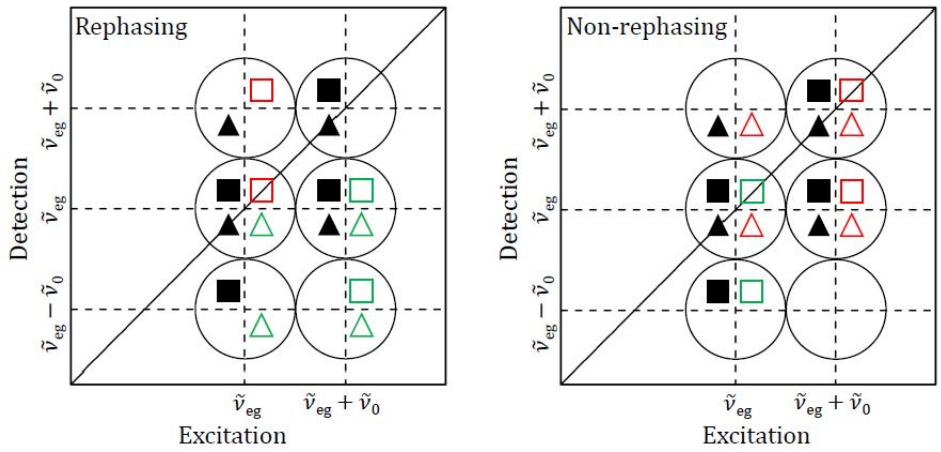

Figure 2.9: Scheme of Liouville-space pathways in rephasing (left) and non-rephasing (right) 2D-ES maps. Each geometrical figure represents a pathway, with squares representing an excited state and triangles representing a ground state population during T. Black symbols are used to indicate population (non-oscillatory pathways), whereas coherences (oscillatory) are marked with open symbols, which are red for pathways oscillating at negative frequencies and green for positive oscillation frequencies. The signal corresponding to each geometric figure is contained in the circle centered at the relevant pair of $(\tilde{\nu}_1, \tilde{\nu}_3)$ coordinates.

In the next section we are going to focus on another kind of system which can generate similar features to the ones just described: the electronic coupling case.

2.8 Electronically Coupled Systems

In this section we describe and present an interpretation of the Liouville-space pathways that can be obtained when applying the third order response formalism to a three-level system, like the one shown in Figure 2.10.

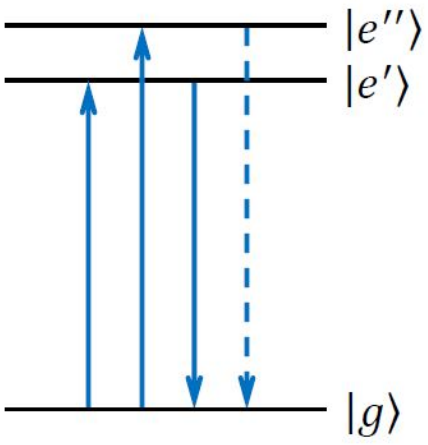

Figure 2.10: Scheme of the energy level for a three level system with two excited states with a small energy separation between them.

This model gives a good description of the energy level structure of molecular dimers, such as the perylene bisimide dimers studied in Chapter 5. In these systems, dipole-dipole coupling between closely spaced chromophores induces a splitting of the excited state in two excitonic states with different symmetry, and an energy gap between them which scales with the third power of the reciprocal distance, as described by Kasha[80] in 1963.
Typically, the gap between the two exciton state is in the same energy range as molecular vibrations,[79] and this can potentially lead to incorrect assignments, where vibrational coherences are misinterpreted as electronic ones, or vice versa. All the relevant double-sided Feynman diagrams can be written following the same approach used in the previous section, leading to diagrams for the non rephasing (Figure 2.11), and rephasing pathways in Figure 2.12.

The first difference to be highlighted is that the pathways due to ground state coherence are not present in this case. The key result is the different contributions given by oscillating pathways in the vibronic case (Figure 2.9) and in the electronic one (Figure 2.13). In the DHO model, rephasing and non rephasing maps have eight possible coherence diagrams, that form a "chair pattern" around five pairs of $(\tilde{\nu}_1, \tilde{\nu}_3)$ coordinates. On the other hand, in electronic coupling it is impossible to prepare ground state coherences, therefore only four excited state pathways are expected: the one which will produce oscillating signals on the diagonal will be non rephasing, while oscillations on the off-diagonal peaks will be produced by rephasing pathways.

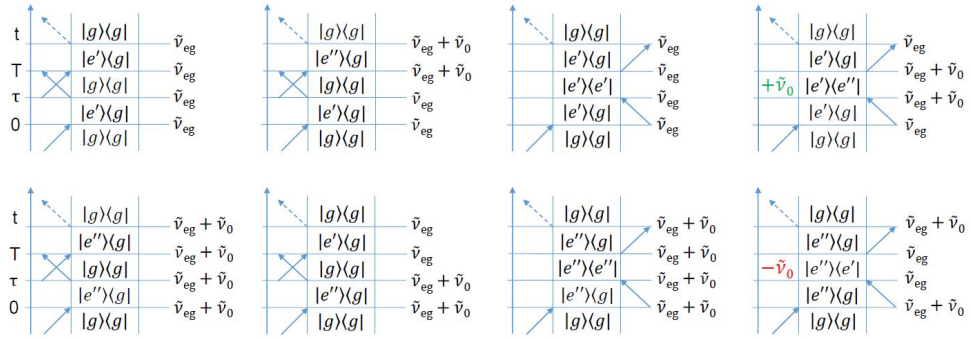

Figure 2.11: non rephasing double-sided Feynman diagrams resulting from the electronically coupled three level system shown in Figure 2.10

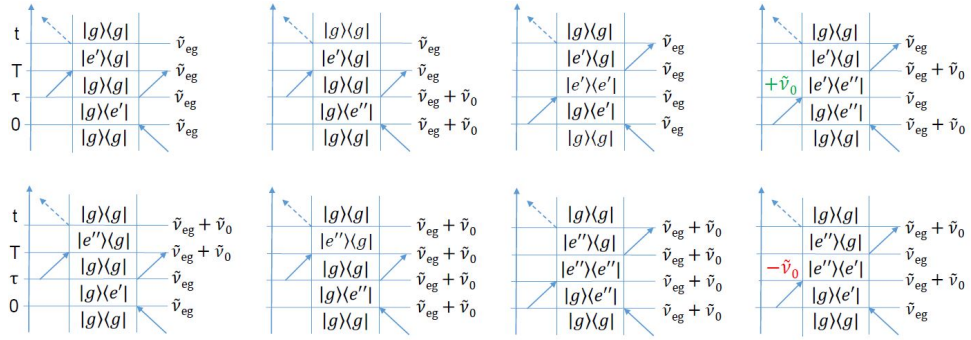

Figure 2.12: rephasing double-sided Feynman diagrams resulting from the electronically coupled three level system shown in Figure 2.10

Tying these results together, it is possible to conclude that the lack of vibrational (ground state) coherence in a 2D map, combined with the presence of oscillations on the diagonal for non rephasing signals and oscillations on the cross-peaks for the rephasing pathways is a strong signature of the electronic origin of the beating observed during T, as observed first by Cheng[81] and Cassette.[82]

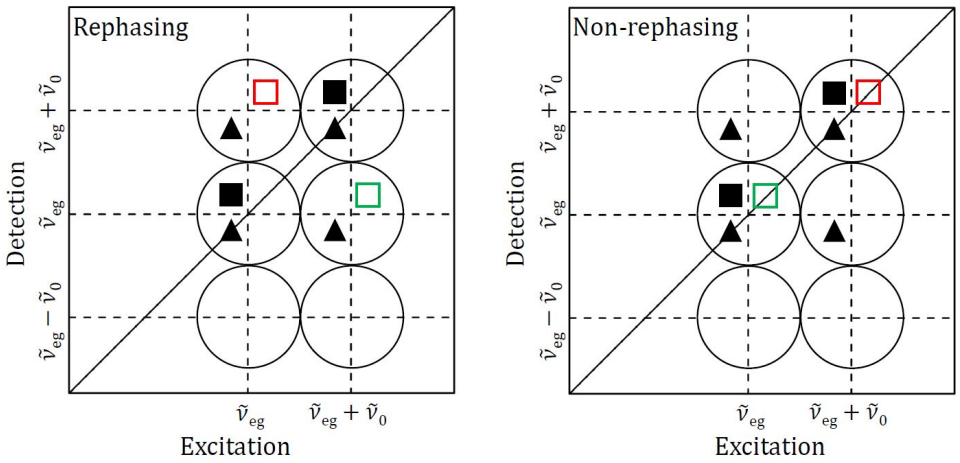

Figure 2.13: Scheme of Liouville-space pathways in rephasing (left) and non-rephasing (right) 2D-ES maps. Each geometrical figure represents a pathway, with squares representing an excited state and triangles representing a ground state population during T. Black symbols are used to indicate population (non-oscillatory pathways), whereas coherences (oscillatory) are marked with open symbols, which are red for pathways oscillating at negative frequencies and green for positive oscillation frequencies. The signal corresponding to each geometric figure is contained in the circle centered at the relevant pair of $(\tilde{\nu}_1, \tilde{\nu}_3)$ coordinates.

Chapter 3

Femtosecond Transient Absorption (fsTA) and Transient Anisotropy (fsTAn)

3.1 Principles of fsTA

After commercial lasers capable of generating ultrashort pulses became available in the 1990s, a new area of research flourished, with the goal of resolving in real time ultrafast processes of primary importance in chemistry and biology, such as the dynamics of: photosynthetic systems,[83] the first events in vision;[84] organic and inorganic semiconducting materials with applications in solar energy conversion.[85] To study these dynamics, fsTA is one of the most commonly used techniques.[86]

In fsTA, a small fraction of the molecules located at the focal position are excited to a higher electronic (vibronic) state $|e_n\rangle \langle e_n|$ through the interaction with a pump pulse (which, in the double sided Feynman diagram picture, interacts twice with the density matrix, with no defined time-ordering between the two perturbations). After a time interval T, a second weaker pulse, named probe, interacts again with the system generating a signal that will be collinear with the probe pulse. By chopping the pump at a frequency which is usually chosen to be half of the repetition rate of the laser, a differential absorption spectrum (ΔA) between the spectra of the pump-perturbed and the unperturbed sample can be computed. During a fsTA measurement a ΔA spectrum is measured at a number of different time delays T between the pump and the probe pulses, so that a map representing $\Delta A(\lambda, T)$ can be obtained. The surface $\Delta A(\lambda, T)$ contains all the dynamical and spectral information of the molecular system under investigation, such as excitation energy transfer (EET), isomerisations, charge separation and recombination and intersystem crossing (ISC). Information about these processes, and their timescales, can be extracted from global analysis procedures, which will be described in Section 3.2.5.

An fsTA dataset will have contributions, which are often overlapped, due to its lack

of frequency resolution on the excitation energies including:

- **Ground State Bleach (GSB)**: for the DHO model shown in Section 2.7 GSB is described by the double sided Feynman diagrams R_3 and R_4 in Figures 2.8 and 2.6, which have their corresponding density matrix in the ground state density matrix $|g_n\rangle\langle g_m|$, where $n = m$ (for populations) or $n \neq m$ (for coherences) during the delay time T. This effect can be intuitively understood thinking that the sample excited by the pump pulse will have fewer molecules in the ground state than the unperturbed sample, so a GSB signal will have a negative ΔA signal, which will appear in the spectral region corresponding to the steady-state absorption.

- **Stimulated Emission (SE)**: for the DHO model introduced in Section 2.7, SE is described by the double-sided Feynman diagrams labelled R_1 and R_2 in Figures 2.5 and 2.7. This process arises from the fact that, for a two-level (electronic) system, the Einstein coefficients for the absorption A_{12} and for the stimulated emission A_{21} must be equivalent. Therefore, once the excited state density matrix $|e_n\rangle\langle e_m|$, where $n = m$ or $n \neq m$, is prepared, the probe pulse photons can de-excite the molecule back to its ground state $|g_n\rangle\langle g_m|$ causing it to emit photons. SE will produce a negative ΔA signal because those photons add to the probe intensity, and it will spectrally match the steady-state fluorescence spectrum. When the molecular system under investigation has a small Stokes shift (small reorganisation energy), the GSB and SE negative signals tend to overlap into a broader negative band.

- **Excited State Absorption (ESA)**: this contribution cannot be modelled in the framework of a two-level system, and double-sided Feynman diagrams which account for higher excited (such as two-exciton) states will be introduced later on in this thesis, in order to discuss the spectral features of PBI excitonic dimers in Chapter 5 properly. For now, ESA can be intuitively described thinking that, after an excited state density matrix $|e_n\rangle\langle e_m|$, where $n = m$ or $n \neq m$, is created by the pump pulse, the delayed probe can induce optically allowed transitions to higher energy states that can be generally written as $|f_n\rangle\langle e_m|$ (or their complex conjugates). GSB will thus produce an increase of the ΔA, so a positive signal, which has no correspondence with any kind of steady-state feature, will be detected.

A fsTA example dataset is shown in Figure 3.2, before (a) and after (b) chirp correction (chirp comes from the group velocity dispersion (GVD) added by transmissive optics, and it is removed using the procedure described in 3.2.3), in which the probe frequency is the horizontal axis and the pump-probe delay time T is the vertical axis, with negative GSB and SE features coloured in light and dark blue and positive ESA features coloured in yellow/red.

3.2 Experimental Implementation of fsTA

3.2.1 Time Resolution and Spectral Selectivity of a fsTA Experiment

There is literature describing fsTA experiments carried out with laser pulses as short as 5 fs.[87] Due to the time-bandwidth uncertainty, which for Gaussian pulses states that the product $\Delta t \times \Delta \nu = 0.44$, a short pulse will be extremely broad-band, causing spectral selectivity problems. Moreover, when dealing with such short pulses, additional contributions arising from the simultaneous interaction of two pulses with the material system, have to be taken into account. These contributions are non-resonant and are usually merged together under the name of "coherent artefact","coherence spike" or"cross-phase modulation".[66]
Usually these signals are just ignored discarding the data points close to $T = 0$ during the data analysis process, alternatively an explicit term accounting for these effects can be added to the model which is used to fit the data. The coherent artefact manifests in fsTA as oscillations around $T = 0$[88] and in practice is usually subtracted from the data recording a blank measurement of a cuvette filled with solvent.

3.2.2 Light Sources: Ti:Sa Amplified Lasers and (Noncollinear) Optical Parametric Amplifiers

Nowadays, fsTA setups can be divided in two macro-categories based on which kind of amplified laser system is used to drive them. The first one makes use of high repetition rate (40 - 250 kHz) amplifiers which provide small pulse energy,[86] the second one uses much lower repetition rate laser systems (1 - 5 kHz) which deliver higher energy per pulse. Since the system used for this work belongs to the second category, we will not give further details on fsTA experiments with high repetition rate amplifiers.
Amplified laser systems which operate in the 1 - 5 kHz frequency range usually provide 5 - 100 nJ pump pulses which, once focused down to $150 - 200\ \mu m$ at the sample position, can cause the excitation of 2 - 20 % of the molecules depending on the extinction coefficient of the molecule and its concentration. The high energy per pulse allows the study of diluted or weakly absorbing samples but at the same time has some drawbacks, for instance the possibility of triggering multi-photon processes and in general highly nonlinear processes, including Exciton-Excition Annihilation, (EEA)[89] as shown for a series of porphyrin nanorings in Chapter 8.
The amplified laser system which drives our fsTA setup is a regenerative Ti:Sapphire unit (Spectra Physics Spitfire ACE pumped by an Empower ns laser and seeded by MAITAI, a Ti:Sa oscillator) providing 120 fs pulses at 800 nm with 5 mJ energy

per pulse when operated at 1 kHz. It can drive different, collinear (OPA) and noncollinear (NOPA) parametric amplifiers which are available in the laboratory. The fsTA data shown in this thesis were obtained using two systems. First, one OPA (TOPAS Prime, Light Conversion) was used to provide $\sim$ 80 fs pump pulses centred at 560 nm while a fraction of the fundamental (800 nm) of the amplified laser, generated supercontinuum white light (SWLG) in a 3 mm thick sapphire plate, resulting in a probe spectrum spanning from 440 to 750 nm; this configuration of the experiment is sketched in Figure 3.1 and it has been used to acquire the data shown in Chapter 6. The alternative configuration, adopts the TOPAS White NOPA (Light Conversion) described in Chapter 4 to generate broader (shorter, $\sim$ 15 fs) pump pulses centred either at 720 or 850 nm, synchronised with a TOPAS Prime (Light Conversion) OPA tuned at 1200 nm, which is used as a seed for SWLG in a 3 mm thick sapphire plate, producing a probe spectrum extending from 650 nm to 1150 nm. This experimental setup, sketched in Figure 3.3 has been employed to acquire the data shown in Chapters 7 and 8. In this configuration, the relative polarisation of pump and probe beams is set at 45 °, which, in combination with a cubic beam splitter set after the sample, allows transient anisotropy to be measured, as described in Section 3.2.4.

3.2.3 fsTA Setup and Data Collection

In order to measure transient spectra at different delay times T, the pump is delayed with respect to the probe with a mechanical linear delay stage (Physik Instrumente), which allows delay times up to 3 ns. Pump and probe beams are focused with reflective optics at the sample position in order to obtain spot sizes of 170 and 30 μm (FWHM) respectively, resulting in excitation powers $\sim$ 0.4 GW/cm^2. The pump beam is set at the magic angle i.e. 54.7° with a half-wave plate and a polariser* to suppress effects of rotational reorientation. The pump is then chopped at 500 Hz to allow calculation of differential absorption between adjacent pairs of pulses.

*When performing Transient Anisotropy measurements, the probe polarisation is set at 45° relative to pump and the parallel and perpendicular components of the probe are split after the sample, and simultaneously measured on two different CCD cameras.

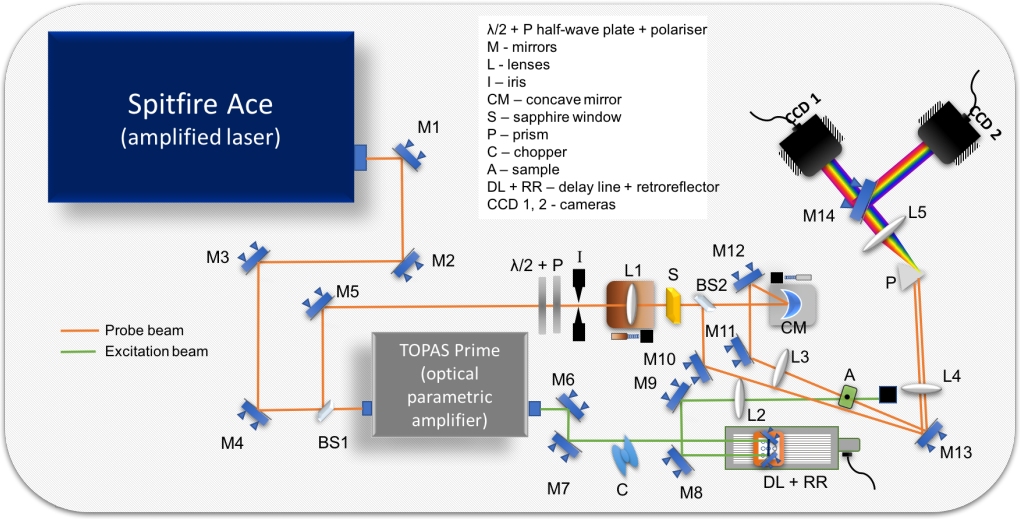

Figure 3.1: Sketch of the fsTA experimental setup used for the measurements shown in Chapter 6 where $\lambda/2$ + P are a half-wave plate and a polariser, M are mirrors, L are lenses, I is an iris, BS are beam splitters, CM is a concave mirror, S is a sapphire window, P is a prism, C is a chopper, A is the sample, DL + RR are the delay line and retroreflector mounted on it and CCD 1, 2 are the signal and reference cameras. BS2 allows the use of a reference probe beam which does not travel through the sample, the signal and the reference beam are vertically offset after M13, then dispersed using the same prism and imaged on CCD1 and CCD2, after the bottom beam (Ref) is steered onto CCD2 by M14. The data imaged onto the two cameras are then used to compute the transient absorption Equation 3.1.

After the sample the probe beam is recollimated, focused onto a home-built ultrafast prism-based spectrometer with 3 nm spectral resolution and imaged on a CCD Camera (Stresing) triggered at 1 kHz by the amplified laser; a 50:50 beamsplitter set before the sample holder sends half of the probe intensity into the same spectrometer and onto a reference camera (the second camera can also be used to measure both parallel and perpendicular polarisation at the same time when transient anistotropy experiments are performed, see Section 3.2.4). A sketch of the experimental setup described in this section is shown in Figure 3.1.
In practice, the fsTA experiment is carried out in the following way: the delay stage is set to a fixed position, corresponding to an inter-pulse delay T, then a mechanical chopper (Thorlabs MC2000B) synchronised with the amplifier at 500 Hz blocks every other pump pulse. In this way, the probe pulse will alternatively interact with a pump-perturbed and with a non perturbed sample, until a number of shots high enough to give a good signal-to-noise ratio (SNR), usually around $10^3 - 10^4$, is recorded on the detector, and subsequently averaged. In order to improve the SNR, a reference camera records probe pulses which have not interacted with the sample, the four spectra are then used to compute the $\Delta A(\lambda, T)$ using Equation 3.1, where $Pr(\lambda)$ and $Ref(\lambda)$ are probe and reference spectra.

$$\Delta A(\lambda, T) = -\log_{10}\left(\frac{Pr_{odd}(\lambda, T) \times Ref_{even}(\lambda)}{Pr_{even}(\lambda) \times Ref_{odd(\lambda)}}\right) \tag{3.1}$$

When the desired number of transient spectra has been collected, the delay stage is moved to another position and the procedure described above is iterated, shutting down the cameras while the delay stage is moving. This is repeated until all the desired time points T are collected. Usually, 100 - 200 transient spectra between 0 and 3 ns are collected, with a short interval between them for T close to 0 (in order to reconstruct the coherence spike and capture fast oscillations), with increased spacing for longer pump-probe delay times. Moreover, a number of transient spectra at negative delays are collected to estimate the baseline. Samples sensitive to photo degradation have been flowed using a flow cell and a peristaltic pump.

Because of the way in which SWLG is generated, it is highly chirped, meaning that it will have an intrinsic group-velocity dispersion (GVD); in addition to this, every transmissive optic (including the sample cell) which it encounters on its path will increase its dispersion, to values within the ps range. The continuum could be recompressed using prisms, gratings, chirped mirrors or combinations of these optical elements,[90;91] but in practice it is often more convenient to measure transient spectra with a chirped probe pulse and to correct for its dispersion during the data processing stage, fitting the T vs wavelength profile of the coherent artefact with a fourth order polynomial function and then subtracting it from the $\Delta OD(\lambda, T)$ 2D dataset, an example of this procedure in shown in Figure 3.2.

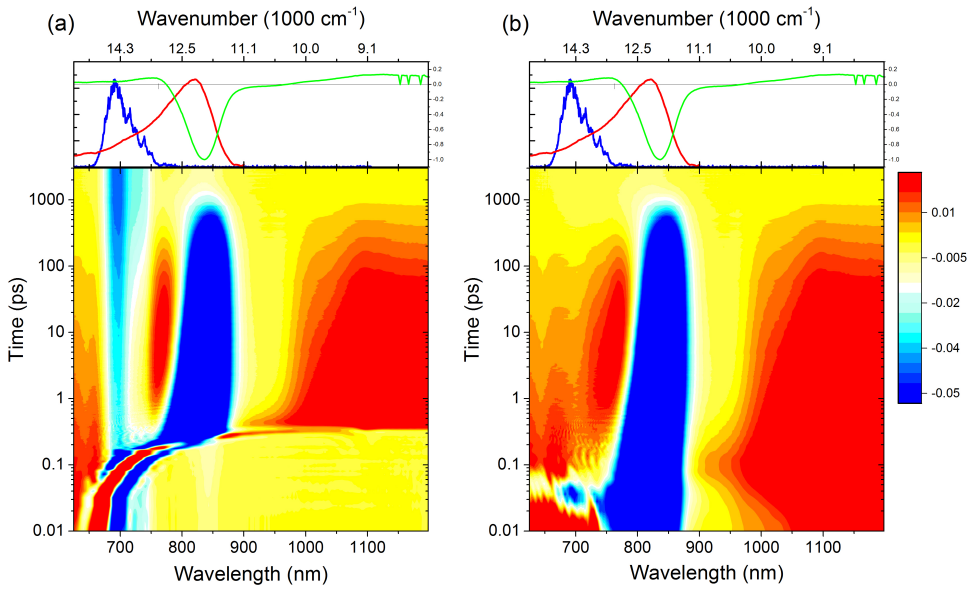

Figure 3.2: fsTA example dataset without (a) and with (b) correction and background subtraction for white light chirp (see text for details) of a 40-membered porphyrin macrocyle. Probe frequency is on the x axis and pump-probe delay time is on the y axis on a log scale; yellow, orange and red represent positive signals while light and dark blue represent negative signals. On the top panel the transient spectrum at $T = 500$ fs is shown in green, the pump spectrum is shown in blue and the steady-state absorption spectrum of the sample is shown in red.

3.2.4 Transient Anisotropy

Ultrafast excitonic delocalisation and energy transfer dynamics in supramolecular systems with a defined structure can be gauged through fsTA experiment performed with specific relative polarisation of pump and probe pulses.[86;92] The time-dependent anisotropy $r(T)$ is an experimentally measurable parameter which is defined in the following equation:

$$r(T) = \frac{\Delta A_{\parallel}(T) - \Delta A_{\perp}(T)}{\Delta A_{\parallel}(T) + 2\Delta A_{\perp}(T)} \tag{3.2}$$

In Equation 3.2 $\Delta A_{\parallel}(T)$ is the transient spectrum at a given T measured with parallel pump and probe polarisations, while $\Delta A_{\perp}(T)$ is the transient spectrum measured with perpendicular pump and probe polarisations. The denominator of Equation 3.2 corresponds to the isotropic signal, i.e. the signal measured when the relative pump-probe polarisation is at 54.7°.

Usually exciton migration and diffusion dynamics produce small changes and shifts in transient spectra, which make them difficult to detect in the magic angle polarisation conditions, while ultrafast Transient Anisotropy provides an efficient (and relatively easy to implement) way to disentangle energy migrations from the underlying population relaxation dynamics, because exciton motion will translate to reorientation of transition dipole moments and depolarisation.[93;94]

In our laboratory, Transient Anisotropy (fsTAn) measurements have been carried out measuring the parallel and perpendicular components simultaneously. To do this, the relative pump and probe polarisation angle has been set to 45° with a half-wave plate, a polariser and a cubic beam splitter added after the sample cell, as schematised in Figure 3.3. Doing this, the parallel and perpendicular probe signals are split and then directed to the cameras through the home-built prism spectrometer at the same time using both cameras described in Section 3.2.3. Subsequently, the parallel and perpendicular $\Delta A(\lambda, T)$ scans are averaged and Equation 3.2 is computed.

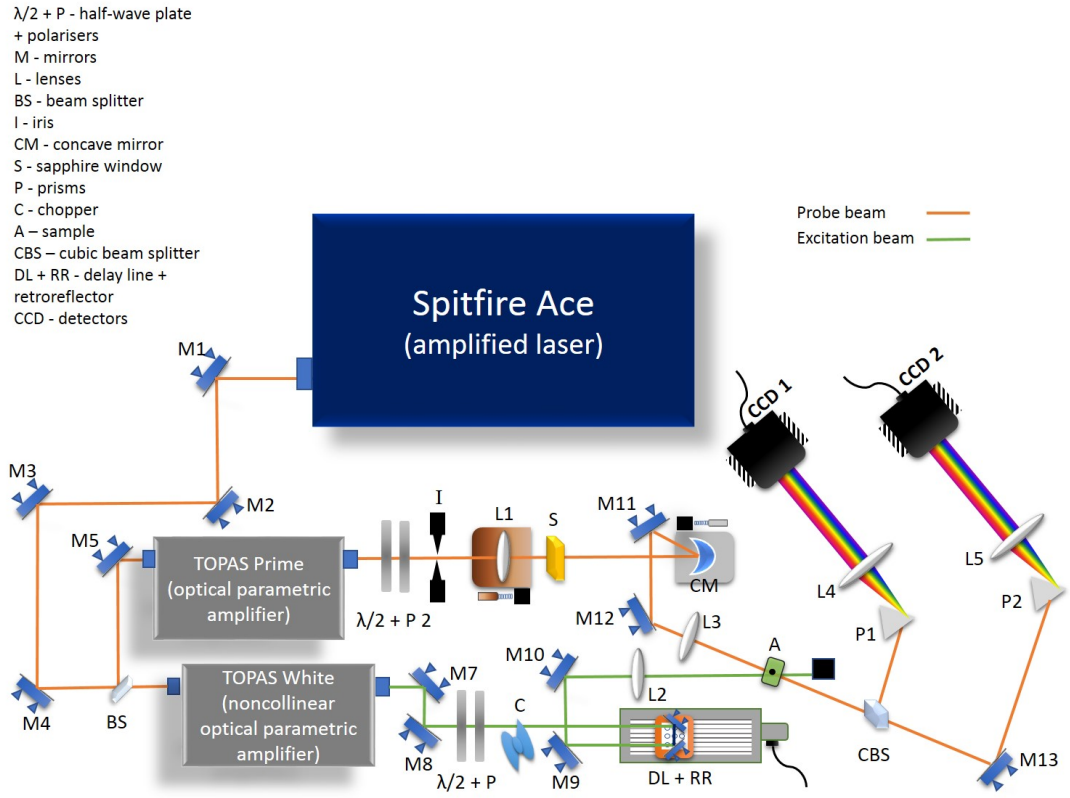

Figure 3.3: Sketch of the fsTAn experimental setup used for the measurements shown in Chapters 7 and 8, in which $\lambda/2$ + P are half-wave plates and polarisers, M are mirrors, L are lenses, I is an iris, BS is a beam splitter, CBS is a cubic beam splitter, CM is a concave mirror, S is a sapphire window, P are prisms, C is a chopper, A is the sample, DL + RR are the delay line and retroreflector mounted on it and CCD are the signal and reference cameras.The CBS allows the parallel and perpendicular components of the probe beam to be separated. They are then dispersed by the prisms and imaged onto the two cameras, making it possible to compute Equation 3.2.

This way of measuring fsTAn is less cumbersome and gives more reproducible results than acquiring two separate fsTA datasets at different polarisation conditions at the price of losing the reference channel. An example fsTAn dataset of a 40-membered porphyrin macrocyle in toluene with 1% pyridine is shown in Figure 3.4.

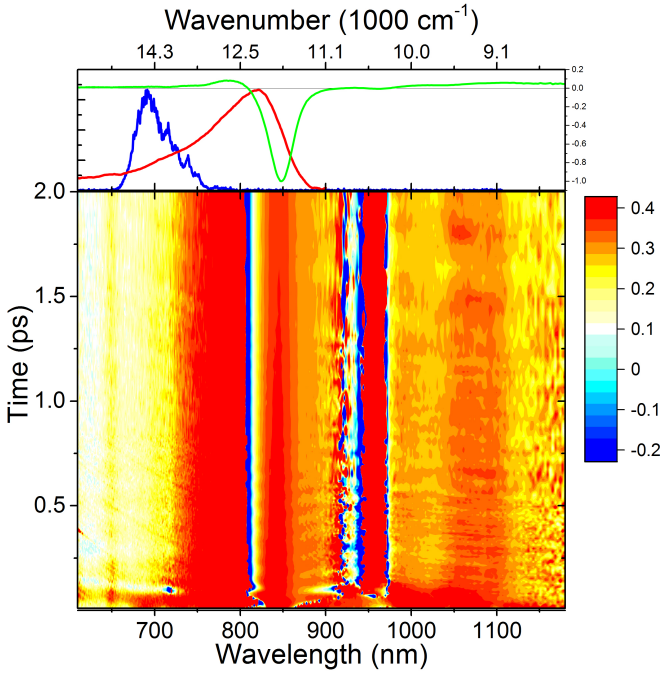

Figure 3.4: fsTAn example dataset after correction for white light chirp (see text for details) of a 40-membered porphyrin macrocyle. Probe frequency is on the x axis and pump-probe delay time is on the y axis on a log scale; yellow, orange and red represent positive signals (maximum + 0.4) while light and dark blue represent negative signals (minimum - 0.2). On the top panel the isotropic transient spectrum at $T = 500$ fs is shown in green, the pump spectrum is shown in blue and the steady-state absorption spectrum of the sample is shown in red.

3.2.5 Data Analysis

A typical dataset $\Delta A(\lambda, T)$ from a fsTA experiment will comprise thousands of data points: hundreds of wavelengths being sampled for one to two hundreds pump-probe delays T.[95] In the first place, as a preliminary analysis, it can be convenient to take slices parallel to the wavelength (transient spectra) and look at their appearance, or to the time axes (time trace at a given wavelength) and look at their evolution, and try to fit them individually with a sum of n exponentially decaying (rising) functions. Such visible inspection or simple fitting gives an important indication of the nature of the dynamics and their timescales.

Subsequently, a Global Analysis procedure can be applied to the dataset, in order to condensate the large amount of dynamical information into a reasonably small number of different spectra, each of these associated with its characteristic time constant τ_n. In the crudest model, the data are globally fit to a kinetic model which reproduces a number n of Decay-Associated Difference Spectra (DADS), which evolve in a parallel fashion through first order steps, with time constant τ_n with $n = 1, 2, 3, ..., \infty$ and $\tau_n > \tau_{n-1}$. With this procedure, the evolution of the ground and excited states after photoexcitation can be rationalised.

The global analysis model can be extended in order to include a polynomial function that will account for the chirp of the SWL and for oscillations around $T = 0$ making it possible to fit the coherence spike together with the multiexponential decays, without the need of removing the points close to 0, where significant features concerning wavepacket dynamics and ultrafast internal conversion are often located. These analysis methods are extensively reviewed by Van Stokkum *et al.*[95] and here we give a brief description of how the Glotaran global/target data analysis software works, and what kind of output data it produces.[96] fsTA and fsTAn data are a function of the experimentally measured wavelength λ and the independent variable T, which is the interpulse delay time. A model which describes the experimental data can be a matrix Ψ, which will be a superposition of a number of different components n_{comp}, as described by Equation 3.3:

$$\Psi(\lambda, T) = \sum_{l=1}^{n_{comp}} c_l(T)\varepsilon_l(\lambda) \tag{3.3}$$

Where c_l is the unknown concentration profile and ε_l is the spectrum of the l component. The data matrix is then processed using a singular value decompostion (SVD) procedure. SVD factorises the matrix into a number of spectral and time independent components, which is critical to define an initial model. The SVD of the dataset is defined in Equation 3.4:

$$\Psi(\lambda, T) = \sum_{n=1}^{n_{max}} u_n(T)\omega_n(\lambda)SV_n \tag{3.4}$$

Where n_{max} is the minimum number of rows and columns in the matrix. Typically, a number of different SVD components should be added to the model until the left and right singular vectors of the SVD start to show little structure and/or noisy behaviour, this indicates that the number of independent components has been reached.

It is now possible to fit the dataset giving as an input reasonable initial guess values for the minimum set of unknown parameters which are needed to properly fit the dataset. The controllable parameters are:

- A number of kinetic rates, which will be the reciprocal of the lifetimes τ_l,
- the instrument response function (IRF),
- the dispersion of the IRF, in case it has a wavelength dependence,
- weighting parameters, if we want to give different weights to regions of the 2D matrix, on one or on both axes (T, λ),
- specifications for the coherent artefact, which is modelled on the basis of the IRF.

All the parameters mentioned above are estimated by means of variable projection and used to calculate Equation 3.5 after Equation 3.3:

$$\Psi(\lambda, T) = \sum_{l=1}^{n_{comp}} c_{l,\lambda}(T, \theta)\varepsilon_l(\lambda) \tag{3.5}$$

Where θ and $\varepsilon_l(\lambda)$ are the unknown parameters and the conditionally linear parameters, respectively. Once the fit is accepted it is possible to look at the results, in particular we are going to focus on DADS and evolution associated difference spectra (EADS).
DADS can be included in Equation 3.3 yielding Equation 3.6:

$$\Psi(\lambda, T) = \sum_{l=1}^{n_{comp}} c_l^{DADS}(T, \theta)DADS_l(\lambda) \tag{3.6}$$

in which $c_l^{DADS}(T, \theta)$ is the convolution of the IRF with the concentration of the component l, which will exponentially decay with a time constant (reciprocal of the rate) τ_l. In a sequential non-branched model, the associated spectra will evolve one into the other until the final spectrum is reached. These spectra are called EADS, and the model shown in Equation 3.3 becomes Equation 3.7

$$\Psi(\lambda, T) = \sum_{l=1}^{n_{comp}} c_l^{EADS}(T, \theta)EADS_l(\lambda) \tag{3.7}$$

With the condition of having successively decreasing rates (increasing lifetimes), with EADS it is possible to visualise the spectral evolution of the system. As an example, DADS and EADS for each lifetime τ_{1-5} (where $\tau_5 = \infty$) from Glotaran fit of the fsTA dataset of a 40-membered porphyrin macrocycle (cP40, shown in Figure 3.2) are shown in Figure 3.5.

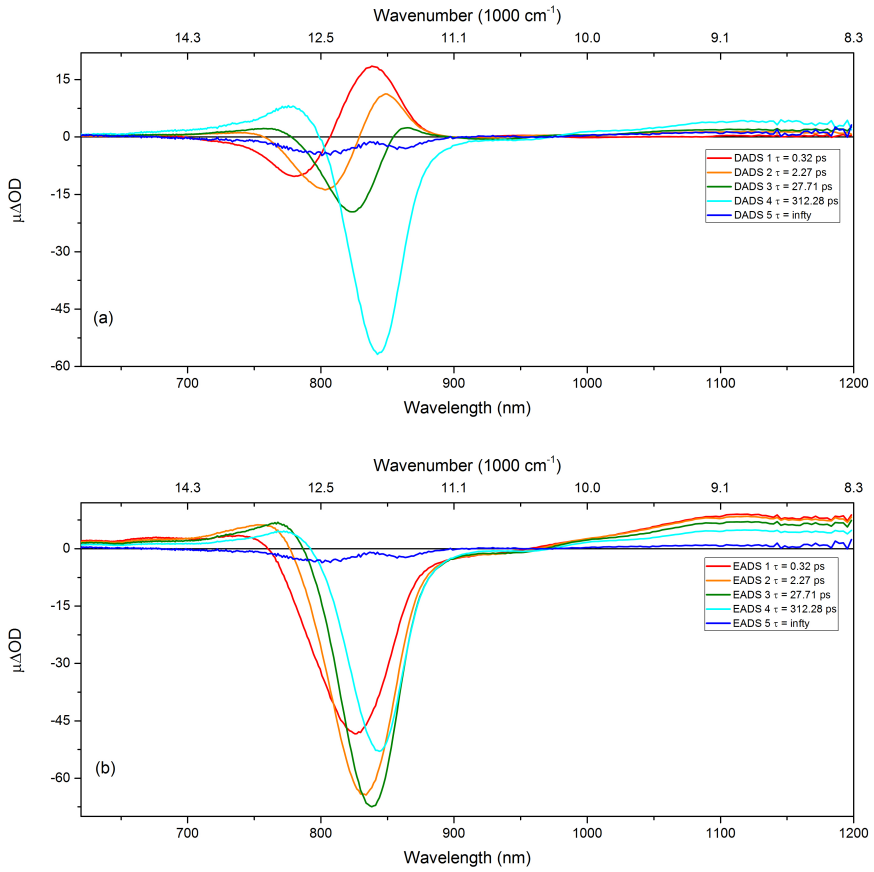

Figure 3.5: Example of DADS (a) and EADS (b) obtained from global analysis of the fsTA dataset of a 40-membered porphyrin macrocycle (cP40) in toluene with 1% pyridine shown in Figure 3.2.

3.3 Summary

In this Chapter a brief description of the principles of fsTA has been presented. In Section 3.1 we have briefly reviewed the developments and the state of the art of femtosecond transient absorption spectroscopy. Subsequently we have listed the photophysical processes that can be detected with a fsTA experiment and how they can be connected to the different Liouville-space pathways listed in Section 2.5.
In Section 3.2 a description of the experimental setup used to collect the fsTA data shown in this thesis is given, explaining which light sources have been used for the study of different molecular systems (Section 3.2.2), the geometry of the experiment and the data acquisition and processing. Also described was how to perform Transient Anisotropy measurements with small adjustments to a standard fsTA experiment (Section 3.2.4).
Finally, the global analysis procedure, which is routinely employed to extract timescales, (DADS and EADS) of the many overlapping components which are simultaneously probed within a fsTA experiment were described in Section 3.2.5.

Chapter 4

Two-Dimensional Electronic Spectroscopy

4.1 Historical Context

The first two-dimensional electronic spectroscopy (2D-ES) experiment operating in the visible was demonstrated by the Jonas group[14] at the same time as the first implementation of multidimensional spectroscopy experiments in the infrared (2D-IR)[18], but developments on the latter thrived better than the former[67]. The main reason for the gap between the advancement of the technique in the two different spectral regions is the difficulty in achieving phase stability. Good quality data can only be recovered with sufficiently good phase stability, i.e. if the relative phase between pulses does not change or drifts during a measurement.[14]

Since the first realisation of a 2D-ES setup, a number of different designs have been proposed and tested to overcome the phase stability problem[70], making it possible to build experiments capable of measuring 2D spectra even in the ultraviolet (UV).[97;98] A full review of the historical advances of 2D-ES will not be given to the reader here, instead the following discussion will focus on the development of the setup used for this work and how it can be compared to others.[72]

Many experimental setups for two-dimensional spectroscopy are based on the BOXCARS geometry, which employs four parallel beams sitting at the corners of a square which are then focused to a common position on the sample cell. In this configuration, the third order signal will be generated in its phase-matched direction, which will overlap with the fourth beam, which is used as a local oscillator (LO) for heterodyne detection.[99] The alternative is the simpler pump-probe geometry which has been applied in 2D electronic, vibrational and electronic-vibrational spectroscopy experiments have been carried out in the pump-probe configuration.[74] 2D spectrometers in pump-probe geometries have three convenient features when compared to fully noncollinear designs:

- they automatically produce absorptive data (equally weighted sum of rephas-

ing and non rephasing), without the need of phasing procedures, because of the self-heterodyne condition imposed by their geometry, in which the probe beam and the signal are forced to be collinear;

- they are inherently phase stable, because the optical elements used to generate the pair of pump pulses separated by τ (acousto-optic modulators, spatial light modulators, pairs of birefringent wedges[100]) generate phase stable collinear pump pulses, with controllable relative phase shift between them;

- building a setup which is broadband, at least on the detection axis, is easier in the pump-probe geometry, because the introduction of a supercontinuum white-light (SWL) probe, is much easier in this configuration.[101]

Pump-probe setups also present some disadvantages, namely:

- the self-heterodyne condition, which simplifies the recovery of absorptive spectra, makes it more difficult to discriminate between rephasing and Non-rephasing signals. In 2D experiments conducted in the pump-probe geometry, this disadvantage can be overcome systematically shifting the relative phases of pulses 1 and 2 by a controlled amount, this procedure is known as phase-cycling;[102]

- the quasi-collinear geometry makes it impossible to control each beam polarisation independently.

A considerable amount of effort is being put in the improvement of 2D-ES spectrometers in different configurations operating in different spectral regions and with different light sources.[69;103–106] In the next sections the laser system, the light sources and the setup which have been used for this thesis will be described in detail.

4.2 Amplified Laser and Noncollinear Optical Parametric Amplifier

The 2D setup used to collect the data shown in this thesis hinges on a commercial Chirped Pulse Amplifier (CPA) which drives a commercial noncollinear optical parametric amplifier (NOPA). The CPA has already been described in Chapter 3. When performing 2D experiments, its output is sent through a 90:10 beamsplitter which sends 10 % of the energy to a TOPAS White (Light Conversion), a commercial NOPA capable of providing $\sim$ 15 fs pulses in the 490-750 nm range, with a typical power (at 550 nm central wavelength) of 25 mW. The NOPA output is recompressed with an external folded prism compressor and it is highly attenuated before entering the 2D setup (usually to 0.6 mW) with a variable neutral density filter. The pulse to pulse fluctuation of the NOPA system is typically below 1 % RMS at the central wavelength at which the NOPA is set.

4.3 Two-Dimensional Electronic Spectroscopy Setup

The experimental setup described in the present work relies on the BOXCAR geometry and was based on earlier work by Selig *et al.*[107] It only uses conventional optics to generate the four phase-coherent beams, and the fully-noncollinear geometry makes possible the separate detection of rephasing and non-rephasing signals.

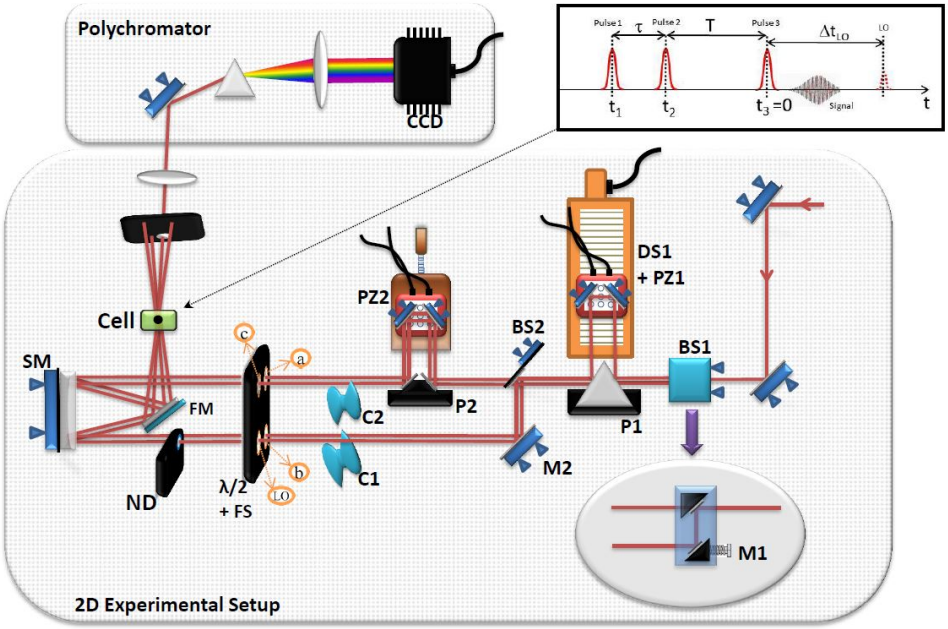

Figure 4.1: Sketch of the experimental setup assembled where: BS1,2 are beamsplitters; P1,2 are aluminium coated knife-edge right angle prisms; DS1 and PZ1,2 are mechanical and piezoelectric delay stages respectively; C1,2 are optical choppers; $\lambda/2$+FS are half wave plates plus fused silica windows; ND is a neutral density filter; SM is a spherical mirror; FM is a folding mirror. The pulse arrival sequence on the sample as well as the signal emission and LO position in time relative to pulse c are shown in the upper right corner. In the upper left corner the home-built polychromator is shown: it is composed of a mirror, a highly dispersive flint glass prism, a lens and the CCD camera.

This approach differs to the others reported in literature because two beamsplitters are used to generate four replicas of the attenuated NOPA beam rather than diffractive optics,[108] and the coherence τ and population T time delays are introduced with the synchronous movement of two (three) mechanical translation stages as shown in Figure 4.1. When employing a noncollinear geomtery, additional problems in achieving phase-stability must be taken into account, because any vibrations of the optical table could introduce alterations of the relative pathlength difference between the arms, which will translate to unpredictable phase-shifts. In our experiment, this problem has been overcome adding pulse delays in a pairwise fashion, which makes the pathlength fluctuations anti-correlated and leads to passive stabilisation of the phase jitter.[108] Further details and demonstration of this

effect will be given later in this Chapter (Section 4.5).
A sketch of the spectrometer is shown in Figure 4.1, the NOPA beam, attenuated to 0.6 mW is steered to the setup with two mirrors. Two irises at the entrance of the experiment (and more along the way) are kept in place to ensure reproducibility. BS 1 and 2 are tailor made through thin film deposition onto a 0.5 mm thick fused silica window (Vortex Optical Coatings) in order to give 50:50 transmission-reflection in the 350-950 nm spectral region. BS1 splits the incoming beam into two at two different heights, at 7 and 9.5 cm from the optical table surface, with the goal of keeping all the beams as low as possible, to minimise the impact of angular oscillations of the optical mounts on the different beam paths.
Subsequently, the top beam is split in two beams, which will be called c and local oscillator (LO), while the lower one is also split to generate beams a and b. Before that, the top beam travels through a pair of delay stages which are sitting on the top of each other. The lower DS1 (Newport, UTS100CC) has a bidirectional precision of 2 fs and can travel over 0.25 m, while PZ1, sitting on top of DS1 (Physik Instrumente, P-622.ZCD) is a piezoelectric mover and it can travel over 250 μm with sub-femtosecond precision (0.5 fs). The whole setup is aligned in a way that the position of DS1 compensates the extra distance (2.5 cm) travelled by the bottom beam after BS1.
Both the lower and the upper beam are then sent through a second 50:50 beamsplitter (BS2), which generates the four phase-coherent collinear beams propagating at the corners of a square with a 2.5 cm side. Afterwards, beams a and c encounter another piezoelectric delay stage PZ2, aligned to compensate for the longer pathlengths travelled by beams b and LO after BS2. The beams pass through four different achromatic half-wave plates, that allow control of their individual polarisation. Here a neutral density filter and a plate of fused silica are added on the LO path, to delay it in time with respect to the homodyne signal and to make it weak enough not to generate competing signals. Before the sample, all four beams hit a spherical focusing mirror (SM, focal length 0.15 m) which focuses all of them to a common spot at the sample position, via a single folding mirror (FM). Two optical choppers are placed between the waveplates and the SM, and since they are the most significant novelty of this 2D spectrometer the chopping sequence will be explained in detail in Section 4.4.

The sample lies at the focal position of the spherical mirror and beams a, b and c are blocked by a mask while LO is collimated with a lens (see Figure 4.2) and guided to a home-made polychromator[109]. In this, a highly dispersive flint glass prism disperses the interference between signal and local oscillator, which is imaged (using a 0.3 m focal length lens) onto a CCD camera which consists of a single line of 1024 pixels. The CCD used in our setup is a e2v AVIIVA EM1, which

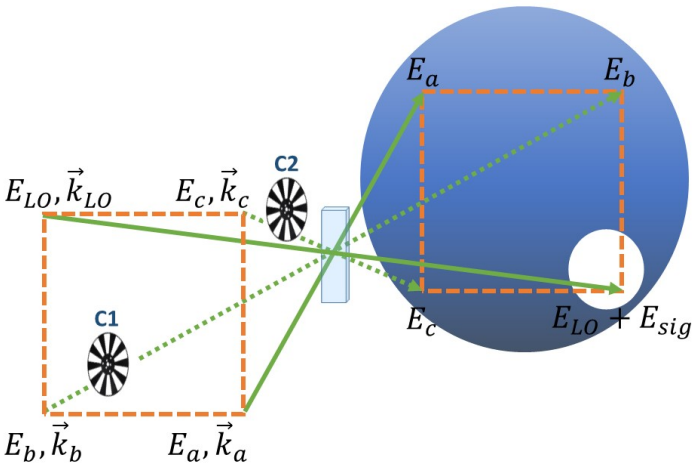

Figure 4.2: BOXCARS beams arrangement and choppers employed in the 2D-ES setup.

acquisition rate can be regulated up to 77 kHz. The amplifier triggers the camera via TTL at 1 kHz and a TTL signal is sent to a voltage acquisition board, which records the chopper state for every shot. In this way, every time the camera records a spectrum, the state of choppers 1 and 2 is acquired as well, allowing the data acquisition software to track if b and c beams were blocked or unblocked for each spectrum. All this information allows computation of the different signals, as will be described in Section 4.4.

4.4 Data Acquisition and Removal of Scattered Light

The camera employed in our experiments allows data acquisition at frequencies up to 77 kHz, but the amplified laser system is operated at 1 kHz and subsequently the camera is triggered at 1 kHz, while the chopper frequencies have been chosen in order to be one half of the fundamental for C1 (500 Hz) and one quarter of it for C2 (250 Hz). Together, the two choppers give four possible combinations, and one laser shot is individually acquired for each of those, which will be explained in detail in this Section.

Before focusing on how the chopper sequence permits fast data acquisition and efficient scattering removal, a brief excursion into how other BOXCARS-type experimental setups deal with the scattering problem will be given to the reader. The biggest experimental concern here is diffusively scattered light from the sample propagating with the same wavevector of the signal and LO. Light scattered from the pump beam will be phase coherent with LO and signal and will produce interferometric signals on the camera.[99] Another problem is that, because the LO beam is

delayed from the signal by 550 fs, it can act as a probe pulse for transient grating (TG) signals produced by the interaction between every possible combination of a, b and c.[102]

In some setups the pump-probe contributions are negated by having the LO beam travelling around the sample cell. For heterodyne detection this is not ideal because, when the LO is transmitted through the sample, it acquires the same envelope and phase distortions experienced by the signal itself,"cleaning" the resulting heterodyned signal from these contributions. This makes it possible to study high concentration samples (OD > 0.3).[110]

A number of other methods to deal with scattering are present in literature, among those it is worth mentioning double modulation with lock-in detection[111] or the use of shutters.[99] The drawback of the first is that lock-in has to use high-repetition rate laser systems, while in the second, the mechanical shutter considerably slows down the measurement procedure. The scattering removal procedure employed in our laboratory is an intermediate of those, because choppers act like a shutter, but they have the advantage that they can be synced to the laser output and the data acquisition electronics, allowing us to detect one single laser shot for the different condition of the two choppers C1 and C2, blocking and unblocking beams b and c at different frequencies, as sketched in Figure 4.3.

Chopper C1 which modulates beam b with wavevector $\vec{k_b}$, is synchronised with the amplifier at one half of its repetition rate (one cycle takes 2 ms) while C2 acts on beam c with wavevector $\vec{k_c}$, at one quarter of the laser repetition rate (one cycle every 4 ms). The combined effect of C1 and C2 is to create four different combinations A, B, C, D which will be repeated over time*; every time b will be blocked or unblocked, the sample will be illuminated by beam c once, while in the other case c will be blocked. Since the camera is synchronised with the laser, it is possible to acquire each single shot modulated by the pattern imposed by the combined action of C1 and C2, resulting in the $A, ..., D$ conditions shown in figure 4.3. This permits incorporation in the data acquisition software of a routine to process these combinations. Defining S_n as scattering and pump-probe contributions from beams $n \in \{a, b, c\}$ and with E_{LO} and E_{sig} defined as the electric fields of the local oscillator and of the signal, the software is set to compute the following quantities:

$$\begin{aligned} \alpha = A - B &= |S_a + S_b + E_{LO}|^2 - |S_a + E_{LO}|^2 \\ &= |S_b|^2 + 2\Re\{S_a S_b^*\} + 2\Re\{S_b E_{LO}^*\}, \end{aligned} \tag{4.1}$$

*for a given pair of τ, T times, corresponding to a defined position of the delay stages, until a number of laser pulses high enough to ensure a good SNR (usually 300) is recorded on the CCD camera.

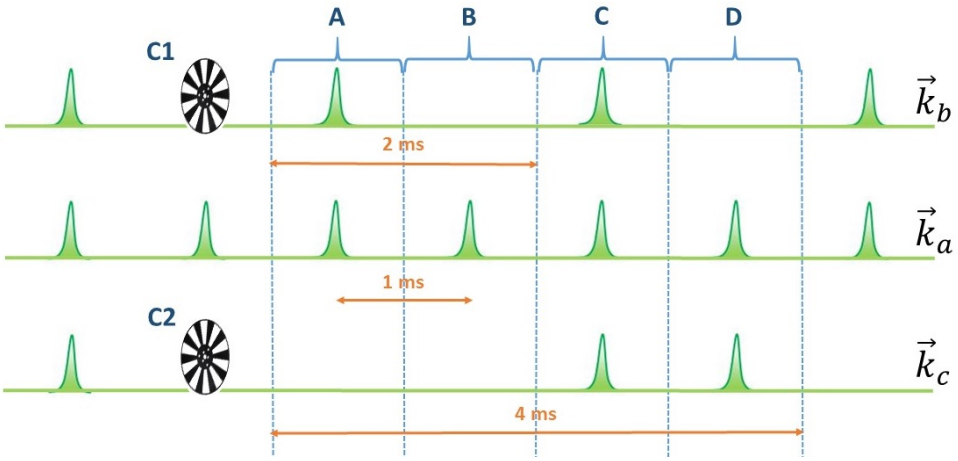

Figure 4.3: Scheme showing the different sample illumination conditions created by the chopper sequence used. Chopper C1 acts on beam b with a frequency of 500 Hz and chopper C2 acts on beam c with a frequency of 250 Hz

$$\begin{aligned}\beta = C - D = |S_a + S_b + E_{sig}E_{LO}|^2 - |S_a + S_c + E_{LO}|^2 \\ = |E_{sig}^2| + |S_b|^2 + 2\Re\{S_a S_b^*\} + 2\Re\{S_b E_{LO}^*\} + 2\Re\{S_a E_{sig}^*\} + ... \\ ... + 2\Re\{S_b E_{sig}^*\} + 2\Re\{S_c E_{sig}^*\} + 2\Re\{S_b S_c^*\} + 2\Re\{E_s E_{LO}^*\},\end{aligned} \tag{4.2}$$

$$\begin{aligned}\beta - \alpha = |E_{sig}|^2 + 2\Re\{S_a E_{sig}^*\} + 2\Re\{S_b E_{sig}^*\} + 2\Re\{S_c E_{sig}^*\} + ... \\ ... + 2\Re\{S_b S_c^*\} + 2\Re\{E_{sig} E_{LO}^*\}\end{aligned} \tag{4.3}$$

The only term which should reach the detector is the last of Equation 4.3, which coincides to the signal heterodyned by the local oscillator, but the five other terms are phase coherent with it and will be detected as well. However, for the reasons listed below, they produce negligible contributions:

- the three products $\Re\{S_n E_{sig}^*\}$ arise from interference between elastic scattering of the nth beam along the phase matched direction and the signal electric field, but these terms become small because of the small amplitude of the signal, although they could become significant for highly scattering samples such as thin films, nanocrystal or nanoparticle suspensions, or in general for large (molecular) aggregates of dimensions comparable to the laser wavelength,

- the fifth term $\Re\{S_b S_c^*\}$ does not carry any pump-probe contribution along the LO wavevector, but only along the directions of either beams b or c. Its actual impact on the detected signal will then just be the interference of Rayleigh scattering of beams b and c, which it is reasonable to consider as very small,

- finally, the first term corresponds to the homodyne signal, which is strong enough to be detectable. Despite this, the spectral interferometry procedure which is applied to the detected signal, comprises a time windowing of the signal's inverse Fourier transform over the $\tilde{\nu}_3$ axis, so that the signal will be resolved on the conjugated detection time t axis.[99] On this axis, the homodyne

contribution, since it is generated by beams a, b, c, will appear at an earlier time (0 fs) compared to the heterodyne signal, centred at t_{LO}, which arises from the interaction of beams a, b, c, LO, where LO is delayed by an amount of time depending on the amount of glass inserted on its path (550 fs in our case). Hence, the homodyne signal is discarded because it is centred at a time point which is outside the Fourier window.

The time windowing procedure not only makes it possible to distinguish between homo- and heterodyned signals, but also to filter out all the scattering components which are not centred at t_{LO}.

Another point to be highlighted is that chopping beam c with C2 allows elimination of the term $2\Re\{S_b E^*_{LO}\}$ from Equation 4.2. This product contains pump-probe contributions from b and LO, which cannot be time-windowed out of the signal and can be significant for samples with high $\chi(3)$ values.[72]

A further advantage of employing the double-chopper scheme is that, together with a 2D spectrum, at each population time T, a pump-probe and a LO spectra are obtained, in identical experimental conditions and without the need for extra acquisition time. The explanation is illustrated in Figure 4.3, following the procedure at one T. Initially, when we are in the condition B of Figure 4.3, both beams b and c are blocked, so that only a and LO can induce perturbations in the sample. Some small pump-probe contamination arising from interactions of a and LO could be detected, but what is being measured here is essentially the spectrum of LO.

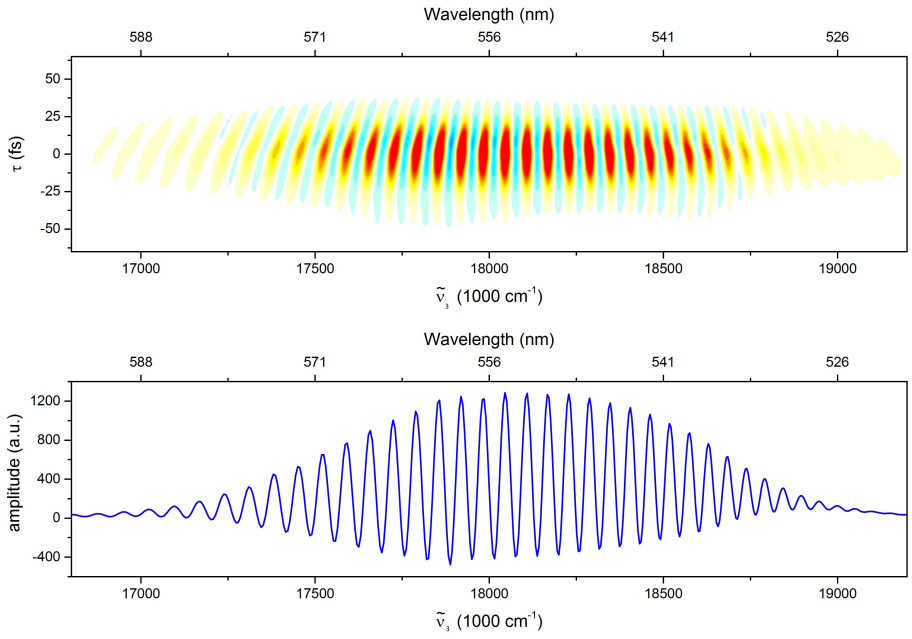

Figure 4.4: Top: example of an interferogram measured with the 2DES setup. Bottom: a horizontal cut from the interferogram, displaying the signal acquired in a single coherence time ($\tau = 0$) in the spectral domain.

After the acquisition of the LO spectrum, a pump-probe spectrum (at the given

T) is measured, through the use of Equation 4.1, which subtracts the data recorded when only a and LO are present from the data recorded with a, b and LO unblocked. To obtain a pump-probe spectrum for the correct value of T, the long DS1 delay stage moves in order to compensate the delay between c and LO, which is experimentally determined before the start of the experiment. Doing this, the LO is shifted to time 0 fs in order to generate a pump-probe signal where b is the pump perturbation and LO probes it. Now that LO and pump-probe spectra have been collected DS1 moves back to its previous position and the 2D interferogram, shown in Figure 4.4 is acquired by scanning τ in 4 fs steps. Usually, acquiring 2D interferogram, pump-probe and LO spectra requires 90 seconds (when averaging over 300 laser shots for each coherence time point) per each T point.

4.4.1 Delay Stages Movement Sequence

We have anticipated in the previous section that a complicated sequence of delay stage movements is required in order to recover a 2D-ES spectrum. In this section we will explain how this procedure is carried out in our experimental design. The final objective of the measurement is to recover a complex third-order function $S^{(3)}(\omega_t, T, \omega_\tau)$ (see Section 2.5) which will be made up of the Real absorptive $\Re\{(\omega_t, T, \omega_\tau)\}$ and the Imaginary dispersive $\Im\{(\omega_t, T, \omega_\tau)\}$ responses of the sample under investigation.

The complex function $S^{(3)}(\omega_t, T, \omega_\tau)$ is not straightforwardly obtained from the 2D measurement, and in the BOXCARS geometry the relative timing of the pulses will affect the direction on which the different nonlinear signals will be emitted. Moreover, the absorptive 2D lineshape is given by the sum of equally weighted rephasing and non-rephasing signals.[112] so it will be necessary to separately record these two components. After the sample is perturbed by the interactions with beams a, b, c (neglecting here interactions with the weaker LO pulse), it will contain contributions propagating on one of the $\pm\vec{k}_a \pm \vec{k}_b \pm \vec{k}_c$ directions, as highlighted in Section 2.5.

In the (fully noncollinear) BOXCAR geometry the third order signals generated by a first interactions with a, followed by interactions with b and c will be emitted in a direction along which no other contributions are supposed to interfere, it is in fact a "background-free" geometry. In Section 2.5 we have also stressed out how the 864 possible interactions, reduce to four if we invoke the rotating wave approximation and the semi-impulsive condition. Two of these (rephasing) response functions will propagate along $\vec{k}_{sR} = -\vec{k}_1 + \vec{k}_2 + \vec{k}_3$ while the other two (non-rephasing) will have a resulting wavevector of the form $\vec{k}_{sNR} = +\vec{k}_1 - \vec{k}_2 + \vec{k}_3$; in these equations the numeric indexes are related to the time ordering of the pulses, so there is no fixed correspondence between $1, 2, 3$ and a, b, c. The experiment is designed in such a way that only signals propagating collinearly with the LO will reach the detector, which will carry contributions which will now be described, using Figures 4.5 and 4.6 as

references. In these two figures the BOXCAR beam arrangement is sketched in a coordinate system and and the time ordering of the three pulses is shown.
The wavevector of pulses a, b, c can be written in this coordinate system (as shown in Figure 4.5) as:

$$\mathbf{k_a} = (p, -p, 2p)$$
$$\mathbf{k_b} = (p, p, 2p)$$
$$\mathbf{k_c} = (-p, -p, 2p)$$
$$\mathbf{k_{LO}} = (-p, p, 2p)$$

Now that a framework has been established, it is possible to correlate the pulse

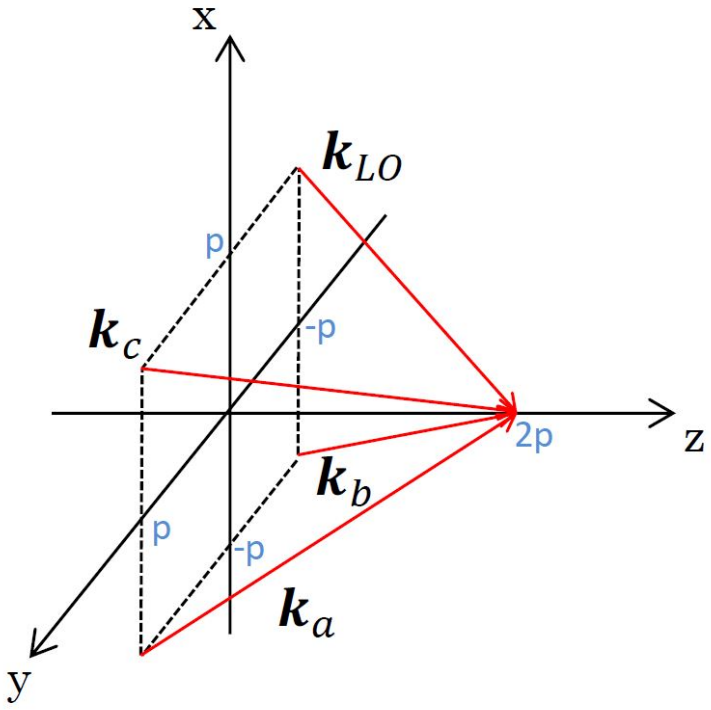

Figure 4.5: Scheme of the wavevectors in the BOXCAR geometry with a coordinate system centred at the centre of the square formed by beams a, b, c, LO. The component along the z axis is equal for every beam, while the components along x and y are equal in module, set to p, while the $2p$ component along z has been chosen arbitrarily.

arrival sequence with the signals which are detected in each case. If the sample first interacts with pulse a, and subsequently with pulses b and c, as shown in Figure 4.6 (right-hand side) for the particular $T = 0$ condition, at which b and c are coincident in time $\vec{k}_1 = \mathbf{k_a}$, $\vec{k}_2 = \mathbf{k_b}$ and $\vec{k}_3 = \mathbf{k_c}$, the only combination of plus and minus sign which will give a detectable signal, which has to be collinear with the local oscillator, will be:

$$-\vec{k}_1 + \vec{k}_2 + \vec{k}_3 = -\mathbf{k_a} + \mathbf{k_b} + \mathbf{k_c} = \mathbf{k_{LO}} \tag{4.4}$$

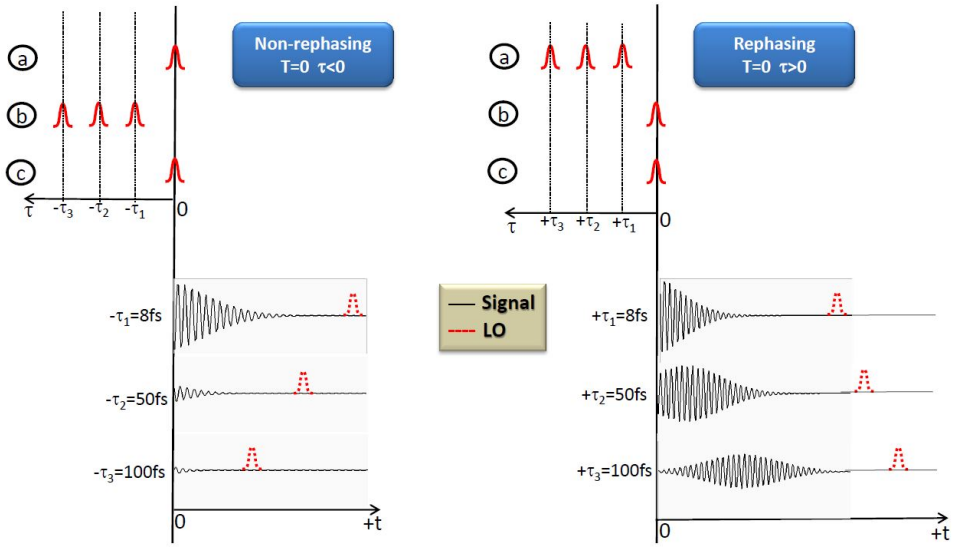

Figure 4.6: Time-ordering of the pulses for the rephasing and non-rephasing conditions

Which corresponds to the rephasing contribution already discussed. Therefore, the rephasing dataset will be acquired in our experiments when the time ordering of the pulses is a first, followed by b, and then by c.
It is important to recall that, in this experimental configuration, a non rephasing signal is still being emitted, but its propagation direction will be $\mathbf{k_a} - \mathbf{k_b} + \mathbf{k_c} = (-p, -3p, 2p)$ so it will not reach the detector. In principle, another detector (and a second LO beam) could be added on this direction but its implementation would make the setup even more complicated, and the further problem of requiring exactly balanced detectors will appear, given that the absorptive 2D spectrum is the sum of equally weighted rephasing and non rephasing spectra. Experimentally, this problem is bypassed making use of the phase-matching condition:[73] if the time ordering between first and second field-matter interactions is reversed, namely if the arrival order is b, a and c, then $\vec{k}_1 = \mathbf{k_b}$ $\vec{k}_2 = \mathbf{k_a}$ and $\vec{k}3 = \mathbf{k_c}$, the non rephasing signal will have a wavevector given by:

$$\vec{k}_1 - \vec{k}_2 + \vec{k}_3 = \mathbf{k_a} - \mathbf{k_b} + \mathbf{k_c} = \mathbf{k_{LO}} \tag{4.5}$$

Thus, it is possible to avoid the additional complications and expense of having another LO and detector placed in another direction, and just obtaining a Non-rephasing signal generated on the same direction as the rephasing one (and of the LO) merely swapping pulses a and b in time.
Now that we have emphasised the fact that rephasing and Non-rephasing contributions can be obtained in such a convenient way, it is possible to move on and describe the actual delay stages movement sequence. The starting position is taken as the one in which a, b, c coincide in time, followed by LO, delayed by ~ 550 fs. In Figure 4.6 both the rephasing (left hand side) and Non-rephasing (right hand side)

conditions are schematised, with LO depicted as a dashed red Gaussian.
T, the population time, is marked by the condition of having either beams a or b being overlapped in time with c. This point also serves as a reference to determine coherence τ and signal t times; the population time T is defined $T = t_c - t_n$ where n is the last pulse which arrives in the sample (can be either a or b). Conversely, the coherence time τ is defined as $\tau = t_b - t_a$, basically τ will have positive values for rephasing signals (if $t_b > t_a$, then the pulse arrival order will be a, b, c which corresponds to a detectable rephasing signal) while negative values of τ will correspond to non rephasing signals being collected at the detector (if $t_b < t_a$, then the pulse arrival order will be b, a, c which corresponds to a detectable non rephasing signal). When scanning the τ time interval the "more negative means earlier" convention does not apply for the coherence time. The condition stated above still holds for the detection time t, for this reason in Figure 4.6 coherence times are reported as a support, but in order to evaluate which pulses arrives at which time, their position along the t scale has to be considered. The net result is that left means earlier while right means later.
When performing a measurement, the first step is setting T at the desired point, this is done moving DS1, which in turn will change the interpulse delay between the pulse pairs (a, b) and (c, LO). Afterwards, the coherence time can be scanned stepping PZ2, which acts orthogonally to PZ1, altering the relative delays between (a, c) and (b, LO). As a side effect of the scan over the coherence time τ, the delay between c and LO will change as well. This could have an effect on the aforementioned Fourier windowing procedure, which requires a fixed delay between the third-order signal (which is linked in time to the arrival of the third pulse c on the sample) and LO. The signal emission maximum in time is regulated by τ, as shown in Figure 4.6, where it is more evident for the rephasing case. The Non-rephasing signal is less straightforward to imagine, and one has to think as if the signal was continuing at negative detection times, where the maximum amplitude will be located. Therefore, the delay added between LO and c allows manteinance of a constant delay between the maximum of the third-order signal and LO.[72]
In fact, to acquire the non rephasing signal, which corresponds to negative coherence times, PZ2 has to be scanned forwards. The arrival order is swapped and pulse b arrives first at the sample, and the delay stage movement changes the relative time delays of pulses a and c with b. Scanning positive coherence times has an additional complication, in this case PZ2 is translated backwards, to ensure the pulse ordering to be (a, b, c), but when PZ2 is moved backwards, c and a will arrive at the sample before b, generating a third-order signal with a different phase matching condition. To correct for this effect, PZ1 has to be moved forwards in order to counterbalance the backwards movement of PZ2.[113]
Moving the delay stages in the fashion described automatically gives the rotating

frame conditions[74] (introduced in Section 2.5). This derives from the fact that the phase shift between signal and *LO* is inherently locked to the phase shift of the coherence time (between a and b). To elucidate this effect the phase of the measured signal has to be taken into account. If $\Delta\phi_{ab} = \phi_a - \phi_b$ and $\Delta\phi_{cLO} = \phi_c - \phi_{LO}$ the signal will be proportional to:

$$I_s \propto \Re(e^{-i(\Delta\phi_{ab}-\Delta\phi_{cLO})}e^{-i\omega(t-\tau)}R'(\tau,T,t)) = \Re(e^{-i(\Delta\phi_{ab}-\omega t)}e^{i(\Delta\phi_{cLO}-\omega\tau)}R'(\tau,T,t)) \tag{4.6}$$

in which $R'(\tau,T,t)$ is the envelope of the response function. We have already shown how shifting the coherence time by a $\Delta\tau$ so that $\tau' = \tau + \Delta\tau$ will produce an opposite shift in the timing of the local oscillator $t'_{LO} = t_{LO} - \Delta\tau$. Using Equation 4.6 it is easy to prove that the phase shift induced in the signal by the shift in the coherence time will also be canceled by the local oscillator delay.
The signal we are measuring will not be oscillating close to the optical frequency during the acquisition of the coherence times, because of the phase offset which is constantly added to *LO* while τ is being scanned bringing the resulting frequency to zero, making it possible to undersample τ by only taking enough points to reconstruct the envelope of the response functions, rather than their fast oscillations. This condition is convenient for two principal reasons:

- The signal acquisition time becomes substantially shorter: for the whole response function to be measured, at least two time points for each cycle of the highest optical frequency contained in the signal have to be acquired in order not to lose information, as stated by the Nyquist-Shannon theorem. As an example, at 600 nm the optical cycle is roughly 2 fs, requiring τ to be sampled at least with 1 fs time steps. In our setup, due to the rotating wave condition, coherence time steps of 4 fs, which are dense enough to accurately track the envelope of the response function, are routinely used, speeding up the acquisition by, at least, a factor of four.

- Phase stability requirement: since we are only measuring the envelope of the response function, the phase stability constraint over a fraction of the optical cycle is relaxed, it is in fact sufficient to keep the phase stable for a fraction of the pulse duration (15 fs).

4.5 Phase Stability

As said earlier, the key issue for 2D-ES experiments is keeping the phase stability between pulses. Mechanical displacement of the optical components, vibrations of the optical table or air flow in the laboratory can negatively affect it, having a detrimental effect on the quality and accuracy of the recorded data.
As anticipated in the previous Section 4.4.1, the resulting phase of the signal depends

on its phase matching conditions (see Equation 4.6). Because of the way in which our setup was designed, the rephasing signal will have wavevector $\mathbf{k_s} - \mathbf{k_a} + \mathbf{k_b} + \mathbf{k_c}$ and the heterodyned 2D signal will carry a phase:

$$\Delta\phi_s = -\phi_a + \phi_b + \phi_c - \phi_{LO} + \phi_{sig} \tag{4.7}$$

where ϕ_s and ϕ_{sig} are the phase contributions carried by the heterodyned and homodyned signals, respectively. The fluctuations in the phase components can be written as follows:

$$\delta(\Delta\phi_s) = (\delta\phi_b - \delta\phi_a) + (\delta\phi_c - \delta\phi_{LO}) \tag{4.8}$$

It is possible to find an analytical expression for the total phase fluctuation by going through the experimental setup for each of the four beams (referring to Figure 4.1), keeping track of every possible fluctuation induced by each of the optics along their paths. As an example, if we do so for beam a, we get:

$$\delta\phi_a = \delta\phi_{BS1} + \delta\phi_{M1} + \delta\phi_{BS2L} + \delta\phi_{PZ2+P2} + \delta\phi_{SM} + \delta\phi_{FM} \tag{4.9}$$

If the same analysis is carried out for beams b, c, LO it is possible to calculate the two bracketed sums on the right-hand side of Equation 4.8:

$$\delta\phi_b - \delta\phi_a = \delta\phi_{M2} - \delta\phi_{PZ2+P2} \tag{4.10}$$

$$\delta\phi_c - \delta\phi_{LO} = -\delta\phi_{M2} + \delta\phi_{PZ2+P2} \tag{4.11}$$

From these two equations is is evident that the contributions are anti-correlated, this results in a net zero phase fluctuation: $\delta(\Delta\phi_s) = 0$. Thus, even if the phase between all the possible beam pairs experiences fast fluctuations during the acquisition time, our 2D-ES setup is designed in such a way that they cancel out, improving the phase stability without the need to actively correct for it.[108]

Here it is important to highlight that the just described self-compensation for phase fluctuations only holds for perturbations induced by the optics in the setup, and it does not account for single beam fluctuations that could be generated, for instance, by strong air currents. To minimise this problem the whole setup is enclosed in a plastic box and the footprint of the whole 2D spectrometer is kept as small as possible (30 × 50 cm) on the optical table.

4.6 Data Processing

The aim of this section is to illustrate the steps required to obtain complex-valued 2D spectra from the raw datasets recorded from the experimental setup used in this work. At any given population time T, the raw output is made up of three files:

- The interference between the transient grating signal of the sample and the local oscillator, resolved along the emission axis $\tilde{\nu}_3$ and recorded as a function of the coherence time τ, shown in Figure 4.7, which contains the information needed to generate a 2D-ES spectrum. This file will be indicated as spectral interferogram;

- the pump-probe signal recorded for the same value of T, using beam b as a pump and probing with the LO beam. The pump-probe data are used to recover the phase information of the 2D-ES spectrum, as explained in Section 4.6;

- the spectrum of the local oscillator, measured after it has travelled through the whole experimental setup and the sample (shown as a red solid line in Figure 4.10).

It is useful to recall that all three file are obtained through acquisition at different combinations of choppers C1 and C2, as described in Section 4.3. Before starting the acquisition of a dataset, two preliminary steps need to be executed. To begin with, a Transient Grating-Frequency Resolved Optical Gating (TG-FROG) scan between beams a, b and LO on a cell filled with neat solvent (typically cyclohexane) is acquired to measure phase, and also to check the time resolution, the temporal position and the recompression of the NOPA pulses. The delay stages used here are DS1 + PZ1 (refer to Figure 4.1), which move beams c (which for this TG-FROG measurement is blocked) and LO against beams a, b. The phase matching condition of this signal is that it will be emitted collinearly with beam c, which makes it necessary to introduce a flip mirror in its path to steer it to the detection section.

After acquisition of the TG-FROG signal between a, b and LO, the experiment is brought back to the standard configuration, to perform a 2D-ES scan of the solvent cell. The interference pattern between TG-FROG data on the solvent cell and LO are reported in Figure 4.7 (a), while in (b) the same result is reported for a perylene bisimide monomer sample dissolved in toluene, at $T = 75$ fs. The details of this sample will be extensively discussed in the next Chapter, for now they are just shown in order to help the discussion of the data processing method. The final purpose is to use the spectral interferograms, such as the one shown in Figure 4.7, to compute complex-valued 2D-ES spectra for every population time T, as a function of excitation and detection wavenumbers $(\tilde{\nu}_1, \tilde{\nu}_3)$. The spectral interferogram shown in Figure 4.7b can be written as:

$$\begin{aligned} I_{SI}(\tau, T = 75fs, \tilde{\nu}_3) = &|E_s(\tau, T = 75fs, \tilde{\nu}_3)|^2 \\ &+ E_S(\tau, T = 75fs, \tilde{\nu}_3) E^*_{LO}(\tilde{\nu}_3) e^{i2\pi c\tilde{\nu}_3(t_s - t_{LO})} \\ &+ E^*_S(\tau, T = 75fs, \tilde{\nu}_3) E_{LO}(\tilde{\nu}_3) e^{-i2\pi c\tilde{\nu}_3(t_s - t_{LO})} \end{aligned} \quad (4.12)$$

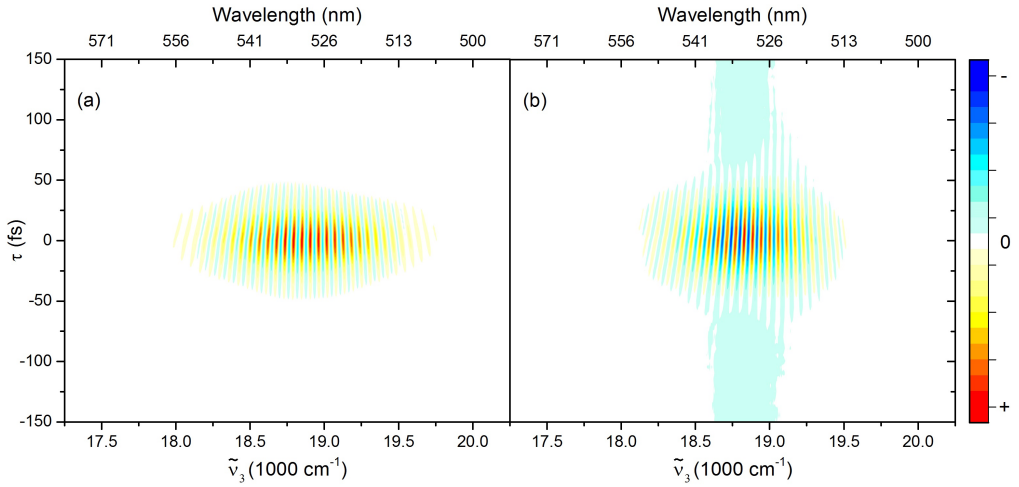

Figure 4.7: (**a**) spectral interferogram arising from the interference of the local oscillator with the transient grating signal from a 1 mm static cell filled with cyclohexane at $T = 0$ fs. For this measurement, the delay between signal and LO was measured to be 588.4 fs (measurement procedure described in Section 4.6). **(b)** same as **(a)**, but for a perylene bisimide monomer sample at $T = 75$ fs. The weak negative time independent signal is due to residual scattering of beams a, b, c or LO in the detection direction. This file is a part of the data shown in the next Chapter.

Where the scattering contributions explained in Equation 4.3 have been omitted, and due to the chopping sequence the intensity of the LO does not have to be introduced in this equation. We now highlight how all the three terms of 4.12 are separated if shown on the detection time axis (the Fourier pair of the detection frequency $2\pi c\tilde{\nu}_3$): the first term, which is the homodyne signal, is centred at $t = 0$ while the second and third terms of the expression appear at $\pm t_{LO}$, respectively. Since we want to extract the component $E_s(\tau, T = 75$ fs, $\tilde{\nu}_3)$ from the spectral interferogram, we can perform a discrete Fourier transform over the $\tilde{\nu}_3$ axis. The result of this operation is shown in Figure 4.8 (in terms of their absolute value and for $T = 0$) for the cyclohexane cell and for the perylene bisimide monomer for $T = 75$ fs. All the terms present in Equation 4.12 can be identified according to their different timing in t.

The Fourier transform along the detection axis is applied for each point on τ and then a rectangular window applied in the time domain filters out the undesired signals contributions (the ones appearing at $t = 0, -t_{LO}$), leaving only:

$$E_s(\tau, T = 75fs, \tilde{\nu}_3)E^*_{LO}(\tilde{\nu}_3)e^{i2\pi c\tilde{\nu}_3(t_s - t_{LO})} = |E_S(\tau, T, \tilde{\nu}_3)||E_{LO}(\tilde{\nu}_3)| \times e^{i2\pi c\tilde{\nu}_3(t_S - t_{LO})}e^{t(\phi_S - \phi_{LO})} \quad (4.13)$$

here the signal and (conjugated) local oscillator electric fields have been rewritten in order to highlight their absolute values and phases. The intensity of the LO beam after transmission through the sample $|E_{LO}(\tilde{\nu_3})|$ is acquired for every value of T, and the phase $e^{i2\pi c\tilde{\nu}_3(t_S - t_{LO})}e^{t(\phi_S - \phi_{LO})}$ can be extracted from the measurement on

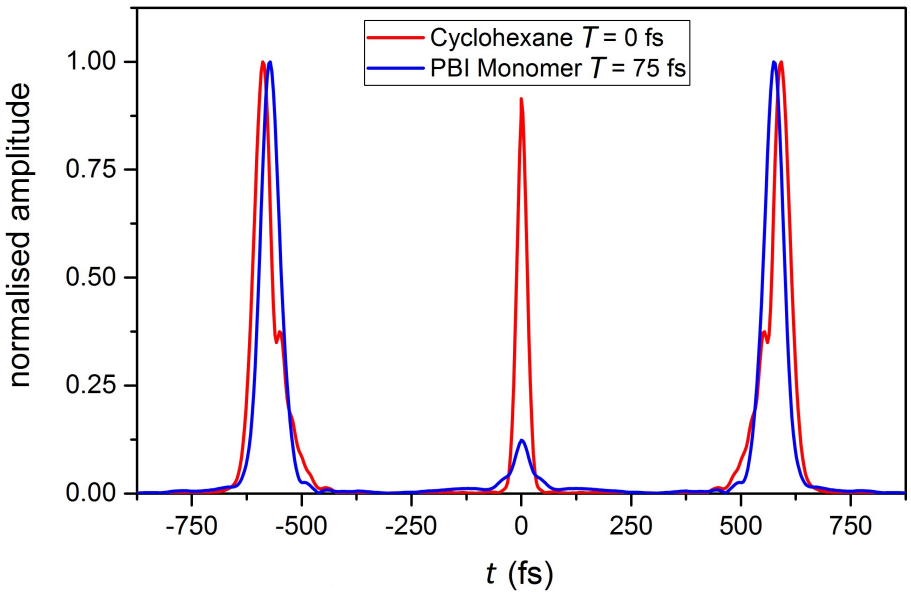

Figure 4.8: Discrete Fourier transform of the spectral interferograms shown in Figure 4.7 for $\tau = 0$. The desired component of the signal in the time domain can be isolated windowing a rectangle around the signal centred at positive times.

the cyclohexane cell (Figure 4.7 (a) and red solid line in Figure 4.8) since the delay between *LO* and transient grating is known.

However, the information gathered so far are not sufficient to recover the phase of the 2D-ES spectra. This is because the phase component ϕ_S of the non-resonant solvent transient grating signal is measured in a different phase-matched direction ($-\mathbf{k_a}+\mathbf{k_b}+\mathbf{k_c}$) and will thus be different from that of the sample, which arises from resonant rephasing and Non-rephasing interactions. To overcome this problem, the projection-slice theorem is used,[114] taking as a reference the pump-probe spectrum at the same value of T. Note that, to pre-process the data before applying the projection-slice theorem, we isolated the modulus $|E_S(\tau, T, t)|$ and collected the phase value on the detection frequencies $\tilde{\nu}_3$ for every value of τ. Because of the validity of the rotating wave frame condition, this function will be a slowly varying function of τ; hence, the product of the measured signal with an exponential of the form $e^{i2\pi c\tilde{\nu}_0\tau}$, in which $\tilde{\nu}_0$ is the central wavenumber of the NOPA pulse spectrum, will yield the desired signal oscillating over τ. The outcome of this procedure (the real part of the signal, for $\tilde{\nu}_3$= 18865 cm^{-1}) for the data shown in Figures 4.7 and 4.8 is shown in Figure 4.9. From this figure it is also obvious that, if we were not in the rotating frame condition, sub-fs time steps would become necessary when sampling the coherence time τ.

Through all the steps mentioned so far, we obtained a time- and frequency-dependent signal electric field $E_S(\tau, T, \tilde{\nu}_3)$ which now, will yield rephasing and non rephasing 2D spectra after applying a Fourier transform over the positive and negative coherence time axes, respectively. Nevertheless, the phase of the 2D maps we have just obtained still needs to be adjusted, this is done applying a phasing

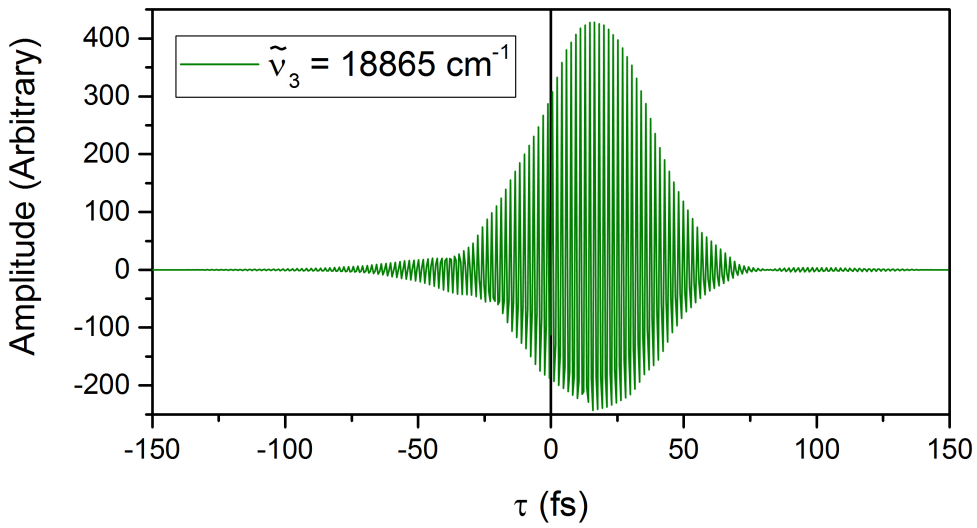

Figure 4.9: Real part of the signal field oscillating over τ, at $\tilde{\nu_3} = 18865$ cm^{-1}. Here, coherence times $\tau > 0$ (< 0) identify the rephasing (non rephasing) component of the third order signal.

algorithm.[14;113;114] This algorithm, is based on the projection-slice theorem, which, in the appropriate formulation for 2D-ES case, declares that a broadband transient absorption spectrum (colloquially known as pump-probe spectrum) is equal to the integration over the excitation frequency axis ($\tilde{\nu}_1$) of an absorptive 2D-ES spectrum,[14] apart from a phase factor which is the value we are going to determine.

The pump probe signal is self-heterodyned so it is automatically phased, moreover it contains contributions from both the rephasing and Non-rephasing pathways, while an absorptive 2D spectrum is the equally weighted sum of rephasing and Non-rephasing 2D spectra.[73;112] Consequently, to recover the phase information, the rephasing and non rephasing 2D maps are summed over the detection axis and then multiplied by a total phase $e^{i((\tilde{\nu}_3-\tilde{\nu}_0)2\pi c t_c+\phi_c)}$, where t_c and ϕ_c are parameters chosen in order to give the best fit between the integral over $\tilde{\nu}_1$[99] of the 2D data and the pump probe spectrum. An amplitude scaling factor is also used to match the amplitudes of the 2D and of the pump-probe signals. The result of this operation for the perylene bisimide monomer dataset used above can be seen in Figure 4.10.
The final results of the whole procedure are the complex-valued Absorptive (Real, $\Re$) and Dispersive (Imaginary, $\Im$) 2D spectra, shown in Figure 4.11 (a) and (b), respectively.

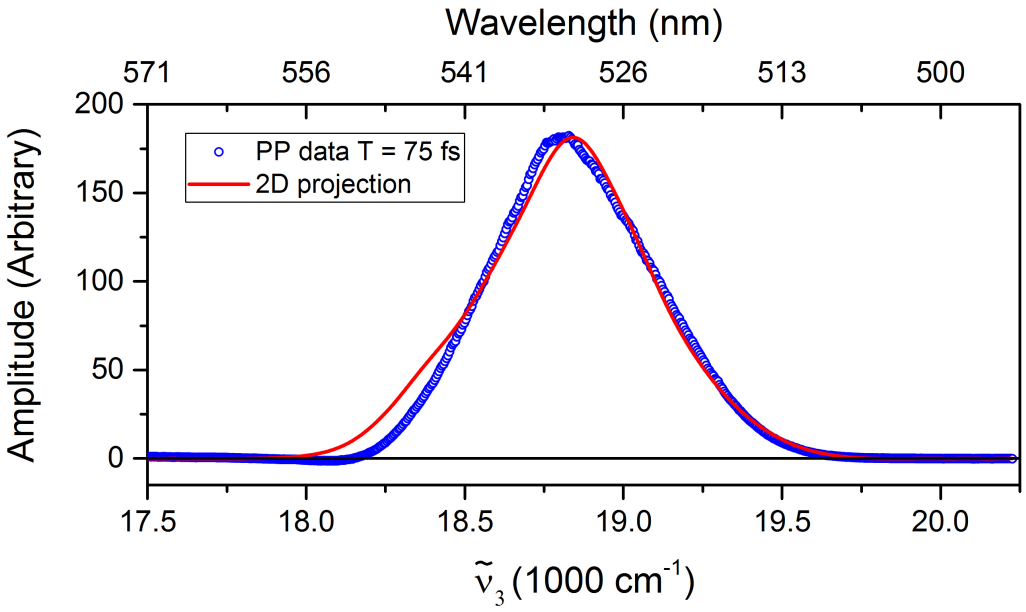

Figure 4.10: Juxtaposition of the pump-probe data and the integration over $\tilde{\nu_1}$ of the real part of the equally weighted, rephasing and non rephasing, 2D maps, all taken at $T = 75$ fs. The phase of the 2D dataset has been adjusted in order to give the best match with the pump-probe data.

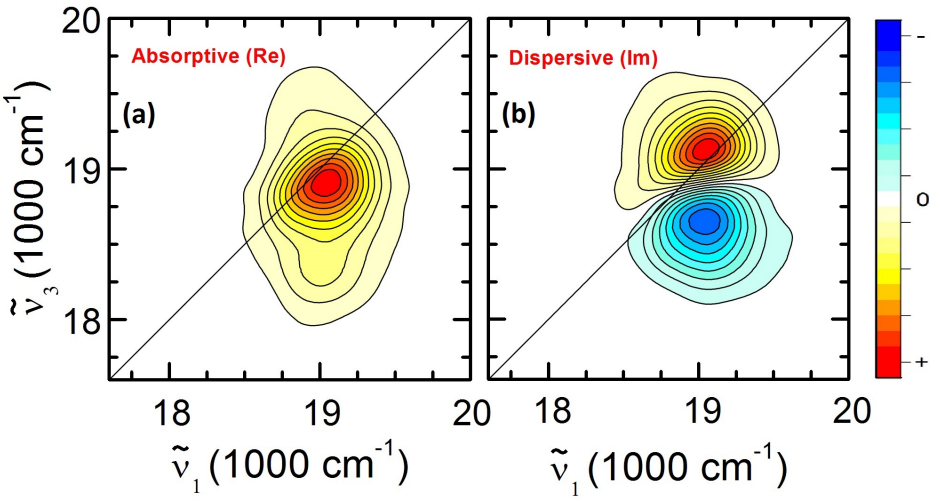

Figure 4.11: Phased (a) Absorptive (Real) and (b) Dispersive (Imaginary) 2D-ES maps of perylene bisimide monomer at $T = 75$ fs. Each map has been normalised to its positive maximum.

4.7 Summary

To summarise, in this Chapter we have explained how the 2D-ES spectrometer works, emphasising its advantages. The fully non-collinear BOXCARS beams arrangement helps to minimise the background signal and permits independent acquisition of the rephasing and non rephasing third order signals. The way in which the four beams are generated (conventional optics) and the relative delays introduced between beams a, b, c and LO ensures passive phase stabilisation and set the conditions for the rotating wave frame, which speeds up the acquisition time. Moreover, the double chopper solution allows a better removal of scattered light in the detector direction and also a quasi-simultaneous measurement of local oscillator, pump-probe spectra and the spectral interferogram, from which the 2D-ES spectra are reconstructed. In Chapter 5 we will show the results of measurements performed using this setup on two covalently-bound perylene bisimide J dimers with increasing interchromophoric separation and in Chapter 6 on a subphtalocyanine - zinc porphyrin flexible heterodimer.

Chapter 5

One- to Two-Exciton Transitions in Perylene Bisimide Dimers

5.1 Introduction

Perylene bisimide (PBI) based molecular structures have attracted a lot of interest because of their exceptional fundamental photophysical properties, such as extremely high emission yield,[115;116] efficient energy[117–119] and electron transfer[120;121] and singlet fission.[122;123] In addition they are good candidate molecules for applications as active materials in optoelectronic devices; studies are presented in the literature in which PBIs have been used in solar light harvesting,[124;125] optical sensors[126;127] and optical power limiters.[128]

In the aforementioned systems, many chromophores are in close proximity to one another, making it impossible to understand and rationalise their behaviour without accounting for collective effects such as excitonic coupling.[129–131] For this reason, the properties of PBI aggregates prepared by chemical synthesis[132;133] or via self-assembly[134;135] strategies have begun to be investigated. These newly synthesised PBI-based structures display exciting new optical properties which stem from the formation of new collective excited states of different energy and symmetry, which produce narrowed (or broadened) blue- or red- shifted absorption peaks. Intermolecular coupling can also lead to the emergence of new properties such as superradiance.[136] Determining the role and mechanisms of electronic couplings, their interplay with molecular vibrations, and how coupling affects exciton dynamics is critical to develop more efficient, next generation optoelectronic and photovoltaic devices.

The first description of optical properties of chromophore dimers was given by Kasha more than five decades ago.[80] Electronic coupling between (at least) two chromophoric units generates delocalised Frenkel exciton states, which can be observed as energy shifts of the absorption peaks and changes in the radiative emission rate compared to the uncoupled monomers.[136] The symmetry of the dimer will affect the direction of the energy shift. In so called H-dimers, in which transition dipole

moments are aligned in a side-by-side fashion, the higher in energy, out of phase, exciton state will carry oscillator strength, causing the absorption spectrum to be blue-shifted compared to the monomer. Conversely, in J-dimers, in which the transition dipole moments are aligned in a head-to-tail fashion, the allowed exciton state will be the lowest energy, in-phase one, which will give rise to red-shifted absorption peaks and an enhanced radiative rate.[137]

A dimer which behaves according to Kasha theory will also necessarily display features linked to the existence of two-exciton states, in which both the chromophores in the dimer are in their excited state, and will lie at (approximately) twice the energy of the one-exciton states. The one- to two-exciton excited state absorption (ESA) appears to be blue-shifted compared to the ground to one-exciton state transition because of the Pauli exclusion principle.[48;138;139] The mismatch between these two transitions correlates with the size of the exciton, and thus can be used to determine the coherence length.[48] Two- and, in general, multiexciton states and their dynamics have to be carefully characterised because they can be the gateway to detrimental processes, for instance Exciton-Exciton Annihilation (EEA), in light-harvesting structures, materials and optoelectronic devices.[137]

In this Chapter the exciton structure of two covalently bound dimers based on the PBI repeating unit will be studied and characterised using two-dimensional electronic spectroscopy (2D-ES), in order to obtain a full picture of their vibronic[140;141] and interchromophoric coupling.[70;142] 2D-ES has previously been used to study photophysics and photodynamics of excitons in PBI heterodimers.[143]

The main result shown in this Chapter is the unambiguous demonstration of the presence of a one- to two- exciton ESA in a strongly coupled dimer; this transition is not affected by vibrational motions which are quasi-resonant with the ESA transition. This result is compared to 2D-ES measurements of the PBI monomer and another dimer in which the interchromophoric separation has been increased by adding a para-phenylene spacer between the two PBI units, in order to decrease the strength of dipole-dipole coupling. The experimental data are accurately reproduced by theory, employing a model in which only electronic levels are included.

5.2 Steady-State Spectroscopy of Perylene Bisimide Monomer and Dimers

The ball-and-stick molecular structures of the PBI samples studied here are shown in Figure 5.1, and labeled as M for the monomer, D0 for the strongly coupled dimer and D1 for the dimer with a para phenylene spacer between the PBI units. In D0, in which the center to center distance R is 1.27 nm, there is a nitrogen-nitrogen single bond connecting the two PBI units at one of the imide positions, restricting the two PBIs to lie on two planes, perpendicular to each other. In the D1 dimer, the

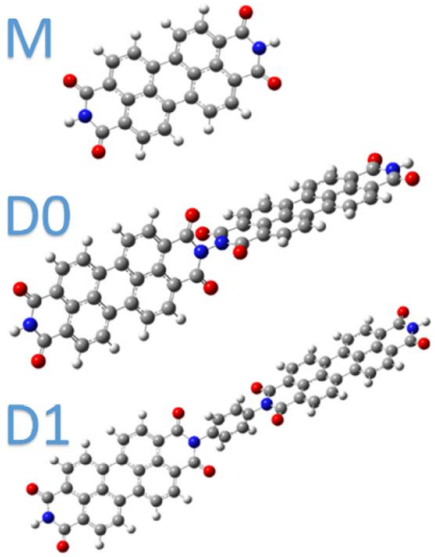

Figure 5.1: Molecular structures of PBI M, D0 and D1. End aliphatic chains (C_{19}, linked at C_{10} position) added at the N- position to improve solubility have been replaced with hydrogen to aid visualisation.

PBI units are linked with a para phenylene spacer connecting them at the amide N position, causing them to be 1.70 nm apart, and adding conformational flexibility to the molecule. The samples were synthesised as previously reported.[144–146]
The steady-state absorption data of M, D0 and D1 are reported in Figure 5.2. The monomer spectrum (blue solid line) shows a strong Franck-Condon progression starting at the pure electronic $S_0 \rightarrow S_1$ transition at 527 nm. The electronic transition is coupled to a number of vibrational modes, the most strongly coupled of them are $\nu_{12} = 231$ cm^{-1} assigned to in plane C-C stretching, $\nu_{30} = 550$ cm^{-1}, corresponding to C-C-C in plane bending of the perylene core, $\nu_{77} = 1308$ cm^{-1} given by C-C stretching and C-H bending and $\nu_{100} = 1660$ cm^{-1}, assigned to in plane C-C bending. This assignments follow the detailed work by Clark *et al.*[147]
The D0 dimer spectrum, shown in solid orange, has a number of different characteristics compared to its parent monomer M. Its main $S_0 \rightarrow S_1$ transition is red-shifted by 9 nm compared to M, with its maximum at 536 nm. Furthermore, the amplitude ratio between the pure electronic $S_0 \rightarrow S_1$ transition ($I_{0,0}$) and its closest energy vibronic replica ($I_{0,1}$) is increased with respect to M. Both features are indications of a J-coupling scheme for the excited states of D0.[148] The $S_0 \rightarrow S_1$ electronic transition in D1 dimer, reported in solid green, lies at roughly the same wavelength as its parent monomer (527 nm) and presents a similar vibronic progression, but all the peaks undergo some broadening toward the high-energy end of the spectrum; this effect might be caused by the additional flexibility given by the para phenylene spacer.

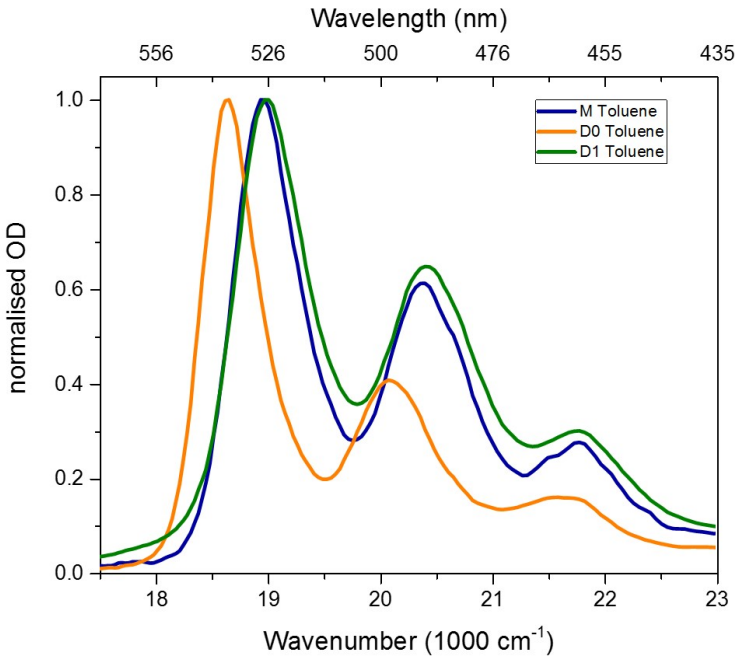

Figure 5.2: Normalised steady-state absorption spectra of PBI M, D0 and D1 in toluene. Peak OD of 0.3 and optical path length of 1 mm.

5.3 2D-ES Experiments on PBI Monomer and Dimers and Comparison with Theory

Experimental two-dimensional absorptive electronic spectra for M (left), D0 (centre) and D1 (right) at population time $T = 0.105$ ps are shown in Figure 5.3 and compared to calculated 2D-ES spectra, reported in Figure 5.4, obtained using the three-level pure electronic model described in our recently published paper[149]. In the 2D-ES spectra positive signals, shown in red and yellow, represent ground state bleaching (GSB) and stimulated emission (SE), the negative excited state absorption (ESA) signals, when present, are colored in light blue.

The monomer spectrum does not show any negative ESA feature. The overall signal only comprises of a mixed GSB/SE peak appearing in the region covered by the NOPA spectrum, with an elongation toward the red region on the detection axis explicable in terms of a SE contribution, given that it is spectrally matching the steady-state fluorescence spectrum of M. The positive peak appears to be stretched along the diagonal, this effect is caused by inhomogeneous broadening and is a signature of static disorder among the ground state population of M in solution.
The dimer D0 spectrum, shown at the centre of Figure 5.3, has a positive signal down-shifted in energy, with respect to M, as expected from the steady-state data, but its main new feature is the presence of an off-diagonal negative ESA peak, not present in M, centred at the coordinate $\tilde{\nu}_1 = 18612$ cm^{-1}, $\tilde{\nu}_3 = 19202$ cm^{-1}. Differently, the D1 spectrum (shown at the right-hand side of Figure 5.3) resembles more

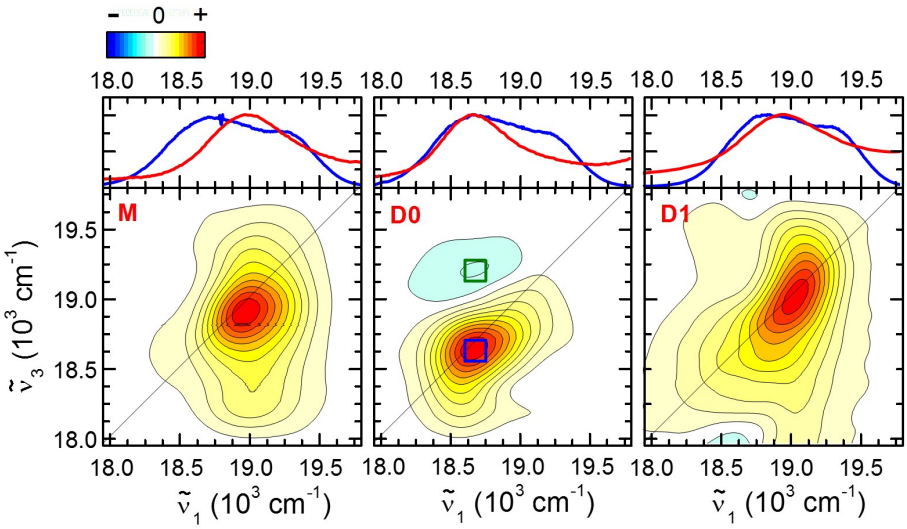

Figure 5.3: Measured $\Delta T/T$ 2D-ES absorptive spectra for M (left), D0 (centre) and D1 (right) at $T = 0.105$ ps. Each 2D spectrum has been normalised to its positive maximum and the contour plot has 21 evenly spaced lines. In the top panels the red and blue solid lines are the steady-state absorption spectrum of each molecule and the NOPA spectrum used for that measurement. Blue and green squares highlight the area that was integrated to give the time traces shown in Figure 5.6(b).

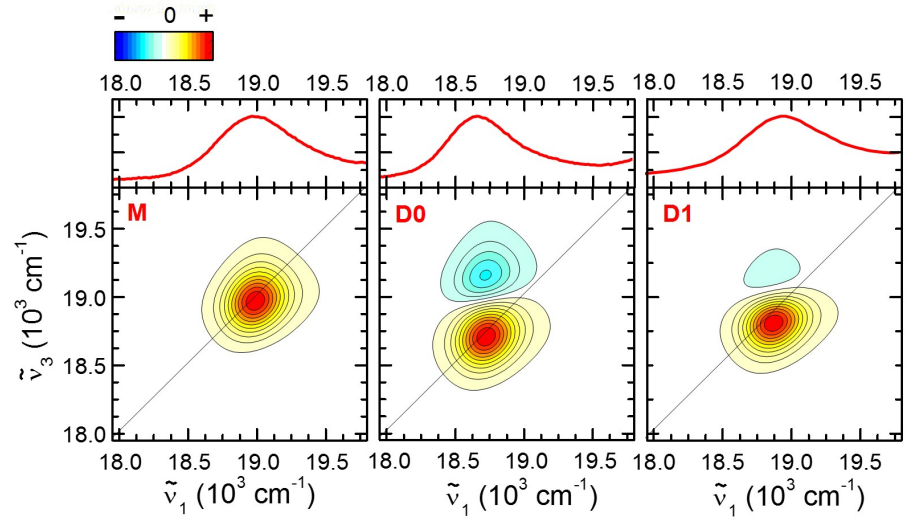

Figure 5.4: Calculated 2D-ES absorptive spectra for M (left), D0 (centre) and D1 (right) at $T = 0.105$ ps. Each 2D spectrum has been normalised to its positive maximum and the contour plot has 21 evenly spaced lines. In the top panels the red solid line is the steady-state absorption spectrum of each molecule.

M, as it only has positive, diagonal, GSB/SE features centred at the frequency coordinate $\tilde{\nu}_1 = 19875$ cm^{-1}, $\tilde{\nu}_3 = 19875$ cm^{-1}, this signal is broader than in M, as was also observed in the steady-state absorption spectrum.

The observed photophysics of the series of PBI structures can be described referring to the proposed energy level scheme shown in Figure 5.5a, which is obtained from Kasha theory for excitation in coupled chromophores. In D0 and D1, the two PBI units are disposed in a "head-to-tail" fashion, hence the coupling mechanism obeys

the rules for J-aggregates. In fact, the new fully allowed transition (Solid arrow in Figure 5.5a) connects ground $|g\rangle$ and bottom (in-phase) exciton $|e'\rangle$ states, while the transition to the upper (out of phase) $|e''\rangle$ state does not carry any oscillator strength, so it cannot contribute to the linear and nonlinear spectra of the dimer and it is therefore drawn as a dashed arrow in Figure 5.5a. The new allowed transition is the reason for the red-shifted signal (if compared to M) observed in D0 in steady-state and 2D-ES measurements. In D1, the para phenylene spacer causes the centre to centre distance between the PBI units to be bigger than in D0, dramatically reducing the coupling strength in this dimer, consistent with the absence of a red-shift for its positive peak.

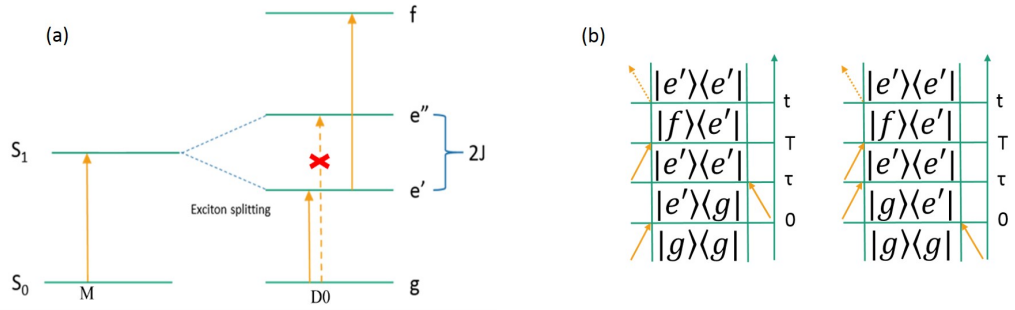

Figure 5.5: (a) Jablonski diagram showing energy levels and transitions for a PBI monomer (left) and excitonically coupled J-type dimer (right). Solid arrows represent allowed transitions and dashed arrows represent forbidden transitions. The energy difference between the bottom e' (allowed) and the top e" (forbidden) exciton states corresponds to 2J (twice the exciton coupling energy). (b) the two Feynman (non rephasing, left and rephasing, right) diagrams for the ESA to a 2-exciton state are reported. The model is purely electronic and it involves transitions which couple three states: $|g\rangle$ (ground), $|e'\rangle$ (in phase, low energy, allowed 1-exciton) and $|f\rangle$ (two-exciton). These pathways will generate a cross peak above the diagonal ($\tilde{\nu}_3 > \tilde{\nu}_1$) with negative amplitude, because of the odd number of interactions from the right.

The new ESA (negative) signal present in D0 can be explained in the framework of the proposed energy level scheme as well. The first two NOPA pulses can create an excited state population during T $|e'\rangle\langle e'|$ in the in-phase exciton state, and the third laser pulse can convert this population to a coherence between the higher energy two-exciton state $|f\rangle$ and $\langle e'|$. This superposition will generate a negative ESA, which is only observed in the 2D spectra of D0. The Feynman diagrams representing the field-matter interactions that lead to the one- to two-exciton state ESA [150] are rationalised in the Feynman diagrams shown in Figure 5.5b.

The excitonic coupling strength, J, in D0 can be retrieved by looking at the spectral separation between the centre of the positive GSB transition (corresponding to $g \rightarrow e'$) and the negative ESA (due to $e' \rightarrow f$) observed in the 2D spectrum. A vertical cut, taken at a fixed excitation frequency ($\tilde{\nu}_1 = 18682$ cm^{-1}) of the absorp-

tive 2D spectrum of D0 in toluene is shown in Figure 5.6a. The particular value of excitation frequency has been selected because it matches the maximum of the absorption for a given excitation frequency (which has been marked with blue and green squares in Figure 5.3) in order to maximise the contrast between positive and negative maxima. Even though the magnitude of the exciton coupling is not dependent on the specific frequency, the error in its evaluation is minimised when looking at the frequency gap between the GSB and ESA maxima.

Dashed lines in Figure 5.6 match and highlight the positive and negative maxima, and their frequency splitting, 520 cm^{-1}. Thus, the energy stabilisation given by the coupling of the two PBI units in D0 is half of this value, i.e. 260 cm^{-1}, in good agreement with the red-shift observed in the steady-state spectrum (Figure 5.2) and with literature data.[133] As mentioned before, the strong ESA peak is a unique characteristic of the 2D-ES spectrum of D0, and it is not present in D1 and M. This feature has been assigned to a one- to two- exciton transition, and its absence in D1 implies that the coupling is absent, or much weaker, in this molecule. This is in agreement with our hypothesis because the distance between PBI units increases by more than 30% going from D0 to D1. Assuming a dipole-dipole coupling scheme, the interaction energy scales with the third power of the inverse of the distance, $J \propto R^{-3}$. So, the interaction energy in D1, J_{D1}, should be about the 40% of D0, i.e. $J_{D1} = 0.4 J_{D0}$, which, in wavenumbers, should translate to a J_{D1} value around 100 cm^{-1}. Again, this value matches well the calculated spectrum of D1 (Figure 5.4, right), in which the weaker coupling produces a much smaller downshift (108 cm^{-1}, from spectra in Figure 5.3) with the large majority of the ESA peak being overlapping with the positive GSB/SE peak.

The spectra were calculated defining the transition energy of M as $\tilde{\nu}_{eg} = 18939$ cm^{-1} and its transition dipole moment was calculated from steady-state absorption as $|\vec{\mu}| = 11.218$ D. $R = 1.27$ nm and $J_{D0} = -260$ cm^{-1} were used for D0 while for D1 $R = 1.70$ nm and $J_{D1} = -108.4$ cm^{-1}, where $\varepsilon_r = 2.38$ for toluene.[151] The simulations were run at 298 K, with the strength of the system-bath coupling $\eta = 20$ cm^{-1} and the inverse of the correlation time of the bath $\gamma = 75$ cm^{-1}. The laser (NOPA) spectra were centred at $\nu_m = \tilde{\nu}_{eg}$ for M and at $\nu_m = \tilde{\nu}_{e'g}$ for D0 and D1, with FWHM of 5 fs and $\chi_m = 1 \times 10^7$ V/m.

The simulated spectra reproduce the positive GSB-SE feature and the inhomogeneous broadening (obtained with the η and γ parameters) observed in M (Figure 5.3, left). The elongation to lower $\tilde{\nu}_3$ frequencies observed in the experimental data is given by contributions of vibrational modes which were not included in the simulations, therefore it is absent in the calculated spectrum of M, shown on the left of Figure 5.4. The red-shift of the $g \rightarrow e'$ transition, present in the experimental spectra of D0 and D1 (Figure 5.3 centre and right, respectively) is also well reproduced by the simulations (centre and right of Figure 5.4). Nevertheless, because of

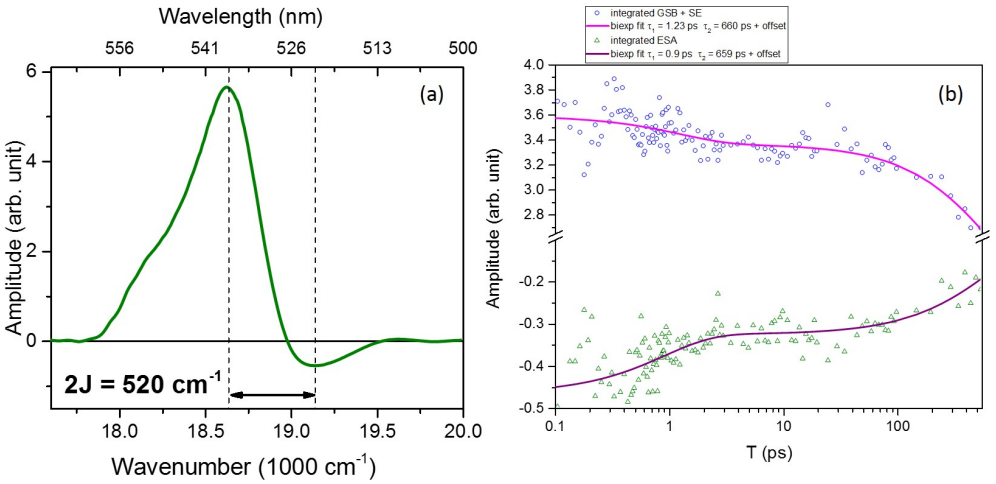

Figure 5.6: (a) Vertical slice at a fixed excitation frequency ($\tilde{\nu}_1 = 18682$ cm^{-1}) from the absorptive 2D electronic spectrum of D0 in toluene shown in Figure 5.3 (centre). The frequency axis reported here corresponds to the detection frequency $\tilde{\nu}_3$ of Figure 5.3. Dashed lines are added to highlight the frequency difference (proportional to the excitonic splitting) between the minimum of the ESA signal and the maximum of the GSB/SE signals. (b) Evolution over T of the amplitude, integrated over 150 cm^{-1} square area centred at the GSB/SE positive maximum (blue circles) and ESA negative minimum (green triangles). Magenta and purple solid lines are the biexponential fits of the integrated amplitudes vs T, which have similar time constants, suggesting the hypothesis of the two transition sharing a common state ($|e'\rangle\langle e'|$).

a higher degree of flexibility due to the present of a para phenylene spacer, D1 will present an higher amount of static disorder compared to D0 (and to M), as seen in the steady-state absorption data in Figure 5.2. Consequently, the ESA feature in the 2D spectrum of D1, reported in Figure 5.3 (right), is not detectable. Such disorder also tends to interfere with coherence, disrupting the excitonic coupling between the two PBI units in D1. However, the amounts of static disorder in the calculated spectra of M, D0 and D1 were kept constants in order to better demonstrate the diminished dipole-dipole coupling resulting from the increased interchromophoric separation, as predicted by Kasha model.

The dynamics of the negative and positive peaks in D0 are mirroring each other, as shown in Figure 5.6b. Here, the evolution over the population time T of the integrated ESA (green triangles) and GSB/SE signals (blue circles) are shown. This plot has been obtained by integration of a 150 × 150 cm^{-1} square of the D0 2D electronic spectrum around the positive (blue square) and the negative (green square) maxima, as highlighted in Figure 5.3 (centre). These curves have been fit with a biexponential function and the recovered time constant are very similar. The fast dynamics have been assigned to vibrational cooling (VC), while the slow decaying component is assigned to population relaxation. Similar sub-ps cooling dynamics are taking place in the excited states of M and D1, and they can be observed as a spectral reshaping, occurring within the same time window (see top row of spectral

progressions for M, D0 and D1, for T ranging from 0.1 to 300 ps in the Appendix of this Chapter).

5.4 Oscillations Analysis

In the Theory chapter we have highlighted how it is possible to use two-dimensional electronic spectroscopy to discriminate between electronic and vibrational (vibronic) coherences. To assess the origin of amplitude oscillations during T observed in PBI samples, we first took the power spectrum of M and D0*, integrating each 2D spectrum over $\tilde{\nu}_1$ and $\tilde{\nu}_3$ to obtain a single trace as a function of T, over which a FFT is taken. In the monomer power spectrum (Figure 5.7, red solid line), the main oscillating contributions are Raman active vibrational modes coupled to the electronic transition, producing a broad band at frequencies < 250 cm^{-1} and a narrow band at 532 cm^{-1}, assigned to a C-C-C in-plane bending of the perylene core.[147] The power spectrum of D0 can be described in terms of vibronic oscillations as well. For this dimer, a new low frequency signal (100 cm^{-1}), corresponding to the N-N stretching (not present either in M or D1) is anticipated from DFT calculations.† A narrow, medium intensity signal is in fact detected at this frequency in the experimental power spectrum of D0 only (Figure 5.7, blue solid line). Similarly to M, the strongest oscillation is given by the C-C-C in-plane bending, slightly blue-shifted for D0 (550 cm^{-1}). From the power spectra of D0 we can assume that there is no hint of energy transfer from the upper (e") to the lower (e') exciton states, proving again that the higher energy transition to the out-of-phase exciton state is completely dipole forbidden. If there was any coherence between the two excitonic states, we would observe a fast dephasing oscillation in the population time domain, yielding a broad peak centred at 520 cm^{-1} in the frequency domain.

In order to characterise the amplitude and the position of the signals on the $\tilde{\nu}_1, \tilde{\nu}_3$ plane resulting from the modes contributing to the power spectra of M and D0, we focused on the rephasing signals because they contain half of the Liouville-space pathways contributions compared to the absorptive signals. We took a Fourier transform over all population time traces in the 3D matrix obtained by stacking together all the measured population times T, in order to obtain a data matrix which will be a function of $(\tilde{\nu}_1, \tilde{\nu}_2, \tilde{\nu}_3)$, in which $\tilde{\nu}_2$ will be the Fourier pair of T. If this operation is performed on the dataset as it is, the part of the signal which is not oscillating during T will produce a large baseline around $\tilde{\nu}_2 = 0$. To remove this artefact from the FT data, a global multi-exponential fit of the whole rephasing 2D dataset is

*D1 was excluded from this analysis because the distance between PBI units is increased, and so the exciton coupling strength is strongly decreased.

†DFT calculations are not reported in this thesis, although they can be found in the Supplementary Information of Bressan *et al.*[152]

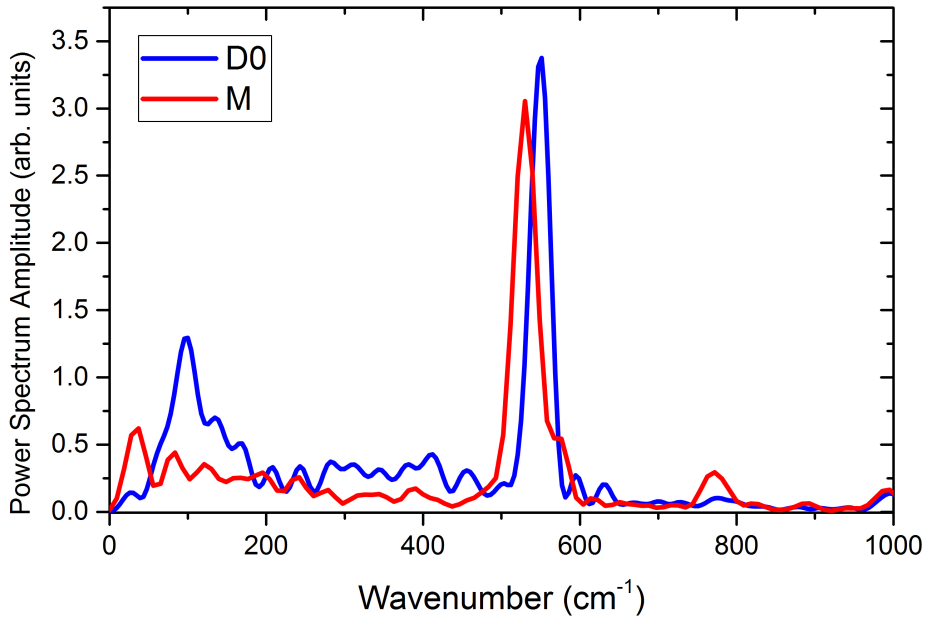

Figure 5.7: Power spectra of the residuals of the two-dimensional global fit performed on M (red) and D0 (blue) 2D datasets. M has a main contribution centred at 532 cm^{-1}, given by a C-C-C in-plane bending mode of the perylene core, the same mode, blue-shifted to 550 cm^{-1}, is the strongest feature in the power spectrum of D0. In addition to that, a new low frequency vibrational mode (100 cm^{-1}), assigned to N-N stretching is present in D0 spectrum.

done beforehand, i.e. the FFT is only applied to the residuals of the fit. The resulting Fourier transformed 3D matrix will contain amplitude and phase information for every excitation, population and detection wavenumbers triad $(\tilde{\nu}_1, \tilde{\nu}_2, \tilde{\nu}_3)$. These 3D matrices have been inspected using home-built LabVIEW software which makes it possible to scan over the different population wavenumbers $(\tilde{\nu}_2)$ and observe in real time the contribution of this frequency to the overall oscillatory amplitude on the usual excitation-detection $(\tilde{\nu}_1, \tilde{\nu}_3)$ plane. From the power spectra shown in Figure 5.7, the emerging frequencies correspond to the C-C-C in-plane bending mode of the perylene core (present at 532 cm^{-1} in M and at 550 cm^{-1} in D0) and to the N-N stretching in D0 only, occurring at 100 cm^{-1}.

The Fourier pair of T was then fixed to these frequencies and the amplitude distribution of the Fourier transformed 3D frequency matrix as a function of the excitation-detection frequency pair $(\tilde{\nu}_1, \tilde{\nu}_3)$ was plotted to obtain the maps shown in Figure 5.8. In Figure 5.8(a) are the data for M at $\tilde{\nu}_2 = 532$ cm^{-1}, (b) and (c) are the data for D0 at $\tilde{\nu}_2 = 550$ cm^{-1} and $\tilde{\nu}_2 = 100$ cm^{-1}, respectively. By comparison of these maps with the Figures shown in Section 2.7 we can conclude that the origin of the oscillations during the population time is due to coherent superposition of vibrational states in the ground and in the excited state electronic potential energy surfaces. The quasi-resonance between the excitonic and the vibronic (due to coupling of the electronic transition in the PBI to the C-C-C in-plane bending) splittings could lead

to the existence of some Liovulle-space pathways which are involved in coherence transfer between the electronic and vibronic off-diagonal elements of the density matrices. However, the lifetime of the oscillations (i.e. the narrow bandwidth of the signal at 550 cm^{-1}) in D0 together with the FT amplitude pattern matching well with what is expected from the vibronic model described in Section 2.7, allow us to confirm that this oscillation is completely vibronic in its nature.

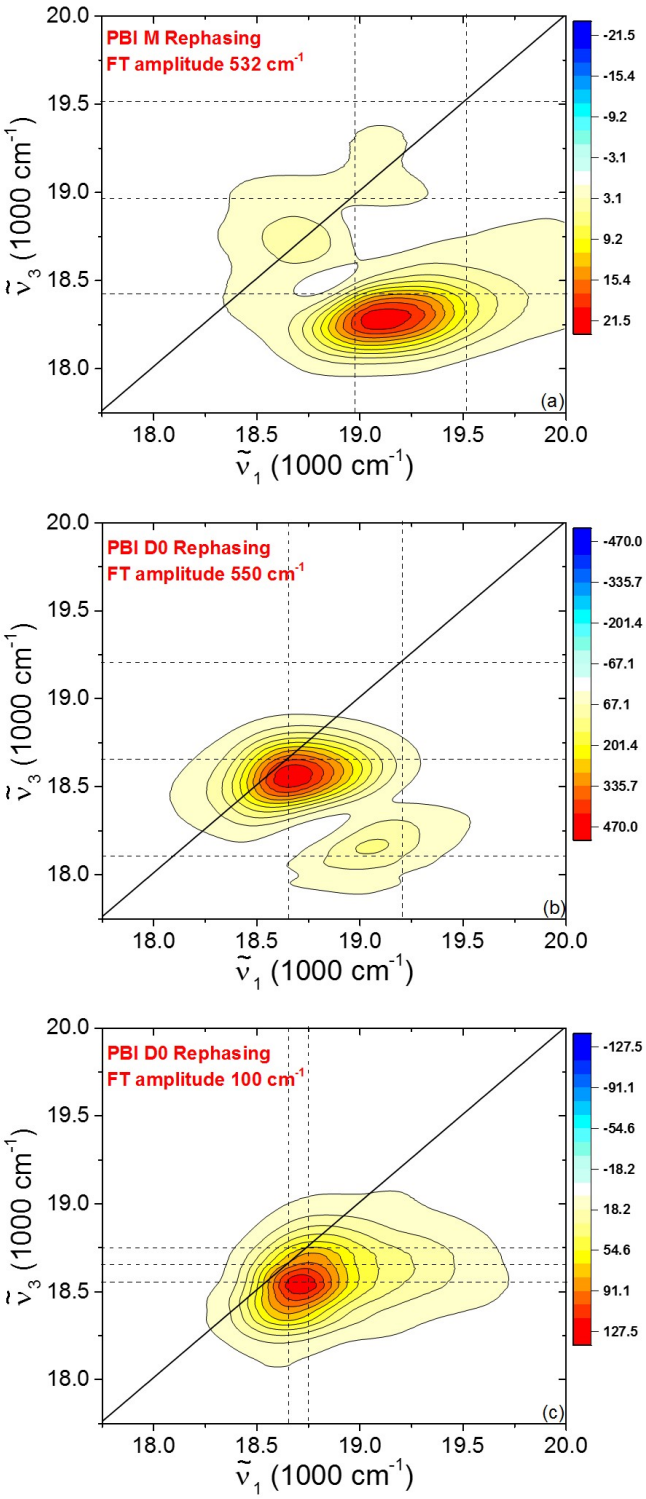

Figure 5.8: rephasing FT amplitude maps, defined on the on the usual excitation-detection $(\tilde{\nu}_1, \tilde{\nu}_3)$ plane (in wavenumbers). Each 2D graph has been normalised to its positive maximum and the amplitude has 21 evenly-spaced contour lines. 2D plots have been extracted out of the 3D matrix $(\tilde{\nu}_1, \tilde{\nu}_2, \tilde{\nu}_3)$ at frequencies corresponding to the in-plane C-C-C bending mode of M (a, $\tilde{\nu}_2 = 532$ cm^{-1}), D0 (b, $\tilde{\nu}_2 = 550$ cm^{-1}) and at the imide N-N stretching for D0 only (c, $\tilde{\nu}_2 = 100$ cm^{-1}). The position of the peaks suggest that the origin of these oscillations during T is the presence of vibrational (ground state) and vibronic (excited state) coherences.

5.5 Summary

To summarise, transitions between exciton states in two covalently bound PBI dimers were studied with two-dimensional electronic spectroscopy. The presence of a one- to two- exciton state was unambiguously demonstrated in D0, the dimer with the smallest interchromophoric separation (strongest coupling). D0 has a transition which is red shifted compared to the monomer M, and the one- to two- exciton state transition appears as an off-diagonal peak excited state absorption (negative signal, at $\tilde{\nu}_1 = 18612$ cm^{-1} and $\tilde{\nu}_3 = 19202$ cm^{-1}) not detected in either M and D1. This new feature, unique to D0, has been explained in the framework of a molecular exciton energy level scheme which follows the Kasha model for coupled chromophores, and it has been supported by calculated spectra obtained with the equation of motion-phase matching approach.[153]

5.A 2D-ES Spectral Progressions of M, D0 and D1

The positive signal in M undergoes spectral reshaping within the first 10 ps, as it can be seen in Figure 5.9 (top row). This effect is assigned to spectral diffusion.[154] Moreover, Figure 5.9 reveals dynamic Stokes shift within the first few ps, due to the vibrationally-aided processes happening in the electronic excited state potential energy surface (PES), whose detailed characterisation is not related to this work. Similar fast dynamics are present (and have not been characterised) in the spectral progressions of D0 and D1, shown in the Appendix in Figures 5.10 and 5.11, respectively.

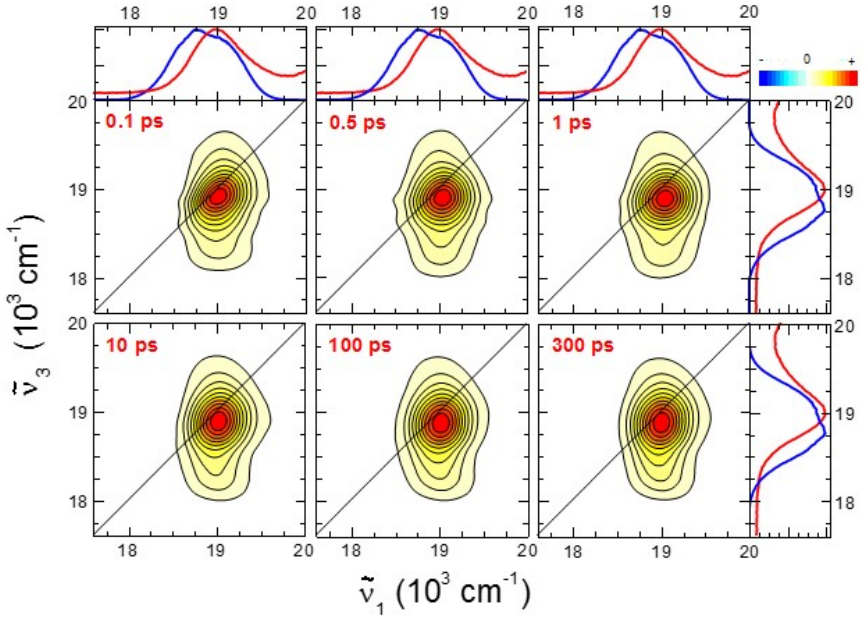

Figure 5.9: Absorptive 2D-ES spectral progression for PBI M in toluene where $\tilde{\nu}_1$ is the excitation and $\tilde{\nu}_3$ is the detection scale (in wavenumbers). Each 2D graph has been normalised to its positive maximum and the amplitude has 21 evenly-spaced contour lines. Red numbers on the top left of each map indicate the population time T and in the top and right panel the steady-state absorption of M (red) and NOPA spectra (blue) are shown.

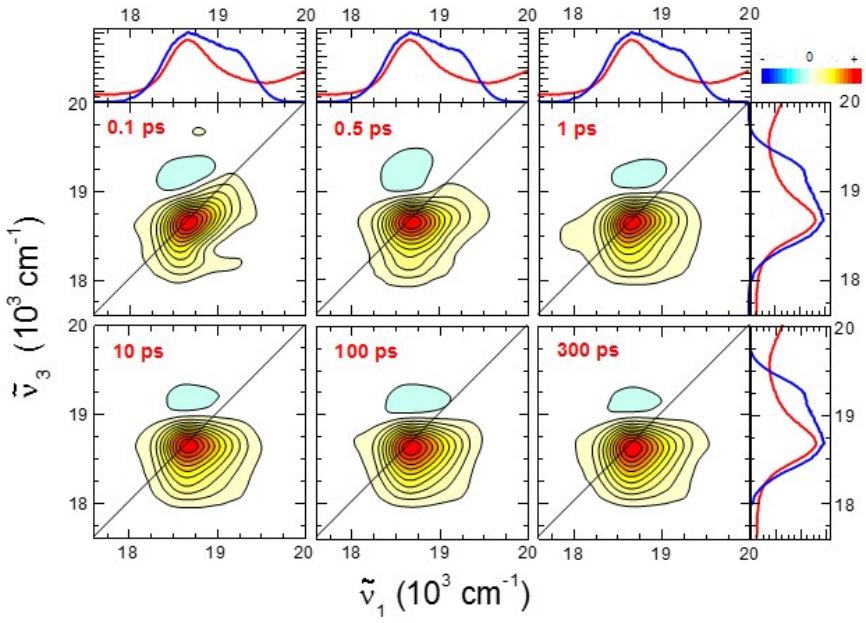

Figure 5.10: Absorptive 2D-ES spectral progression for PBI D0 in toluene where $\tilde{\nu}_1$ is the excitation and $\tilde{\nu}_3$ is the detection scale (in wavenumbers). Each 2D graph has been normalised to its positive maximum and the amplitude has 21 evenly-spaced contour lines. Red numbers on the top left of each map indicate the population time T and in the top and right panel the steady-state absorption of D0 (red) and NOPA spectra (blue) are shown.

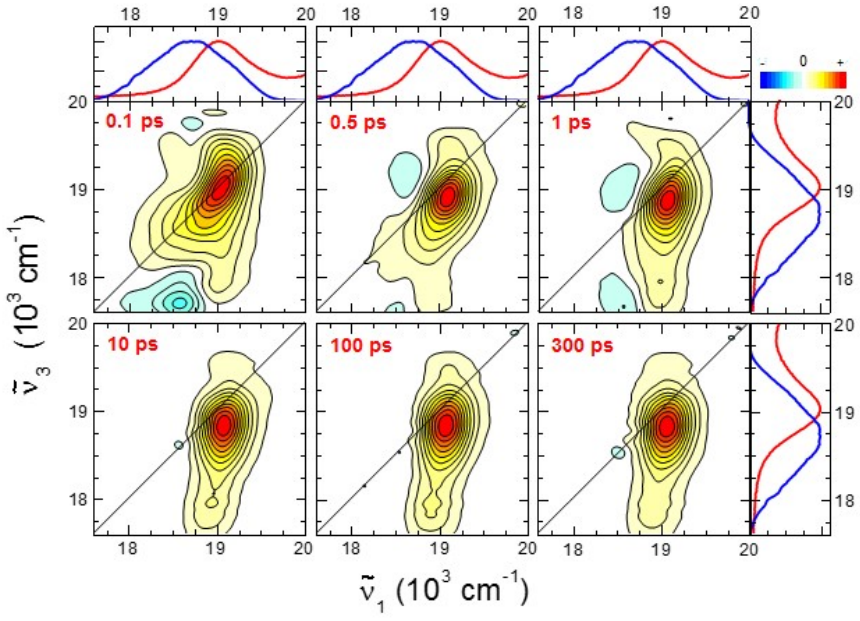

Figure 5.11: Absorptive 2D-ES spectral progression for PBI D1 in toluene where $\tilde{\nu}_1$ is the excitation and $\tilde{\nu}_3$ is the detection scale (in wavenumbers). Each 2D graph has been normalised to its positive maximum and the amplitude has 21 evenly-spaced contour lines. Red numbers on the top left of each map indicate the population time T and in the top and right panel the steady-state absorption of M (red) and NOPA spectra (blue) are shown.

Chapter 6

Excitation Energy Transfer in a Subphthalocyanine-Zn Porphyrin Dimer

6.1 Introduction

The understanding of electronic excitation energy transfer (EET) processes in covalently linked molecular model systems can help to understand the behaviour of more complex man-made light-harvesting structures and materials.[155–157] Through real-time studies of the ultrafast photodynamics taking place in model systems it is possible to pinpoint which processes can enhance or disrupt the efficiency of energy transport, making it possible to design new, more efficient, synthetic light harvesting molecules and supramolecular architectures for applications in, for example, organic photovoltaic (OPV) devices.[41;158–160] Among the different families of organic molecules which have been used as the active material in organic photovoltaics, porphyrins have always been under the spotlight because of their occurrence in biological systems.[161;162] Moreover, porphyrins have been employed as building blocks in the design of supramolecular structures of different dimensionality[163–165] (nanorings, nanowires, nanoballs) in which they have displayed outstanding physical properties, such as high conductivity.[166] Porphyrins have also been used as sensitisers in dye-sensitised solar cells[167;168] and as photocatalysts.[169;170]

The unique photophysics of porphyrins stem from their extended 18 π-electron planar aromatic ring.[171] Nonetheless, one of the major drawbacks in the utilisation of porphyrins for solar energy conversion is that their Q-band absorptions lie toward the red region of the visible spectrum, with a transition moment which is much smaller than their strongest Soret (or B-) band absorption, which is usually located between 400 and 450 nm.[172;173] Thus, the electronic structure allows only relatively poor utilisation of the solar spectrum.[174] To overcome this obstacle, it is possible to link an antenna chromophore, absorbing light more efficiently in the visible spectrum, to

a porphyrin. The subphthalocyanines studied here have been used as antennas for a number of different chromophore acceptors.[175;176] In this Chapter we studied the time-resolved photophysics of an heterodimer in which a light-harvesting boron-subphthalocyanine (SubPc), was linked through a phenoxy bridge at the meso position of Zn(II) 5-(4-hydroxyphenyl)-10,15,20-triphenylporphyrin (ZnTPP), as shown in Figure 6.1. Other structures in which SubPc is axially linked have been synthesised and studied,[177;178] but most of them are linked through alkene or alkyne spacers, which have planar or cylindrical symmetry and are intrinsically rigid. In contrast, the dimer studied in this Chapter bears a flexible phenoxy axial group at the boron position which links it to the ZnTPP acceptor, the flexible nature of the linker can substantially affect the rate and efficiency of the energy transfer mechanism.

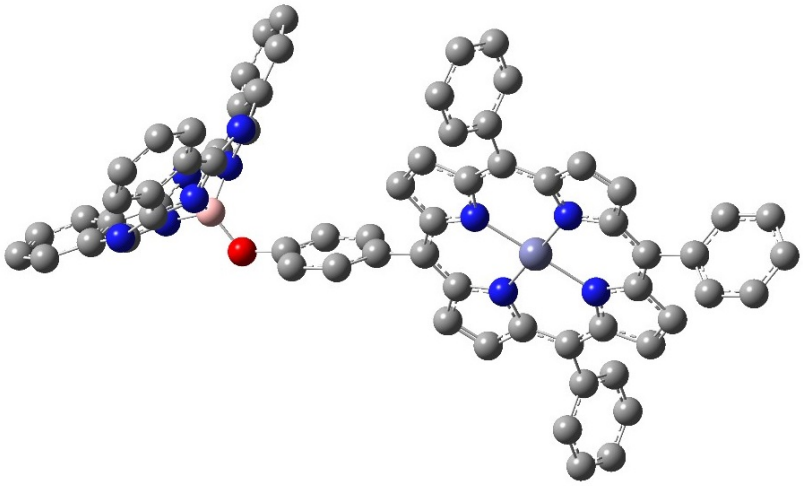

Figure 6.1: DFT optimised structure of ZnTPP-O-SubPc calculated with B3LYP functional and a 6-31G(d) basis set.

SubPc structures possess a unique nonplanar cone-shaped 14 π-electron aromatic macrocycle, with intense absorption and emission peaks in the middle of the visible region (λ_{max} = 560 nm)[179;180] of the electromagnetic spectrum. SubPcs spectral properties, together with the simplicity of functionalising them, at both the ring position and on the boron core[181;182], has made them molecules of choice for optoelectronic (e.g., organic light-emitting diodes)[183;184] and OPV applications[157;185]. In this Chapter the steady-state and time-resolved photophysics of the ZnTPP-O-SubPc heterodimer and its parent monomers are studied with visible absorption, fluorescence, femtosecond transient absorption (fsTA) and two-dimensional electronic spectroscopy (2D-ES) experiments in toluene solution.

6.2 Steady-State Spectroscopy of Subphthalocyanine-Zn Porphyrin Dimer and SubPc and ZnTPP Monomers

Steady-state normalised absorption and emission spectra of the two parent monomers SubPc-Cl and ZnTPP-OH are shown in Figure 6.2a, while the absorption and emission spectra of ZnTPP-O-SubPc are reported in Figure 6.2b. All samples have been synthesised as previously reported.[186] All emission (fluorescence) spectra were measured exciting the samples at 530 nm.

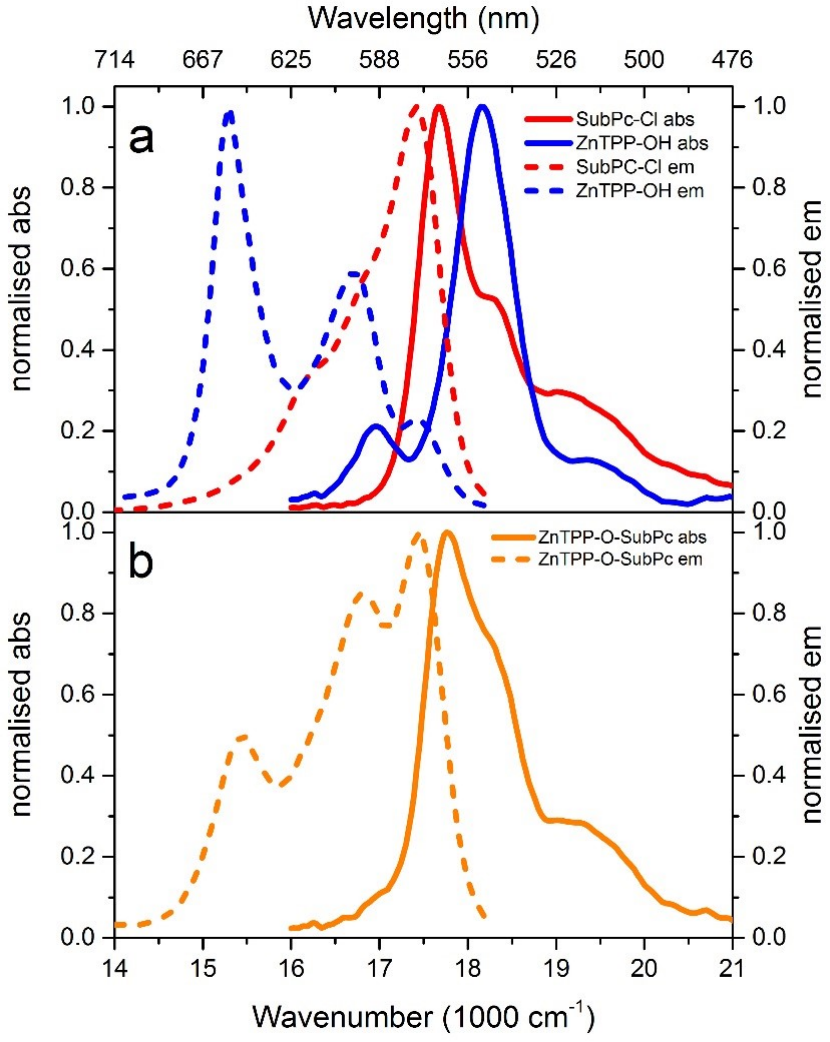

Figure 6.2: Normalised steady-state absorption (solid lines) and emission (dashed lines) of SubPc-Cl (a, red), ZnTPP-OH (a, blue) and ZnTPP-O-SubPc (b, orange). All emission (fluorescence) spectra were recorded after excitation at 530 nm

This dimeric system has been investigated before with steady-state spectroscopy and calculations.[186] The absorption and emission spectra of ZnTPP-O-SubPc were

shown to approximate well the weighted sum of the two parent monomers (SubPc-Cl and ZnTPP-OH) spectra, indicating weak coupling between the donor and acceptor chromophores, with negligible perturbation of their individual electronic structure.[186] The steady-state absorption spectrum of SubPc-Cl (Figure 6.2a, red solid line) has its maximum centred at 566 nm (17688 cm^{-1}) as a result of the 0-0 transition in the Q-band, as previously reported;[179] the vibronic progression matches well the literature data. The emission spectrum (excitation at 530 nm, red dashed line) of SubPc monomer is a quasi mirror image of the absorption, its maximum is at 574 nm, corresponding to 17421 cm^{-1}, and the literature fluorescence quantum yield was reported to be 0.25.[185] The measured Stokes shift is 8 nm (247 cm^{-1}), indicating a very small stabilisation effect of the excited state by the solvent, as expected for nonpolar media, or when there is a small change in permanent dipole between ground and excited states.

The steady-state absorption of ZnTPP-OH (Figure 6.2a, blue solid line) has two main peaks: the vibronic Q(1,0) band, centred at 551 nm (18148 cm^{-1}) and a weaker $S_0 \rightarrow S_1$ Q(0,0) transition, red-shifted to 590 nm (16949 cm^{-1}). The steady-state emission spectrum (excitation at 530 nm, blue dashed line) is mirroring the absorption in terms of peak positions: Q(0,0) lies at 600 nm (16680 cm^{-1}) and Q(1,0) is centred at 653 nm (15302 cm^{-1}). An extra feature of the fluorescence spectrum of ZnTPP-OH is the Q(0,1) "hot band" shoulder appearing at 574 nm (17391 cm^{-1}); these measurements are consistent with previously reported data on the same molecule[173]. The Stokes shift between the Q(0,0) absorption and emission bands is 10 nm (270 cm^{-1}). ZnTPP-OH fluorescence is strongly quenched because of the spin-orbit coupling owed to the presence of a heavy Zn atom, fluorescence quantum yield of ZnTPP-OH in toluene has been reported to be 0.03.[187]

No major new features are observed in the steady-state absorption spectrum of ZnTPP-O-SubPc (Figure 6.2b, solid orange line), this observation is in agreement with a weak coupling between the SubPc and ZnTPP units. The dimer absorption maximum is blue-shifted by ca. 350 cm^{-1} with respect to the subphthalocyanine monomer (this effect is assigned to the different substituent at the boron core, -Cl for the monomer, -OPh for the dimer), and shows an overall broadening, due to overlap of the Q-bands of SubPc and ZnTPP. The dimer steady-state emission (excitation at 530 nm, orange dashed line) spectrum is, again, a combination of the emission spectra of its parent monomers, even though the intensity of the signal due to the ZnTPP acceptor is enhanced compared to what is predicted from absorption spectra and quantum yield, while the overall signal is quenched. Such a change in relative emission of the SubPc donor and ZnTPP acceptor intensities can be a sign of electronic energy transfer. To confirm this hypothesis, the expected emission spectrum of the dimer, assuming no energy transfer between the S_1 states of SubPc-Cl and ZnTPP-OH was calculated and compared to the measured dimer spectrum. The

expected dimer spectrum was calculated as follows.
The emission spectrum of the dimer, the absorption spectra of the two monomers and the ZnTPP-O-SubPc dimer shown in Figure 6.2 were used. Then, coefficients X and Y of the linear combination of the monomer spectra were chosen in order to obtain the best match with the dimer spectrum according to Equation 6.1:

$$\mathrm{Abs}^{\mathrm{Calc}}_{\mathrm{ZnTPP-O-SubPc}}(\lambda) = X \times \mathrm{Abs}^{\mathrm{Exp}}_{\mathrm{SubPc-Cl}}(\lambda) + Y \times \mathrm{Abs}^{\mathrm{Exp}}_{\mathrm{ZnTPP-OH}}(\lambda) \tag{6.1}$$

In which the coefficients $X = 0.855$ and $Y = 0.275$ have been determined by comparison with the dimer, and they can be used to rescale each monomeric absorption spectrum (Equations 6.2)

$$\mathrm{Abs}^{\mathrm{Corr}}_{\mathrm{SubPc-Cl}}(\lambda) = X \times \mathrm{Abs}^{\mathrm{Exp}}_{\mathrm{SubPc-Cl}}(\lambda) \tag{6.2a}$$

$$\mathrm{Abs}^{\mathrm{Corr}}_{\mathrm{ZnTPP-OH}}(\lambda) = Y \times \mathrm{Abs}^{\mathrm{Exp}}_{\mathrm{ZnTPP-OH}}(\lambda) \tag{6.2b}$$

of which the separate contributions are shown in Figure 6.3.

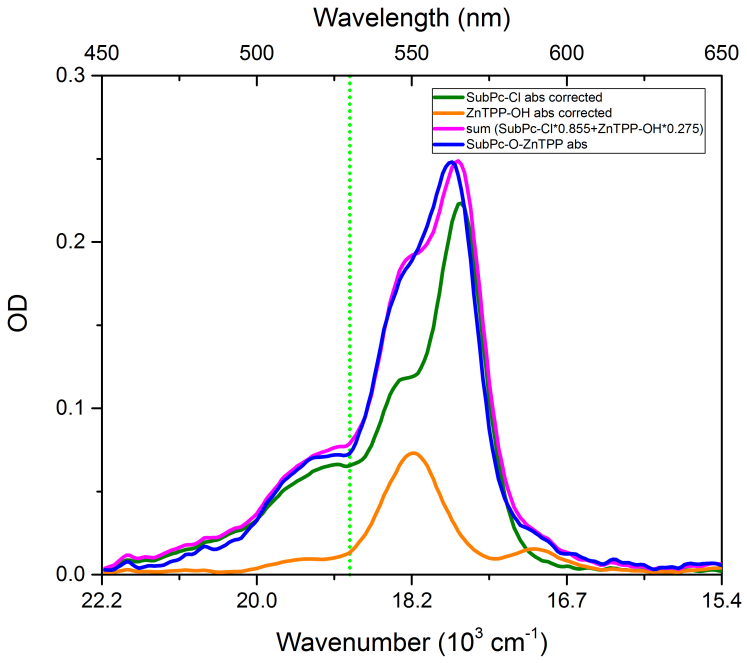

Figure 6.3: Calculated components of steady-state absorption spectra for ZnTPP-OH (orange) and SubPc-Cl (green) required in order to obtain the best match between their sum (magenta) and the measured ZnTPP-O-SubPc spectrum (blue). We speculate that the small shift between the maxima of the experimental and calculated spectra is due to a different substituent at the boron core (-Cl for the monomer, -OPh- for the dimer). Light green vertical dotted line marks the excitation wavelength (530 nm) for the fluorescence measurements.

The measured SubPc-Cl and ZnTPP-OH emission spectra are now rescaled by the corrected OD measured at the excitation wavelength (530 nm) and then summed

together, following Equation 6.3 to create an emission spectrum in absence of EET.

$$\mathrm{Em}^{\mathrm{Calc}}_{\mathrm{ZnTPP-O-SubPc}}(\lambda) = \mathrm{Abs}^{\mathrm{Corr}}_{\mathrm{SubPc-Cl}}(530\ \mathrm{nm}) \times \mathrm{Em}^{\mathrm{Exp}}_{\mathrm{SubPc-Cl}}(\lambda) + \mathrm{Abs}^{\mathrm{Corr}}_{\mathrm{ZnTPP-OH}}(530\ \mathrm{nm}) \times \mathrm{Em}^{\mathrm{Exp}}_{\mathrm{ZnTPP-OH}}(\lambda) \quad (6.3)$$

Comparing the normalised calculated and experimentally measured dimer emission spectra, as shown in Figure 6.4, it is clear how the amplitude in the region of the ZnTPP emission is enhanced in the dimer spectrum. This effect gives a first hint of EET from the excited singlet of the SubPc antenna, to the excited singlet state of the ZnTPP.

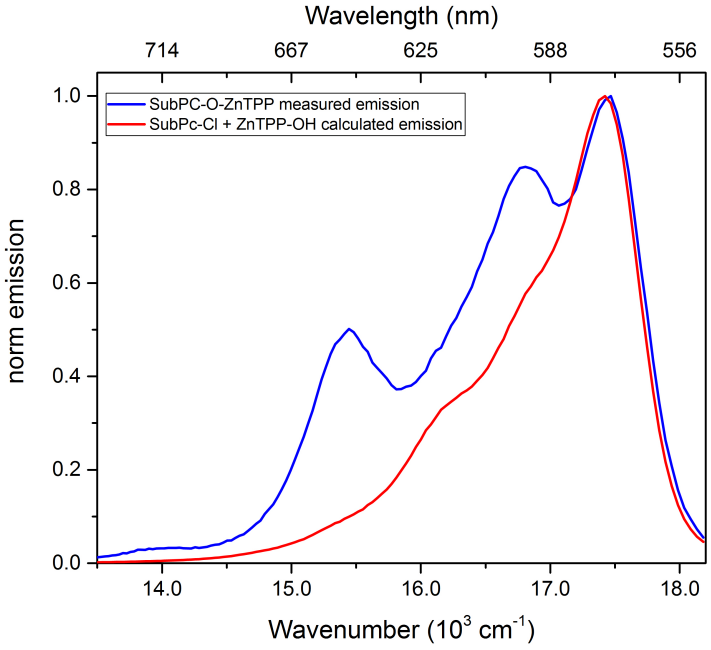

Figure 6.4: Comparison between the ZnTPP-O-SubPc calculated emission spectrum (solid red line) and the experimentally measured one (solid blue line).

6.3 fsTA Experiments and Global Fitting

The results from steady-state measurements indicate weak coupling between the excited states of the SubPc and ZnTPP moiety in the dimer, supporting a Förster Resonant Energy Transfer (FRET) model. In order to give a more complete characterisation of rate and mechanism of the energy transfer, broadband fsTA measurements were carried on the dimer and on its two parent monomers in toluene at room temperature, with pump wavelength fixed at 560 nm.

Transient spectra from SubPc-Cl at selected pump-probe delay times are reported in Figure 6.5a. The earliest transient spectrum ($T = 0.2$ ps, earlier spectra are still influenced by the coherent artefact) of SubPc-Cl has a strong negative band, origi-

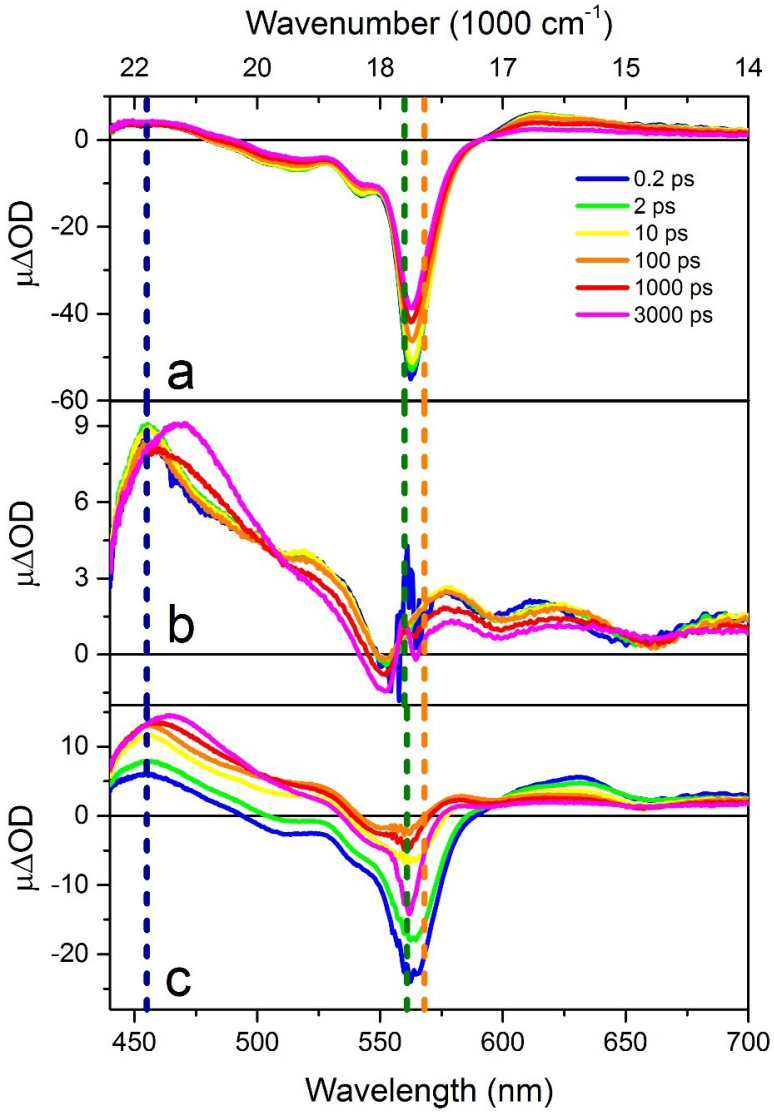

Figure 6.5: fsTA spectra of SubPc-Cl (a), ZnTPP-OH (b) and ZnTPP-O-SubPc (c) in toluene at selected pump-probe time delays, after photoexcitation at 560 nm (green dashed line). Notice that the pump scattering contributions appear to be more intense in (b) because of the small amplitude of the ZnTPP-OH signals, compared to (a) and (c). Dark blue and orange dashed lines at 455 nm and 568 nm highlight the wavelength at which the intensity-time traces shown in Figure 6.6 were recorded.

nating from a combined effect of ground state bleach (GSB), matching the steady-state absorption maximum (566 nm), and stimulated emission (SE), corresponding to the spectral position of the steady-state fluorescence maximum (574 nm). Two broad positive signals centred at 460 nm and 610 nm are also detected, and assigned to $S_1 \rightarrow S_n$ excited state absorption (ESA). The consequent spectral evolution is straightforwardly explained in the framework of simple population decay of the S_1 state, followed by formation of an excited triplet state T_1 via intersystem crossing

(ISC) on the nanosecond timescale, as proved by the decay of the broad $S_1 \rightarrow S_n$ ESA peaked at 610 nm and elongated toward the red end of the spectrum. The GSB does not fully recover at the longest experimentally probed pump-probe delay time (3 ns, τ_{fluo} lifetime reported to be 2.1 ns[188]), in the same way the triplet excited state absorption persists. The triplet lifetime for a related SubPc structure was reported to be in the microsecond range.[189]

Figure 6.5b presents the transient spectra of ZnTPP-OH after excitation at 560 nm. At least four $S_0 \rightarrow S_1$ ESA features are present at the earliest reported time delay ($T = 0.2$ ps). Some of the ESA signals are in part overlapping with a weak GSB, matching the position of the ZnTPP-OH steady-state absorption (551 nm). In general, the fsTA signal of ZnTPP-OH is lower than the one of SubPc-Cl because the molecule is weakly absorbing at the pump wavelength, which has been kept fixed across all measurements in order to make them directly comparable. Curiously, the strongest ESA signal experiences a rise within the first 2 ps, followed by slower relaxation in the first nanosecond after interaction with the exciting pulse. In the two spectra collected at longest times (1 and 3 ns, red and magenta) the most intense positive signal is shifted to the red (460 nm) in comparison to the singlet ESA. This lower energy signal is explained as a $T_1 \rightarrow T_n$ ESA transition,[190] occurring after T_1 is generated via ISC on the nanosecond timescale (τ_{fluo} reported to be 1.8 ns[191]). Further proof of the occurrence of ISC is the incomplete recovery of the ground state bleach, whereas the singlet ESA peaks at 575, 620 and 691 nm, due to $S_1 \rightarrow S_n$ transitions undergo partial decay to leave a signal which is also assigned to the triplet.

After excitation at 560 nm of the ZnTPP-O-SubPc dimer, a mixture of signals attributed to the excitation of the two moieties is detected at 0.2 ps, as predicted from their common absorption at 560 nm. Conversely, the spectral evolution of the transient signals is dramatically different from either of the two monomers. In the first 10 ps, the negative GSB and SE signal from SubPc centred at 555 nm is quenched by 80 % of its initial (at 0.2 ps) amplitude, while the positive ESA observed in the ZnTPP-OH monomer at 455 nm undergoes a three-fold increase within the same time scale. These early time dynamics are highlighted in Figure 6.6 (orange triangles are used to plot the behaviour of GSB+SE, blue triangles used to plot the behaviour of ESA in the dimer dataset). The SubPc ESA peaked at 630 nm decays with the same kinetics of the recovery of the negative feature.

The different dynamics in the first 10 ps is in good agreement with the expectations for EET between the electronically excited SubPc antenna and the ZnTPP acceptor. During this time interval, the excitation moves away from the S_1 excited state of the subphthalocyanine moiety to populate the excited singlet state S_1 of the Zn porphyrin.

At increasing pump-probe delays, the overall signal experiences a decay of the pos-

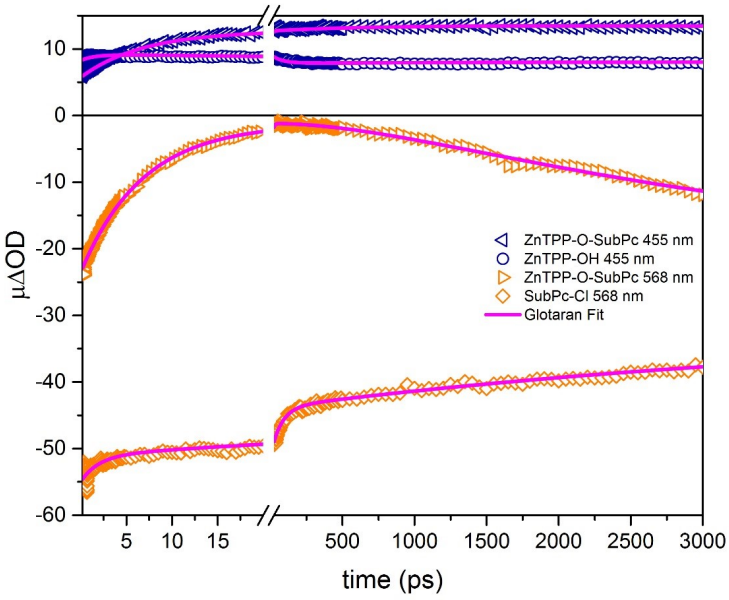

Figure 6.6: Pump-probe time delay T vs $\mu\Delta$OD traces at 455 nm (dark blue) and 568 nm (orange) for SubPc-Cl (diamonds), ZnTPP-OH (circles) and ZnTPP-O-SubPc (triangles), overlaid with traces of Glotaran fit of the corresponding datasets at the same wavelength (magenta). The break on the horizontal axis highlights the EET dynamics, happening within the first 20 ps.

itive features and recovery of the negative ones, due to population relaxation and formation of the ZnTPP triplet on the nanosecond timescale. The deepening of the GSB at 568 nm observed in the long time behaviour of the orange triangles in Figure 6.6 and in the latest transient spectrum of Figure 6.5c (magenta) is unexpected and cannot be rationalised within the model proposed so far. The increase of the bleach is too large to be simply due to the quenching of a broad underlying $S_1 \rightarrow S_n$ ESA of the ZnTPP moiety (which is sufficient to explain the small effect in ZnTPP-OH monomer, Figure 6.5b) but looks like development of a true bleach on the nanosecond time scale. The solid magenta lines superimposed to the datapoints in Figure 6.6 are single curves extracted from the global analysis matrix. Global analysis has been performed on both the monomers and the dimer dataset and is discussed in the next Section.

6.3.1 Global Fitting of the fsTA Data of ZnTPP-O-SubPc and its Parent Monomers

The fsTA data shown in Figures 6.5 and 6.6 have been analysed with the global fitting method introduced in Section 3.2.5, using Glotaran. The 2D fsTA matrices were fit to a single model in which a number of monoexponential relaxations are summed together.[95;96] The model used here adopts a parallel decay scheme, and

the pre exponential factors recovered are called decay-associated difference spectra (DADS, shown in the Appendix 6.A.) Through a matrix operation, it is possible to obtain a sequential model which will give an evolution-associated difference spectrum (EADS) for each exponentially decaying function. Such a sequential model is more appropriate to describe the EET dynamics observed in the dimer of this study because the processes studied here take place in sequential steps. For consistency, EADS for SubPc-Cl and ZnTPP-OH monomers have also been included for comparison with Figure 6.5, although, the behaviour of the isolated SubPc-Cl and ZnTPP-OH monomers shows nonsingle exponential decay, which is probably better described through DADS. The parallel decay scheme yielding DADS for each time constant for the two parent monomers are discussed in the Appendix 6.A of this Chapter; here we are focusing on the EADS, which are shown in Figure 6.7a, b and c for SubPc-Cl, ZnTPP-OH and ZnTPP-O-SubPc, respectively.

To obtain a satisfactory fit, the dataset of each molecule required a model with three steps, evolving toward a final spectrum, which was assumed to have an infinite time constant. All EADS of the SubPc fsTA, shown in Figure 6.7a, have essentially the same shape, according to the postulated dominant singlet-state decay. The fastest relaxation (1.9 ± 0.1 ps, red) may be due to intramolecular vibrational energy redistribution (IVR) and/or vibrational cooling (VC) in the S_1 state; this timescale may also be associated with solvent dynamics, but the nonpolar nature of toluene, and the small Stokes shift observed in the steady-state data, should make this contribution insignificant. The 70.2 ± 2.1 ps lifetime (yellow) was required to obtain a good fit to the experimental data, but its timescale is not suitable to describe any vibrationally-driven relaxation process, and we have not been able to assign it to a specific molecular dynamical process. Also, this component does not carry any new spectral feature, indicating nonexponential population relaxation in the SubPc-Cl monomer. The second longest component (2.2 ± 0.2 ns, green) reflects the decay of the excited singlet state, and its timescale is in good agreement with fluorescence lifetime data reported in the literature data (2.1 ns[188]). The intersystem crossing (ISC) causes partial recovery of the GSB and loss of amplitude of the $S_1 \rightarrow S_n$ ESA at 620 nm. The final spectrum (blue) is assigned to population of the T_1 state, with a broad triplet-triplet ESA peaked at 470 nm and broadened to the low-energy side of the spectrum.[189]

The time constants, DADS (shown in Appendix 6.A) and EADS of ZnTPP-OH have also been obtained. EADS for the Zn porphyrin monomer are reported in Figure 6.7b. Its fastest component (1.6 ± 0.2 ps, red) is again assigned to IVR or VC dynamics, including possible internal conversion (IC) from two-photon-excited high energy electronic states, considering that the cross section for two-photon transitions to the N-band of ZnTPP has been reported to be remarkably large.[191] The second fastest component (74.5 ± 1.9 ps, yellow) has an EADS equivalent to the

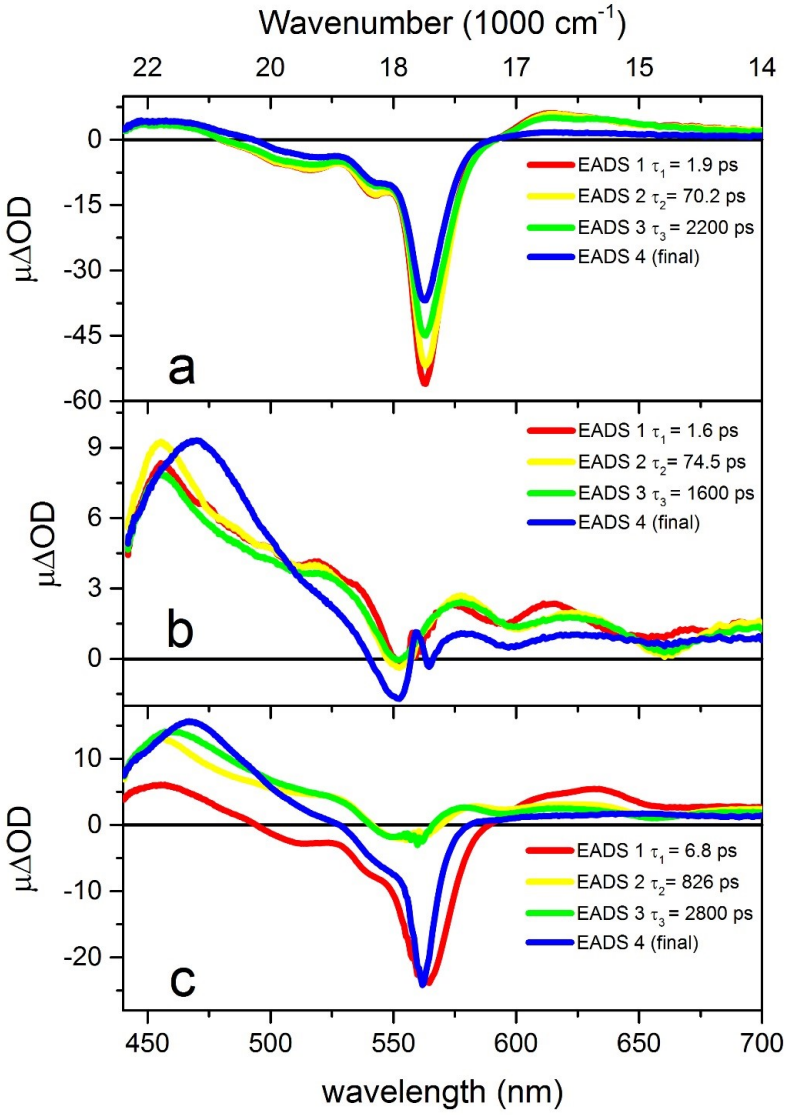

Figure 6.7: EADS spectra extracted from 4 component global fit of SubPc-Cl (a), ZnTPP-OH (b) and ZnTPP-O-SubPc (c). EADS 1, 2, 3 and the final spectrum are reported in solid red, yellow, green and blue lines, respectively. The lifetimes associated with each spectrum are summarised in Table 6.1.

one associated to the nanosecond component, so it probably reflects nonsingle exponential decay of the excited S_1 state. The above-mentioned 1.6 ± 0.1 ns component (green) accounts for the decay of the singlet excited state of ZnTPP-OH (literature fluorescence lifetime reported to be 1.8 ns[191]), producing a final EADS assigned to the triplet population of the Zn porphyrin; in which the singlet-singlet ESA at 460 nm and between 570 and 720 nm have decayed and a new broad $T_1 \rightarrow T_n$ ESA centred at 471 nm appears with weaker signals on the low-energy side (for comparison, the triplet-triplet ESA was reported elsewhere to be centred at 474 nm[190]). Also an apparent enhancement of the negative GSB at 551 is present, but this feature can be explained in terms of quenching of the underlying positive singlet ESA signal.

Fitting the ZnTPP-O-SubPc data required four EADS as well, these are shown in Figure 6.7c. Here, the fastest retrieved timescale (6.8 ± 0.6 ps, red) is assigned to EET from the SubPc antenna to the ZnTPP acceptor, because it has strong negative signals, matching the features of the transient spectra of SubPc-Cl and the simultaneous presence of the strong singlet-singlet ESA at 460 and 620 nm, typical features of the ZnTPP transient spectra, in which the S_1 state is being populated. The second EADS (yellow) has a time constant of 826.0 ± 8.9 ps and it shows contributions from the combined decay of the S_1 of ZnTPP and from the residual population trapped in the excited singlet state of SubPc, the residual population might be due to a slow (hundreds of ps or even slower) back-EET from the S_1 of ZnTPP to the S_1 of SubPc. The third EADS spectrum (2.8 ± 0.1 ns, green) matches well the one associated with the 826 ps time constant (yellow), apart from a difference (a rise) of the ESA centred at 460 nm. Comparing the dimer and ZnTPP EADS, it is logical to assign the nanosecond component to the S_1 decay by ISC of the Zn porphyrin. The product spectrum (blue) exhibits the unexpected increased bleach of the SubPc spectrum on a nanosecond timescale observed in the experimental dimer data. All the lifetimes retrieved from global analysis of SubPc-Cl, ZnTPP-OH and ZnTPP-O-SubPc are summarised in Table 6.1.

	SubPc-Cl	ZnTPP-OH	ZnTPP-O-SubPc
τ_1 / [ps]	1.9 ± 0.1	1.6 ± 0.2	6.8 ± 0.6
τ_2 / [ps]	70.2 ± 2.1	74.5 ± 1.9	826.0 ± 8.9
τ_3 / [ns]	2.2 ± 0.2	1.6 ± 0.1	2.8 ± 0.1

Table 6.1: Lifetimes and relative errors determined from global fitting of the fsTA data

6.4 2D-ES Experiments and Center Line Slope Analysis

Two-dimensional electronic spectroscopy measurements on SubPc-Cl and ZnTPP-O-SubPc in toluene were carried at room temperature, using the setup described in Section 4.1, with 30 nm FWHM NOPA pulses centred at 560 nm, in order to cover both the Q-bands of the SubPc and ZnTPP steady-state absorptions (Figure 6.2). Two-dimensional electronic spectra were acquired for T up to 600 ps. The EET dynamics discussed in the previous Section are clearly observed in the 2D-ES data of the dimer as well (see Appendix 6.B); here, instead, we focused on the spectral diffusion and the dynamic Stokes shift, as they can provide excited-state information about the vibrational cooling and solvent rearrangement on a sub-picosecond

timescale.
2D absorptive (equally weighted sum of the Real part of rephasing and Non-rephasing spectra) spectral progressions for SubPc-Cl and ZnTPP-O-SubPc are reported in Figures 6.8a and b, respectively. The 2D-ES data of the Zn porphyrin monomer are not relevant in this context, because we analyse the reshaping and dynamic Stokes shift (red-shift) of the positive signal in ZnTPP-O-SubPc, which is only due to the contribution of the SubPc moiety of the dimer, in the spectral region interrogated.
At the earliest value of T (105 fs), SubPc-Cl has a positive signal arising from mixed contributions of GSB and SE Liouville-space pathways. This signal has a maximum at ($\tilde{\nu}_1 = 17712$ cm^{-1}, $\tilde{\nu}_3 = 17642$ cm^{-1}) and it is stretched along the diagonal, a clear indication of inhomogeneous broadening of the $S_0 \rightarrow S_1$ electronic transition at early times.[192] A small, negative, off-diagonal ESA peak ($\tilde{\nu}_1 = 17398$ cm^{-1}, $\tilde{\nu}_3 = 16953$ cm^{-1}) is detected as well. IVR and solvent reorientatiion lower the energy of the S_1 state, which translate to a reshaping of the GSB/SE signal within the first ps; this effect can be quantified by recovering and analysing the center line slope (CLS) of the 2D signal,[154;193] as shown in the next part.
The ESA cross peak disappears in $\sim$ 200 fs, an effect which can be explained in terms of relaxation on the excited singlet state potential energy surface (PES) of SubPc-Cl: the initially prepared "hot" population in S_1 can absorb another photon to give $S_1 \rightarrow S_n$ ESA (see Figure 6.9), but once the molecule has lost its excess energy, the third laser pulse will not have enough bandwidth to be resonant with the relaxed ESA. The blue-shift along the detection axis ($\tilde{\nu}_3$) of the negative peak is consistent with this hypothesis.

At early population times (T = 150 and 200 fs), ZnTPP-O-SubPc 2D spectra (Figure 6.8b) show an off-diagonal positive GSB and SE signal above the diagonal ($\tilde{\nu}_1 = 17489$ cm^{-1}, $\tilde{\nu}_3 = 17619$ cm^{-1}), matching with the steady-state absorption and emission spectra (solid red and green lines, top and right panels), as noted in SubPc-Cl. Although, the dimer signal is broader, we speculate this could stem from the increased flexibility of the dimer, which can explore wider ranges of conformations, both in the S_0 and in the S_1 PESs. The initially detected broad structure evolves over the population time into a more elliptical shape (at $T > 200$ fs), this is accompanied by a red-shift of the maximum of the signal. This effect, assigned to a dynamic Stokes shift mechanism, is due to relaxation of the first excited singlet state, parallel with spectral diffusion, as confirmed by CLS analysis. The main difference in the dimer spectra at early population times (top row of Figure 6.8b), are two strong negative ESA signals, assigned to the Zn porphyrin moiety, and matching the fsTA behaviour of the isolated ZnTPP-OH and of the dimer (Figure 6.5b and c). The most relevant effect of the negative peaks in this context is to perturb the shape of the positive SubPc signal, making the estimate of dynamic Stokes shift and spectral diffusion

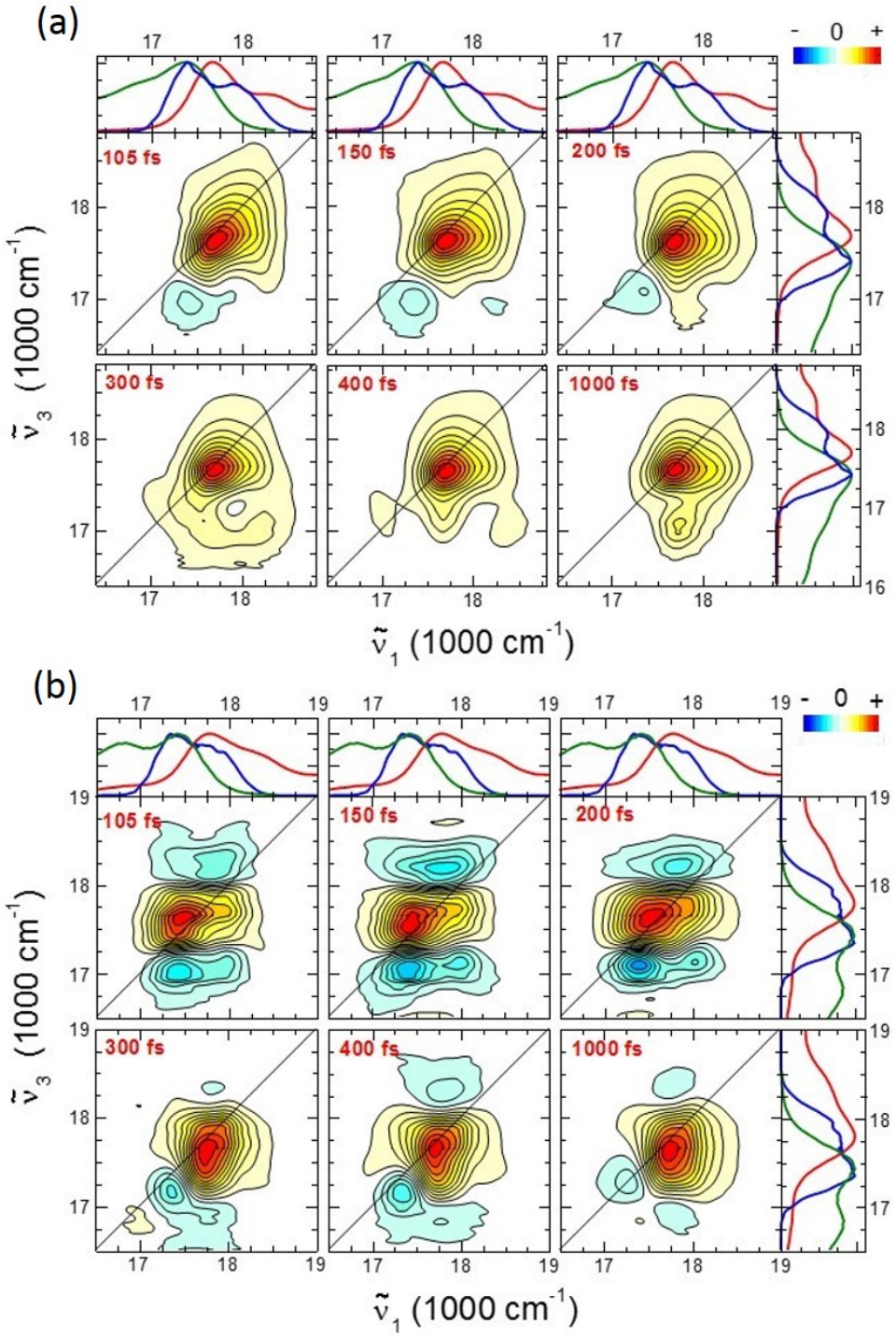

Figure 6.8: Absorptive 2D-ES spectral progressions for SubPc-Cl (a) and ZnTPP-O-SubPc (b) in toluene, in which $\tilde{\nu}_1$ and $\tilde{\nu}_3$ are the excitation and the detection frequency, respectively (plotted in wavenumber). Each 2D graph is normalised to its positive maximum and the amplitude has 21 evenly-spaced contour lines. Positive signals are represented as yellow or red, and correspond to Ground State Bleaches or Stimulated Emission pathways, while negative signals are represented in blue and correspond to Excited State Absorption pathways. Red numbers on the top left of each map indicate the population times T and in the top and right panel the steady-state absorption (red), emission (green) and NOPA spectra (blue) are shown.

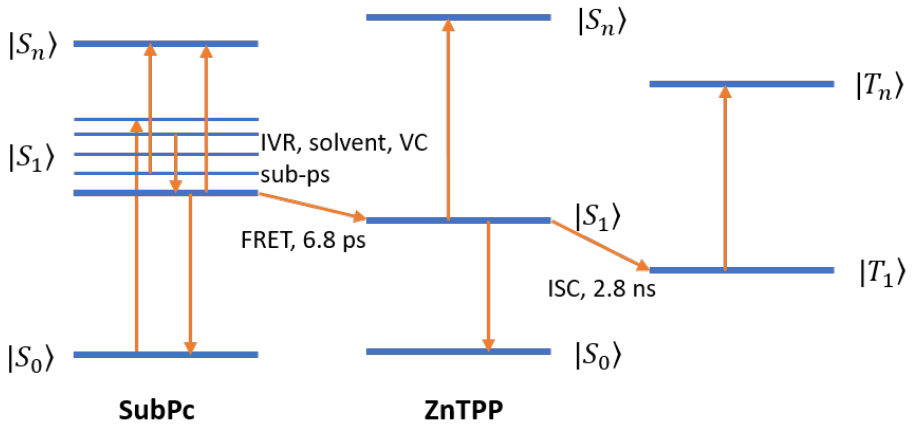

Figure 6.9: Level diagram representing ground and excited states of SubPc and ZnTPP moieties in the dimer. Transitions observed via fsTA and 2D-ES are depicted with solid arrows, their assignment and lifetimes are reported as well.

from 2D-ES data of ZnTPP-O-SubPc more challenging.

6.4.1 CLS analysis of the sub-ps dynamics

Through analysis of the centre line slope (CLS) of a 2D electronic spectrum it is possible to quantify the fluctuations in the energy-gap of the electronic transition. These variations can be caused by the interplay of electronic-vibrational and/or electronic-solvent degrees of freedom. Here, CLS analysis has been carried out on the positive signals of SubPc-Cl and ZnTPP-O-SubPc up to $T = 2$ ps, as shown in Figure 6.10.

The centre line slope is relaxing on a 1 ps timescale in both SubPc-Cl (green dots) and ZnTPP-O-SubPc (red dots). The signal-to-noise ratio of these signals is poor, due to coexistence of positive and negative signals and non-Gaussian shaped peaks, making it difficult to obtain more exact lifetimes for the peak reshaping. In the dimer, the CLS hits a plateau in the first 500 fs and does not evolve further, whereas SubPc-Cl decays until CLS reaches zero. To summarise, these data indicate fast spectral diffusion in both SubPc-Cl and ZnTPP-O-SubPc, but the timescale of these relaxations is too fast to have any significant impact on the incoherent picosecond EET dynamics observed with fsTA.

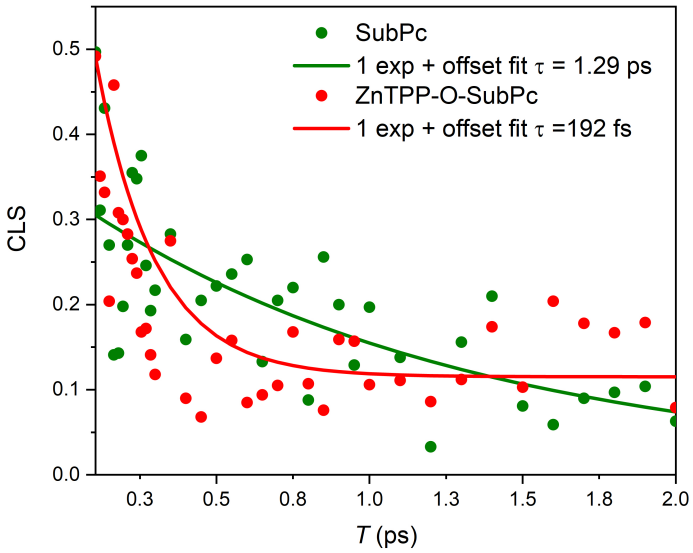

Figure 6.10: Values of CLS against T (75 - 2000 fs) for SubPc-Cl (green dots) and ZnTPP-O-SubPc (red dots) and their biexponential fit (green and red solid lines, respectively).

6.5 Förster Resonant Energy Transfer (FRET) and Orientational Factor (κ^2) Calculations

From global fitting of the fsTA data of ZnTPP-O-SubPc an experimental EET time of 6.8 ps was recovered. This value can be compared to the value calculated using the Förster resonant energy transfer (FRET) model, which allows calculation of the rate of the energy transfer k^{FRET} (reciprocal of τ^{FRET}) according to Equation 6.4:

$$k^{\mathrm{FRET}} = \frac{9\ln(10)\kappa^2\varphi_D J^F}{128\pi^5 N_A n^4 \tau_D} \times \frac{1}{R^6} \tag{6.4}$$

in which τ_D and φ_D are the donor (SubPc-Cl) fluorescence lifetime and quantum yield in absence of acceptor (2.1 ns and 0.25, respectively); κ^2 is a factor which depends on the relative orientations of donor and acceptor transition dipole moments;[194] J^F is the overlap integral between the fluorescence emission spectrum of SubPc-Cl and the absorption spectrum of ZnTPP-OH (4.62×10^{-14} $\mathrm{M^{-1}\,cm^{-1}\,nm^4}$); n is the refractive index of the solvent, in our case toluene ($n = 1.5$), and R is the center-to-center distance between the boron atom of the donor and the zinc atom of the acceptor moieties (1.01 nm), obtained from the DFT calculation of the ground state of ZnTPP-O-SubPc, including a dielectric continuum simulating the shielding effects of the solvent.

The calculation of κ^2 was done with the help of DFT. The ground state geometry of the dimer was optimised employing the hybrid functional B3LYP, using the 6-31G* basis set. Harmonic analysis of the frequencies of the minimised energy structure

has shown that it is a genuine minimum, with no imaginary frequencies. Looking at the dimer molecular structure (Figure 6.1) we can assume that there is potential for rotations around three single bonds, namely C-C, B-O and C-O, which are labeled R1, R2 and R3 in Figure 6.11. Constrained optimisations have been run for each

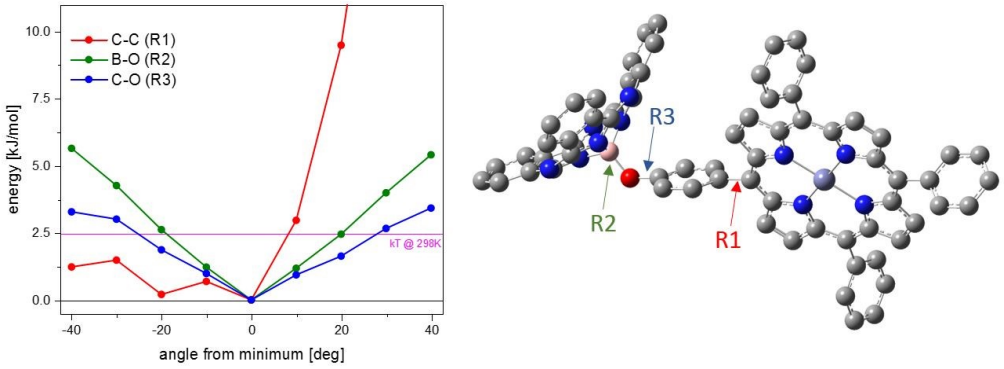

Figure 6.11: Potential energy against angle from their minimum energy structure for torsions around the C-C (R1, red), B-O (R2, green) and C-O (R3, blue) in ZnTPP-O-SubPc. The value of kT at 298 K is shown as a horizontal solid magenta line. All energies have been obtained from DFT calculations (left). Ground state DFT minimised energy structure for ZnTPP-O-SubPc (protons hidden for clarity), where the bonds around which the rotations were calculated are highlighted with arrows and labelled according to text (right).

of these tortional degrees of freedom, in order to obtain a map of the PES along each molecular coordinate. As shown in Figure 6.11 (left) each rotational barrier is higher that kT at room temperature (298 K,$kT \sim 2.5$ kJ/mol): the torsion around C-O (R3) has the smallest energy barrier at 3.4 kJ/mol, the torsion around B-O (R2) is $\sim$ 5.0 kJ/mol and the rotation around C-C (R1) has a very high barrier, because of steric clashes between protons bound to the carbon atoms of the phenoxy bridge and of the porphyrin ring.
Hence, we can use the optimised ground-state geometry of ZnTPP-O-SubPc to calculate the value of κ^2. In order to obtain its value, calculations of the parent monomers were performed at the same level of theory, starting from ground-state optimisations followed by single-point time-dependent density functional theory (TD-DFT) methods to extract transition dipole moments (TDM) of SubPc and ZnTPP moieties. Both chromophores have two degenerate $S_0 \rightarrow S_1$ transitions in their Q-bands with transition dipole moments, as shown in Figure 6.12. The TDMs of each molecule were vector summed, and the resulting vectors, in addition to the displacement vector (defined by B and Zn centres in SubPc and ZnTPP respectively) were used to calculate κ^2, obtaining a value of 0.218.

The orientational factor can assume values ranging from 0 to 4, depending on the relative orientations of the donor and acceptor TDMs. Thus, ZnTPP-O-SubPc has a minimum energy structure which yields a value close to the lower limit of

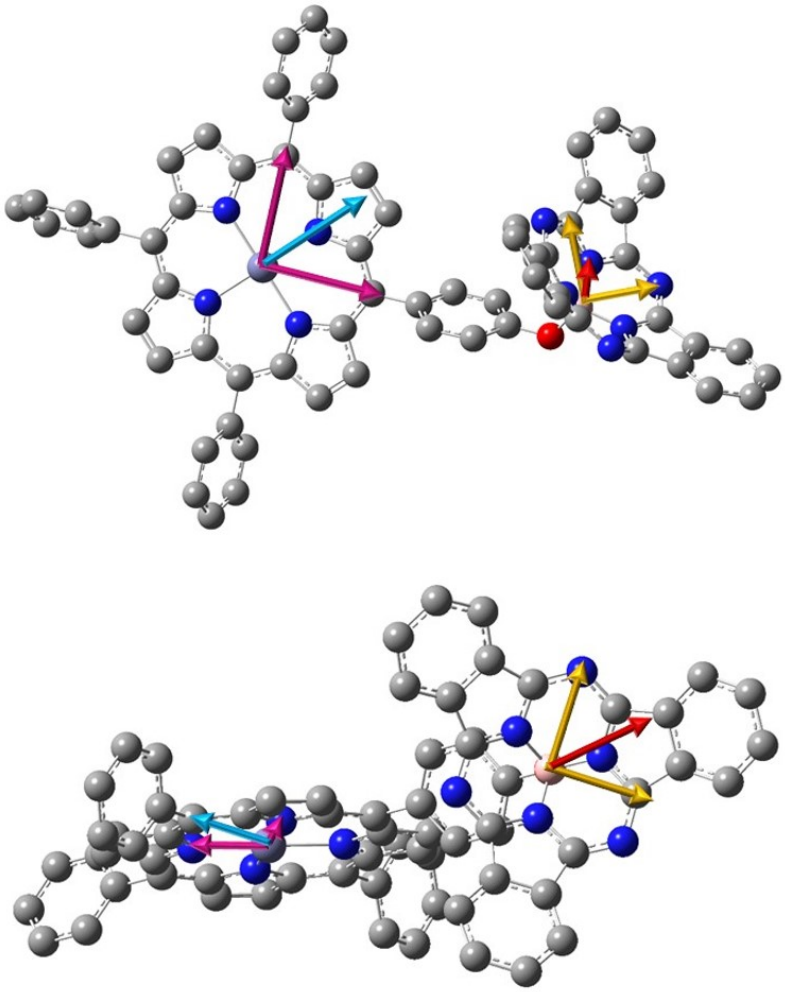

Figure 6.12: Structure of ZnTPP-O-SubPc at two different orientations, with superimposed transition dipole moments (obtained by TD-DFT) of the ZnTPP (magenta arrows) and SubPc (yellow arrows) moieties, and their vector sums (light blue for ZnTPP and red for SubPc). The vector sum of TDMs has been used to determine the orientational factor κ^2 used in Equation 6.4.

this range. In the dynamic averaging condition, which would hold if SubPc and ZnTPP were sampling all possible orientations (i.e. isotropic condition), κ^2 would be 0.444, giving a $k_{\text{calc}}^{\text{FRET}} = 3.81 \times 10^{11}$ s^{-1}, corresponding to a lifetime $\tau_{\text{calc}}^{\text{FRET}} = 2.62$ ps, considerably lower than the experimentally measured value. Using the κ^2 from minimum energy structure into Equation 6.4, we obtain a $k_{\text{calc}}^{\text{FRET}} = 1.88 \times 10^{11}$ s^{-1} ($\tau_{\text{calc}}^{\text{FRET}} = 5.32$ ps), in satisfactory agreement, given the experimental error, with the experimental rate $k_{\text{calc}}^{\text{FRET}} = 1.47 \times 10^{11}$ s^{-1} ($\tau_{\text{calc}}^{\text{FRET}} = 6.81$ ps). Thus, it is possible to conclude that the minimum energy geometry of this dimer is not optimal for light harvesting and funnelling via EET. These conclusions can be helpful for synthetic chemists who could investigate modifications of this structure to enhance the electronic energy transfer efficiency.

We speculate that the unexpected slow bleaching of the SubPc signal at 568 nm observed in the dimer data (Figures 6.5 and 6.7) might be due to EET as well. From Figure 6.2 it is evident that there is significant overlap between the emssion spec-

trum of ZnTPP-OH and the absorption of SubPc-Cl (4.127×10^{-14} M^{-1} cm^{-1} nm^4). Using again Equation 6.4 to calculate the rate of the reverse EET, and making the assumption the orientational factor does not change when changing the direction of the energy transfer process, we obtain a slower rate $k_{calc}^{backFRET} = 2.46 \times 10^{10}$ s^{-1} ($\tau_{calc}^{backFRET} = 40.7$ ps).

	SubPc → ZnTPP	ZnTPP → SubPc	ZnTPP → SubPc *
J^F / [M^{-1} cm^{-1} nm^4]	4.617 $\times 10^{-14}$	4.127 $\times 10^{-14}$	1.163 $\times 10^{-14}$
τ_D / [ns]	2.1	1.8	1.8
φ_D	0.25	0.03	0.03
κ^2	0.218	0.218	0.218
R / [nm]	1.01	1.01	1.01
n	1.5	1.5	1.5
k_{calc}^{FRET} / [s^{-1}]	1.88 $\times 10^{11}$	2.46 $\times 10^{10}$	6.93 $\times 10^{9}$
τ_{calc}^{FRET} / [ps]	5.32	40.7	144.0

Table 6.2: FRET parameters and results for the calculations of forward and backward energy transfer.

This result points in the direction of an equilibration between forward and back energy transfer (the ZnTPP moiety is also directly excited by the laser pump at 560 nm) at times shorter than 100 ps. This effect is however too fast to explain the slow bleaching of the SubPc GSB signal, which happens at times longer than 500 ps. However, the ZnTPP-OH steady-state fluorescence spectrum (Figure 6.2) has a "hot" band (Q(0,1)), which is expected to have a shorter lifetime than the relaxed fluorescence emission from the S_1 state, and hence contribute less to the reverse energy transfer. The contribution from the "hot" band to the ZnTPP-OH emission spectrum can be excluded by fitting a Gaussian to the Q(0,0) band. The lifetime of the EET process experiences a three-fold increase if we consider only the overlap between the relaxed emission spectrum from the Zn porphyrin and the SubPc-Cl absorption. The rate obtained in this way is on the same order of magnitude as the slow bleach, but it is clearly the slowest possible retrievable rate in the framework of a Förster-type energy transfer mechanism. We hypothesise that the slow back EET reflects a change in the dimer structure after the ps energy transfer (from SubPc to ZnTPP), whose complete explanation can only be obtained via calculation of the time-dependent excited state structure of ZnTPP-O-SubPc and geometry-dependent EET. All the constants used to calculate the FRET rates discussed above amd the results of such calculations are summarised in Table 6.2.

*using the reduced emission spectrum (see text)

6.6 Summary

In this Chapter steady-state and time-resolved spectroscopic techniques were used to study energy transfer dynamics in a covalently-bound, flexible heterodimer constituted by a strongly visible absorbing donor moiety (SubPc) and a ZnTPP acceptor. The dimer spectrum can be accurately reproduced assuming only weak dipole coupling, even though the centre-to-centre distance between donor and acceptor is small (1.01 nm). The time-resolved data show energy transfer on the picosecond timescale, which can be explained in the framework of Förster energy transfer. The rate of the FRET process is slow, considering the small center-to-center distance. This was explained by the non-ideal relative orientations of the two chromophores. After the picosecond EET from SubPc to ZnTPP, the zinc porphyrin undergoes intersystem crossing to populate its triplet state. An unexpected bleach of the SubPc signal, on the nanosecond time scale, might be indication of a back-EET, but in order to prove this, more detailed calculations would be needed. Sub-picosecond dynamics have been observed in both fsTA and 2D-ES experiments, but these are also present in the isolated SubPc-Cl parent monomer and they are too fast to have an impact on the electronic energy transfer dynamics.

6.A Decay Associated Differential Spectra of SubPc-Cl, ZnTPP-OH and ZnTPP-O-SubPc

The first DADS for SubPc-Cl (6.13a) with $\tau_1 = 1.9$ ps (red) shows attenuation and redshift of the main negative GSB + SE band, due to cooling of the S_1 state via VR, IVR and interactions with the solvent, as shown by the 2D-ES data in Figure 6.8). The DADS associated with $\tau_2 = 70$ ps (yellow) shows a further attenuation and red shift of the negative part of the spectrum, although its time constant is too slow to be due to relaxation of the first singlet excited state, and it reflects non-exponential decay of the population in SubPc-Cl. The main feature of the third DADS spectrum (green), with time constant $\tau_3 = 2.2$ ns is the suppression of the broad ESA extending from 600 nm to the red end of the spectrum, together with general reduction in amplitude on the SE region. The quenching of SE and ESA while GSB persists, together with the timescale associated to this spectrum, allow us to assign it to intersystem crossing, forming the T_1 state of the SubPc-Cl, which has the DADS shown as "final" (blue).

The fitting of the ZnTPP monomer dataset required four time constants as well, and the corresponding DADS spectra are shown in Figure 6.13b. The fastest component, with time constant $\tau_1 = 1.6$ ps (red) shows a small redshift of both the positive and the negative signals and it also has a negative component (risetime) in the ESA at the blue end of the spectrum, which could indicate rapid IC populating the S_1 state

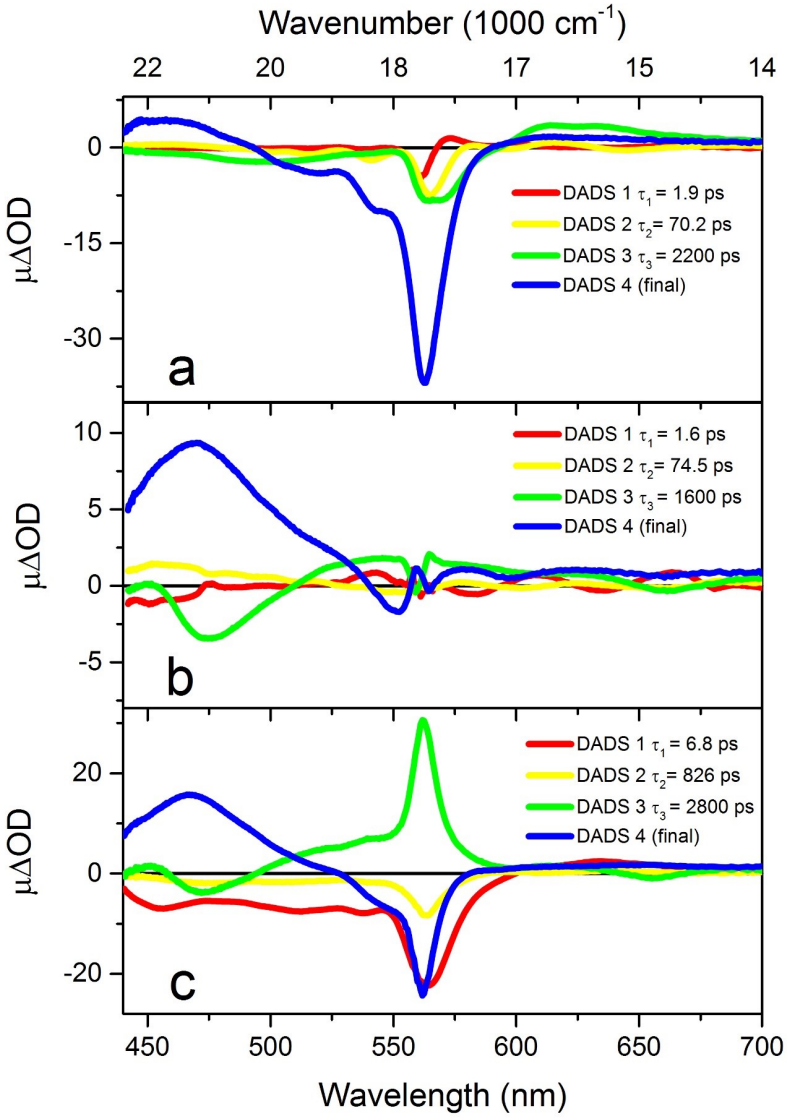

Figure 6.13: DADS spectra extracted from 4 component global fit of SubPc-Cl (a), ZnTPP-OH (b) and ZnTPP-O-SubPc (c). DADS 1, 2, 3 and the final spectrum are reported in solid red, yellow, green and blue lines, respectively. The time constants associated with each spectrum are summarised in Table 6.1.

after 2-photon absorption to the high excited states of ZnTPP-OH. As in the SubPc dataset, an intermediate time constant $\tau_2 = 74.5$ ps is needed to obtain a good fit but its DADS (yellow) cannot realistically be assigned to any physically meaningful phenomenon, and it just reflects non-exponential relaxation of the excited ZnTPP-OH. The main feature of the third DADS (green), with time constant $\tau_3 = 1.6$ ns, is the emergence of a new ESA, which is red shifted if compared to the $S_1 \rightarrow S_n$ ESA intense band around 450 nm. This feature is assigned to ISC and to triplet ESA. The final DADS corresponds to the triplet transient spectrum of ZnTPP and it is shown in blue.

6.B Evidence of EET from 2D-ES

Signatures of the EET between SubPc and ZnTPP moieties within the ZnTPP-O-SubPc dimer, taking place in the first 10 ps after photoexcitation are evident from absorptive 2D-ES data shown in Figure 6.14. The positive (red and yellow) signals due to GSB+SE of SubPc decay within this time window while a negative (blue) signal, assigned to ESA of the ZnTPP moiety, grows in at lower detection frequencies. 2D-ES shows the same behaviour observed with fsTA (Figures 6.5 and 6.6), which has been commented earlier in this Chapter. We decided to restrict the use of 2D-ES to the analysis of the sub-ps dynamics and use the fsTA data to extract time constants of the excitation energy transfer due to the broader spectral coverage of fsTA compared to 2D-ES.

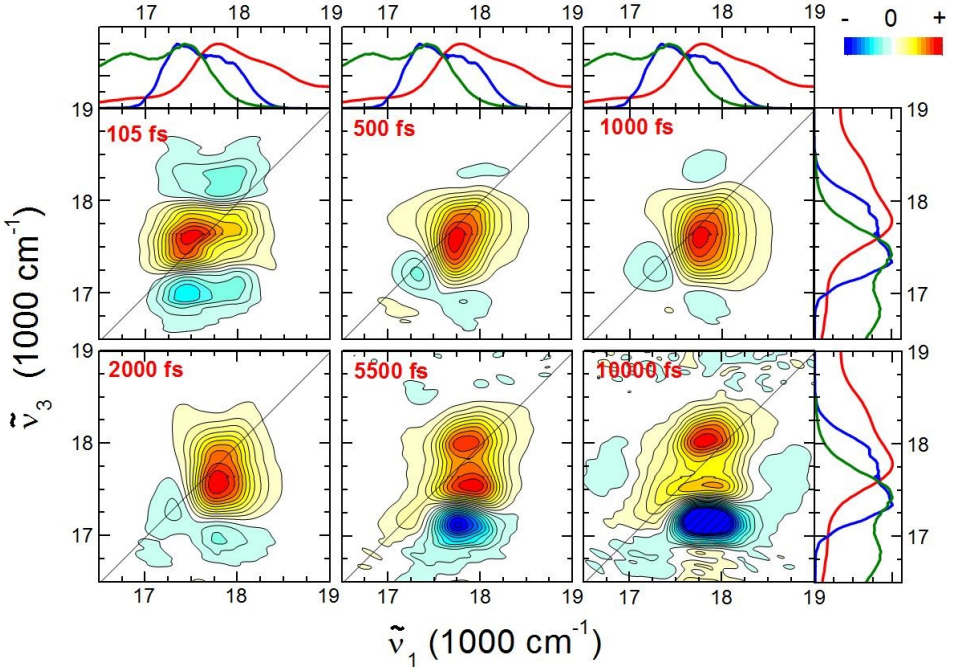

Figure 6.14: Absorptive 2D-ES spectral progression for ZnTPP-O-SubPc in toluene, where $\tilde{\nu}_1$ is the excitation and $\tilde{\nu}_3$ is the detection frequency (plotted in wavenumber). Each 2D graph is normalised to its positive maximum and the amplitude has 21 evenly spaced contour lines. Positive signals are coloured in yellow or red, and represent Ground State Bleaches or Stimulated Emission pathways, while negative signals are coloured in blue and represent Excited State Absorption pathways. Red numbers on the top left of each map indicate the population time T and in the top and right panel the steady-state absorption (red), emission (green) and NOPA spectra (blue) are shown. The spectral reshaping in the first ps is shown in the top row while in the 2-10 ps population time window (bottom row) the EET process is revealed by the quenching of the positive SubPc GSB + SE signal and synchronous growth of the negative ZnTPP ESA.

Chapter 7

Time-Resolved Structural Dynamics of Extended π-Electron Porphyrin Nanorings

7.1 Introduction

Molecular systems constructed using π-conjugated chromophores as building blocks present alluring properties such as semiconducting behaviour[6;125;195] and high non-linear optical susceptibilities.[191;196–198] Because of their unique properties, these structures find applications in electroluminescent devices,[199;200] solar cells,[201;202] optical switches[203;204] and fluorescent biosensors.[126;205] A number of different synthetic strategies to build multi-chromophore structures based on conjugated porphyrins designed for specific applications have been proposed during the last twenty years.[206;207] A large number of studies have been carried out on π-conjugated molecular structures composed of extended mono-dimensional linear oligomers,[149;208;209] for which it is possible to establish a relationship between the length of the conjugated chain and the physical properties of the system.[210] However, in these systems, end-effects, which can modify the physical behaviour,[198;211;212] must be taken into account. Such effects can be particularly severe for short oligomers. One way of overcoming this drawback, is to work with fixed-shape and cyclic conjugated two-dimensional porphyrin macrocycles. These systems can perform as ideally infinite π-conjugated oligomers, and they usually display totally new photophysics and photodynamics.[213;214] A number of species have evolved to exploit the properties of such ring-like structures to harvest sunlight and transfer its energy to reaction centers for photosynthesis,[76;215–217] which lends these structures an added significance.

Thus, understanding the photophysics and excited state dyamics of conjugated nanorings is of great interest. In such structures, excitons tend to manifest high delocalisation.[214] However, large chromophoric macrocycles will necessarily exhibit conformational heterogeneity, creating perturbations which can localise the excita-

tion in a given chromophore or on a region of the cyclic structure.[218] Such effects can compromise the efficient operation required for photonic structures and light-harvesting applications.

In this Chapter we present a comprehensive investigation of ultrafast excited and ground state dynamics of π-conjugated six-membered Zn porphyrin nanorings, with (cP6T6) and without (cP6) a hexapyridyl inner template which ensures structural rigidity. The structure of such compounds, together with a parent dimer (P2), is shown in Figure 7.1. The aim of this work is to study the interplay between the electronic states and conformational disorder of these cyclic macromolecules.

7.2 Steady-state Spectroscopy of Six-Membered Porphyrin Nanorings with (cP6T6) and Without (cP6) a Template

The porphyrin nanorings have been synthesised as previously reported[164;219], and dissolved in toluene with 1% pyridine v/v (to avoid aggregation). The solutions were placed in 1 mm static cells for both steady-state and fsTA measurements, adjusting the concentration in order to get OD ∼ 0.3 at their steady-state absorption maxima. Control measurements at lower concentrations have been performed to make certain that no aggregation was present. The nanoring samples studied here are made up

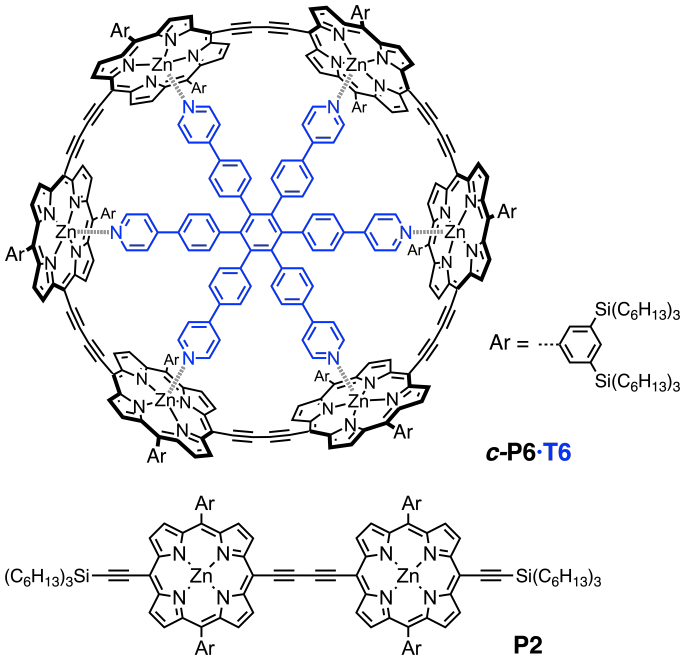

Figure 7.1: Porphyrin nanorings composed by six meso-substituted Zn porphyrin units (aryl groups (3,5-bis(trihexylsilyl)benzene) at meso-positions) forming a circular structure through butadiyne links. cP6T6 is the templated ring, cP6 is the same structure without the hexapyridyl template (shown in blue). P2 is their parent dimer.

of six Zn porphyrin units substituted at the meso- position with aryl groups (3,5-bis(trihexylsilyl)benzene) which are linked together by butadiyne spacers, to build a supramolecular circular structure. These structures were synthesised as reported previously[164;219] and are shown in Figure 7.1. Such a structure can be stiffened by the presence of an inner hexapyridyl template (represented in blue in Figure 7.1). The butadiyne linkers allow complete π-conjugation across the whole nanoring, this effect is manifested spectroscopically as a large red-shift of the Q-band (lowest singlet absorption) relative to the Zn porphyrin parent monomer.[220] The steady-state absorption spectra of cP6 and cP6T6 with band assignments are shown in Figure 7.2. Like other substituted porphyrins, the electronic transition located at the low-

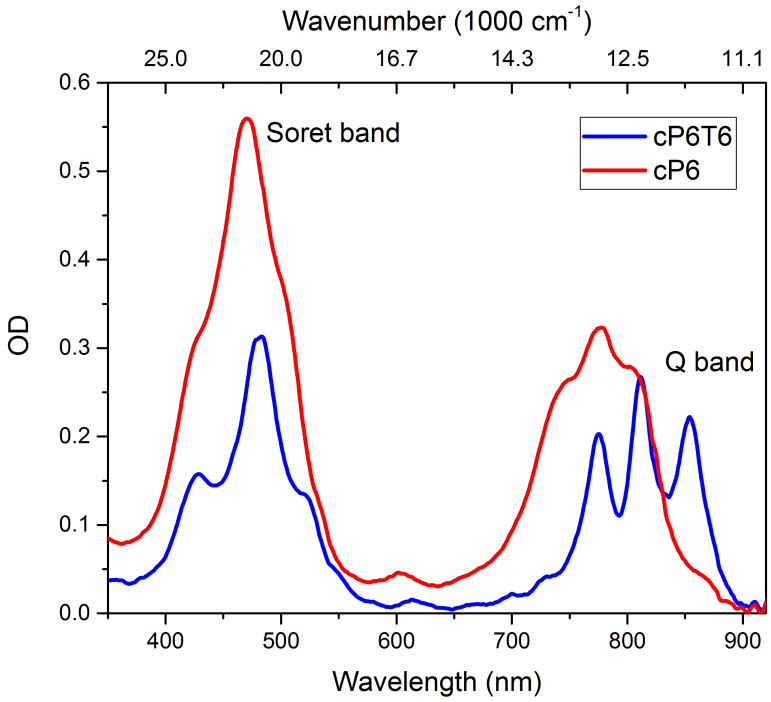

Figure 7.2: NIR-Visible-near UV absorption spectrum of cP6 (red) and cP6T6 (blue), with respective band assignments.

est energy are due to transitions between the ground state and the Q-band.[220] The degeneracy between the two orthogonal Q_x and Q_y transition dipole moments is lifted because of asymmetrical substituents on the zinc porphyrins.

Assessing the energy gap of the lowest transition in six-membered nanorings is not straightforward. These systems, including naturally occurring ones, such as the light harvesting complex LH2, belong to a circular symmetry group, making it possible to describe their excited energy level scheme using the Hückel molecular orbital theory developed for π-conjugated systems.[221] The main result of the model is the presence of two non-degenerate $k^* = 0$ (S_1) and $k = 3$ (S_4) states accompanied by two pairwise degenerate $k = \pm 1$ (S_2) and $k = \pm 2$ (S_3) excited electronic states.

*k is a quantum number which accounts for the number of nodes in the molecular orbitals of the nanorings

In addition to this, Hückel theory predicts that the only transitions that will carry significant oscillator strength will be the two degenerate $k = \pm 1$ (S_2) states, which will have orthogonal relative polarisations. Moreover, according to Kasha's model for electronic transitions in coupled chromophores, the net sum of the transition dipole moments for a circular structure will be zero, i.e. the lowest energy electronic transition $S_0 \rightarrow S_1$ ($k = 0$) will be completely dark. Hence, after photoexcitation, when the nanoring has reached its lowest energy state through internal conversion, its fluorescence emission will be heavily quenched. This effect has been reported for both cP6 and cP6T6, which show reduced fluorescence quantum yields (0.43 % and 0.12 %, respectively) and low radiative rates (0.029 ns^{-1} and 0.0048 ns^{-1}, respectively) when compared to the porphyrin monomer, which has 3 % fluorescence quantum yield and 0.014 ns^{-1} radiative rate. Therefore, the intense bands between 750 and 900 nm are assigned to $S_0 \rightarrow S_2$ transitions, with fast internal conversion to populate S_1, from which fluorescence is suppressed. The cP6 structure is more flexible than cP6T6 because of the absence of the inner template, so the predicted net sum to zero of all the transition dipole moments is expected to be less efficient due to static disorder, resulting in a larger transition dipole moment for the emission of this system. For all the reasons discussed above, determining the energy gap of the first excited state transition $S_0 \rightarrow S_1$ is difficult. This transition has been calculated to take place at $\sim$ 945 nm with the help of time dependent density functional theory. Another open question is the assignment of the similarly-spaced strong absorption bands observed in the spectrum of the templated nanoring (cP6T6), centered at 777, 813 and 858 nm (Figure 7.2, blue solid line). These peaks have been assigned to a Franck-Condon vibronic progression due to a vibrational mode coupled to the $S_0 \rightarrow S_2$ transition, with a fundamental wavenumber $\sim$ 605 cm^{-1}. Alternatively, an electronic origin for the observed peaks was proposed, based on two-dimensional electronic spectroscopy measurements,[31] in which all the coherent superpositions were analysed and classified according to their origin. Nevertheless, explaining unequivocally the origin of these peaks appearing in absoprtion and emission spectra of cP6T6, remains an open question.

7.3 Ground and Excited State Structural Dynamics in cP6T6 and cP6 Observed via fsTA

fsTA measurements on cP6 and cP6T6 have been performed using the setup described in Chapter 3 (Figure 3.3) and their transient spectra, in the first 500 fs, are shown in the main graphs of Figure 7.3(a) and (c), combined with their steady-state absorption and pump spectra (top graphs, solid red and blue lines, respectively). Both the untemplated and the templated ring show an intense ground state bleach (GSB) extending from 680 to 890 nm, and due to $S_0 \rightarrow S_n$ transitions, and an

excited state absorption (ESA), extending towards both extremes of the spectrum. Both positive and negative signals are well-established in $\sim$ 50 fs, which is the time resolution of our experiment, as can be observed in the time domain traces in panels (b) and (d) of Figure 7.3 for cP6 and cP6T6, respectively.

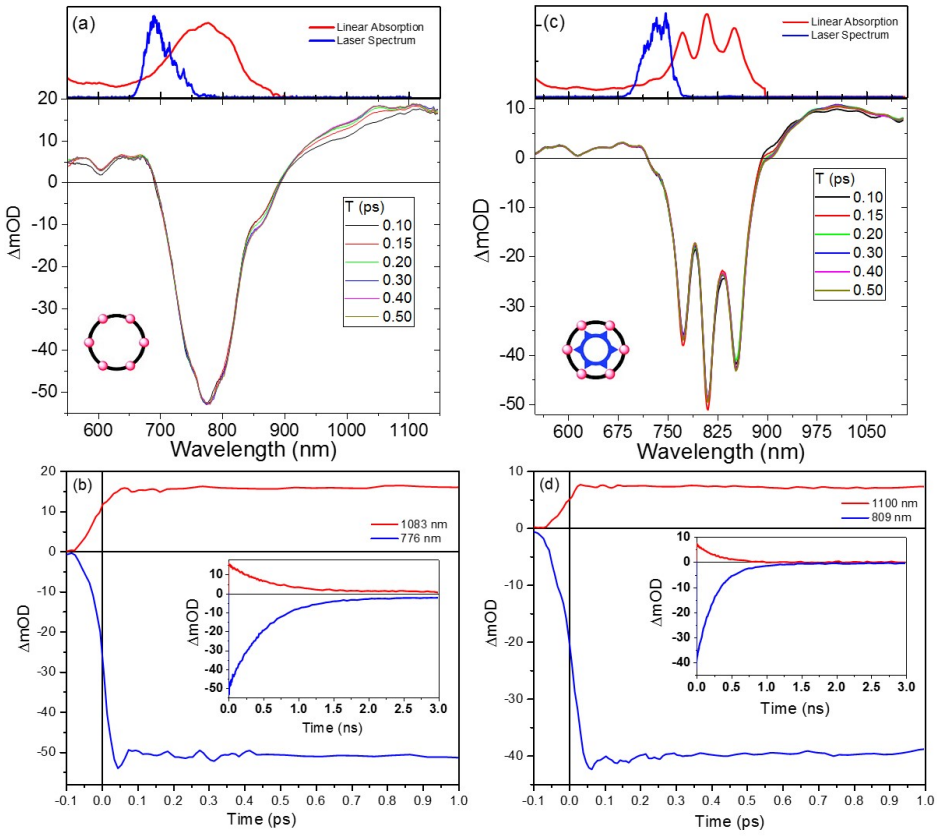

Figure 7.3: fsTA spectra at several pump-probe delays for (a) cP6 and (c) cP6T6. Panels (b) and (d) show time resolved transient absorption curves taken at selected probe wavelengths of 1083 (red) and 776 nm (blue) for cP6 and 1100 (red) and 809 nm (blue) for cP6T6.

The immediate appearance of the GSB and ESA signals implies that the internal conversion (IC) $S_2 \rightarrow S_1$ is an extremely efficient process, as found for analogous cyclic structures. Calculations carried out on conjugated cycloparaphenylenes,[222] made up of 14 constituting units, confirm that the internal conversion which populates the lowest excited singlet state happens in 50 fs, and the time evolution of signals of cP6 and cP6T6 (panels (b) and (d) of Figure 7.3) proves that IC must be this fast in porphyrin nanorings as well. In fact, no fast decays or risetime are noticeable here for the positive ESA contribution. Such dynamics would indicate population transfer between S_2 and S_1. Thus, the internal conversion must be taking place during the pump and probe pulses overlap, on a timescale which is too fast to be resolved with our experimental setup.

The insets of panels (c) and (d) in Figure 7.3 show the long-time behaviour of the positive and negative signals of cP6 and cP6T6, from which it is clear that the ESA

is fully relaxed after a couple of nanoseconds, while a small GSB persists for a time longer than the range probed with our fsTA setup. Incomplete recovery of GSB can be assigned to formation of triplet states, which will relax back to the ground state on a timescale which is orders of magnitude slower (μs). Such triplet states have been observed with Electronic Paramagnetic Resonance spectroscopy at 80 K by Tait *et al.*[223] and also have a highly nonlocal character. The nonradiative decay rate constant of cP6T6 is $k = 1.60$ ns^{-1}, which is slower than for the nontemplated cP6 ring ($k = 2.03$ ns^{-1}), reducing the capability of the templated ring to accumulate population in the T_1 state, which translates to a reduced offset in the value of the GSB at 3 ns. Aside from this slow population decay, fast spectral evolution during the fist 500 fs in observed in both structures, mainly in the spectral interval spanning 820 to 1100 nm.

To give a quantitative description of the transient behaviour of the two nanorings, a global fitting analysis, using Glotaran[96] (as described in Chapter 3), has been applied to the time-frequency 2D data matrices to obtain time constants and their relative decay-associated differential spectra (DADS), which are reported in Figure 7.4(a) and (b), for cP6 and cP6T6, respectively.

Three components were needed in order to fit the data of the templated ring

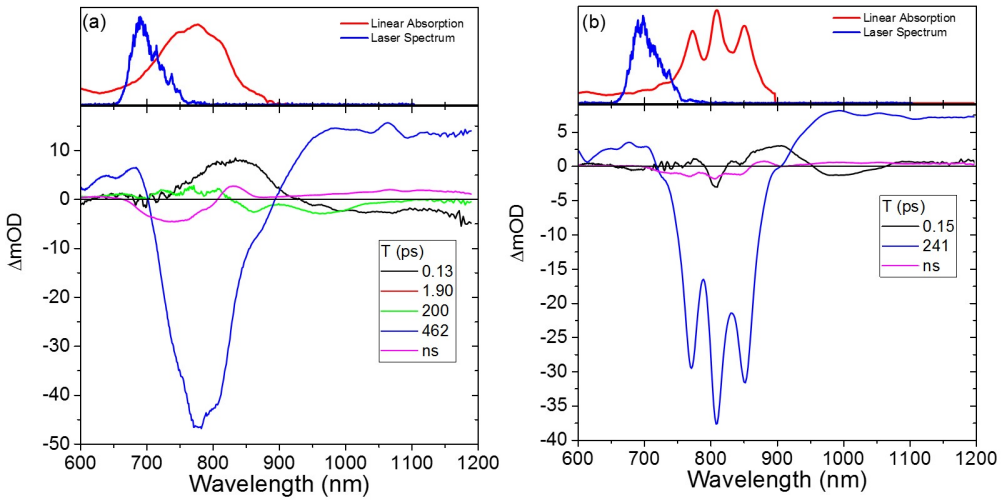

Figure 7.4: Decay associated difference spectra (DADS) for (a) cP6 and (b) cP6T6.

cP6T6, while one additional time component was required for the cP6 data. The fastest component, around 140 fs, corresponds to the fast spectral evolution in the region between 820 and 1100 nm mentioned above. This component can be rationalised assuming energy equilibration within the vibronic levels of the excited electronic state. The other components are much slower (241 ps for the templated ring and 462 ps for the untemplated one) and account for decay of the ESA and refilling of the GSB, while the nanosecond components, not resolved in out experiment, correspond to the population of T_1 states. The extra component, required to describe the spectral evolution of cP6 only, is 200 ps and it is assigned to structural

dynamics in the excited state, namely planarisation (minimisation of the dihedral angles between neighbouring porphyrins) of the nanoring structure, as previously reported.[224] To further support this assignment, time traces extracted from the ESA at 900 nm (for cP6) and 910 nm (for cP6T6) are shown in Figure 7.5, from which the absence of a risetime in the ESA for cP6T6 is clear. The different behaviour

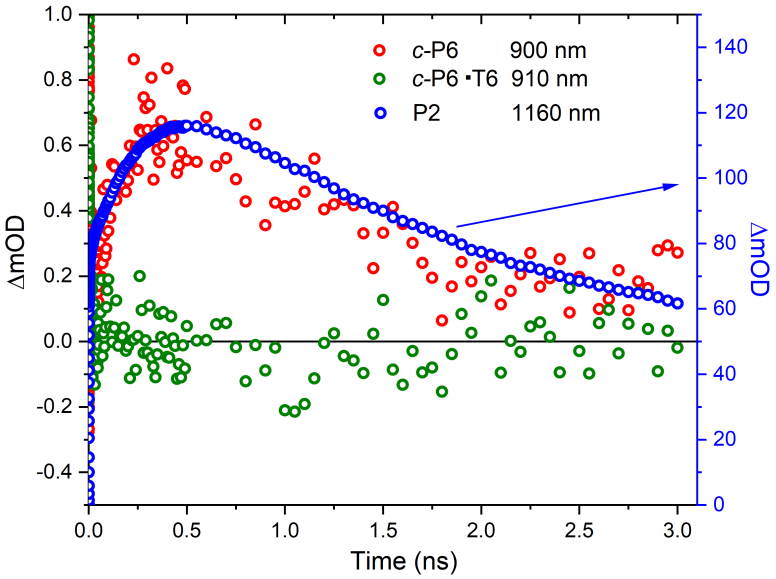

Figure 7.5: Comparison of time resolved fsTA traces taken at selected probing wavelengths: 900 nm for cP6 (red circles), 910 nm for cP6T6 (green circles) and 1160 nm for P2 (blue circles). The right hand side scale, shown in blue, is related only to the P2 data.

between cP6 and cP6T6 is due to the fact that cP6T6 structure is rigidified by the inner hexapyridyl template, which holds in place the porphyrins, keeping the overall structure planar. Moreover, in Figure 7.5, a comparison has been made with the ESA behaviour (at 1160 nm) of a parent dimer of cP6, P2, whose excited state planarisation has already been studied,[224] and whose structure is shown in Figure 7.1. The time traces of cP6 and P2 are overlapping very well, giving strong indications of the origin of this dynamical evolution in the fsTA signal of cP6.

Structural inhomogeneity of cP6 in solution is further corroborated by the results shown in Figure 7.6(a-c). Here, a comparison between transient spectra obtained exciting cP6 on the blue (720 nm, blue solid lines) and on the red (850 nm, red solid lines) sides of its steady-state absorption spectrum has been made. At early times (T = 100 fs, Figure 7.6(a)), if cP6 is pumped on the low energy side, its transient absoprtion spectrum has nicely resolved narrow peaks as observed in the transients of its templated counterpart, cP6T6 (Figure 7.6(d)). At the same pump-probe delay, the transient spectrum obtained when exciting cP6 on the high energy side of its steady-state absorption, is much smoother and does not show the three closely-spaced peaks. This difference can be rationalised if we assume that the cP6 nanorings within the solution possess a significant amount of static disorder, given by the distribution of dihedral angles spanned by porphyrins constituting the cyclic

structure. Structures which display, on average, larger values of dihedral angles will also have their electronic transitions lying at higher energies, whilst the same electronic transition will take place at lower energies in rings with smaller dihedral angles (more planarised); similar shifts were observed in the parent dimer P2 .[11] Hence, excitations centred at lower energies (850 nm) will produce transient spectra approximating the behaviour of cP6T6, shown in Figure 7.6(d-f), where the dihedral angles are kept locked to small values by the inner hexapyridyl templating structure. The dynamics also match the observations from cP6 and cP6T6 steady-state absorption spectra (Figure 7.2), in which the electronic transition of cP6T6, in which the porphyrins are kept coplanar to each other by the template, lies at lower energies if compared to the, less ordered, untemplated cP6 ring.

Consequently, Figure 7.6(a-c) shows that the planarised cP6 molecules are preferentially excited by low energy pump pulses. This phenomenon can be thought as time-resolved hole-burning, through changing the energy of the pump pulse, selective excitation of various subsets contained within the whole inhomogeneously broadened ensemble of cP6 structures present in solution is performed, picking a relatively narrow distribution of dihedral angles (more twisted when exciting at 720 nm, more planar when exciting at 850 nm).

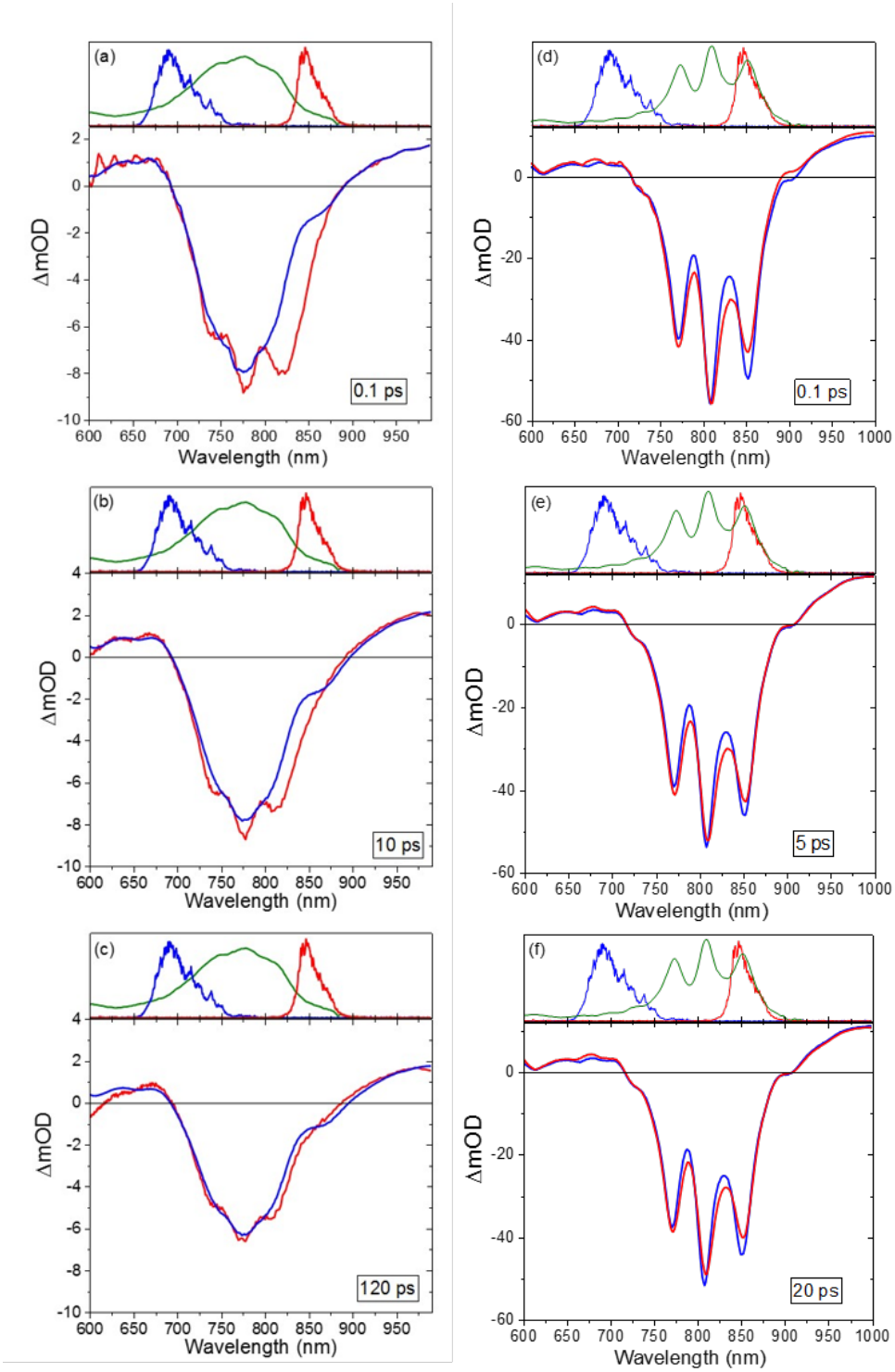

Figure 7.6: fsTA spectra for cP6 and cP6T6 excited on the blue and on the red sides of their steady-state absorption spectra (green), as shown in the upper panel on each graph, centred at 720 nm (blue) and 850 nm (red). The different graphs correspond to different pump-probe delay times as for (a) $T = 0.1$ ps, (b) $T = 10$ ps and (c) $T = 120$ ps for cP6 and (d) $T = 0.1$ ps, (e) $T = 5$ ps and (f) $T = 20$ ps for cP6T6.

At longer pump-probe delay times, dihedral angles can change due to dynamical structural evolution, which can change the transient spectrum of the distribution. This effect is shown in 7.6(b) where $T = 10$ ps and (c), where $T = 120$ ps. As

the interpulse delay increases, the peaks start to look more depleted, culminating in transient spectra which look very similar, even though they have been obtained with high and low energy side excitations. This effect is analogous to the spectral diffusion which can be observed in 2D electronic spectroscopy as a rounding of the peak when the population time T is increased. Conversely, Figure 7.6(d-f) shows how such dynamical evolution of the transient spectra is absent in cP6T6, due to the presence of a template, which is locking the dihedral angles between neighbouring porphyrins to fixed values.

To characterise the timescale of randomisation of the dihedral angles in the ground state (in this case we are looking at the GSB dynamics), the difference between time traces obtained from the high (720 nm) and the low (850 nm) energy pump measurements has been computed, and the residuals have been fit with a multiexponential decaying function, as shown in Figure 7.7. The averaged lifetime obtained is 55 ± 11 ps, so the planarisation takes place almost four times faster in the ground state than in the excited state.

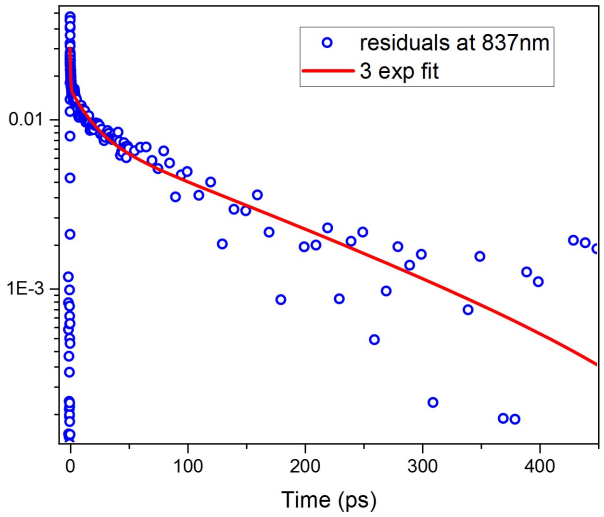

Figure 7.7: Time trace obtained by matching amplitudes of cP6 (excited at 720 nm) with cP6 (excited at 850 nm) spectra at $T = 100$ ps and by subtracting them. The inverse of the residuals at a probe wavelength equal to 837 nm are shown as blue dots. The fit consists of a sum of 3 exponentials with time constants, 0.42 ps, 18 ps, 166 ps. The weighted average lifetime is 55 ± 11 ps.

7.4 Evidence of Exciton Delocalisation via Transient Anisotropy

Wavelength resolved femtosecond transient anisotropy measurements (fsTAn) have been performed, as shown in Figure 7.8, on cP6(a, b) and cP6T6(c, d), as explained

in Section 3.2.4. The two-dimensional plots report anisotropy on a colour scale for each given pump-probe delay and wavelength. As a reference, a steady-state absorption spectrum (red solid line) and an isotropic fsTA spectrum at $T = 200$ fs (green solid line) are reported on the top panels of Figure 7.8. When the isotropic signals cross 0 (both sides of the GSB, at ~ 657 nm and ~ 900 nm), the anisotropy value becomes undefined, as predicted from Equation 3.2. The main characteristic of these 2D plots is that the anisotropy is substantially independent of the probe wavelength, and it assumes a value ~ 0.1 in the whole spectral region analysed, apart from very early times. Anisotropy time traces taken at 1050 nm for cP6 and 1060 nm for cP6T6 are shown in Figure 7.8(b, d) respectively. In both of them it is possible to resolve a ~ 50 fs fast decaying component within the first 200 fs, but after this the anisotropy values settle to 0.1, and this value is kept until full relaxation of the excited state in both the molecules, as shown in the inset of (b). The anisotropy takes a value of 0.1 in a system in which there is no preferential direction for the polarisation of the excitation and emission dipole moments. Electronic transitions in a ring-shaped system are expected to belong to this case, in which there is complete loss of the polarisation memory in two dimensions.

It has been shown by Wynne and Hochstrasser[92] that, when two degenerate states with orthogonal transition dipole monments are simultaneously excited, the coherent superposition between the two states has to be taken into account. In this context, it is possible to measure inital anisotropy values as high as 0.7, which will quickly decay to 0.1, due to decoherence of the electronic excited states. Hence, the 50 fs decaying component measured in cP6 and cP6T6 originates from loss of coherence between $k = \pm 1$ states. This gives further confirmation of the fact that the excitation is delocalised over the whole nanoring structure within this ultrafast timescale. This result supports the previous indication[218] that the absorbing and emitting states are both completely delocalised over the whole nanoring structure, this is true whether or not the ring structure is rigidified by the presence of a template .

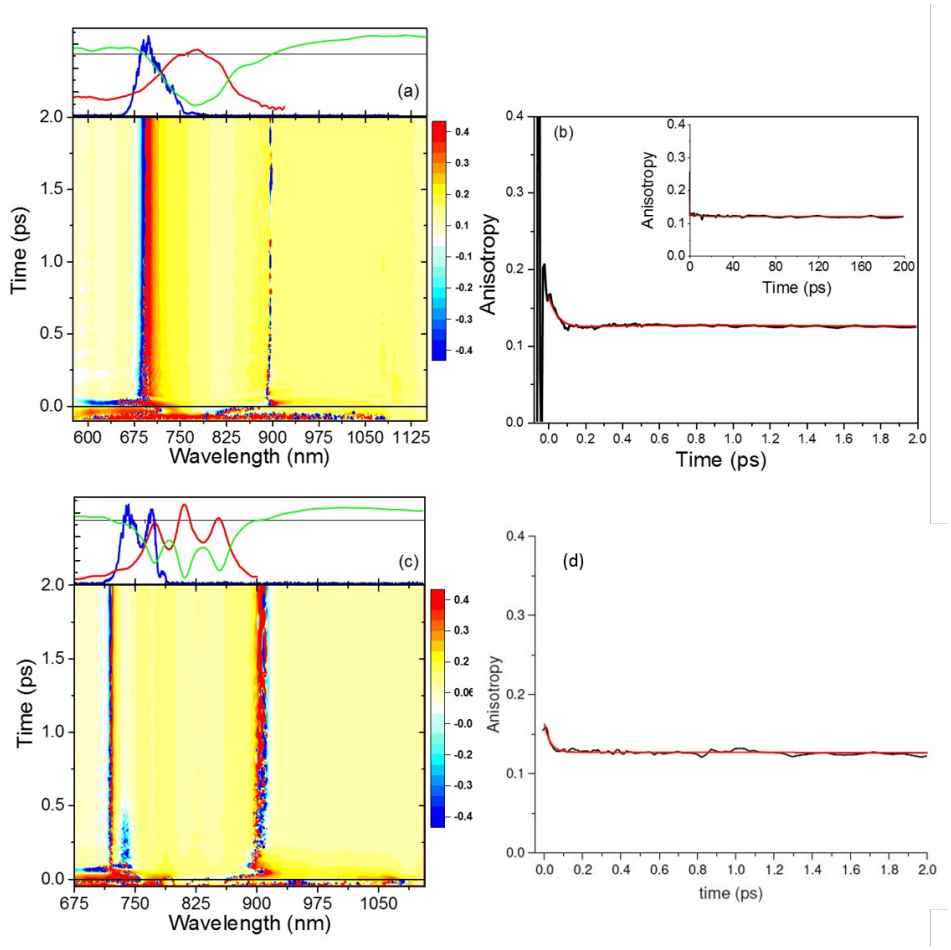

Figure 7.8: (a, c) Two-dimensional plots showing the anisotropy as a colour scale for cP6 and cP6T6, respectively. The top panels show steady-state absorption spectrum (solid red line) and an isotropic transient absorption curve at $T = 200$ fs (green solid line). (b, d) Anisotropy time traces taken at a selected probing wavelength of 1051 nm for cP6 and 1060 nm for cP6T6 (solid black line) and their monoexponential fit (plus offset set at 0.1) to the data (solid red line).

7.5 Summary

The photodynamics of templated and untemplated π-conjugated porphyrin nanorings has been studied with time-resolved femtosecond transient absorption and transient anisotropy. The untemplated cP6 structure shows structural dynamics both in the ground and excited electronic states. In the excited state, minimisation of the dihedral angles between neighbouring porphyrin units (planarisation) happens on a 200 ps timescale, while planarisation of dihedral angles in the ground state occurs almost four times faster (55 ps). On the other hand, cP6T6, whose structure is stiffened by an inner hexapyridyl template, does not display any structural dynamics. Through fsTAn we can conclude that the delocalisation of the exciton occurs over the whole ring on an ultrafast timescale ($\sim$ 50 fs) which is faster than our instrument response function. Surprisingly, the structural motions in cP6 do not cause the localisation of the excitation, which remains delocalised for the whole excited state population time as in cP6T6.

Chapter 8

Exciton-Exciton Annhilation in Large Porphyrin Nanorings

8.1 Introduction

Cyclic extended π structures are molecular systems with unique topology[217;225] and characteristics,[213;226;227] such as the absence of end groups. These are ideally infinite π-conjugated rings which possess high symmetry and show diameter-dependent strain.[218] These topological characteristics have a huge impact on their optical and electronic properties,[164;222] and lead to the emergence of new phenomena, not present in their linear counterparts,[214;228] such as intensity borrowing due to Herzberg-Teller coupling.[221] Nature exploits cyclic oligomers for light harvesting in photosynthesis. These oligomers have excitonically coupled conjugated dye molecules (e.g. chlorophylls) as building blocks assembled by protein scaffolds.[229–231] Typically, the excited states of these macrocycles, known as excitons,[80;232] are delocalised over a large number of chromophore units and display linear and non-linear optical properties that are absent in the monomoers. Such delocalised excitations, which stem from electronic coupling between neighbouring chromophores, can facilitate energy transfer between them.[20;32;233] Bio-inspired synthetic materials which mimic the structures of naturally-occurring porphyrin-like based macrocycles also display non-localised excitations,[218;221] and are thus good candidates for light-absorbing and energy transfer applications.

However, the properties of devices in which biomimetic nanorings are used, will be determined by the size and mobility of their delocalised excitations. These are in-turn affected by the local environment experienced by the exciton in the cyclic structure. It has been reported that, when the ring size of fully-conjugated porphyrin macrocycles increases above a certain value (around 20 porphyrin units),[218] the excitons can only delocalise across a section of the whole macromolecule, tending toward the behaviour of an exciton placed on an infinite linear chain. In addition, large porphyrin rings, while thought of as having a circular shape and symmetry, in

fact have a range of folding properties, and can form nested and stacked structures in solution.[234]

One adverse photophysical phenomenon affecting the light harvesting efficiency of extended π-conjugated structures is Exciton-Exciton Annihilation (EEA),[54;57] which has also been shown to have significant effects on the photodynamics of linear extended chains of chromophores.[48;235] EEA takes place when two excitons, due to their spatial proximity, combine their individual energy, gaining access to higher electronic states, which have fast nonradiative decay channels, such as internal conversion (IC), back to the first excited state. In order to obey the total energy conservation criterion, while one exciton is promoted to a higher excited state, the other one is down-converted to the electronic ground state.[54;56] This process is depicted in Figure 8.1.

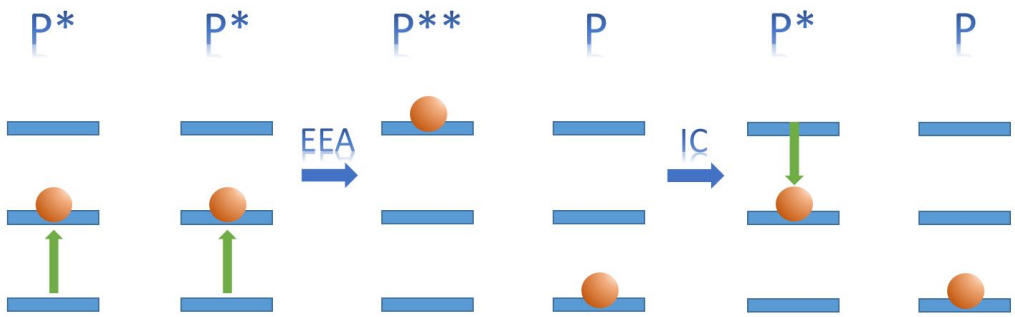

Figure 8.1: EEA relaxation dynamics after light-induced excitation (upwards vertical arrows). Two S_1 excitons (P*P*) interact such that one is promoted to its second excited state, whereas the other one is de-excited to the ground state (P**P). In a second step, internal conversion takes place (downwards vertical arrow). This pathway ends up in the final configuration (P*P), where one quantum of excitation energy is missing; EEA is thus a quenching mechanism.

The EEA dynamics depend both on the rate of collisions between two (or more) excitons on the same chain, and on their mobility along it.[57] Both parameters depend on the size and the topology of the nanorings. EEA has been predicted and experimentally observed in a multitude of excitonic systems of various nature and dimensionality,[46;47;50;236;237] and it has been modelled including the effects of exciton lifetime or of the exciton diffusion time as the rate-determining steps.[54;57]

In this Chapter we present the results of visible femtosecond transient absorption (fsTA) measurements, performed at increasing pump fluences, on a series of conjugated porphyrin nanorings ranging in circumference from 10 to 40 chromophore units. EEA dynamics have been observed and characterised, allowing us to determine the threshold excitation intensity at which EEA occurs in each ring. EEA dynamics have been analysed assuming a one-dimensional diffusion model, modified in order to account for the ring size, which allowed us to retrieve the diffusion coefficients of excitons on the rings. The results are in agreement with literature data, obtained through fluorescence upconversion measurements on the same series

of molecules,[218] and confirm that bigger rings have localised excitations with a coherence length ≤ 20 porphyrin units, while the excitation on the smallest, 10-membered ring, is fully delocalised. Furthermore, the diffusion coefficient of the exciton on the ring, decreases when increasing ring size, consistent with a hypothesis that conformational disorder decreases exciton mobility (and/or size) by creating trap sites, which cause the excitons to localise on a subsegment of the macromolecules.

8.2 Steady-State Spectroscopy of Large Porphyrin Nanorings

Nanorings comprised of 10 (cP10), 20 (cP20), 30 (cP30) and 40 (cP40) porphyrins were synthesised as previously reported[207;238] and dissolved in toluene with 1% v/v pyridine to prevent aggregation. The solutions were placed in static cells with 1 mm optical path for both the steady-state and time-resolved measurements. Their concentrations were adjusted in order to obtain OD around 0.3 at their steady-state maxima. Studies at lower concentrations were made in order to ensure that no aggregation was present. Steady-state absorption spectra were recorded with a UV-Vis spectrophotometer (Lambda XLS, Perkin-Elmer). Room temperature, normalised, steady-state absorption spectra of cP10, cP20, cP30 and cP40 are reported in Figure 8.2 in red, orange, green and blue, respectively. The normalised spectrum of the pump laser used for the fsTA measurements reported in the next Section is shown in magenta as comparison.

cP30 (green) and cP40 (blue) have substantially overlapping spectra, with peaks at 821 nm, due to the coupled Q_x transitions of the Zn porphyrin units.[220] The smaller rings cP10 (red) and cP20 (orange) have their Q_x transitions shifted to the blue (807 and 814 nm respectively) and have slightly broader bands, a signature of a shorter conjugation span that might be due to the limited circumference length of these rings and to the higher amount of strain present in smaller ring structures. A previous report on these rings has employed their steady-state absorption spectra to compute a Meier plot, which points to an effective conjugation length of ca. 20 monomers.[218]

From the steady-state spectra it is also possible to determine the average number of excitons per ring $\langle n^* \rangle$ generated by a pump pulse[57] of known energy, a parameter which is required in order to model the exciton-exciton annihilation dynamics discussed below. The average number of excitons in the probe volume can be calculated according to Equation 8.1:[57]

$$\langle n^* \rangle_{\text{vol}} = \frac{N_{\text{pump}}}{\pi d r^2_{\text{probe}}} [1 - 10^{-\text{OD}(\lambda_{\text{pump}})}] \tag{8.1}$$

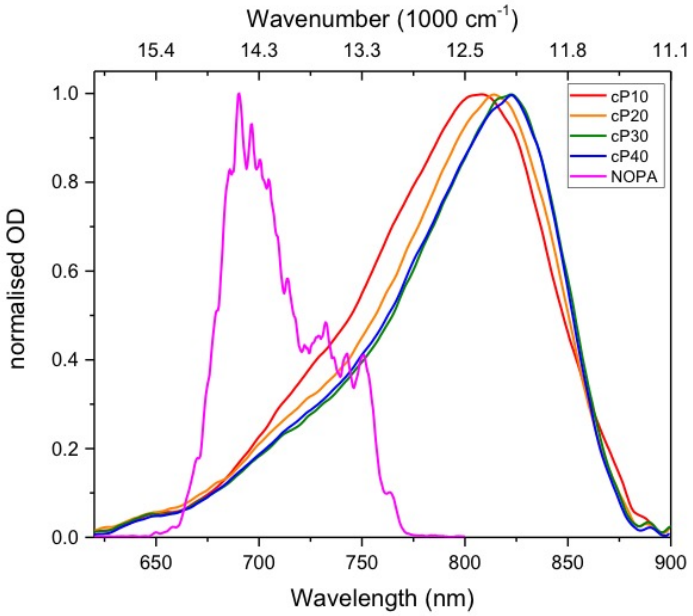

Figure 8.2: Normalised steady-state absorption spectra of cP10 (solid red line), cP20 (solid orange line), cP30 (solid green line) and cP40 (solid blue line). The spectra have been measured at room temperature in toluene with 1% volume pyridine. The normalised spectrum of the NOPA used as pump for the fsTA measurements reported in the next Section is shown in magenta as comparison.

in which N_{pump} is the number of photons in the region of the sample in which pump and probe pulses are overlapping, d is the sample thickness (1 mm) and $OD(\lambda_{\text{pump}})$ is the optical density of each nanoring at the central wavelength (720 nm) of the pump pulses used in the experiments (typically ~ 0.1). N_{pump} is defined in Equation 8.2:

$$N_{\text{pump}} = \frac{\int_0^{r_{\text{probe}}} re^{-2r^2/r_{\text{pump}}^2} dr}{\int_0^{\infty} re^{-2r^2/r_{\text{pump}}^2} dr} \times \frac{E_{\text{pump}}\lambda_{\text{pump}}}{hc} \tag{8.2}$$

With pump and probe radii measured to be $r_{\text{pump}} = 105$ μm and $r_{\text{probe}} = 50$ μm, respectively, and E_{pump} and λ_{pump} defined as energy and central wavelength of the pump pulse. From Equation 8.1, we obtain a value of $\langle n^* \rangle_{\text{vol}}$ which will be proportional to E_{pump}, from which the average number of excitons per molecule $\langle n^* \rangle_{\text{mol}}$ can be calculated, using Equation 8.3:

$$\langle n^* \rangle_{\text{mol}} = \frac{\langle n^* \rangle_{\text{vol}}}{c_{\text{nanoring}}} \tag{8.3}$$

In which c_{nanoring} is the molar concentration of each nanoring sample, which can, in turn, be calculated using Beer-Lambert relation, knowing the molar extinction coefficient $\varepsilon_{\text{nanoring}}(\lambda)$ of each nanoring. $\varepsilon_{\text{nanoring}}(\lambda)$ and $\langle n^* \rangle_{\text{mol}}$ (for each value of E_{pump}) for cP10, 20, 30 and 40 are reported in Table 8.1.

	$\varepsilon_{\text{nanoring}}(\lambda)$ / [M^{-1} cm^{-1}]	E_{pump} / [nJ]	$\langle n^* \rangle_{\text{mol}}$
cP10	630650	10	0.02
		30	0.06
		50	0.10
		70	0.15
cP20	1261301	10	0.04
		50	0.22
		70	0.31
cP30	1891952	15	0.08
		30	0.17
		63	0.35
		74	0.46
cP40	2522603	10	0.07
		30	0.21
		50	0.36
		70	0.50

Table 8.1: $\varepsilon_{\text{nanoring}}(\lambda)$ and $\langle n^* \rangle_{\text{mol}}$ (for each value of E_{pump}) for cP10, 20, 30 and 40.

8.3 fs Transient Absorption of Large Porprhyrin Nanorings

Transient spectra recorded after excitation of the four nanorings with the pump pulses shown in magenta in Figure 8.2 are presented in Figure 8.3 at ten different pump-probe delay times (T) between 0.1 and 500 ps. All these rings show similar fsTA spectra and dynamics, thus a collective description of their fsTA data, highlighting the differences between them when necessary, will be given. The main feature of the series of transient spectra is a strong negative band, present from the earliest measurable time (T = 0.1 ps) peaking at 811 nm (cP10), 825 nm (cP20) and at 830 nm (cP30, cP40). These signals match the positions of the steady state absorption spectra of each ring and are therefore assigned to a ground state bleach (GSB). The negative signal is extended further towards the red than the steady-state absorption. This is where we expect to find fluorescence emission from the nanorings, so, the negative signal is assigned to a stimulated emission (SE) contribution. The linewidth of the negative, mixed GSB + SE, signal is almost constant in cP20-cP40, while the bandwidth is broader in cP10. This, together with the redshift of the negative band which accompanies an increase in ring size, confirms

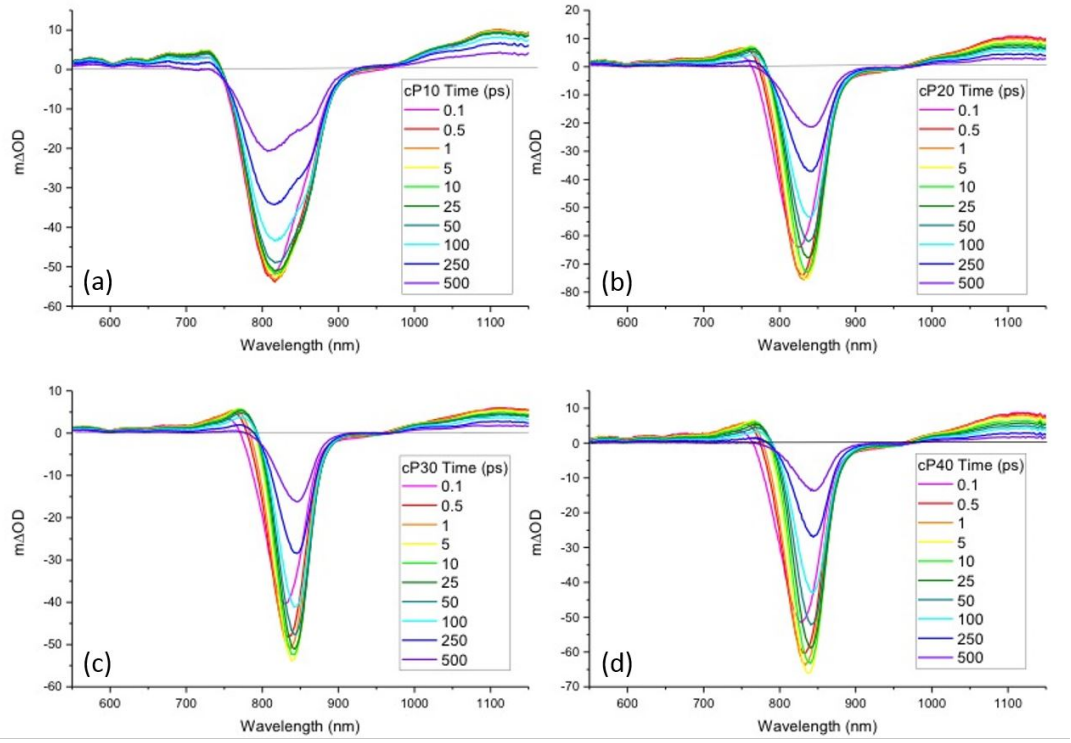

Figure 8.3: fsTA spectra after excitation with pump pulses shown in magenta in Figure 8.2, at ten different pump-probe delay times (T) between 0.1 and 500 ps of cP10 (a), cP20 (b), cP30 (c) and cP40 (d) are shown.

the hypothesis of a J-aggregate-like behaviour of these macrocyclic systems.[218] This is assigned to evolution of the excited state energy, reflected in the stimulated emission. Such a red shift could arise from vibrational cooling (VC), intramolecular vibrational energy redistribution (IVR) or solvent interactions taking place in less than 10 ps for every sample. The slower redshift present in cP20, 30 and 40 data might have to do with the motion of the exciton across the ring, this hypothesis is confirmed by the fact that the 10-100 ps redshift is absent in cP10, which has fully delocalised excitation. The redshift in the negative bands of cP10, 20, 30 and 40 is highlighted in Figure 8.4, in which the wavelength at which the minimum lies versus time is reported for cP10 (blue dots), cP20 (green dots), cP30 (orange dots) and cP40 (red dots).

The "relaxed" negative minima are located at 816 nm in cP10, 839 nm in cP20 and at 844 nm in cP30 and cP40. At longer times, the negative signals recover and, in the case of cP10 only, the bleach develops a shoulder centred at 865 nm, appearing after 100 ps and becoming more prominent and better resolved at longer times. This behaviour of cP10 ideally bridges the structured transients observed in the six-membered ring of the same family (cP6, whose fsTA data are shown in Chapter 7, Figure 7.3), which has fully delocalised excitations, and the bigger cP20 ring, in which the linear J-aggregate-like behaviour is starting to occur[239] due to increased size of the ring.

Risetimes in the GSB + SE contribution occurring in the first 5 ps after photoex-

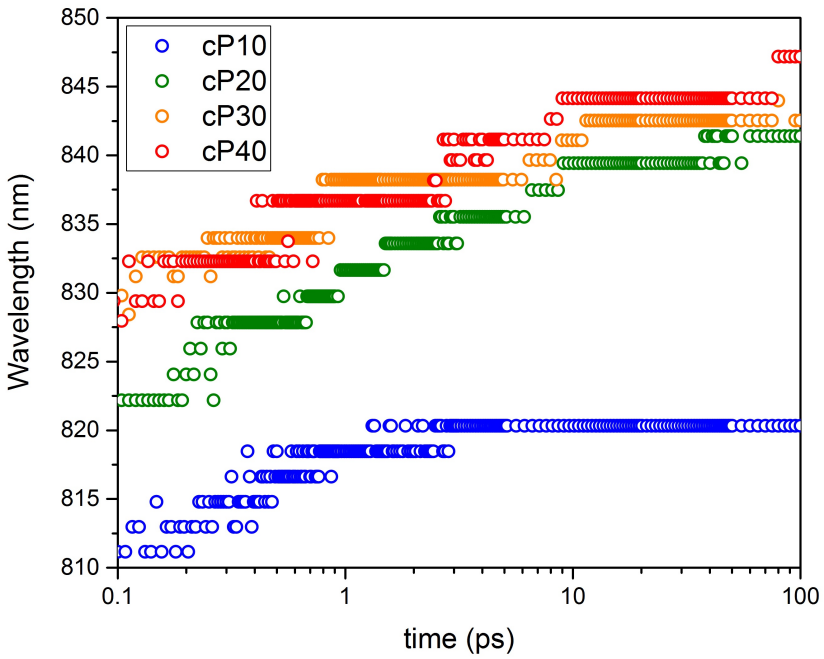

Figure 8.4: Wavelength corresponding to the minimum of the negative signal versus time for cP10 (blue dots), cP20 (green dots), cP30 (orange dots) and cP40 (red dots) highlighting the redshift of the GSB + SE signal in the 0.1 - 100 ps time window.

citation are noticeable in the dynamics of cP20, cP30 and cP40 (8.3b, c, d). A fast risetime has been previously observed by Parkinson *et al.* (see Supplementary information of reference 218) in fluorescence upconversion measurements (excitation at 780 nm, probed at 860 nm) and it has been assigned to energy migration along the ring structure and relaxation of the molecules. We speculate that the risetime in the negative signals might be due to a blue-shifting $S_1 \rightarrow S_n$ underlying excited state absorption, which we are unable to resolve spectrally with fsTA. VR and IVR in S_1 will increase the energy of the ESA transition over time, shifting the positive signal to the blue and generating an apparent risetime in the negative signal. An alternative hypothesis for the risetime in the negative signal could be that the relaxed exciton has a stronger transition dipole moment than the initial exciton, hence its relaxation will be accompanied by an increase in the stimulated emission. Conversely, the structural dynamics which are shown to happen in smaller porphyrin nanorings (see Chapter 7) in the hundreds of picoseconds timescale, while the dynamics here observed take place in the first 10 ps after photoexcitation, suggesting that structural dynamics cannot explain the observed effect. From our experiments we are unable to state which of these scenarios is responsible for the observed transient behaviour of cP20-40. Further investigation of each of these hypotheses will also require TD-DFT calculations on the ring structures.

On the blue edge of the negative signal an ESA positive peak (initially) centred at 728 nm (cP10), 738 nm (cP20) and 744 nm (cP30, cP40), is already well resolved at 0.1 ps. The spectral evolution observed in the first 5-10 ps for the negative peak,

such as redshift and increasing bleach, are present, and occur on the same timescales, in the ESA signals of cP20 - cP40. A relatively narrow ESA on the blue side of a bleach has been observed before in (linear) J-aggregates and has been explained in terms of 1- to 2-exciton state transitions,[139;149] which has already been observed in perylene bisimide homodimers, and described in Chapter 5. The broad positive ESA signals extending toward the low-energy side of the spectrum, in the near infrared (NIR), have a maximum at ca. 1100 nm for all the rings. ESA decay reflects relaxation of the excited state populations created by the pump pulse, accompanied by triplet formation via ISC taking place on hundreds of picoseconds, evidenced by the isosbestic points located at ca. 960 nm. The incomplete recovery of the ground state bleaches at long times, while the ESA has substantially recovered after 250 ps is consistent with population of a triplet state. The interpretation of the dynamics of the ESA located in the NIR is more straightforward due to the reduced spectral congestion in this region, and for this reason we have chosen to focus on the 1100-1200 nm region of the transient spectra of cP10 - 40 to investigate pump fluence-dependent dynamics.

8.4 Intensity Dependent Studies: Modeling of Exciton Diffusion and Annihilation in Large Porphyrin Nanorings

With increasing pump fluence we observed a faster decay of the excited state absorption in cP20-40, as shown in Figure 8.5; this effect is not observed in either cP6 (Chapter 7) or cP10. The fast decaying component is absent in measurement performed at low fluences and only appears when the pump fluence is increased above a certain threshold value, which depends on the size of the ring. Similar fluence-dependent fast dynamics have been observed in linear perylene bisimide and squaraine aggregates[57;237] or in light harvesting complexes,[214;229;240] and have been interpreted as exciton-exciton annihilation.

Since in the EEA process, one exciton is deactivated, and the other one is promoted to higher-lying excited states which quickly decay back to the one-exciton level (as explained in Section 8.1) the net effect of exciton-exciton annihilation, is the loss of one half of the excitons. A rate equation for the number of excitons as a function of time $n(t)$ was developed by Wolter *et al.*:[51]

$$\frac{dn(t)}{dt} = -\frac{n(t)}{\tau} - \frac{1}{2}\gamma(t)n^2(t) \tag{8.4}$$

in which, $n(t)$ is the number density of excitons as a function of time t, τ is the

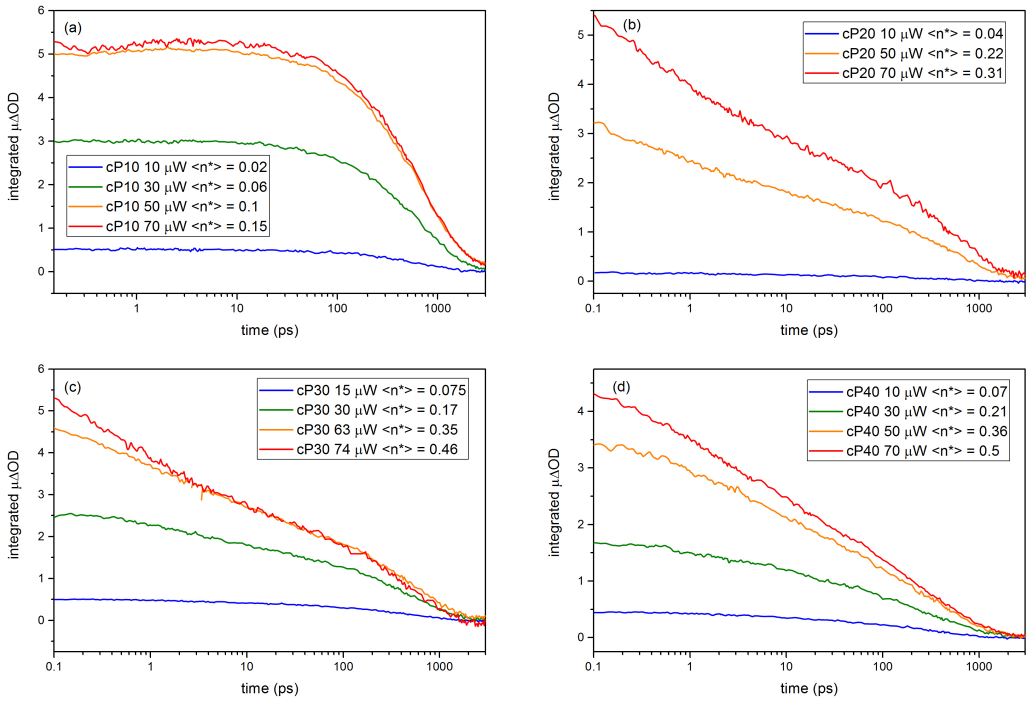

Figure 8.5: fsTA integrated traces (1100-1200 nm) of cP10 (a), cP20 (b), cP30 (c) and cP40 (d) at increasing pump power. Time axis is shown on a log scale to emphasise the differences between the traces at early times.

intrinsic lifetime of the one-exciton state (average lifetime of the 1100 - 1200 nm ESA measured at the lowest possible fluence) and $\gamma(t)$ is the rate at which the annihilation takes place, which can be time-dependent. The factor of $1/2$ is introduced to account for the fact that every EEA event causes the loss of one of the two interacting excitons. Given the structure of the nanorings, it seems reasonable to assume a one dimensional diffusive motion of the excitons along the chain, which allows us to use Equation 8.5 for the rate of the exciton transport .[51]

$$\gamma(t) = \frac{1}{aN_0}\sqrt{\frac{8D}{\pi t}} \tag{8.5}$$

Parameters included in Equation 8.5 are the diffusion coefficient D, the ring circumference a, which has replaced the lattice parameter in the original model, and the number of molecules per volume unit N_0. The circumference of the ring appears in the model because our N_0 values are the concentration of the rings, rather than the concentrations of monomers. So the distance between two neighbouring porphyrins has to be multiplied by the number of porphyrin in a ring in order to make the two equations equivalent. Equations 8.4 and 8.5 have been developed to model exciton behaviour on infinite linear chains, but they can be applied to model dynamics taking place in ring structures, given the absence of end groups. Integration of Equation

8.4 yields:

$$n(t) = \frac{n_0 e^{-t/\tau}}{1 + n_0/aN_0\sqrt{2D\tau}\mathrm{erf}(\sqrt{t/\tau})} \tag{8.6}$$

here, n_0 is the density of excitons created by the pump pulse at $T = 0$. The integrated optical density $I(t)$ will then be:

$$I(t) = a_1 \times \frac{e^{-t/\tau}}{1 + \langle n^* \rangle_{\mathrm{mol}}/a\sqrt{2D\tau}\mathrm{erf}(\sqrt{t/\tau})} \tag{8.7}$$

Where a_1 is a rescaling factor used to match the model and the experimental integrated traces at $T = 0.15$ ps and $\langle n^* \rangle_{\mathrm{mol}}$ is the number of excitons per molecule and erf is the error function. The behaviour of the 1D diffusion model with respect to diffusion coefficient (D), average number of excitons per ring($\langle n^* \rangle_{\mathrm{mol}}$), ring circumference ($a$), and intrinsic exciton lifetime (τ), when all other parameters are kept fixed, is shown in Figure 8.6. From Figure 8.6 it is clear how the population decay becomes faster if the exciton diffusion coefficient D is increasing (a), if the average number of excitons per ring $\langle n^* \rangle_{\mathrm{mol}}$ increases (b), if the intrinsic lifetime of the one-exciton level τ shortens (c) and when the circumference of the ring a becomes smaller (d), when all the other variables are kept fixed.

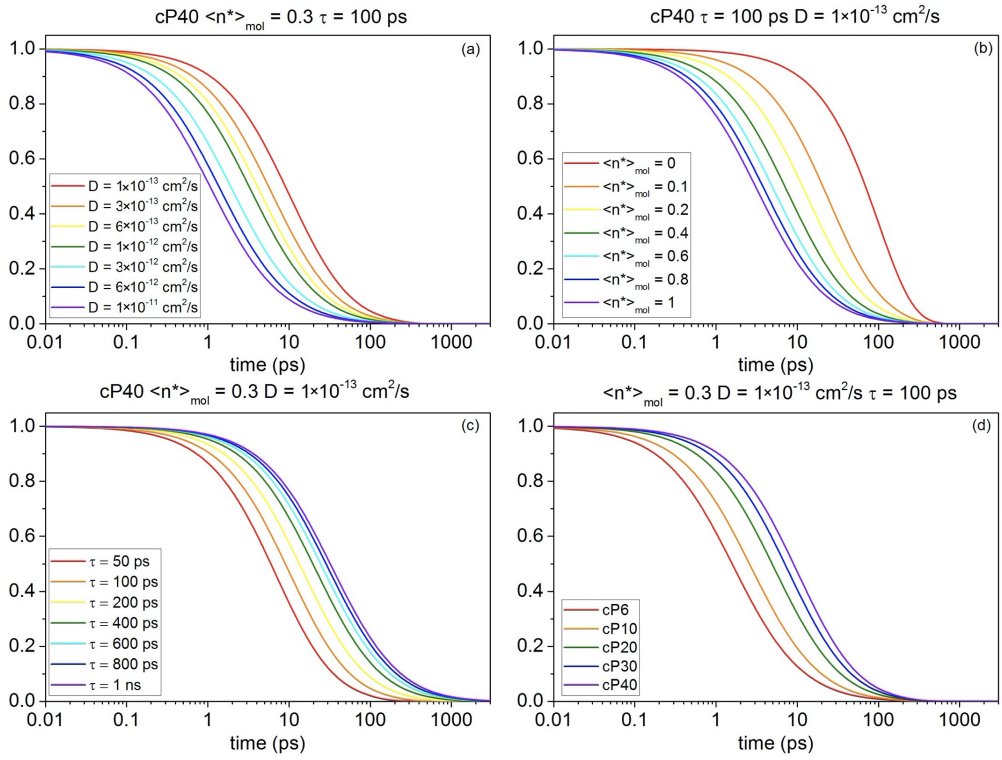

Figure 8.6: Modelled integrated intensity of the fsTA signal versus time for a one-dimensional exciton-exciton annihilation case (see Equation 8.7) for different values of the exciton diffusion coefficient D (a), average number of excitons per mole $\langle n^* \rangle_{\mathrm{mol}}$ (b), intrinsic exciton lifetime τ (c) and ring size a (d). All other parameters have been kept fixed to the values reported above each panel.

In this Chapter, the evolution of the integrated near infrared (1100 - 1200 nm) ESA amplitude has been used as a measure of the pump-fluence dependent exciton decay dynamics. Analysing a portion of the wavelength-time 2D fsTA surface rather than a single time trace allows us to deconvolute the population dynamics from the spectral shifts that occur at early pump-probe delay times, due to the fast excited state dynamics described in the previous Section.
The 1D diffusion model (Equation 8.7) does not account for the decay of the single-exciton level. Thus, in order to compare it to the experimental data, it is necessary to separate the single exciton decay from the EEA dynamics. To do so, measurements at different pump energies (typical values ranging from 10 to 74 nJ, we recall here that μW = nJ, if the repetition rate of the laser is 1kHz) were acquired for each sample, and the integrated trace measured at the lowest fluence (10 nJ) was then rescaled in order to match the long-time behaviour ($T \geq 50$ ps) of the traces recorded at higher pump energies. Subtraction yields the exciton dynamics to be modelled. The lower pump-fluence limit of 10 nJ was chosen as a compromise between an acceptable signal to noise ratio (SNR) and values of $\langle n^* \rangle_{\mathrm{mol}}$ lower than ten percent (see Table 8.1). The tail-matched integrated traces before subtraction are shown, for cP10 and cP40, as an example, in Figure 8.7.

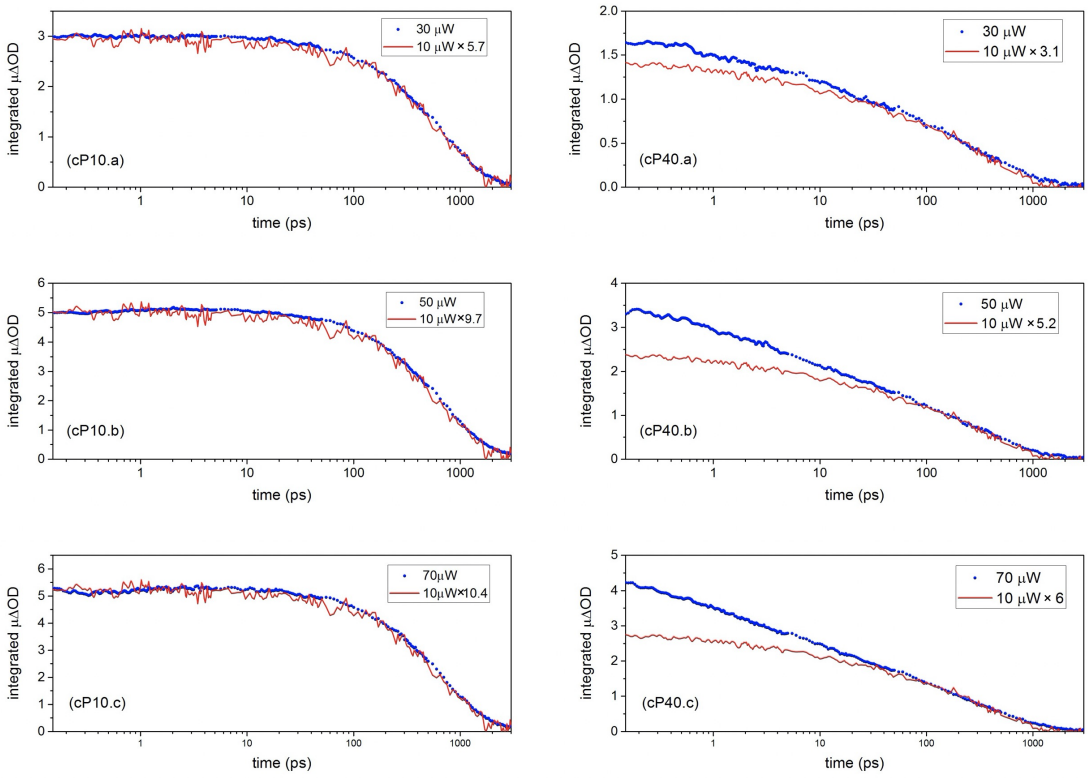

Figure 8.7: Comparison between rescaled 10 nJ (red solid line) and higher (blue dots) pump fluences integrated fsTA traces (1100 - 1200 nm) for cP10 (left) and cP40 (right). The rescaling factors have been chosen in order to tail match the 10 nJ trace with the traces measured at higher pump powers.

The tail matching procedure and subsequent subtraction have been applied to

cP10, 20, 30 and 40 and the resulting traces fitted with the 1D diffusion model (Equation 8.7). The subtracted data and the corresponding fitting curves are shown in Figure 8.8a(cP10), b(cP20), c(cP30) and d(cP40). Looking at Figure 8.8, the first difference which can be noticed, is that the procedure described above allows a fast-decaying component to be isolated from the data of cP20, 30 and 40. This component is clearly absent or negligible in the time traces of cP10. An explanation of this effect is that the excitation on cP10 is delocalised over the whole ring structure. With this constraint, even if two excitations are put on the ten-membered ring, they will instantaneously annihilate. Conversely, the EEA dynamics obtained from the fluence-dependent cP20, 30 and 40 data, for pump-probe interpulse delays between 0.15-10 ps, are well fit by the 1-dimensional diffusive model of the exciton motion on the ring.

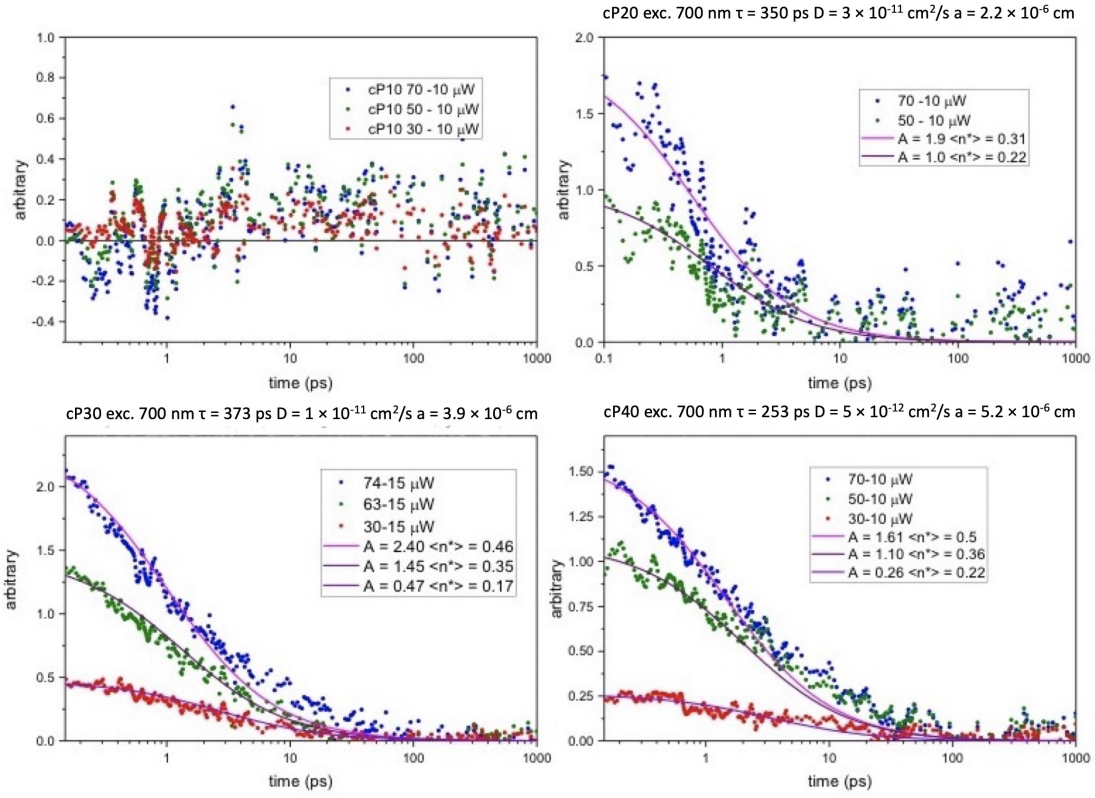

Figure 8.8: Subtracted integrated traces for cP10 (a), and fits (using Equation 8.7) for cP20 (b), cP30 (c) and cP40 (d) at different pump fluences. The parameters used for the fit are summarised in Table 8.2.

To disentangle the single exciton population dynamics, whose timescale is a variable of the 1D diffusion fit model, from the fast EEA process, the average decay constant of the single-exciton population τ must be known. τ is extracted from the nonexponential decay of the single-exciton level, by mean of a biexponential fit of the lowest fluence integrated ESA traces of each molecule, followed by weighted averaging of their τ_1 and τ_2. The initial number of excitons per molecule $\langle n^* \rangle_{\mathrm{mol}}$ has been calculated from the steady-state data and the pump probe overlap integrals

as previously described. The ring circumference a has been calculated multiplying the distance between two adjacent porphyrins on a similar linear chain (1.3 nm[164]) by the number of porphyrins on each ring. The rescaling factor has been chosen in order to match model and integrated experimental data at $T = 0.15$ ps. Thus, the only free parameter of the fit is the diffusion coefficient D. All the values used to fit the data of cP20, cP30 and cP40 are summarised in Table 8.2.

	Fluence sub. / [nJ]	$\langle n^* \rangle_{\mathrm{mol}}$	c	τ / [ps]	a / [cm]	D / [cm^2/s]
cP20	70 - 10	0.31	1.90	350 ± 2.1	2.6×10^{-6}	3.00×10^{-11}
	50 - 10	0.22	1.01			
cP30	74 - 15	0.46	2.40	373 ± 2.0	3.9×10^{-6}	1.05×10^{-11}
	63 - 15	0.35	1.45			
	30 - 15	0.17	0.47			
cP40	70 - 10	0.50	1.61	253 ± 2.3	5.2×10^{-6}	5.20×10^{-12}
	50 - 10	0.36	1.10			
	30 - 10	0.22	0.26			

Table 8.2: Parameters for the 1D diffusion fit applied to the subtracted integrated ESA data of cP20, 30 and 40. Fit results shown in Figure 8.8.

As expected from the correlation between static disorder and ring size,[234] there is a trend in the values of the diffusion coefficient. The best fit for cP40 is obtained when $D = 5.2 \times 10^{-12}$ cm^2/s, this value increases to 1.05×10^{-11} cm^2/s for cP30 and to 3.0×10^{-11} cm^2/s for cP20. Bigger rings are more disordered and have a broader distribution of conformations,[234] and such disorder reduces the mobility of the excitons,[241] this corresponds to an increase in the time needed for the two excitations to interact on an arbitrary subsegment of the ring.[57] Moreover, the disorder can disrupt coherence causing the exciton size to become smaller. Both phenomena will contribute to a smaller value of D in the fit with increasing ring size. A different model, specifically designed for naturally occurring cyclic chromophore assemblies B850, proposed by Trinkunas *et al.*,[242] has also been applied to the data. In that model, the time constants of the anisotropy decay (at low pump fluence) and of the EEA (at high pump fluence) are used to estimate the coherence length and the hopping time of the exciton, which can be related to the diffusion coefficient D. This model, when applied to our data, did not produce any meaningful data (complex values for the exciton size). One explanation can be that, in their work, a monoexponential excited state population decay is observed, while the decay dynamics observed in cP20-40 are much more complicated. These differences are probably due to the fact that, in natural systems, chromophores are held in place by

protein scaffolds which keep static disorder low, while we speculate that the different conformations that large rings assume in solution have a non-negligible role on the observed exciton-exciton annihilation dynamics.

8.5 Summary

fsTA measurements on the fs-ns time window on fully conjugated, alkyne bridged macrocycles composed of 10, 20, 30 and 40 Zn porphyrin repeating units have been carried out as a function of pump power fluence, in order to characterise power dependent exciton-exciton annihilation (EEA) dynamics.

The ten-member ring (cP10) does not show any fluence-dependent fast decaying components and has transient spectra that resemble the smallest molecule of this series ever synthesised (cP6, see Chapter 7). This result is consistent with fully delocalised excitations. A change in behaviour is observed when the ring size is increased to 20 (or more) porphyrin units. In their transient spectra a narrowing of the negative band and appearance of the one- to two-exciton state ESA transition are observed. These changes are more subtle in cP30 and cP40, suggesting that in the bigger rings, the coherence size of the exciton becomes independent of ring size. This would imply that the exciton is experiencing a local environment which begins to resemble a linear chain, and it is not bigger than 20 monomers.

A one dimensional diffusion model developed to describe exciton motion on linear infinite chromophore chains has been modified to account for the ring size. This model reproduces well the fast decaying component extracted from the experimentally measured data of cP20-40, and allows us to estimate the diffusion coefficient of the excitons. The value of D decreases in larger rings, due to their more disordered structures which can affect both the size and the mobility of the excitons.

Chapter 9

Conclusions

9.1 Concluding Remarks

In this thesis a number of results from ultrafast optical spectroscopic techniques applied to the study of exciton dynamics in synthetic multichromophoric model systems have been presented. In Chapter 2 we introduced a semiclassical approach, which employs the time-dependent perturbation theory, to describe and model the interactions between electromagnetic fields and matter, as they take place in two-dimensional electronic spectroscopy and transient absorption experiments. The focus was put on making connections between the third order response equation and the corresponding pathways in Liouville space. Such connections allowed us to draw double-sided Feynman diagrams for the cases of pure electronic transitions, vibronically and excitonically coupled systems.

I then presented the fsTA setup (Chapter 3) which has been used throughout this thesis, describing the light sources employed, its experimental design, how to remove the effect of the dispersion in the white light from the spectra, how to measure isotropic and anisotropic signal. The data acquisition procedure and the data analysis were also described. Data analysis relies on a global fitting routine which yielded decay and evolutionary associated difference spectra for each time constant.

The same approach was used in Chapter 4 for the 2D-ES setup, which was built in a BOXCAR (fully noncollinear) geometry, with the four beams focusing and overlapping at the sample position from the four corners of a square. This geometry ensures intrinsic phase stability, background-free detection, ease of acquisition of separate rephasing and non rephasing signals, and it relies on conventional optics, three synchronous mechanical delay stages and a double chopping scheme.

Furthermore, I described the data acquisition routine, emphasising how this setup permits better removal of the scattered light, quasi simultaneous acquisition of NOPA, 2D and fsTA spectra and shot-to-shot data acquisition. Finally, we discussed the data processing algorithm required to convert the raw heterodyne detected signal to the complex-valued 2D-ES absorptive, rephasing and non rephasing maps.

The remainder of the thesis was dedicated to a summary of our results from four different experimental studies of different synthetic multichromophoric model systems.

- In Chapter 5 I discussed the effect of an increase in the interchromophore separation in a series of covalently-bound perylene bisimide dimers. I showed how 2D-ES on the strongest excitonically coupled dimer allowed us to measure a new excited state absorption signal, assigned to a one- to two-exciton state transition, absent in both the perylene bisimide monomer and in a dimer in which the interchromophoric separation has been increased. The experimental 2D data were compared to simulations performed using the hierarchical equation of motion-phase matching approach, which confirmed the hypothesis of a pure electronic origin for the extra excited state absorption detected in the strongly coupled dimer.

- In Chapter 6 I revealed and characterised, using linear (steady-state fluorescence) and nonlinear (fsTA and 2D-ES) spectroscopies, excitation energy transfer in a flexible subphthalocyanine-Zn porphyrin dimer. Through fsTA the time constant of the energy transfer was measured to be 5.8 ps, while 2D-ES allowed to observe fast spectral diffusion both in the dimer and in the subphthalocyanine monomer; although, this phenomenon was too fast to impact on the energy transfer process. The experimentally measured timescale of the energy transfer was in good agreement with a Förster model, in which we accounted for all the possible conformations of the dimer molecule. A question regarding the growth of the subphthalocyanine signal on the ns timescale in the dimer fsTA dataset remains open and will need more detailed calculations to be answered.

- In Chapter 7 I described transient absorption and transient anisotropy on a six-membered fully conjugated Zn porphyrin ring, with or without an inner rigidifying hexapyridyl template. fsTA measurements at different pump wavelength and comparison with the transient behaviour of a parent dimer allowed identification of structural dynamics (planarisation) in the non-templated ring, taking place on 200 ps in the excited state and 55 ps on the ground state. Transient anisotropy measurements show how, apart from a sub-50 fs decay, which might be due to fast decoherence between electronic states, the anisotropy was time independent at 0.1. This is the value expected for an exciton which is delocalised on a 2D plane. This proves that the structural dynamics do not cause the excitation to localise on a subsegment of the ring.

- In Chapter 8 I outlined transient absorption at increasing pump powers on a series of fully conjugated porphyrin nanorings made up of 10, 20, 30 and 40 porphyrin units. Electronic structure in these rings is heterogenoeous, the

excitation only spans ca. 20 chromophore units as previously reported, so the 10 membered rings are have fully delocalised excitations, while in the the 20, 30 and 40 membered rings the excitations only span a section of the structure. We were able to identify power-dependent fast decaying components in the 20, 30 and 40 membered rings, which were assigned to exciton-exciton annihilation. These fast dynamics were fit with a one-dimensional diffusion model, which retrieved the diffusion coefficient of the exciton. The diffusion coefficient decreases when increasing the ring size, confirming the hypothesis that the static disorder, which is also increasing with the ring size, acts as a trap and causes the exciton to localise on a section of the macrocyclic structure and/or to diffuse more slowly.

Overall, our results show that 2D-ES, fsTA and fsTAn can indeed be used in a combined fashion to study thoroughly a variety of exciton dynamics in synthetic multichromophoric model systems.

9.2 Future Work

Broadband Two-Dimensional Electronic Spectroscopy

The results from Chapters 5 and 6 show that one of the main drawbacks of the 2D-ES setup used in this thesis is the limited spectral regions which can be interrogated by the NOPA, and its limited bandwidth. This makes it difficult to study systems in which the donor and the acceptor electronic transitions are located at substantially different energies, or molecules whose transitions are centred around 800 nm, such as the porphyrin nanorings studied in Chapters 7 and 8. Moreover, the use of spectrally broader pulses, if such pulses are transform limited, translates as improved time resolution in the experiment, which can make possible observation of, for example, fast relaxations or electronic coherences dephasing in tens of fs.[243]
In the recent years, a number of alternatives to NOPAs, such as supercontinuum generation in YAG crystals,[244] filamentation in gas filled chambers,[245;246] and hollow core fiber compressors[247] have been shown to be good ultrabroadband candidate light sources for a 2D-ES experiment. Such light sources can produce outputs which span more than an octave across the whole visible spectrum, and extend to the near UV and have sub-5 fs duration.[248]
In Chapter 2 we have shown how, both vibronic and excitonic, ground and excited state coherences, will appear at different position of the excitation-emission plane in rephasing and non rephasing spectra, making their assignment much easier. The only way of experimentally separating rephasing and non rephasing contributions, when working with such broad pulses, is to use a 2D spectrometer in a fully-noncollinear (BOXCAR) fashion. This stems from the fact that the phase-cycling

procedure, which is normally employed in collinear setups to separate the Absorptive signal in its rephasing and non rephasing components,[73;74] requires the use of pulse shapers or acousto-optic modulators which do not have enough operational bandwidth to process the whole white light spectrum.[100;101;103] Consequently, it follows that our 2D setup, whose design and working principle have been extensively described in Chapter 4, could be transformed into a ultra broadband two-dimensional spectrometer, by replacing the NOPA with a broadband light source, such as an hollow-core fiber based compressor filled with noble gases. To manage the higher dispersion of such broad pulses, the folded prism compressor will have to be replaced with two pairs of chirped mirrors, which allow compensation for higher order dispersion, critical in order to obtain sub-5 fs resolution.[247;248]

An alternative approach which allows relatively straightforward implementation of two-dimensional electronic spectroscopy, with broadband detection, is the conversion of a fsTA setup, such as the one described in Chapter 3, into a 2D-ES collinear spectrometer. This can be done placing an extra component, such as a acousto-optical modulator or an interferometer,[100;103;249] in the pump optical path of a TA experiment, like the one depicted in Figure 3.1. The purpose of the extra optical component is to reshape the single pump pulse used in a fsTA experiment into a pair of (collinear) pump pulses, with controllable interpulse delay (interferometer)[100] or delay and relative phase (acousto-optic modulator).[101;103] As usual, Fourier transforming over the time delay between the pair of pump pulses will yield the excitation frequencies, while the relative phase control allows separation of rephasing and non rephasing components, using a phase-cycling algorithm.[70]

As a probe pulse, it is possible to use the same continuum white light, generated focusing a fraction of the fundamental of the Ti:Sa amplifier at 800 nm (or parametric light at 1200 nm) onto a sapphire window, as has been described in Chapter 3 for fsTA and fsTAn experiments. A chirp removal procedure, analogous to the one explained in Chapter 3, can be used to correct for white light dispersion in 2D spectra as well, lifting the need to work with recompressed probe pulses.[91;101]

Both of the 2D spectrometers discussed above could be obtained with relatively simple modifications of the setups which are already existing and currently used in our lab, and these upgrades are among the experimental developments planned for the future.

Excitonic Coherences in μ-Subphthalocyanine Dimers

One of the main driving forces behind the development of 2D-ES has been the study of systems in which coupling between vibrational and/or electronic degrees of freedom can alter their optical and electronic properties. While a considerable amount of effort has been exerted by various groups in studying the nature of such couplings in large, supramolecular systems of biological interest,[4;25;75;76;240;250;251] only

a few investigations on dimers with excitonic character have been carried out so far.[32;149;252;253]

J-dimers, such as the PBI dimers we studied in Chapter 5, due to their geometry, can only have an allowed transition to the bottom, in-phase, exciton state, while the transition to the higher energy, out-of-phase state will be completely dark, according to Kasha's model for coupled dyes.[80] The same model predicts that in the case of H-dimers, such as slip-stacked perylene bisimides,[254;255] only transitions to the higher-lying state will be allowed. Thus, in both the extreme cases of head-to-tail (J-) or face-to-face (H-) dimers, it is impossible to use broadband laser pulses to prepare coherent superpositions of excitonic states, which will eventually generate quantum beats during T. Hence, it is interesting to study dimers with intermediate geometries between the J- and the H-dimer limit cases, which will have allowed transitions to both the in-phase and the out-of-phase exciton states.

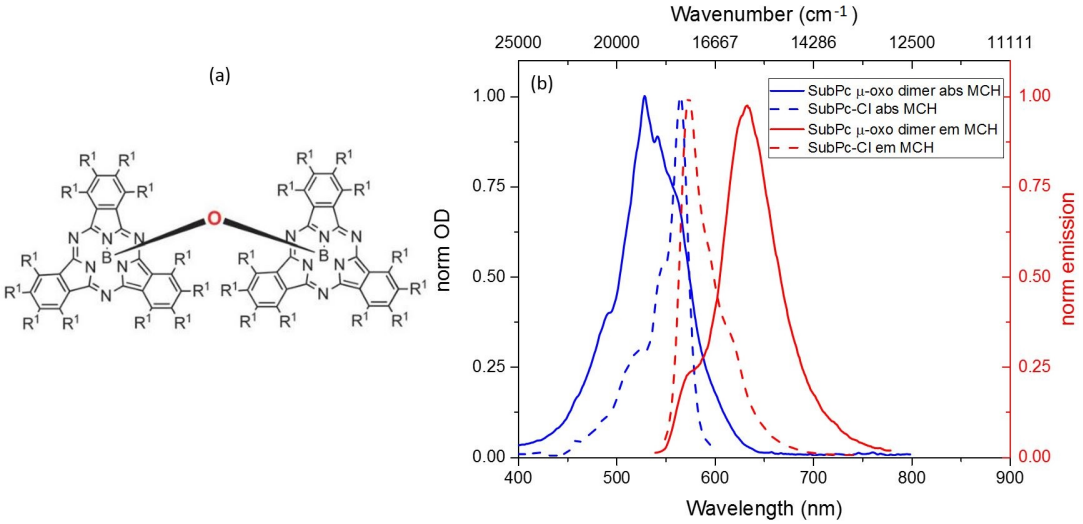

Figure 9.1: (a) molecular structure of the SubPc μ-oxo dimer reprinted from Guilleme *et al.*[256] and (b) normalised steady-state absorption (blue) and emission (red, excitation at 530 nm) spectra of SubPc-Cl (dashed lines) and SubPc μ-oxo dimer (solid lines) in methylcyclohexane.

Among the classes of organic dyes, subphtalocyanines have unique structural and optical characteristics, which have been briefly reviewed in Chapter 6. Such properties make them interesting model systems with relatively unexplored photophysics and photodynamics, if compared, for example, to the much more widely studied porphyrin-based systems (see Chapters 7 and 8). For this reason we are interested in studying the transient behaviour of the μ-oxo bridged subphthalocyanine dimer shown in Figure 9.1(a) by fsTA and 2D-ES, whose steady-state normalised absorption and emission spectra are contrasted with the monomer in Figure 9.1(b). The maximum of the absorption spectrum of the μ-oxo dimer (solid blue line) is shifted to the blue, but also broadened to the low energy side, if compared to SubPc-Cl

(dashed blue line), indicating the presence of new transitions due to excitonic coupling in the dimer. Further proofs of excited state interactions between the two SubPc units in the μ-oxo dimer are given by the large Stokes shift observed in the dimer fluorescence spectrum (solid red line) if compared to SubPc-Cl (dashed red line), and by a three-fold decrease in its quantum yield[256] (0.08 for the dimer, 0.25 for SubPc-Cl). Details on the mechanism of the excitonic coupling, and on how molecular vibrations, environment polarity and structural dynamics can affect its strength and timescale will be inferred through fsTA and 2D-ES measurements carried out in a variety of solvents and at different temperatures.

Bibliography

[1] A. H. Zewail, *The Journal of Physical Chemistry A*, 2000, **104**, 5660–5694.

[2] P. H. Bucksbaum, *Nature*, 2003, **421**, 593–594.

[3] P. Agostini and L. F. DiMauro, *Reports on Progress in Physics*, 2004, **67**, 813–855.

[4] E. Thyrhaug, C. N. Lincoln, F. Branchi, G. Cerullo, V. Perlík, F. Šanda, H. Lokstein and J. Hauer, *Photosynthesis Research*, 2018, **135**, 45–54.

[5] G. Cerullo, C. Manzoni, L. Lüer and D. Polli, *Photochem. Photobiol. Sci.*, 2007, **6**, 135–144.

[6] R. J. Hafner, L. Tian, J. C. Brauer, T. Schmaltz, A. Sienkiewicz, S. Balog, V. Flauraud, J. Brugger and H. Frauenrath, *ACS Nano*, 2018, **12**, 9116–9125.

[7] A. De Sio and C. Lienau, *Phys. Chem. Chem. Phys.*, 2017, **19**, 18813–18830.

[8] I. A. Heisler and S. R. Meech, *Journal of Physical Chemistry B*, 2008, **112**, 12976–12984.

[9] J. Conyard, K. Addison, I. A. Heisler, A. Cnossen, W. R. Browne, B. L. Feringa and S. R. Meech, *Nature Chemistry*, 2012, **4**, 547–551.

[10] M. Maiuri, E. E. Ostroumov, R. G. Saer, R. E. Blankenship and G. D. Scholes, *Nature Chemistry*, 2018, **10**, 177–183.

[11] F. V. A. Camargo, H. L. Anderson, S. R. Meech and I. A. Heisler, *Journal of Physical Chemistry B*, 2015, **119**, 14660–14667.

[12] A. Gelzinis, R. Augulis, V. Butkus, B. Robert and L. Valkunas, *Biochimica et Biophysica Acta - Bioenergetics*, 2019, **1860**, 271–285.

[13] R. F. Loring and S. Mukamel, *The Journal of Chemical Physics*, 1987, **87**, 1272–1283.

[14] D. M. Jonas, *Annual Review of Physical Chemistry*, 2003, **54**, 425–463.

[15] N. Ginsberg, Y. Cheng and G. Fleming, *Accounts of Chemical Research*, 2009, **42**, 1352–63.

[16] W. P. Aue, E. Bartholdi and Ernst, *The Journal of Chemical Physics*, 1976, **64**, 2229–2246.

[17] J. D. Hybl, A. W. Albrecht, S. M. Gallagher Faeder and D. M. Jonas, *Chemical Physics Letters*, 1998, **297**, 307–313.

[18] P. Hamm, M. Lim and R. M. Hochstrasser, *Journal of Physical Chemistry B*, 1998, **102**, 6123–6138.

[19] Y. S. Kim and R. M. Hochstrasser, *Journal of Physical Chemistry B*, 2009, **113**, 8231–8251.

[20] L. Bolzonello, F. Fassioli and E. Collini, *The Journal of Physical Chemistry Letters*, 2016, **7**, 4996–5001.

[21] C. N. Borca, T. Zhang, X. Li and S. T. Cundiff, *Chemical Physics Letters*, 2005, **416**, 311–315.

[22] K. W. Stone, K. Gundogdu, D. B. Turner, X. Li, S. T. Cundiff and K. A. Nelson, *Science*, 2009, **324**, 1169–1174.

[23] G. Nardin, G. Moody, R. Singh, T. M. Autry, H. Li, F. Morier-Genoud and S. T. Cundiff, *Physical Review Letters*, 2014, **112**, 1–6.

[24] E. Meneghin, A. Volpato, L. Cupellini, L. Bolzonello, S. Jurinovich, V. Mascoli, D. Carbonera, B. Mennucci and E. Collini, *Nature Communications*, 2018, **9**, 1–9.

[25] T. Brixner, J. Stenger, H. M. Vaswani, M. Cho, R. E. Blankenship and G. R. Fleming, *Nature*, 2005, **434**, 625–628.

[26] C. Lambert, F. Koch, S. F. Völker, A. Schmiedel, M. Holzapfel, A. Humeniuk, M. I. S. Röhr, R. Mitric and T. Brixner, *Journal of the American Chemical Society*, 2015, **137**, 7851–7861.

[27] A. Nemeth, F. Milota, T. Mančal, V. Lukeš, J. Hauer, H. F. Kauffmann and J. Sperling, *The Journal of Chemical Physics*, 2010, **132**, 184514.

[28] M. Cho, *Chemical Reviews*, 2008, **108**, 1331–1418.

[29] H. Li and S. T. Cundiff, *2D Coherent Spectroscopy of Electronic Transitions*, Elsevier Inc., 1st edn., 2017, pp. 1–48.

[30] F. V. de A. Camargo, L. Grimmelsmann, H. L. Anderson, S. R. Meech and I. A. Heisler, *Physical Review Letters*, 2017, **118**, 033001.

[31] V. Butkus, J. Alster, E. Bašinskaite, R. Augulis, P. Neuhaus, L. Valkunas, H. L. Anderson, D. Abramavicius and D. Zigmantas, *Journal of Physical Chemistry Letters*, 2017, **8**, 2344–2349.

[32] A. Halpin, P. J. M. Johnson, R. Tempelaar, R. S. Murphy, J. Knoester, T. L. C. Jansen and R. J. D. Miller, *Nature chemistry*, 2014, **6**, 196–201.

[33] D. Zigmantas, E. L. Read, T. Mancal, T. Brixner, A. T. Gardiner, R. J. Cogdell and G. R. Fleming, *Proceedings of the National Academy of Sciences of the United States of America*, 2006, **103**, 12672–7.

[34] G. S. Schlau-Cohen, T. R. Calhoun, N. S. Ginsberg, E. L. Read, M. Ballottari, R. Bassi, R. van Grondelle and G. R. Fleming, *The Journal of Physical Chemistry B*, 2009, **113**, 15352–15363.

[35] J. Dostál, T. Mančal, R.-n. Augulis, F. Vácha, J. Pšenčík and D. Zigmantas, *Journal of the American Chemical Society*, 2012, **134**, 11611–11617.

[36] E. E. Ostroumov, R. M. Mulvaney, R. J. Cogdell and G. D. Scholes, *Science*, 2013, **340**, 52–56.

[37] E. Thyrhaug, K. Žídek, J. Dostál, D. Bína and D. Zigmantas, *The Journal of Physical Chemistry Letters*, 2016, **7**, 1653–1660.

[38] H.-G. Duan, A. L. Stevens, P. Nalbach, M. Thorwart, V. I. Prokhorenko and R. J. Dwayne Miller, *The Journal of Physical Chemistry B*, 2015, **119**, 12017–12027.

[39] F. Milota, J. Sperling, A. Nemeth, T. Mancal and H. F. Kauffmann, *Accounts of chemical research*, 2009, **42**, 1364–1374.

[40] F. Koch, A. Steinbacher, C. Consani, A. Zitzler-Kunkel, M. Stolte, F. Würthner and T. Brixner, *Physical Chemistry Chemical Physics*, 2016, **18**, 19820–19831.

[41] B. Kudisch, M. Maiuri, V. M. Blas-Ferrando, J. Ortiz, A. Sastre-Santos and G. Scholes, *Phys. Chem. Chem. Phys.*, 2017, **19**, 21078–21089.

[42] V. Tiwari, W. K. Peters and D. M. Jonas, *Proceedings of the National Academy of Sciences*, 2013, **110**, 1203–1208.

[43] K. L. Wells, P. H. Lambrev, Z. Zhang, G. Garab and H.-S. Tan, *Phys. Chem. Chem. Phys.*, 2014, **16**, 11640–11646.

[44] D. Sun, Y. Rao, G. A. Reider, G. Chen, Y. You, L. Brézin, A. R. Harutyunyan and T. F. Heinz, *Nano Letters*, 2014, **14**, 5625–5629.

[45] F. Ma, *Journal of Physical Chemistry B*, 2018, **122**, 10746–10753.

[46] G. Soavi, S. Dal Conte, C. Manzoni, D. Viola, A. Narita, Y. Hu, X. Feng, U. Hohenester, E. Molinari, D. Prezzi, K. Müllen and G. Cerullo, *Nature Communications*, 2016, **7**, 11010.

[47] E. Engel, K. Leo and M. Hoffmann, *Chemical Physics*, 2006, **325**, 170–177.

[48] A. E. Johnson, S. Kumazaki and K. Yoshihara, *Chemical Physics Letters*, 1993, **211**, 511–515.

[49] H. Marciniak, X. Q. Li, F. Würthner and S. Lochbrunner, *Journal of Physical Chemistry A*, 2011, **115**, 648–654.

[50] F. Fennel and S. Lochbrunner, *Physical Review B - Condensed Matter and Materials Physics*, 2015, **92**, 1–5.

[51] S. Wolter, J. Aizezers, F. Fennel, M. Seidel, F. Würthner, O. Kühn and S. Lochbrunner, *New Journal of Physics*, 2012, **14**, 105027.

[52] Y.-Z. Ma, R. J. Cogdell and T. Gillbro, *The Journal of Physical Chemistry B*, 1997, **101**, 1087–1095.

[53] T. Bittner, K.-D. Irrgang, G. Renger and M. R. Wasielewski, *The Journal of Physical Chemistry*, 2002, **98**, 11821–11826.

[54] V. May, *The Journal of Chemical Physics*, 2014, **140**, 054103.

[55] I. V. Ryzhov, G. G. Kozlov, V. A. Malyshev and J. Knoester, *Journal of Chemical Physics*, 2001, **114**, 5322–5329.

[56] K. Hader, C. Consani, T. Brixner and V. Engel, *Physical Chemistry Chemical Physics*, 2017, **19**, 31989–31996.

[57] H. Marciniak, X. Q. Li, F. Würthner and S. Lochbrunner, *Journal of Physical Chemistry A*, 2011, **115**, 648–654.

[58] F. Cohen-Tannoudji C.;Diu, B.; Laloe, *Quantum Mechanics, Vol. 1*, 1991.

[59] J. J. Sakurai, *Modern Quantum Mechanics*, Addison-Wesley, 1994, p. 568.

[60] J. D. Jackson, *Classical Electrodynamics*, Wiley, 3rd edn., 1962, p. 641.

[61] R. Kubo, *Statistical Mechanics: An Advanced Course with Problems and Solutions*, North Holland, 1998.

[62] K. Blum, *Density Matrix Theory and Applications*, Springer US, 2011.

[63] R. W. Boyd, in *Nonlinear Optics*, Elsevier, 2003, pp. 533–559.

[64] L. Valkunas, D. Abramavicius and T. Mancal, *Molecular Excitation Dynamics and Relaxation*, Wiley-VCH, 2013.

[65] J.-C. Diels and W. Rudolph, *Ultrashort Laser Pulse Phenomena: Fundamentals, Techniques, and Applications on a Femtosecond Timescale*, Academic Press, 2006.

[66] S. Mukamel, *Principles of Nonlinear Optical Spectroscopy*, Oxford University Press, New York, 1995, p. 576.

[67] P. Hamm and M. Zanni, *Concepts and Methods of 2D Infrared Spectroscopy*, Cambridge University Press, Cambridge, 2011, vol. 1, p. 286.

[68] G. S. Schlau-Cohen, A. Ishizaki and G. R. Fleming, *Chemical Physics*, 2011, **386**, 1–22.

[69] J. O. Tollerud and J. A. Davis, *Progress in Quantum Electronics*, 2017, **55**, 1–34.

[70] F. D. Fuller and J. P. Ogilvie, *Annual review of physical chemistry*, 2015, **66**, 667–90.

[71] T. A. A. Oliver, *Royal Society Open Science*, 2018, **5**, 171425.

[72] I. A. Heisler, R. Moca, F. V. A. Camargo and S. R. Meech, *Review of Scientific Instruments*, 2014, **85**, 063103.

[73] M. Khalil, N. Demirdöven and A. Tokmakoff, *Journal of Physical Chemistry A*, 2003, **107**, 5258–5279.

[74] S. H. Shim and M. T. Zanni, *Physical Chemistry Chemical Physics*, 2009, **11**, 748–761.

[75] G. D. Scholes, G. R. Fleming, L. X. Chen, A. Aspuru-Guzik, A. Buchleitner, D. F. Coker, G. S. Engel, R. van Grondelle, A. Ishizaki, D. M. Jonas, J. S. Lundeen, J. K. McCusker, S. Mukamel, J. P. Ogilvie, A. Olaya-Castro, M. A. Ratner, F. C. Spano, K. B. Whaley and X. Zhu, *Nature*, 2017, **543**, 647–656.

[76] G. D. Scholes, *The Journal of Physical Chemistry Letters*, 2010, **1**, 2–8.

[77] J. M. Benoit, J. P. Buisson, O. Chauvet, C. Godon and S. Lefrant, *Physical Review B - Condensed Matter and Materials Physics*, 2002, **66**, 1–4.

[78] P. C. Painter, L. E. Mosher and C. Rhoads, *Biopolymers*, 1982, **21**, 1469–1472.

[79] V. Butkus, L. Valkunas and D. Abramavicius, *The Journal of Chemical Physics*, 2012, **137**, 44513.

[80] M. Kasha, *Radiation Research*, 1963, **20**, 55–70.

[81] Y.-C. Cheng and G. R. Fleming, *The Journal of Physical Chemistry A*, 2008, **112**, 4254–4260.

[82] E. Cassette, R. D. Pensack, B. Mahler and G. D. Scholes, *Nature Communications*, 2015, **6**, 6086.

[83] V. Sundström, *Annual Review of Physical Chemistry*, 2008, **59**, 53–77.

[84] P. J. M. Johnson, M. H. Farag, A. Halpin, T. Morizumi, V. I. Prokhorenko, J. Knoester, T. L. C. Jansen, O. P. Ernst and R. J. D. Miller, *The Journal of Physical Chemistry B*, 2017, **121**, 4040–4047.

[85] J. Cabanillas-Gonzalez, G. Grancini and G. Lanzani, *Advanced Materials*, 2011, **23**, 5468–5485.

[86] R. Berera, R. van Grondelle and J. T. M. Kennis, *Photosynthesis Research*, 2009, **101**, 105–118.

[87] G. Cerullo, D. Polli, G. Lanzani, S. De Silvestri, H. Hashimoto and R. J. Cogdell, *Science*, 2002, **298**, 2395 LP – 2398.

[88] S. A. Kovalenko, A. L. Dobryakov, J. Ruthmann and N. P. Ernsting, *Physical Review A*, 1999, **59**, 2369–2384.

[89] Y.-Z. Ma, R. J. Cogdell and T. Gillbro, *The Journal of Physical Chemistry B*, 1997, **101**, 1087–1095.

[90] R. Trebino, K. DeLong, D. Fittinghoff, J. Sweetser, M. Krumbuegel, B. Richman and D. Kane, *Review of Scientific Instruments*, 1997, **68**, 3277.

[91] P. A. Tekavec, K. L. Lewis, F. D. Fuller, J. A. Myers and J. P. Ogilvie, *IEEE Journal on Selected Topics in Quantum Electronics*, 2012, **18**, 210–217.

[92] K. Wynne and R. M. Hochstrasser, *Journal of Raman Spectroscopy*, 1995, **26**, 561–569.

[93] S. I. E. Vulto, A. M. Streltsov and T. J. Aartsma, *The Journal of Physical Chemistry B*, 1997, **101**, 4845–4850.

[94] R. van Grondelle and V. I. Novoderezhkin, *Phys. Chem. Chem. Phys.*, 2006, **8**, 793–807.

[95] I. H. Van Stokkum, D. S. Larsen and R. Van Grondelle, *Biochimica et Biophysica Acta - Bioenergetics*, 2004, **1657**, 82–104.

[96] J. J. Snellenburg, S. P. Laptenok, R. Seger, K. M. Mullen and I. H. M. v. Stokkum, *Journal of Statistical Software*, 2012, **49**, 1–22.

[97] N. Krebs, I. Pugliesi, J. Hauer and E. Riedle, *New Journal of Physics*, 2013, **15**, 085016.

[98] C. Consani, G. Aubock, F. van Mourik and M. Chergui, *Science*, 2013, **339**, 1586–1589.

[99] T. Brixner, T. Mančal, I. V. Stiopkin and G. R. Fleming, *The Journal of Chemical Physics*, 2004, **121**, 4221–4236.

[100] J. Réhault, M. Maiuri, A. Oriana and G. Cerullo, *Review of Scientific Instruments*, 2014, **85**, 123107.

[101] P. F. Tekavec, J. A. Myers, K. L. M. Lewis and J. P. Ogilvie, *Optics Letters*, 2009, **34**, 1390–1392.

[102] H. S. Tan, *Journal of Chemical Physics*, 2008, **129**, 124501–124514.

[103] E. M. Grumstrup, S.-H. Shim, M. A. Montgomery, N. H. Damrauer and M. T. Zanni, *Optics Express*, 2007, **15**, 16681.

[104] D. B. Turner, *Results in Chemistry*, 2019, **1**, 100001.

[105] T. A. Gellen, L. A. Bizimana, W. P. Carbery, I. Breen and D. B. Turner, *The Journal of Chemical Physics*, 2016, **145**, 064201.

[106] S. Mueller, S. Draeger, X. Ma, M. Hensen, T. Kenneweg, W. Pfeiffer and T. Brixner, *Journal of Physical Chemistry Letters*, 2018, **9**, 1964–1969.

[107] U. Selig, C.-F. Schleussner, M. Foerster, F. Langhojer, P. Nuernberger and T. Brixner, *Optics Letters*, 2010, **35**, 4178–4180.

[108] M. L. Cowan, J. P. Ogilvie and R. J. Miller, *Chemical Physics Letters*, 2004, **386**, 184–189.

[109] U. Megerle, I. Pugliesi, C. Schriever, C. F. Sailer and E. Riedle, *Applied Physics B: Lasers and Optics*, 2009, **96**, 215–231.

[110] W. Xiong, D. B. Strasfeld, S. H. Shim and M. T. Zanni, *Vibrational Spectroscopy*, 2009, **50**, 136–142.

[111] R. Augulis and D. Zigmantas, *Optics Express*, 2011, **19**, 13126.

[112] M. Khalil, N. Demirdöven and A. Tokmakoff, *Physical Review Letters*, 2003, **90**, 047401.

[113] U. Selig, F. Langhojer, F. Dimler, T. Löhrig, C. Schwarz, B. Gieseking and T. Brixner, *Optics Letters*, 2008, **33**, 2851.

[114] S. M. Gallagher Faeder and D. M. Jonas, *The Journal of Physical Chemistry A*, 1999, **103**, 10489–10505.

[115] Q. Zhao, S. Zhang, Y. Liu, J. Mei, S. Chen, P. Lu, A. Qin, Y. Ma, J. Z. Sun and B. Z. Tang, *Journal of Materials Chemistry*, 2012, **22**, 7387–7394.

[116] F. Würthner, *Pure and Applied Chemistry*, 2006, **78**, 2341–2349.

[117] M. R. Wasielewski, *Accounts of Chemical Research*, 2009, **42**, 1910–1921.

[118] C. Hippius, F. Schlosser, M. O. Vysotsky, V. Bhmer, F. Wrthner, V. Bo and F. Wu, *Journal of the American Chemical Society*, 2006, **128**, 3870–3871.

[119] R. Pandya, R. W. MacQueen, A. Rao and N. J. L. K. Davis, *The Journal of Physical Chemistry C*, 2018, **122**, 22330–22338.

[120] L. Zang, R. Liu, M. W. Holman, K. T. Nguyen and D. M. Adams, *Journal of the American Chemical Society*, 2002, **124**, 10640–10641.

[121] T. Takada, S. Ishino, A. Takata, M. Nakamura, M. Fujitsuka, T. Majima and K. Yamana, *Chemistry - A European Journal*, 2018, **24**, 8228–8232.

[122] S. W. Eaton, L. E. Shoer, S. D. Karlen, S. M. Dyar, E. A. Margulies, B. S. Veldkamp, C. Ramanan, D. A. Hartzler, S. Savikhin, T. J. Marks and M. R. Wasielewski, *Journal of the American Chemical Society*, 2013, **135**, 14701–14712.

[123] C. Ramanan, A. L. Smeigh, J. E. Anthony, T. J. Marks and M. R. Wasielewski, *Journal of the American Chemical Society*, 2012, **134**, 386–397.

[124] K. Sugiyasu, N. Fujita and S. Shinkai, *Angewandte Chemie - International Edition*, 2004, **43**, 1229–1233.

[125] Y. Huang, Z. Xu, S. Jin, C. Li, K. Warncke, F. A. Evangelista, T. Lian and E. Egap, *Chemistry of Materials*, 2018, **30**, 7840–7851.

[126] B. Wang and C. Yu, *Angewandte Chemie - International Edition*, 2010, **49**, 1485–1488.

[127] X. Feng, Y. An, Z. Yao, C. Li and G. Shi, *ACS Applied Materials and Interfaces*, 2012, **4**, 614–618.

[128] C. Kufazvinei, M. Ruether, J. Wang and W. Blau, *Organic Electronics: physics, materials, applications*, 2009, **10**, 674–680.

[129] E. O. Potma and D. A. Wiersma, *Journal of Chemical Physics*, 1998, **108**, 4894.

[130] F. Würthner, C. R. Saha-Möller, B. Fimmel, S. Ogi, P. Leowanawat and D. Schmidt, *Chemical Reviews*, 2016, **116**, 962–1052.

[131] T. Brixner, R. Hildner, J. Köhler, C. Lambert and F. Würthner, *Advanced Energy Materials*, 2017, **1700236**, 1–33.

[132] K. E. Brown, W. A. Salamant, L. E. Shoer, R. M. Young and M. R. Wasielewski, *Journal of Physical Chemistry Letters*, 2014, **5**, 2588–2593.

[133] F. P. Diehl, C. Roos, A. Duymaz, B. Lunkenheimer, A. Köhn and T. Basché, *Journal of Physical Chemistry Letters*, 2014, **5**, 262–269.

[134] K. Balakrishnan, A. Datar, T. Naddo, J. Huang, R. Oitker, M. Yen, J. Zhao and L. Zang, *Journal of the American Chemical Society*, 2006, **128**, 7390–7398.

[135] J. Sung, P. Kim, B. Fimmel, F. Würthner and D. Kim, *Nature communications*, 2015, **6**, 8646.

[136] N. J. Hestand and F. C. Spano, *Chemical Reviews*, 2018, **118**, 7069–7163.

[137] H. Fidder, J. Knoester and D. A. Wiersma, *Chemical Physics Letters*, 1990, **171**, 529–536.

[138] J. R. Durrant, J. Knoester and D. A. Wiersma, *Chemical Physics Letters*, 1994, **222**, 450–456.

[139] H. Fidder, J. Knoester and D. A. Wiersma, *Journal of Chemical Physics*, 1993, **98**, 6564.

[140] F. Milota, V. I. Prokhorenko, T. Mancal, H. Von Berlepsch, O. Bixner, H. F. Kauffmann and J. Hauer, *Journal of Physical Chemistry A*, 2013, **117**, 6007–6014.

[141] A. Anda, D. Abramavičius and T. Hansen, *Physical Chemistry Chemical Physics*, 2018, 1642–1652.

[142] F. Fassioli, R. Dinshaw, P. C. Arpin and G. D. Scholes, *Journal of The Royal Society Interface*, 2014, **11**, 20130901.

[143] U. Selig, P. Nuernberger, V. Dehm, V. Settels, M. Gsänger, B. Engels, F. Würthner and T. Brixner, *ChemPhysChem*, 2013, **14**, 1413–1422.

[144] H. Langhals and W. Jona, *Angewandte Chemie - International Edition*, 1998, **37**, 952–955.

[145] A. Wicklein, A. Lang, M. Muth and M. Thelakkat, *Journal of the American Chemical Society*, 2009, **131**, 14442–14453.

[146] L. D. Wescott and D. L. Mattern, *Journal of Organic Chemistry*, 2003, **68**, 10058–10066.

[147] A. E. Clark, C. Qin and A. D. Q. Li, *Journal of the American Chemical Society*, 2007, **129**, 7586–7595.

[148] N. J. Hestand and F. C. Spano, *Chemical Reviews*, 2018, **118**, 7069–7163.

[149] G. Bressan, D. Green, Y. Chan, P. C. Bulman Page, G. A. Jones, S. R. Meech and I. A. Heisler, *The Journal of Physical Chemistry A*, 2019, **123**, 1594–1601.

[150] P. Kjellberg, B. Brüggemann and T. Pullerits, *Physical Review B - Condensed Matter and Materials Physics*, 2006, **74**, 1–9.

[151] D. R. Lide, *CRC Handbook of Chemistry and Physics*, CRC Press, New York, 85th edn., 2004.

[152] G. Bressan, D. Green, Y. Chan, P. Bulman Page, G. Jones, S. Meech and I. Heisler, *The Journal of Physical Chemistry A*, **123**, 1594 – 1601.

[153] D. Green, F. V. A. Camargo, I. A. Heisler, A. G. Dijkstra and G. A. Jones, *The Journal of Physical Chemistry A*, 2018, **122**, 6206–6213.

[154] R. Moca, S. R. Meech and I. A. Heisler, *Journal of Physical Chemistry B*, 2015, **119**, 8623–8630.

[155] D. Gust, T. A. Moore and A. L. Moore, *Accounts of Chemical Research*, 1993, **26**, 198–205.

[156] P. D. Frischmann, K. Mahata and F. Würthner, *Chemical Society Reviews*, 2013, **42**, 1847–1870.

[157] R. K. Garner, D. S. Josey, S. R. Nyikos, A. Dovijarski, J. M. Wang, G. J. Evans and T. P. Bender, *Solar Energy Materials and Solar Cells*, 2018, **176**, 331–335.

[158] O. G. Reid, R. D. Pensack, Y. Song, G. D. Scholes and G. Rumbles, *Chemistry of Materials*, 2014, **26**, 561–575.

[159] L. Alfonso Hernandez, T. Nelson, S. Tretiak and S. Fernandez-Alberti, *Journal of Physical Chemistry B*, 2015, **119**, 7242–7252.

[160] L. Feng, M. Rudolf, O. Trukhina, Z. Slanina, F. Uhlik, X. Lu, T. Torres, D. M. Guldi and T. Akasaka, *Chemical Communications*, 2015, **51**, 330–333.

[161] T. S. Balaban, *Accounts of Chemical Research*, 2005, **38**, 612–623.

[162] L. M. Günther, M. Jendrny, E. A. Bloemsma, M. Tank, G. T. Oostergetel, D. A. Bryant, J. Knoester and J. Köhler, *Journal of Physical Chemistry B*, 2016, **120**, 5367–5376.

[163] L. Bolzonello, F. Fassioli and E. Collini, *The Journal of Physical Chemistry Letters*, 2016, **7**, 4996–5001.

[164] J. K. Sprafke, D. V. Kondratuk, M. Wykes, A. L. Thompson, M. Hoffmann, R. Drevinskas, W.-H. Chen, C. K. Yong, J. Kärnbratt, J. E. Bullock, M. Malfois, M. R. Wasielewski, B. Albinsson, L. M. Herz, D. Zigmantas, D. Beljonne and H. L. Anderson, *Journal of the American Chemical Society*, 2011, **133**, 17262–17273.

[165] J. Cremers, R. Haver, M. Rickhaus, J. Q. Gong, L. Favereau, M. D. Peeks, T. D. W. Claridge, L. M. Herz and H. L. Anderson, *Journal of the American Chemical Society*, 2018, **140**, 5352–5355.

[166] N. Algethami, H. Sadeghi, S. Sangtarash and C. J. Lambert, *Nano Letters*, 2018, **18**, 4482–4486.

[167] S. Abdulalmohsin and J. B. Cui, *Journal of Physical Chemistry C*, 2012, **116**, 9433–9438.

[168] O. Birel, S. Nadeem and H. Duman, *Journal of Fluorescence*, 2017, **27**, 1075–1085.

[169] Y. Chen, A. Li, Z.-H. Huang, L.-N. Wang and F. Kang, *Nanomaterials*, 2016, **6**, 51.

[170] P. Liao, Y. Hu, Z. Liang, J. Zhang, H. Yang, L. Q. He, Y. X. Tong, J. M. Liu, L. Chen and C. Y. Su, *Journal of Materials Chemistry A*, 2018, **6**, 3195–3201.

[171] M. Gouterman, *Journal of Molecular Spectroscopy*, 1961, **6**, 138–163.

[172] J. S. Baskin, H. Z. Yu and A. H. Zewail, *Journal of Physical Chemistry A*, 2002, **106**, 9837–9844.

[173] H. Z. Yu, J. S. Baskin and A. H. Zewail, *Journal of Physical Chemistry A*, 2002, **106**, 9845–9854.

[174] J. R. Cole and N. J. Halas, *Applied Physics Letters*, 2006, **89**, 28–31.

[175] D. Gonzalez-Rodríguez, T. Torres, M. M. Olmstead, J. Rivera, M. A. Herranz, L. Echegoyen, C. A. Castellanos and D. M. Guldi, *Journal of the American Chemical Society*, 2006, **128**, 10680–10681.

[176] J. S. Lissau, A. Viñas Muñoz, H. Gotfredsen, M. Jevric, M. B. Nielsen and T. I. Sølling, *The Journal of Physical Chemistry A*, 2018, **122**, 6683–6692.

[177] A. V. Munoz, H. Gotfredsen, M. Jevric, A. Kadziola, O. Hammerich and M. B. Nielsen, *Journal of Organic Chemistry*, 2018, **83**, 2227–2234.

[178] K. A. Winterfeld, G. Lavarda, J. Guilleme, M. Sekita, D. M. Guldi, T. Torres and G. Bottari, *Journal of the American Chemical Society*, 2017, **139**, 5520–5529.

[179] C. Azarias, M. Pawelek and D. Jacquemin, *The Journal of Physical Chemistry A*, 2017, **121**, 4306–4317.

[180] M. V. Fulford, D. Jaidka, A. S. Paton, G. E. Morse, E. R. Brisson, A. J. Lough and T. P. Bender, *Journal of Chemical and Engineering Data*, 2012, **57**, 2756–2765.

[181] C. G. Claessens, D. González-Rodríguez and T. Torres, *Chemical Reviews*, 2002, **102**, 835–853.

[182] A. Osuka, Y. Bekki, D. Shimizu and K. Fujimoto, *Chemistry - A European Journal*, 2018, 12708–12715.

[183] G. E. Morse, J. S. Castrucci, M. G. Helander, Z. H. Lu and T. P. Bender, *ACS Applied Materials and Interfaces*, 2011, **3**, 3538–3544.

[184] M. G. Helander, G. E. Morse, J. Qiu, J. S. Castrucci, T. P. Bender and Z. H. Lu, *ACS Applied Materials and Interfaces*, 2010, **2**, 3147–3152.

[185] B. Del Rey, U. Keller, T. Torres, G. Rojo, F. Agulló-López, S. Nonell, C. Martí, S. Brasselet, I. Ledoux and J. Zyss, *Journal of the American Chemical Society*, 1998, **120**, 12808–12817.

[186] M. Managa, J. Mack, D. Gonzalez-Lucasb, S. Remiro-Buenamañana, C. Tshangana, A. N. Cammidge and T. Nyokong, *Journal of Porphyrins and Phthalocyanines*, 2016, **20**, 1–20.

[187] A. Harriman, G. Porter and N. Searle, *Journal of the Chemical Society, Faraday Transactions 2: Molecular and Chemical Physics*, 1979, **75**, 1515–1521.

[188] M. E. El-Khouly, *Physical Chemistry Chemical Physics*, 2010, **12**, 12746–12752.

[189] M. Obłoza, Ł. Łapok, J. Solarski, T. Pędziński and M. Nowakowska, *Chemistry – A European Journal*, 2018, **24**, 17080–17090.

[190] V. A. Walters, J. C. De Paula, B. Jackson, C. Nutaitis, K. Hall, J. Lind, K. Cardozo, K. Chandran, D. Raible and C. M. Phillips, *Journal of Physical Chemistry*, 1995, **99**, 1166–1171.

[191] K. J. McEwan, G. Bourhill, J. M. Robertson and H. L. Anderson, *Journal of Nonlinear Optical Physics & Materials*, 2000, **09**, 451–468.

[192] A. F. Fidler, E. Harel, P. D. Long and G. S. Engel, *Journal of Physical Chemistry A*, 2012, **116**, 282–289.

[193] F. Šanda, V. Perlík, C. N. Lincoln and J. Hauer, *Journal of Physical Chemistry A*, 2015, **119**, 10893–10909.

[194] R. E. Dale, J. Eisinger and W. E. Blumberg, *Biophysical Journal*, 1979, **26**, 161–193.

[195] K. Walzer, B. Maennig, M. Pfeiffer and K. Leo, *Chemical Reviews*, 2007, **107**, 1233–1271.

[196] N. B. Teran, G. S. He, A. Baev, Y. Shi, M. T. Swihart, P. N. Prasad, T. J. Marks and J. R. Reynolds, *Journal of the American Chemical Society*, 2016, **138**, 6975–6984.

[197] M. W. Becker, L. S. Sapochak, R. Ghosen, C. Xu, L. R. Dalton, Y. Shi, W. H. Steier and A. K.-Y. Jen, *Chemistry of Materials*, 2002, **6**, 104–106.

[198] K. Ogawa, T. Zhang, K. Yoshihara and Y. Kobuke, *Journal of the American Chemical Society*, 2001, **124**, 22–23.

[199] G. Qian, B. Dai, M. Luo, D. Yu, J. Zhan, Z. Zhang, D. Ma and Z. Yuan Wang, *Chemistry of Materials*, 2008, **20**, 6208–6216.

[200] A. Gankin, E. Mervinetsky, I. Alshanski, J. Buchwald, A. Dianat, R. Gutierrez, G. Cuniberti, R. Sfez and S. Yitzchaik, *Langmuir*, 2019, **35**, 2997–3004.

[201] S. Chandrabose, K. Chen, A. J. Barker, J. J. Sutton, S. K. K. Prasad, J. Zhu, J. Zhou, K. C. Gordon, Z. Xie, X. Zhan and J. M. Hodgkiss, *Journal of the American Chemical Society*, 2019, **141**, 6922–6929.

[202] A. Kay and M. Graetzel, *The Journal of Physical Chemistry*, 2002, **97**, 6272–6277.

[203] G. S. He, J. Zhu, A. Baev, M. Samoć, D. L. Frattarelli, N. Watanabe, A. Facchetti, H. Ågren, T. J. Marks and P. N. Prasad, *Journal of the American Chemical Society*, 2011, **133**, 6675–6680.

[204] A. Ambroise, R. W. Wagner, P. Dharma Rao, J. A. Riggs, P. Hascoat, J. R. Diers, J. Seth, R. K. Lammi, D. F. Bocian, D. Holten and J. S. Lindsey, *Chemistry of Materials*, 2001, **13**, 1023–1034.

[205] Y. Rong, C. Wu, J. Yu, X. Zhang, F. Ye, M. Zeigler, M. Elena Gallina, I.-C. Wu, Y. Zhang, Y.-H. Chan, W. Sun, K. Uvdal and D. T. Chiu, *ACS Nano*, 2013, **7**, 376–384.

[206] F. J. M. Hoeben, P. Jonkheijm, E. W. Meijer and A. P. H. J. Schenning, *Chemical Reviews*, 2005, **105**, 1491–1546.

[207] P. S. Bols and H. L. Anderson, *Accounts of Chemical Research*, 2018, **51**, 2083–2092.

[208] S. Joong Lee, J. T. Hupp and S. T. Nguyen, *Journal of the American Chemical Society*, 2008, **130**, 9632–9633.

[209] M. Fathalla, A. Neuberger, S.-C. Li, R. Schmehl, U. Diebold and J. Jayawickramarajah, *Journal of the American Chemical Society*, 2010, **132**, 9966–9967.

[210] X. Liu, Y. Sun, L. A. Perez, W. Wen, M. F. Toney, A. J. Heeger and G. C. Bazan, *Journal of the American Chemical Society*, 2012, **134**, 20609–20612.

[211] W. Ma, C. Yang, X. Gong, K. Lee and A. J. Heeger, *Advanced Functional Materials*, 2005, **15**, 1617–1622.

[212] E. Mena-Osteritz, *Advanced Materials*, 2002, **14**, 609–616.

[213] J. E. Donehue, O. P. Varnavski, R. Cemborski, M. Iyoda and T. Goodson, *Journal of the American Chemical Society*, 2011, **133**, 4819–4828.

[214] C.-K. Yong, P. Parkinson, D. V. Kondratuk, W.-H. Chen, A. Stannard, A. Summerfield, J. K. Sprafke, M. C. O'Sullivan, P. H. Beton, H. L. Anderson and L. M. Herz, *Chemical Science*, 2015, **6**, 181–189.

[215] G. McDermott, S. M. Prince, A. A. Freer, A. M. Hawthornthwaite-Lawless, M. Z. Papiz, R. J. Cogdell and N. W. Isaacs, *Nature*, 1995, **374**, 517–521.

[216] S. Wang, M. Bohnsack, S. Megow, F. Renth and F. Temps, *Physical Chemistry Chemical Physics*, 2019, **21**, 2080–2092.

[217] T. Kondo, W. Jia Chen and G. S. Schlau-Cohen, *Chemical Reviews*, 2017, **117**, 860–898.

[218] P. Parkinson, D. V. Kondratuk, C. Menelaou, J. Q. Gong, H. L. Anderson and L. M. Herz, *Journal of Physical Chemistry Letters*, 2014, **5**, 4356–4361.

[219] M. Hoffmann, J. Kärnbratt, M. H. Chang, L. M. Herz, B. Albinsson and H. L. Anderson, *Angewandte Chemie - International Edition*, 2008, **47**, 4993–4996.

[220] F. V. A. Camargo, H. L. Anderson, S. R. Meech and I. A. Heisler, *The Journal of Physical Chemistry A*, 2014, **119**, 95–101.

[221] J. Q. Gong, L. Favereau, H. L. Anderson and L. M. Herz, *Journal of Physical Chemistry Letters*, 2016, **7**, 332–338.

[222] L. Adamska, I. Nayyar, H. Chen, A. K. Swan, N. Oldani, S. Fernandez-Alberti, M. R. Golder, R. Jasti, S. K. Doorn and S. Tretiak, *Nano Letters*, 2014, **14**, 6539–6546.

[223] C. E. Tait, P. Neuhaus, M. D. Peeks, H. L. Anderson and C. R. Timmel, *Journal of the American Chemical Society*, 2015, **137**, 8284–8293.

[224] F. V. A. Camargo, C. R. Hall, H. L. Anderson, S. R. Meech and I. A. Heisler, *Structural Dynamics*, 2016, **3**, 023608.

[225] R. Haver, L. Tejerina, H.-W. Jiang, M. Rickhaus, M. Jirasek, I. Grübner, H. J. Eggimann, L. M. Herz and H. L. Anderson, *Journal of the American Chemical Society*, 2019, **141**, 7965–7971.

[226] Y. Wan, A. Stradomska, S. Fong, Z. Guo, R. D. Schaller, G. P. Wiederrecht, J. Knoester and L. Huang, *Journal of Physical Chemistry C*, 2014, **118**, 24854–24865.

[227] C. Didraga and J. Knoester, *Journal of Chemical Physics*, 2004, **121**, 946–959.

[228] M.-H. Chang, M. Hoffmann, H. L. Anderson and L. M. Herz, *Journal of the American Chemical Society*, 2008, **130**, 10171–10178.

[229] R. J. Cogdell, A. Gall and J. Köhler, *Quarterly Reviews of Biophysics*, 2006, **39**, 227–324.

[230] D. Papillon, Y. Perez, X. Caubit and Y. Le Parco, *Molecular Biology and Evolution*, 2004, **21**, 2122–2129.

[231] R. Hildner, D. Brinks, J. B. Nieder, R. J. Cogdell and N. F. van Hulst, *Science*, 2013, **340**, 1448–1451.

[232] D. Abramavicius, B. Palmieri, D. V. Voronine, F. Sanda and S. Mukamel, *Chemical Reviews*, 2009, **109**, 2350–2408.

[233] G. D. Scholes and C. Smyth, *The Journal of Chemical Physics*, 2014, **140**, 110901.

[234] D. V. Kondratuk, L. M. A. Perdigaõ, A. M. S. Esmail, J. N. O'Shea, P. H. Beton and H. L. Anderson, *Nature Chemistry*, 2015, **7**, 317–322.

[235] S. Wolter, K. Magnus Westphal, M. Hempel, F. Würthner, O. Kühn and S. Lochbrunner, *The Journal of Chemical Physics*, 2017, **50**, 184005.

[236] F. Ma, L.-J. Yu, R. Hendrikx, Z.-Y. Wang-Otomo and R. van Grondelle, *The Journal of Physical Chemistry Letters*, 2017, **8**, 2751–2756.

[237] K. Hader, V. May, C. Lambert and V. Engel, *Physical Chemistry Chemical Physics*, 2016, **18**, 13368–13374.

[238] D. V. Kondratuk, L. M. A. Perdigao, M. C. O'Sullivan, S. Svatek, G. Smith, J. N. O'Shea, P. H. Beton and H. L. Anderson, *Angewandte Chemie International Edition*, 2012, **51**, 6696–6699.

[239] T. Kobayashi, *J-Aggregates*, World Scientific, 2012.

[240] N. Zamzam, M. Kaucikas, D. J. Nürnberg, A. W. Rutherford and J. J. Van Thor, *Physical Chemistry Chemical Physics*, 2019, **21**, 1224–1234.

[241] S. Athanasopoulos, E. V. Emelianova, A. B. Walker and D. Beljonne, *Physical Review B*, 2009, **80**, 195209.

[242] G. Trinkunas, J. L. Herek, T. Polívka, V. Sundström and T. Pullerits, *Physical Review Letters*, 2001, **86**, 4167–4170.

[243] Y. Song, A. Konar, R. Sechrist, V. P. Roy, R. Duan, J. Dziurgot, V. Policht, Y. A. Matutes, K. J. Kubarych and J. P. Ogilvie, *Review of Scientific Instruments*, 2019, **90**, 013108.

[244] N. M. Kearns, R. D. Mehlenbacher, A. C. Jones and M. T. Zanni, *Optics Express*, 2017, **25**, 7869.

[245] M. Son, S. Mosquera-Vázquez and G. S. Schlau-Cohen, *Optics Express*, 2017, **25**, 18950.

[246] B. Spokoyny, C. J. Koh and E. Harel, *Optics Letters*, 2015, **40**, 1014–7.

[247] X. Ma, J. Dostál and T. Brixner, *Optics Express*, 2016, **24**, 20781.

[248] J. C. Travers, T. F. Grigorova, C. Brahms and F. Belli, *Nature Photonics*, 2019, **13**, 547–554.

[249] Z. Zhang, K. L. Wells, M. T. Seidel and H. S. Tan, *Journal of Physical Chemistry B*, 2013, **117**, 15369–15385.

[250] M. Kaucikas, K. Maghlaoui, J. Barber, T. Renger and J. J. van Thor, *Nature Communications*, 2016, **7**, 13977.

[251] E. Romero, V. I. Novoderezhkin and R. van Grondelle, *Nature*, 2017, **543**, 355–365.

[252] F. Koch, M. Kullmann, U. Selig, P. Nuernberger, D. C. G. Götz, G. Bringmann and T. Brixner, *New Journal of Physics*, 2013, **15**, 025006.

[253] C. C. Jumper, J. M. Anna, A. Stradomska, J. Schins, M. Myahkostupov, V. Prusakova, D. G. Oblinsky, F. N. Castellano, J. Knoester and G. D. Scholes, *Chemical Physics Letters*, 2014, **599**, 23–33.

[254] M. Son, K. H. Park, C. Shao, F. Würthner and D. Kim, *Journal of Physical Chemistry Letters*, 2014, **5**, 3601–3607.

[255] C. Kaufmann, W. Kim, A. Nowak-Król, Y. Hong, D. Kim and F. Würthner, *Journal of the American Chemical Society*, 2018, **140**, 4253–4258.

[256] J. Guilleme, D. González-Rodríguez and T. Torres, *Chemical Communications*, 2016, **52**, 9793–9796.